286 p.

N64 11330

CODE-1

NASA CR 52875

ANNUAL SUMMARY REPORT

METALLURGICAL EFFECTS OF EXPLOSIVE
STRAIN RATES ON METAL ALLOYS

0513-01(01)FP

Contract NAS8-2416

27 June 1961 - 26 July 1962

OTS PRICE

XEROX $ 18.00 ph

MICROFILM $ 8.78 mf.

ORDNANCE DIVISION

Aerojet-General®

CORPORATION

A SUBSIDIARY OF THE GENERAL TIRE & RUBBER COMPANY

AZUSA, SACRAMENTO, AND DOWNEY, CALIFORNIA

RQT-6948

ANNUAL SUMMARY REPORT

t: METALLURGICAL EFFECTS OF EXPLOSIVE

STRAIN RATES ON METAL ALLOYS Annual.. 27 Jun.
1961 - 26 Jul. 1962

J. F. Wilkin,
E. K. Henriksen,
I. Lieberman, and
C. A. Landusky date 286 p refs

0131755 AEROJET-GENERAL CORPORATION
Ordnance Division
11711 Woodruff Avenue
Downey, California

(NASA CR-52875; Report No. 0513-01(01)FP) OTS:

(NASA Contract NAS8-2416)
GEORGE C. MARSHALL SPACE FLIGHT CENTER
NASA, Huntsville, Alabama

26 July 1962

COPY No. 30

FOREWORD

This report was prepared by Aerojet-General Corporation under Contract No. NAS8-2416 for the George C. Marshall Space Flight Center of the National Aeronautics and Space Administration. The work was administered under the direction of the Propulsion and Vehicle Engineering Division, Engineering Materials Branch of the George C. Marshall Space Flight Center with W. B. McPherson acting as project manager.

The assistance of the following Aerojet personnel whose contributions did much to aid in the successful completion of the program is acknowledged: R. E. Herfert, T. Matsuda, R. A. Rawe and Dr. L. Zernow.

ABSTRACT

11330

A series of selected alloys has been subjected to conventional and explosive straining in an investigation designed to compare the effects upon the mechanical properties of the material, to observe the changes in the metallurgical structure, and to develop an explanation of the mechanism to explain differences in behavior and structure.

The following materials were subjected to study: 5456-0 aluminum, AISI 301 stainless steel, 17-7PH stainless steel, and the two titanium alloys, 6Al-4V and 13V-11Cr-3Al.

Both uniaxial and biaxial loading conditions were explored, with some materials tested under both ambient and cryogenic (-320°F) temperatures.

From the results obtained, it is concluded that:

(a) The mechanical properties of a metal are sensitive to the magnitude of the applied strain and to the rate and temperature at which the strain is applied. However, with some materials, the general trends which are established may be quantitatively modified or obscured by specific transformation processes peculiar to an individual material.

(b) Changes in metallurgical structure resulting from explosive straining are not prominent, and differences in structural change due to the strain rates within the range investigated are apparently sub-microscopic.

AUTHOR

CONTENTS

LIST OF TABLES

LIST OF TABLES (Cont.)

LIST OF TABLES (Cont.)

LIST OF FIGURES

LIST OF FIGURES (Cont.)

LIST OF FIGURES (Cont.)

LIST OF FIGURES (Cont.)

LIST OF FIGURES (Cont.)

LIST OF FIGURES (Cont.)

LIST OF FIGURES (Cont.)

LIST OF APPENDIXES

1. INTRODUCTION

1.1 AEROSPACE REQUIREMENTS.

Present requirements for space vehicles are such that conventional, well-established fabrication processes are, in many cases, unable to handle the size, shape and accuracy requirements with the new materials required. Because of these factors, it has become necessary or advantageous to employ the explosive forming techniques.

Minimum weight and maximum strength must be maintained in formed parts. Therefore, it is of prime importance that the mechanical properties of materials, after they have been explosively formed, be known. It is also essential that the formability of materials at practical explosive strain rates be established. This information enters into considerations of material selection, production planning, tool design, and blank configuration.

This research program was initiated to supply information on behavior of metals subjected to explosive strain rates. A comprehensive literature survey, conducted within the program, confirmed that the fund of data available in the above categories is indeed meager and in some areas of current interest non-existent.

1.2 OBJECTIVES OF THE RESEARCH PROGRAM

a. To determine the basic mechanisms that occur during forming at practical explosive forming strain rates.

b. To evaluate the effects of these mechanisms on mechanical properties of structural alloys.

To understand and to account for the changes that occur in mechanical properties due to strain rate effects, investigative emphasis is placed on changes in microstructure, phase changes, changes in lattice constants, and unusual behavior of dislocations. An effort to detect trends common to all materials, or to specific groups of materials, will effect an economy of research effort and will make available more information at the earliest possible date.

1.3 LITERATURE SURVEY

The literature survey uncovered a number of publications which were studied and evaluated. Comprehensive studies in book form (Ref. 32 and 33), some bibliographies (Ref. 48, 49, 50 and 51) and individual research reports were examined.

1.3.1 Search Procedure

Form letters soliciting information were mailed to likely sources and the libraries were searched. Despite the large volume of published and otherwise disseminated materials, the returns on the search - in terms of specific numerical strain rate data and their metallurgical effects - were meager.

1.3.2 Brief Historical Outline

The earliest attempts to correlate changes in physical properties with the strain-rate during the loading phase have been traced back to the elder Hopkinson (John Hopkinson) who in 1872 (Ref. 27) performed experiments on steel wires by loading them with dropping weights. Further work on plain carbon steel was done in 1905 by B. Hopkinson (Ref. 28).

The fundamental trend discovered in the early work was that the dynamic yield stress is higher than the static yield stress. It was further found that for a given steel, the increase in yield stress would increase with the loading rate. This strain-rate effect varies from material to material and depends on the static yield. The higher the static yield, the less the strength is increased by high-rate loading. At a strain rate of approximately 1.5 in/in/sec, the increase in yield stress was approximately 88 percent for a low carbon steel.

During this early period, some attempts were made by Ludwik, Prandtl, and Deutler to formulate a law for the experimentally determined strain-rate sensitivity. All three of them worked on the basis of a logarithmic law, according to which the change in stress during a rapid loading operation is proportional to the logarithm of the strain-rate. In 1909, Ludwik (Ref. 3) suggested the logarithmic dependence on empirical grounds. Prandtl (Ref. 4) in 1928 proposed it as a result of a physical theory of plastic flow. Deutler (Ref. 5), published in 1932, in his experimental data gave further support to the same relationship.

In the period 1930-1940, some more attention was drawn to problems of impact loading and dynamic strength of materials. The theories and techniques of wave propagation, elastic as well as plastic, in solids, began to take shape, and experimental equipment became available.

The outbreak of World War II gave the impetus to a strong acceleration of work in these fields. Much of the work done was initially classified, but was subsequently declassified and published in the open literature. Therefore, the publication dates under which the various contributions will appear in the bibliography do not necessarily represent the priority which actually may be due to the authors. Several cases are known where highly important scientific results were rediscovered and published abroad while still kept under security regulations in this country.

1.3.3 The Clark & Wood Data

The most comprehensive set of data on dynamic properties of metals and their alloys is that by Clark and Clark & Wood (Ref. 6 and 7). In these two publications, taken together, they present experimentally obtained dynamic property data for eighty-two different materials and conditions.

It clearly appears from these data that oversimplification and over-generalization is dangerous. Each material behaves in its own individual way with respect to dynamic deviations from static properties. However, with proper grouping of the materials, it is still possible to establish some general trends and thereby make the data usable as a basis for predicting dynamic behavior of materials not yet actually tested dynamically.

As a collection of data on dynamic properties of metals under defined loading conditions, this work still stands unexcelled. Because of its unique value as a reference source, an abbreviated extract with a systematic presentation of the data has been prepared and is submitted as part of Appendix A1.

The Clark and Wood dynamic data are correlated with impact velocity rather than with strain rate. Their experimental procedure does not readily permit a transformation to strain rate.

1.3.4 The Von Karman Theory and Related Subjects

A theory for the uniaxial propagation of a plastic impact wave was published in 1950 by von Karman and Duwez (Ref. 8). The theory was actually developed in 1942, but kept classified during the war. Similar theories were published in the intervening interval by G. I. Taylor (Ref. 9 and 10), and by Rakhmatulin and Shapiro (Ref. 11, 12, and 13).

In the original version of the von Karman theory, for reasons of simplicity, the material is assumed to be strain-rate insensitive. Despite this approximation, the theory was found to be highly valuable. For example, it predicted the existence of a critical impact velocity, at which normally ductile materials exhibit brittle or semi-brittle failure. The Clark and Wood data confirmed this prediction.

However, other measurements indicated the desirability of further refinement of the theory. The lack of complete agreement between observations and theory gave rise to activity in the study of strain-rate effects. Contributions to the clarification of this problem were given by Bohnenblust, Malvern, Riparbelli, Sternglass and Stuart, and Zener and Holloman.

All aspects taken into consideration, it appears that Malvern (Ref. 14) stands as the originator of the most realistic analysis of strain-rate effects.

Malvern's analysis assumes that the increase of the yield stress under dynamic conditions is a logarithmic function of the strain-rate, somewhat similar to the suggestions by Ludwik, Prandtl, and Deutler. Malvern's analysis may, according to Dorn, Hauser and Simmons (Ref. 15) have to be modified in order to account for the acceleration of dislocations.

It should be understood that the interest of this group of investigators appears to concentrate on the behavior of the yield point or yield stress as it occurs instantaneously during the process of straining at an elevated strain rate, including the occurrence of a time delay in the yielding. These works do not attempt to clarify to what extent the yield point and other properties, notably those associated with fracture, are permanently affected as a result of a previously applied high rate of strain.

As to actually applied strain rates, Riparbelli's work is confined to strain rates below 1200 in/in/min, while Malvern studies the range from 6000 to 24000 in/in/min.

1.3.5 British Contributions

Early British contributions are of interest because they show the basic concepts, as well as the general trend of the numerical data at an early date. More recent work has provided conclusive results for a variety of materials, tested over a wide range of well-defined strain rates. The pertinent data are presented in abbreviated form in Appendix A2.

1.3.6 Westinghouse Data

A prominent collection of data, in effect the best hitherto found, has been published by Nadai and Manjoine from tests made in the Westinghouse Laboratories. Ferrous, as well as non-ferrous materials were tested, and almost all were conducted over a strain rate range up to 1000 in/in/sec or higher; in other words, through and above the same range as the one which is covered by this program. Ultimate and yield strength, as well as elongation, were tested. The pertinent data have been consolidated and are presented in Appendix A3.

1.3.7 General Effects of Impulsive Loads on Metals

The need for information on the effects of impact loading on metal structures prompted the publication of a book "Behavior of Metals Under Impulsive Loads", by John S. Rinehart and John Pearson, in 1954 (Ref. 31). With the subsequent intense interest in the explosive forming process, this book has enjoyed a wide circulation and has presumably influenced the thinking of many workers in this field. While the dissemination of knowledge is always desirable, it should always be remembered that it may be dangerous to attempt to extrapolate findings and conclusions outside of the range where they were developed.

This general remark is particularly appropriate in the present case, because the book by Rinehart and Pearson does not cover explosive forming for the simple reason that explosive forming existed only in isolated cases when the book was written and published (in 1954). It deals largely with severe damage effects such as fracture, fragmentation, and scabbing, caused by contact explosions. It is still today a high-ranking source of information about this very special subject. However, the systematic verbal and pictorial presentations, in themselves excellent, of the destructive effects of explosives have undoubtedly in the minds of many persons instilled a feeling of fear of, or at least a suspicion of, explosive forming as a process by which structural materials may suffer mysterious microstructural damage.

There is no reason why this should be the case. The stress intensities and strain rates used in explosive forming are, fortunately, much lower - probably by several orders of magnitude - than the corresponding parameters for explosive damage processes.

The value of the book for the present study lies in the detailed discussion of the various aspect of microstructural changes (not necessarily destructive) supported by some excellent reproductions of micrographs. Condensed extracts from these sections are given in Appendix A4, preceded by definitions and explanations of various terms.

1.3.8 Selected Topics from Other Literature Sources

1.3.8.1 What is the Correct Fundamental Parameter?

It has been assumed, as the basis for this program, that it is possible to correlate dependent variables, such as metallurgical and mechanical properties and microstructural changes, with the applied strain rate as the fundamental independent parameter.

This is a natural parameter selection and the results obtained from the present program indicate that it is also a feasible one. No dirett confirmation has been found from literature, as stated before, because of lack of specific data on properties after prestraining at well-defined strain rates.

The preferred parameter appearing in a number of publications is the shock strength, expressed as the maximum shock pressure, usually measured in kilobars. It has been found repeatedly that iron and some other metals undergo phase changes when the shock strength is sufficiently high.

The phase change involved with iron was originally assumed to be the alpha-gamma transformation, although C. M. Fowler, F. S. Minshall, and E. G. Zukas (Ref. 33, p 308) have expressed some doubt about it. Basically, the actual phase change is considered a reversible one and should therefore reverse itself at unloading so that no permanent trace of a microstructural nature is left behind. A great deal of discussion has taken place as to the origin of slip lines, twins, and other visual indications of permanent microstructural changes. The most common explanation is that they are caused by plastic strain preceding or accompanying the shock. So far, the shock strength should be the fundamental parameter. However, the situation is no longer that simple. In 1958(Ref. 34), C. S. Smith showed that the pattern of slips and twins is controlled, not just by the primary shock, but actually by the interaction between the oncoming shock and the reflected rarefaction wave. Confirmation hereof is found in a contribution by Fowler, Minshall, and Zukas (Ref. 33, p 278) where they show very clearly that two microstructurally different zones may exist in a single specimen, characterized as the high pressure zone and the low pressure zone, caused by interaction as described. The reason for these complications is the wave-nature of the moving shock.

The conclusion to be drawn for actual explosive forming conditions is that attention should be given to the possibility of wave phenomena before attempts are made to correlate results. Such wave phenomena are undoubtedly always present. At low strain rates, such as 100 in/in/sec or 6000 in/in/min, they are barely noticeable, but at higher strain rates, which may come within the range of practical explosive forming, they will be significant and could well be responsible for disturbances in correlations.

1.3.8.2 Hardness Plateaus and Twinning

Rinehart and Pearson (Ref. 31) have drawn attention to the simultaneous occurrence of several intersecting families of twins. This subject has been further studied by Sampoaran Singh, N. R. Krishnaswamy, and A. Soundraraz (Ref. 35). They found that up to four different twin families could exist in a single grain and that the hardness of the individual grain was a function of the number of simultaneously existing twin families. With no change in the number of twin families, there should be no change in the hardness, and they actually determined a hardness curve exhibiting four flats or plateaus, corresponding to the number of twin families. Hardness plateaus were also found by H. P. Tardif, F. Claisse, and P. Chollet (Ref. 33, pp 398-399).

1.3.8.3 Deformation Bands

The occurrence of bands, other than Neumann bands, has been reported by Samuel Katz and R. E. Peterson (Ref. 36) and by Samuel Katz, D. G. Doran, and D. R. Curran (Ref. 37). They found in explosively loaded specimens a pattern consisting of two crossing systems of lines, each under 45° angle with the surface. The origin of the lines has not yet been established. Very similar markings, referred to as a "chevron pattern", have been observed recently in the Aerojet research program conducted under Contract No. AF33(606)-8191 (Ref. 38). The origin of these lines appears to be related to the sheet rolling process.

1.3.8.4 Recrystallization Possibilities

The normal mode of occurrence of twins is within each single grain separately. Twins may also cross grain boundaries, but in such cases they usually suffer a considerable change in direction at the crossing point. This is quite natural and logical when it is remembered how a twin is formed from the existing crystal lattice structure, as explained in Appendix A2.

R. J. Eichelberger (Ref. 32, p 146) has shown a photomicrograph of a twin extending across two adjacent grains with practically no change in direction (Fig. 1). He draws attention to the observation in the text, but does not attempt to explain the reason for it.

The same subject has been examined closer by Tardif, Claisse, and Chollet (Ref. 33, pp 401-406) who investigated cases where twins cross boundaries between ferrite and pearlite grains without change in direction (Fig. 2). They explain the observation by the fact that adjacent ferrite and pearlite grains may have the same orientation because they are formed by a diffusion and precipitation process within one larger grain in the matrix of solid solution of iron carbide in iron.

A similar observation for columbium was made by G. E. Dieter (Ref. 33, p 428) (Fig. 3).

After this observation was made, closer examination of a number of micrographs, particularly from Ref. 38 and 39, shows similar cases of twins extending outside of one grain without or with very small deviation in direction. This was found for ferrite grains as well as for pearlite grains and, in some cases, the twin would be found to extend to a considerable distance (Fig. 4 and Fig. 5).

The frequency with which this observation in oron was made inferred that a mechanism may be present other than the accidental and random occurrence of similarly oriented neighboring grains. The mechanism here proposed is that of recrystallization.

It is known that recrystallization occurs at elevated temperature and that heating may occur during explosive loading operations (see Appendix A4, pp A4-4, and Ref. 33, E. G. Zukas and C. M. Fowler, pp 353-355) by one or two adiabatic processes. The temperature rise may well be of the order of several hundred degrees, and cannot be dismissed as insignificant.

On the other hand, recrystallization is known to be normally a process requiring some time-duration. The question remains as to whether the time available is sufficient for recrystallization to occur with reorientation of crystal structures.

From these considerations, one may be led to the conclusion that recrystallization is a pressure-dependent process and that the recrystallization rate increases (regardless of temperature) with increased pressure.

1.3.8.5 Strain and Strain Rate Problems

The work by Ludwik, Prandtl, Deutler, Malvern and others, together with the increasing understanding of the mechanics of longitudinal impact wave propagation in bars has gradually shifted the emphasis from impact velocity data to strain rate data and has established the need for quantitative strain rate determination in connection with explosive forming.

Excellent and highly accurate methods exist for determination of all parameters, including strain rate, in connection with shock wave propagation through massive bodies; however, these methods are not directly applicable to explosive forming of sheet metal, partly because explosive forming is mainly associated with loading in tension where shock wave theory does not apply, and partly because, in most cases, the stress and strain pattern is biaxial.

Theoretically, the measurement of strain rate requires measurement of infinitesimal increments of dimension and time. This is physically impossible, but by skillful modification it is possible to obtain strain rate data from measurement of finite quantities.

For fundamental research purposes, it is possible to simplify the test system so as to render it uniaxial. As stated before, an impact load applied to one end of a tensile test specimen is bound to create an axial wave propagation through the part. Within the framework of this program, the wave component was found to be insignificant. When higher velocities are used, the wave component cannot be ignored.

A plastic wave leaves the bar with a non-uniform strain pattern, which actually is a permanent record of the wave intensity itself. By strain measurements and application of known theory, it is thus possible to establish knowledge of corresponding values of dynamic stress and strain, if needed. The method is not difficult but somewhat time-consuming.

Above a certain high impact velocity, the so-called critical velocity, the method is no longer applicable because of the fracture which occurs instantaneously at the impact end. This critical velocity is a product of the general wave dynamics of the system rather than an indication of a specific material property, and is therefore a disturbing factor.

For these reasons, it appears desirable to find a uniaxially loaded system without a wave effect. Such a system is found in a circular ring, cylinder or tube, expanding uniformly under the influence of the kinetic energy imparted into its mass by an evenly distributed impact - for example, from an explosive charge. When the tube or cylinder is short, so that the system becomes a ring, then the stress and strain system (after expiration of the energy transmission period) becomes a uniaxial system. With a significant axial length, the system becomes biaxial. The method was first proposed by E. K. Henriksen (Ref. 40) and the theory subsequently applied to design of cylindrical dies and to the process of truing or sizing (Ref. 41, 42, 43).

The same principle was applied to uniaxial strain rate studies by Johnson, Stein and Davis (Ref. 44) and by Wood et al (Ref. 45). In the investigation by Johnson et al, stress developed during the straining cycle was determined but no attempt was made to determine the permanent change in mechanical and metallurgical properties. Wood et al found for the three materials - 17-7 PH stainless steel, Vasco-jet 1000, and 6Al-4V titanium - that the fracture strain increased at increasing strain rate. A similar effect was not observed for Rene 41 and A-286. The strain rate as such was not given, but only the radial velocity. Their data are:

Material	Maximum Fracture Strain (in/in)	Radial Velocity at which Maximum Fracture Strain was obtained (ft/sec)
17-7PH Stainless Steel	0.55	350
Vascojet 1000	0.23	200
6Al-4V Titanium	0.12	100
Rene 41	0.28	Constant for all velocities.
A-286	0.25	

No case is known where a critical velocity, equivalent to the critical impact velocity for prismatic bars, has been observed in an expanding ring.

1.3.8.6 Appropriate Definition of Strain

It is conventional in materials testing to define the elongation at fracture on the basis of a gage length. This procedure is insufficient for dynamic studies because it is not a true material property in that necking usually precedes failure.

Necking has been studied extensively for quite a number of years, and it is understood that it is an instability effect; consequently, since the amount of necking affects the elongation as measured from the gage length, the elongation is no longer a pure material property.

The matter is further aggravated by the fact that multiple necking may occur in a single test specimen. A detailed study of this phenomenon is given by Wood et al (Ref. 45). Their findings are similar to those of the present program, in which multiple necking was observed quite frequently in titanium alloys if the specimen was prestrained too far.

The effect of necking on ductility data is automatically eliminated if all strains are converted to natural (logarithmic) strains. This has been done in the present program, and comparison made with conventional strains. It was repeatedly found that the observed trends become much more consistent and unified when based on terms of natural strain than when based on conventional strain.

1.3.8.7 The Behavior of Austenite

In the present program, it was found that 301 stainless steel, an austenitic material, showed less increase in ductility with increase in strain rate than the other materials tested. It was therefore of particular interest to find, during the preparation of this report, one observation which is in complete agreement with those made under this program, and the explanation offered was along very similar lines. Williams (Ref. 46) has observed this individual behavior of 18/8 type stainless steel. His observation and comments are so significant that they are quoted verbatim:

> "It is of interest to note that the four materials which work hardened more on explosive forming than on pressing all possessed face centred cubic lattices, while mild steel and titanium have lattices of the body centred cubic and close packed hexagonal types respectively at room temperature.
>
> Campbell and Duby [1] have found that the dynamic impact of a 0.24 per cent carbon steel caused a smaller increase in hardening than when the material was slowly deformed to the same extent. They suggested that dynamic impact would activate a larger number of dislocations than static deformation because of the much higher stresses applied during the short period of loading. The larger number of free dislocations might then permit the steel to deform more easily on subsequent re-loading, i.e. hardness testing.

[1] Campbell, J.D. and Duby, J. Proc. Roy. Soc., 1956, 236A, p 24. (Ref. 52)

In the case of stainless steel any such effects are masked by allotropic changes. Austenitic stainless steel of the 18/8 type is only truly stable at temperatures above 400°C, but material quenched to the metastable state will not transform on holding indefinitely at room temperature. For the establishment of equilibrium more energy must be applied to the system, and the application of cold work can provide energy to cause the material to assume, at least partially, the stable condition. The austenite decomposition product appears as low-carbon martensite, and any untransformed austenite remains in a severely stressed state, so that a considerable increase in hardness and loss of ductility are experienced. Under the conditions of shock loading in explosive forming, more martensite is formed than on slow pressing."

In the cryogenic tests in the present program, it was found that prestraining at a low temperature had a similar effect as prestraining at a higher strain rate. A confirmation of an observation of this type, with respect to austenitic stainless steel, was found by Kribovok and Talbot (Ref. 47). They found considerably greater rate of work hardening when stainless steel was formed at cryogenic temperatures than when formed at room temperature.

1.3.9 Conclusion

It was intended to conduct the study of the literature for the purpose of accumulating and presenting existing data on the correlation between strain rate and microstructural changes, the strain rates to be of the same order of magnitude as those used in practical explosive forming; that is, in the range from 100 in/in/sec to 1000 in/in/sec.

Based on this specific definition of the purpose of the literature study, it must be stated that the result has been 100 percent negative, as no attempt to perform this correlation has been found in the literature.

In view of the fact that explosive forming research and development has been underway for approximately six years in numerous places, this situation calls for an explanation. The most likely explanation is that a reasonably exact determination of strain rates is a difficult problem. Direct experimental measurement of strain rates is highly time-consuming and expensive. Indirect determination of strain rates by means of analysis of measured deformations is tedious and complex.

However, despite the absence of this data from the literature study, it did produce a number of observations which are sufficiently closely related to the subject to justify being presented here.

The extensive recent investigations of strain rate effects are mostly aimed at the stress-strain relations in the vicinity of the yield point, at the time-delay in the yielding, and at the effects of strain rates and associated pressures of a much higher level than those found with explosive forming.

Some explosive forming reports did approach the subject: however, they suffer from lack of strain rate data and lack of appropriate and well-defined strain data.

The two major contributions as of today are the Clark & Wood data, and the Westinghouse data.

2. TEST MATERIALS

Five (5) test materials were chosen for the investigation of strain and strain rate effects on mechanical properties and microstructural changes. The five metal alloys are:

5456-0 Aluminum Alloy
AlSl 301 Stainless Steel
17-7 PH Stainless Steel
6Al-4V Titanium Alloy
13V-11Cr-3Al Titanium Alloy

The 5456-0 aluminum alloy was supplied by MSFC, and no chemical certification of the material was furnished. Suppliers' chemical certifications for the other materials are listed in Tables I through IV, together with the applicable specification limits. All test materials were obtained in nominal 0.100-inch thickness.

For control purposes, mechanical properties tests were conducted on all materials as received, both longitudinal and transverse to the rolling direction of the material. All specimens subjected to uniaxial straining prior to testing were prepared in the transverse direction as lower mechanical property values are usually found in the transverse direction and practical design criteria should be based on the lower values.

Test material was subjected to several degrees of strain at both conventional and explosive strain rates prior to mechanical properties testing and metallographic examination. For the purposes of this report, the strain prior to testing is defined by the term "prestrain", and the unit elongation as determined in the standard tensile test subsequent to prestraining is defined as "test strain".

2.1 SPECIMEN CONFIGURATION

In the preparation of specimens for uniaxial prestraining, the sheet material was sheared into 8-inch long by 1-3/8-inch wide blanks and machined to a modified standard tensile specimen with the dimensions as shown in Figure 6. It will be noted that the width in the gage length varies with material, prestraining temperature, and material condition. Widths of the specimens provided allowance for area reduction during prestraining while retaining sufficient stock for remachining the gage length to 0.500-inch width prior to tensile testing. During the course of the program, the widths were revised as shown to eliminate specimen failures which occurred as tensile failure across the load pin hole, as bearing failure behind the load pin hole, or as a result of stress concentration at the radius adjoining the gage length. The same specimen configuration was used in uniaxial prestraining, for subsequent standard tensile testing, for edge-notch tensile testing, and for microstructural examination. The edge-notch tensile specimen is shown in Figure 7.

2.2 HEAT TREATMENTS

In addition to testing as prestrained, the heat-treatable alloys were tested with appropriate intermediate heat treatments, and control tests were run on the heat-treated amterials without prestrain. The heat treatments which were used are as listed below:

2.2.1 17-7PH Stainless Steel

TH1050 - For the Control Specimens:

Heat to 1400°F and hold for 90 minutes.

Air cool to 60°F $^{+\,0^\circ F}_{-10^\circ F}$ and hold for 30 minutes minimum.

Heat to 1050°F and hold for 90 minutes.

Air cool to ambient temperature.

The aging treatment for the CH900 condition consisted of heating to 900°F and holding for one hour and allowing to air cool to ambient.

The TH1050 condition was applied in order to provide a check of the material's response to heat treatment by comparing the results with published minimum values established by the manufacturers. The 1400°F austenite conditioning portion of this treatment would tend to remove the effect of straining in the prestrained specimens; therefore, these specimens were given the CH900 treatment which is an aging treatment. This provided a basis for comparing results with published cold-rolled and aged properties.

2.2.2 6Al-4V Titanium

Solution treatment: 1700°F $^{+\,25^\circ F}_{-\;\,0^\circ F}$ for 1 hr. water quench.

Age: 1000°F for 8 hrs.

The control specimens were solution-treated and aged. The material, which was prestrained, was solution-treated prior to straining and aged after straining. This alloy must be in the solution-treated condition in order to respond to an aging treatment; therefore, it was strained in the solution-treated condition, since application of this treatment subsequent to straining would otherwise tend to remove the effects of straining due to the high temperature employed.

2.2.3 13V-11Cr-3Al Titanium

The material was received in the solution-treated condition and tested "as-received" and "as-received and aged" for control tests. The material was strained in the solution-treated condition and tested for mechanical properties in the strained condition and in the strained and aged condition. The aging cycle used was 800°F for 24 hours.

Since 13V-11Cr-3Al was supplied in the solution-treated condition, it was not necessary to apply any other heat treatment prior to straining. The specimens were aged after straining.

3. EXPERIMENTAL PROGRAM

In this program, the test materials were prestrained under the following conditions:

Strain Field:

- Uniaxial
- Biaxial

Strain Rate:

- Conventional
- Explosive

Applied Strain Temperature:

- Ambient
- Cryogenic

Subsequent to prestraining, the mechanical and metallurgical properties were determined by the following methods. (Control samples were also subjected to these tests.)

Tensile Test:

- Proportional limit
- 0.2% offset yield strength
- Ultimate tensile strength
- % elongation in 2 inches
- % reduction of area
- Modulus of elasticity

Microhardness

Notch sensitivity as determined by the sharp edge-notch tensile test

Optical Microscopy

Electron Microscopy

X-ray Diffraction

Strain data and mechanical properties of control and strained uniaxial specimens are presented in Tables V through IX. The straining techniques and investigative methods will now be discussed in detail.

3.1 UNIAXIAL STRAIN FIELD

Test specimens for uniaxial prestraining were prepared as described in Section 2. They were subjected to purely axial loading. By this system, good control of applied strain could be maintained.

3.1.1 Conventional Strain Rate

3.1.1.1 Ambient Temperature

Conventional straining to simulate normal pressing and forming operations was performed in a standard tensile testing machine. By running the machine in "rapid traverse", the resultant strain rate within the 2-inch gage length was 3 in/in/min. Early prestraining of 301 stainless steel was performed at the highest speed, using the hydraulic system which gave a strain rate of 0.03 in/in/min. The data for these tests are recorded, but the tests were also repeated at the higher strain rate. The specimens were secured in grips, and practically all of the elongation was confined to the 2-inch gage length.

At least two specimens of each material were strained to fracture in order to establish the fracture strain. Subsequent specimens were then strained to prescribed percentages of the fracture strain by unloading the tensile machine at a precise moment during the straining operation.

3.1.1.2 Cryogenic Temperature (Liquid Nitrogen, -320°F)

Conventional prestraining at -320°F was performed essentially as above but with the addition of a special fixture for holding the specimen which could be lowered into a Dewar flask. This permitted the specimen to be completely immersed in liquid nitrogen during prestraining. The specimen was pin-loaded, as the special fixture would not accommodate grips. For 301 stainless steel, the problem of load pin hole elongation resulted in reduced strain rates being obtained within the gage length. Approximately one-half of the total elongation occurred in the grip area, so the strain rate is recorded as 1.5 in/in/min.

3.1.2 Explosive Strain Rate

3.1.2.1 Ambient Temperature

A dynamic test fixture was used as shown in Figure 8 for explosive prestraining. A test specimen was secured in position, an explosive charge was placed on the driver plate, and the charge was detonated. The required explosive charge varied from 33 grams to 120 grams, depending on material and specimen width. The ram was permitted to pull the specimen to fracture. In subsequent tests, after the total strain to fracture had been determined on at least two specimens of each material, the stop was set to a point which would give the desired percentage of total strain at fracture. Allowance had to be made for elongation in the grip area in adjusting the stop. A combination of grip and pin loading was used, and some load pin hole elongation nearly always resulted.

It is estimated that the dynamic test fixture has an upper strain rate limit of approximately 200 in/in/sec. If it is desired to use the fixture at higher strain rates, it will have to be strengthened to withstand higher explosive charges, and the adjustable stop will require a damping arrangement in order to eliminate excessive rebound which would tend to distort the prestrained, non-fractured specimen.

3.1.2.2 Determination of Explosive Strain Rate

Strain rates developed in the dynamic test fixture were determined for each material by high-speed photography. A split frame, 16mm Fastax Camera with framing speeds up to 14,000 fr/sec was used to record the event from just prior to detonation to after fracture. The camera lens and tensile specimen were adjusted to the same height to eliminate parallax, and the lens to object distance was 10 feet. Four photospot lamps were focused on the test specimen, and this lighting proved adequate.

To protect the camera equipment from the explosive and to minimize obscuration of the event by products of detonation, a 1-inch thick steel barricade was welded to the guideplate of the dynamic test fixture and positioned as shown in Figure 9. Despite this precaution, the specimen was obscured during straining on many of the films (see Fig. 10). On such films, measurement of the specimen could not be made after detonation, but for twelve films, the frame at which fracture occurred could be estimated, and the average approximate strain rate was calculated. These strain rate values are tabulated in Table X.

The strain was obtained by measuring the original 2-inch gage length on the fractured specimen. The framing rate was determined by counting the number of frames between the millisecond timing marks on the edge of the film. To obtain the approximate number of frames to fracture, the film was carefully examined in a film reader. Where the first indication of fracture could be observed, the number of frames to fracture as counted from the first indication of detonation gases appearing, are indicated in the table by an approximation sign. Where the first distinguishable frame showed the specimen fractured and separated, the actual number of frames to fracture is indicated as being less than the recorded value. From the three measured quantities, the average strain rate was calculated as follows:

$$\text{Strain Rate} = \frac{\text{Strain (in/in)} \times \text{Frame Rate (Fr/sec)}}{\text{Frames to Fracture (Fr)}} = \text{in/in/sec}$$

One film, Figure 11, was sufficiently free of obscuring gases to allow measurement of every frame from detonation to fracture. The distance between the shoulders formed by the radii and the grip width of the specimen was measured on a microscope with a micrometer stage. Three (3) traverses were run, averaged, and recorded in Table XI. The unit of length is arbitrary. It will be noted that the range of measurements is greater where definition of the specimen is reduced by gases.

Since shoulder length was measured on the specimen before straining and after fracture, the actual lengths represented by the film readings were established for these two points, and all intermediate points were calculated by the proportion:

$$\frac{F-159}{39} = \frac{S-3.14}{0.72}$$

where F is the film measurement and S is the shoulder measurement.

A record was kept of the 2-inch gage length and shoulder length after straining for all explosively strained specimens. These measurements are tabulated for all of the 5456-0 aluminum specimens in Table XII, and gage length is plotted against shoulder length in Figure 12. From this curve, the gage length and corresponding strain at each film frame were recorded. Knowing the framing rate and thus the time interval per frame, strain was plotted against time in Figure 13. The strain-time curve was then graphically differentiated to give the strain rate curve over the complete straining period. Increments taken were sufficiently small to assume, without undue error, that strain was linear within each time interval. The method is thus very discriminating and allows a detailed analysis of the straining process.

The graph for the strain curves from its inception. This is caused by the gradually increased work-hardening of the material. The graph shows also a distinct difference in curvature between the early part and the later part; in fact, the early part of the curve is nearly a straight line. This observation is a visual confirmation of the conclusion, drawn elsewhere in this report from a comparison between the yield point and the true ultimate stress - namely, that the work-hardening is delayed at explosive forming rates. Prior to fracture, the strain curve rises rapidly. This is due to the reduction of the load in the specimen as the necking progresses. The energy for this secondary acceleration is the elastic energy accumulated in the test fixture.

It is the early and near-straight portion of the curve which is of interest here because it represents the complete or the major part of the applied prestrain. The maximum strain rate attaned during this period is 170 in/in/sec and appears shortly before the 40 percent limit is reached. From here on, the strain rate decreases to a minimum of 25 in/in/sec which is reached after passage of the 75 percent limit. The average over the interval up to the 75 percent limit is 95 in/in/sec. This is in fair agreement with the values listed in Table X, considering the experimental difficulties involved in obtaining these values. However, strain rate has been plotted on a log scale in other graphs in this report, and differences of this magnitude do not appreciably change the shape of the resulting curves. The strain rate of greatest interest is in the early portion of straining when the major portion of strain occurs and before necking begins.

In future work, a further effort will be made to reduce the gaseous obscuration by machining an "O" ring groove in the guideplate of the dynamic test fixture to seal around the ram (see Figure 8).

A further modification of the technique would be to highly polish a circular portion, approximately 1/8-inch diameter, at the ends of the gage length which could be used as fiducial marks for directly measuring strains across the gage length. The use of color film and increased illumination in conjunction with the fiducial marks would tend to offer insurance for obtaining greater contrast and simplify the measuring procedures.

In any modification or redesign of the dynamic test fixture, the following basic design principles are suggested:

a. Allowances between moving parts should be generous.

b. Simplicity and ruggedness should be criteria for design.

c. Members adjacent to the explosive should be considered expendable.

d. Means should be provided for rapid assembly and disassembly of the fixture.

3.1.2.3 Cryogenic Temperature (Liquid Nitrogen, -320°F)

Explosive prestraining at -320°F was accomplished with the dynamic test fixture by modifying the fixture to permit the test specimen to be surrounded by liquid nitrogen while being strained. The continuous vertical assembly of the specimen and the ram precluded the use of a Dewar flask. A styrofoam disc was placed on the guideplate with a central hole cut to clear the ram. Its purpose was to serve as the base of the styrofoam container while insulating the nitrogen from the guideplate, which acts as a massive heat source. A styrofoam cylinder was placed around the specimen and all joints were sealed with heavy grease. It was necessary that the cylinder be long enough to cover the upper specimen support by a sufficient depth to ensure complete immersion of the specimen at time of detonation. The styrofoam was expended in the course of each shot.

Due to the adiabatic heating generated by plastic work, the temperature at which prestraining occurred may be expected to vary from -320°F. However, -320°F is considered the nominal temperature for these tests. A similar temperature deviation occurs during tests at ambient or room temperature.

3.2 APPLIED STRAIN

The amount of prestrain to which the specimens were to be formed was originally specified for each test condition as 40 percent and 75 percent, expressed as percent of maximum at fracture. This gave two fairly equal intervals for plotting results and determining trends. These values had to be amended as testing progressed. It may be observed in Table VIII for the 6Al-4V titanium that the applied strain is 30 percent and 60 percent in lieu of 40 percent and 75 percent. This was necessary as it was found that necking in the test specimen occurred at less than 75 percent. In order to produce specimens without necking, the upper limit was set at 60 percent and the lower limit was reduced to 30 percent to provide equal intervals. For the solution-treated material, the elongation was so small that only one applied strain of 50 percent was used. On Table IX, for 13V-11Cr-3Al titanium, a strain value of 50 percent only was established because of low elongation at fracture and low uniform elongation.

To obtain strain measurements, each prestrained specimen was blued, and a 2-inch gage length was scribed. Subsequent to prestraining, the distance between gage marks was measured and the elongation was obtained. This value was recorded in Tables V through IX as measured strain. Measured strain of uniformly prestrained specimens is compared to the average measured strain of specimens strained to fracture at the same strain rate and the result is recorded as actual strain in percent of maximum.

No specimens which showed any indication of necking were used for further testing. Other specimens which differed drastically from the specific applied strain were also discarded. Because of the very small uniform elongations available in the solution-treated titanium alloys, the spread in actual strain is large while the absolute values of strain fall in a narrow range.

3.3 BIAXIAL STRAIN FIELD

Biaxial strains were introduced in the test material by forming test blanks into an elongated dome die, Figure 14. The die was designed with flat areas of sufficient size to allow tensile specimens to be cut from the formed dome for evaluation of biaxially prestrained material. The developed design permits flexibility in depth which in turn permits coverage over a range of strain. Thus the die is not limited to material with a specific elongation.

The original concept in creating the die was to permit obtaining strain combinations typical of strains met in explosive forming and to vary the strain combinations by varying the width of the flange in the flat blank. However, results obtained were somewhat disappointing. With a narrow flange, restraint on the parallel straight sides was insufficient to cause appreciable strains in the transverse direction. The material gave strain combinations in the semicircular dome ends similar to round domes, but the material was not flat in these areas to allow cutting straight tensile specimens. With a wide flange, fracture occurred prematurely at strains far below the normal fracture strain.

It is recommended for any future studies where this approach is applicable that the forming die be designed in a circular configuration rather than as an elongated dome. Provisions for giving flexibility in depth and the use of a flat bottom similar to the elongated dome will duplicate the advantages of the elongated dome die and eliminate its disadvantages.

3.3.1 Test Blank Preparation

Biaxial strain measurements on materials formed in the elongated dome die were made by placing a grid pattern on the test blank and measuring changes in pattern which occurred after forming. The test material was coated with Fruindorfer Cold Top Emulsion, manufactured by Phillip Lachman Company, Evanston, Illinois. A master grid on "mylar" was placed over the coated test material and exposed to light. Among various emulsions previously used, the grid pattern resulting from the above emulsion was the most successful to remain on the metal during the forming operation, although some loss of grid pattern occurred with the above material also. Proper preparation of the metal blank is most important.

3.3.2 Biaxial Conventional Forming of Test Blanks

Using the elongated dome die in conjunction with a "kirksite" punch which was cast from a mold of an explosively formed dome, test blanks were formed in a 375-ton Danly double-acting press. Two of the 5456-0 aluminum domes were sectioned as shown in Figures 15 and 16, where the specimen number defines the location in the dome from which each specimen was taken. Wherever possible, pairs of specimens were cut from symmetrically comparable areas in a dome in order to have nearly equal strain in each specimen of the pair. In Table XIII, where strain data and mechanical properties are tabulated, these pairs are listed together. Most specimens are transverse to the rolling direction for comparison with uniaxially strained specimens.

The strain rate is taken as the average over the total punch travel and was calculated by dividing the measured strain by the elapsed time during forming (7 sec.). The higher of the two strain values as measured in the longitudinal or transverse direction in the elongated dome was used in all cases.

3.3.3 Biaxial Explosive Forming of Test Blanks

In using the elongated dome die to form test blanks, two sheet-explosive charges varying from 50 to 100 grams each were suspended at standoffs ranging from 6 inches to 8.5 inches above the centers of the semicircular ends of the die. The two charges were connected by a strip of sheet explosive and initiated with a No. 8 electric detonator at the center of the strip. This gave simultaneous charge initiation and was adequate for accomplishing the underwater forming. The elongated dome die before and after forming is shown in Figure 17. Three domes were sectioned, and the specimen layouts are shown in Figures 18, 19 and 20, while strain data and mechanical properties are listed in Table XIV.

The specimens were measured for thickness after being machined from the dome and prior to laboratory testing. The value shown in Table XIV represents the thickness at the center of the gage length. In the conventionally strained specimens, maximum range of thickness within a specimen was .002-inch. For the explosively strained specimens, the maximum range of thickness was .020-inch.

The differences in the range of thickness variation between the specimens taken from the conventionally formed domes and the explosively formed domes reflect the frictional effects from the ram used in conventional forming versus the virtually frictionless front which exists between the shock pressure front and the material being formed. The higher thickness values in the explosive formed specimens are from areas further removed from the apex region; the lowest values are located in the apex region. In conventional forming, the ram in contact with the material restrains the material from stretching and all the stretch and thinning occurs in areas other than in the flat bottom.

This pattern has been observed in other forming procedures, where maximum change in thickness (greatest thinning) occurred in the region where the explosive pressures made first contact with the material being formed.

Since thinning is a function of both longitudinal and transverse strain, thickness measurements were recorded to furnish a comparison of total strain. These measurements were taken because of loss of grid pattern experienced in the explosive straining and to permit comparisons to be made between conventional and explosive straining on the basis of thickness.

Microstructural specimens were cut from near the center and at the edge of each dome bottom. The edge specimens included material which impacted against the bottom of the die and which free-formed only. Hence, any effect of die impact on microstructure could be detected since strain is virtually the same in the adjoining impacted and free-formed areas.

3.3.1 Determination of Biaxial Explosive Strain Rate

To determine explosive strain rates in the elongated dome die, it was not possible to use optical techniques. An electronic technique was adopted using pin switches to close timing circuits as the test blank was formed. Photogridding on the test blanks facilitated measurement of strain after forming. Strain rate was determined for each increment between adjacent pairs of pin switches and, by determination of total elapsed time required for forming, the average strain rate was calculated. Velocity of the blank in the vertical direction at the center of the dome was calculated from time and deflection data.

The elongated dome die was adjusted to a 4-inch depth. Five (5) pin switches were grouped near the center of the die at nominally 1-inch height intervals. After mounting in the die, the height of each switch was accurately measured. Each pin switch consisted of two No. 28 magnet wires cemented in a small glass tube. The wires protruded 0.1-inch above the upper end of the tube and were scraped free of insulation. Completion of the electric circuit through each switch was dependent on the metal blank contacting the two protruding wires.

Information was recorded by a polaroid camera attached to a Model 545 Tektronix oscilloscope. The first switch to be closed, which was located just below the blank prior to forming, served to trigger the oscilloscope.

Strain rate data were obtained for one dome as shown in Table XV. Measured strain at the center of the dome was 10 percent, and the measured die depth was 3.950-inch. Time data were obtained from the oscilloscope picture, Figure 21. Full sweep was one millisecond. The table shows measured time and deflection data and calculated values of strain rate and blank velocity. Since the measured time intervals did not include the total time for forming, a time-deflection curve, Figure 22, was plotted and extrapolated over the total deflection to obtain total time.

Since it is known that in dome forming, strain is approximately proportional to the square of the deflection and since the deflection varies approximately proportional to time, then it can be shown that:

$$\text{Average strain rate} = \frac{\text{Total strain (in/in)}}{\text{Total time (sec.)}}$$

Since the strain, ϵ, is proportional to the square of the deflection Z, this relationship may be expressed as $\epsilon = CZ^2$, where C is a constant of proportionality which is defined by the known values of maximum strain and deflection. Differentiating,

$$\frac{d\epsilon}{dZ} = 2CZ$$

Now strain rate,

$$\dot{\epsilon} = \frac{d\epsilon}{dt} = \frac{d\epsilon}{dZ}\,\frac{dZ}{dt} = 2CZ\,\frac{dZ}{dt}$$

or approximately $2CZ \frac{\Delta Z}{\Delta t}$.

The increments of deflection and time are obtained from the recorded data. The deflection, Z, is taken at the midpoint of each corresponding increment. The strain rate-time curve is also plotted in Figure 22. To better define the shape of the curve, the strain rate at maximum deflection was determined graphically. The average strain rate is also shown.

One observation should be made at this point. A comparison between Figures 13 and 22 shows that the general mode of strain rate variation is essentially the same in the two cases except that the rising and fall-parts of the strain rate curve are somewhat straighter in the case of uniaxial straining. For uniaxial straining, the peak appears slightly sharper, which is a result of the larger masses to be accelerated and decelerated, but the order of magnitude of the maximum and the average strain rate is the same in the two cases. Uniaxial testing is, therefore, from a dynamic standpoint, a good simulator for biaxial testing.

3.4 MECHANICAL PROPERTIES TESTS

3.4.1 Standard Tensile Test

In determining mechanical properties by the standard tensile test, some of the values for elastic modulus appear to be extremely low. The values as obtained are presented, but no particular significance should be attached to them. For a critical determination of modulus of elasticity, it would be desirable to use a round test specimen and to apply the load by a purely mechanical system rather than by a hydro-mechanical system as employed in the tensile testing machine.

Accurate determination of reduction of area on flat tensile specimens offers some difficulty, especially where fracture occurs on a diagonal shear plane. Final area of all specimens was first calculated from micrometer measurements. The titanium specimens were remeasured in a tool maker's microscope, and the original and revised reduction of area values are recorded in Tables VIII and IX.

3.4.2 Microhardness

A microhardness traverse was made on each "micro" specimen. The first reading was taken .003-inch from one edge, and additional readings were taken at .010-inch increments. A typical microhardness traverse is shown in Figure 23. The microhardness curves are very flat which indicate that there were no edge effects due to uniaxial straining. Therefore, the Knoop hardness value corresponding to the average indentation measurement is reported in Tables V through IX.

3.4.3 Notch Sensitivity

Notch sensitivity was determined by the sharp edge-notch tensile test. The standard specimen for this test is 1-inch wide in the gage length and, while it may have been preferable to use this configuration from the standpoint of obtaining standard data, limitations of the dynamic test fixture dictated the use of a narrower gage width. The gage width used was the same as the standard tensile specimen, .500-inch, and the notch dimensions are shown in Figure 7. This configuration was designed for a stress-concentration factor, K_T, of 10.

3.5 OPTICAL MICROSCOPY

All "micro" specimens were mounted, polished, and etched for observation under the microscope to determine whether strain rate effects are discernible in the microstructure at optical magnifications. Typical areas were photographed. Selected photomicrographs are included in this report.

3.6 ELECTRON MICROSCOPY

Electron microscopy examinations were performed on replicas made of parlodian, shadowed with chrome and finished off with a carbon deposit. This is a 2-stage replication since the parlodian is dissolved with amyl-acetate leaving the chrome-carbon final replica.

The replicas were made from the same samples as those used for low magnification examination. They were initially prepared as metallographic samples with a light etch.

The electron microscope used is a Hitachi Model HS-6 instrument with a 50 Kvp source and with a resolution capability of 25Å. The total magnification obtainable is 250,000X with a limit of penetration by the electron beam of 100-300Å.

3.7 X-RAY DIFFRACTION

Evaluation of possible atomic and molecular changes in materials can be made with the use of X-ray diffraction techniques. Phase changes, microstress levels, local residual stresses, crystal orientation, etc. may easily be detected from Debye-Scherer diffraction patterns. For this reason, detailed X-ray diffraction studies were made on two of the five materials investigated in this program. The 5456-0 aluminum, both uniaxially strained and biaxially strained, and the 301 stainless steel were selected for study.

A North American Phillips "Norelco" two diffractometer unit was used to obtain the necessary diffraction patterns. Filtered copper radiation at 50 Kvp-20ma was used for examining the aluminum while filtered chromium radiation at 35 Kvp-11ma was used for the 301 stainless steel. Diffraction traces were obtained from representative samples of each material conventionally strained and explosively strained. From these traces, microstress half-height width values were obtained. Lattice parameters were obtained by point-slope methods. Residual stresses were calculated from these parameters.

Quantitative measurements of austenite and martensite in the strained 301 stainless steel were performed using theoretical structural factor "G" constants for analysis.

3.8 RESIDUAL STRESS STUDY

Of the several techniques which are available for measuring residual stresses in formed material, two methods - the X-ray diffraction technique and the sectioning method - were considered in this program.

The X-ray method was rejected because space limitations in the instrument would require that a small piece of material be cut from the part to be tested and the original stress configurations would be largely lost by relaxation during cutting. Also, an X-ray investigation provides one component of one stress only, located at the surface. In order to obtain the stress pattern and to locate and measure the peak stresses, a large number of individual tests would be required.

The sectioning method was selected as being economical, reliable and simple to apply. It provides in one continuous investigation the complete pattern of any desired stress component or components, including the size and location of peak values. When applying the sectioning method, characteristic dimensions are selected, measured and marked, and the piece is then sectioned in a manner to relieve one or several stress components, and the sections are remeasured. The dimensional changes provide the equations for finding the stress components. All equations are elasticity equations and are usually linear. Therefore, the solution to the equations present no major difficulties.

For this study, a 6-inch diameter circular dome was explosively formed in a free-forming die. The axial symmetry of the dome suggests sectioning along circumferential and radial surfaces, performed in two stages as illustrated in Figure 24. By the first stage of sectioning, the meridional normal forces and associated shearing forces will relax. These forces have significant radial resultants and their elimination causes a measurable change in the ring diameter.

Although the rings have not yet been sectioned, the peripheral normal forces have also vanished at this time because an unloaded circular ring cannot sustain any single normal force on its cross-section. There are no shearing forces in a meridional plane, neither before or after sectioning because of symmetry in the part.

So far, the first stage has provided whatever information can be generated with respect to normal and shearing forces, and also to the meridional bending moment. The peripheral bending moment is unaffected by the first stage of sectioning, and is still present within the ring. When the ring is cut open by radial sectioning (second stage), the peripheral bending moment vanishes, the ring changes its curvature (but not its peripheral length), and the two ends adjacent to the cut move a measurable distance relative to each other, either separating or overlapping (assuming the vanishing moment was not equal to zero).

The analysis requires a number of dimensional measurements, all of which (except thickness measurements) were taken by means of a coordinate cathetometer. The blank for the dome was photogridded with a system of concentric circles and radii. The contour of the formed dome was measured in two coordinates with the dome located in an upright position in front of the instrument. Diameters before and after sectioning were measured from the photogrid with the rings mounted on a vertical fixture. The relative motions of the free ends were measured in a similar setup. Measuring points for these operations were applied by a scriber prior to the second cut.

4. DISCUSSION OF RESULTS

4.1 GENERAL REMARKS ABOUT TEST PROCEDURES AND THEIR EVALUATION

The test procedures employed can be classified as optical and numerical.

Optical test procedures included examination by optical and electron microscopy. A distinctive feature for this type of test procedure is the provision of a visual record - a photograph. The principal difference lies in the magnification and therefore in the resolution possible. It can generally be expected that electron microscopy may reveal details not visible by optical microscopy.

Optical test procedures provide information about the microstructure of the material. Simultaneously, some information may also be obtained about the crystal lattice, or the molecular or atomic structure. However, the crystal lattice or the atomic structure contains much finer details than those which can be made visible by the two types of microscopy.

The supplementary information required in a study of metallurgical effects can be supplied by X-ray diffraction tests and by mechanical testing.

X-ray diffraction tests provide information about the type of crystal lattice and possible distortions thereof, the lattice parameter, the presence of macro- and microstresses, certain cases of grain fragmentation, etc.

A special feature within the study of the metallic structure is the dislocations. Dislocations are disturbances in the lattice on the atomic scale. They are invisible in the optical microscope and have only recently, and in a few cases, been made visible in the electron microscope. However, they have been studied extensively by indirect methods and have provided the explanation for many phases of metal flow behavior.

Mechanical testing provides the numerical data for design of parts and planning of manufacturing operations. Indirectly, they also provide information about the inner structure of the material, regardless of whether it is the microstructure or the crystal lattice. Any change in a physical property is caused by one or several changes in the structure.

While the conventional presentations of the mechanical properties serve the design activities, they tend to obscure the true physical properties. In order to study these, it has been found necessary to use a different presentation of the data, known as true strain and true stress.

The introduction and application of the concepts of true strain and true stress have disclosed important relationships in metal flow. Many data presentations have been greatly simplified and clarified. Specifically within the study of explosive forming, they have been found extremely helpful in discovering the existence of unified fundamental trends in metal behavior, not previously discernible by means of conventional data presentations.

The most important data within this category are the true strain and true stress at fracture.

The true fracture strain is a measure of the maximum deformation which can be imposed upon the material. It is, therefore, an absolute measure of its ductility.

The true fracture stress is a measure of the actual maximum stress which the material can sustain. It is, therefore, an absolute measure of its strength. When compared to the stress at a physically well-defined lower level, such as at the yield point, it becomes a measure of the material's work-hardening properties.

Realizing these facts, the present program has attached particular significance to the true fracture strain, in addition to the conventional (engineering) strain data. In the evaluation of the tests, the true strain and engineering strain respectively have been taken as the fundamental unit, or 100 percent, and the various levels of applied prestrain were selected as, and are expressed as, percentages of this value. The justification of this procedure lies in the high degree of consistency found in the experimental results when analyzed with the true strain values.

Mechanical properties data for each test condition and test material were extracted from Tables V through IX and are presented in tabular and graphical form. The symbols used on the mechanical properties charts are shown in Figure 25.

4.1.1 5456-0 Aluminum

4.1.1.1 Microstructure

Samples of 5456-0 aluminum in the as-received condition and prestrained to 40 and 75 percent, conventionally strained at 3 in/in/min and at an explosive strain rate, were examined microscopically at magnifications 150X, 500X and 2000X. Additional examinations were made at 25,000X with the electron microscope.

The material has a very close texture which chould not be resolved at 150X magnification. Samples of photomicrographs at 500X and 2000X are shown in Figures 26 and 27 respectively, and two electron micrographs are shown in Figure 28. Comparisons may be made of structures observed in the as-received, uniaxial strained, and biaxial strained material in these photographs.

All of the pictures show longitudinal lines, generated during the rolling of the sheet, with a fine texture inside each grain consisting of a precipitate phase, and large dark inclusions. The grain boundaries stand out in more or less pronounced contrast, but this is a matter of etching only and shows no correlation with the strain or the strain rate. The biaxially strained specimen shows no details not already encountered in the other specimens.

Two exposures, Figure 27, with 2000X magnifications, show the same details in a larger scale with no additional features. Even the electron micrographs, Figure 28, fail to show any details not already found with the lower magnifications. The indication of a directional effect discernible visibly in Figure 28 B is ascribed to the geometrical relation between rolling direction and illumination direction. The common indications of internal deformation, slip lines and twins, are conspicuously absent.

4.1.1.2 X-Ray Diffraction Analysis

Microstress levels in the uniaxial specimens increased during conventional and explosive straining. The distortion was nearly twice as great for the explosive mechanism than for the conventional. This was also borne out in residual stress levels. The biaxially strained specimens in general showed a higher microstress level than the uniaxial specimens. The macrostress levels were also higher. In general, all stresses were tensile in nature. No drastic differences appear to exist between conventional and explosively strained samples as far as structural changes or phase changes are observed. The material appears to be rather insensitive to reaction.

Table XVI shows the compilation of data obtained from these specimens. Table XVII shows the intensities of diffraction peaks obtained from the eight biaxially strained specimens. The estimated accuracy in macrostress determinations is $\pm$ 200 psi.

There appears to be an orientation change in the biaxially strained specimens. Dome No. 12 shows a change from conventional (111) to (220) directions as the sample is transversed around the radius. Dome No. 19 has no effect. Dome No. 21 shows change from the (200) to the (220) direction. This is undoubtedly due to the cold working patterns similar to those developed in drawing operations.

4.1.1.3 Mechanical Properties

Prestrain and mechanical properties data are given in Table XVIII and are plotted in Figures 29 and 30. From the graphical presentations, some general trends in the variation of the properties can be seen. An increase in prestrain (in percent of fracture strain) generally causes an increase in strength (yield, ultimate and notch) - less for explosive strain rate than for the conventional strain rate. The elongation (engineering) drops sharply for both strain rates, but the reduction of area shows an uneven trend. For the conventional strain rate, the reduction in area drops sharply, similar to the elongation, but for the explosive strain rate, the reduction in area first increases, then decreases.

When the true strains and stresses are used and plotted against strain rate, with an individual curve for each level of prestrain, the picture changes and the trends appear with greater clarity. Fundamentally, the effect is on ductility, or on true fracture strain, and on the gap between yield and ultimate. From Figure 31, it is observed that the true fracture strain at maximum or 100 percent true prestrain (i.e., the specimen being pulled to fracture in one operation at the appropriate strain rate) increases monotonically with strain rate and rises sharply when the explosive strain rate is approached. From a manufacturing viewpoint, this should prove advantageous, as a strain applied at explosive strain rate is more beneficial to the material than a strain applied at a lower rate.

When a prestrain less than 100 percent is applied at an elevated strain rate (3 in/in/min or higher, up to and including explosively), the beneficial effect is still present, although to a lesser extent. The amount of prestrain is of importance. Apparently, an optimum prestrain exists which cannot be accurately located except that it is somewhere at a level higher than 21 percent and below 100 percent.

The yield stress increases sharply at the lower strain rates and levels off at approximately 3 in/in/min. The true stress at fracture is near constant up to 3 in/in/min., but rises significantly from this value to the explosive strain rate. The effect of prestrain is discernible, but not strong. An increase in prestrain increases the yield but lowers the fracture stress (ultimate). Thus, the gap between yield and ultimate is increased at the explosive strain rate and is greater for the lower prestrain. Compared to the increase in ductility (true fracture strain), this increase is only moderate; at increased strain rates approaching explosive strain rate values, the increase in work-hardening is less than the increase in ductility.

Notch strength (see Figure 32) increases in nearly the same manner as yield, but not nearly as fast, and remains nearly constant from 3 in/in/min to the explosive strain rate. Consequently, the ratio, $\frac{N}{Y}$, drops sharply below 3 in/in/min and stays nearly constant for the remainder of the range. It is significant that the notch strength does not increase with the ultimate, and therefore the ratio $\frac{N}{Y}$ suffers a slight dip when approaching the explosive strain rate.

4.1.1.4 Comments

The most important result of this analysis is that the material increases its ductility sharply and work-hardens only slowly at the higher strain rates. This is in good agreement with the statement made in the discussion of the metallographic observations about the conspicuous absence of visible indicators for work-hardening and with the near-constant behavior of the notch strength.

These observations indicate that a mechanism must exist, on the crystal lattice or atomic level, which is strain rate dependent and which results in delayed work-hardening. Further discussion of such a mechanism shall be postponed until all data have been presented and discussed.

4.1.2 AISI 301 Stainless Steel

4.1.2.1 Microstructure

Austenitic stainless steel is a material with a very photogenic microstructure. The grains have a characteristic polygonal shape, the grain boundaries etch well, and when deformed, the grain surfaces show the development of twins and slip lines in large quantities.

In the present program, the material has been investigated at two prestrains, at two strain rates, and at ambient temperature, as well as at the cryogenic temperature $-320^{o}F$. All samples were examined under the microscope and with the electron microscope. Characteristic samples at 500X magnification are selected and shown in Figures 33 and 34. Characteristic electron micrographs are shown in Figures 35 through 38.

The material in the as-received condition is shown in Figure 33 A. The structure appears completely austenitic. This was also confirmed by X-ray diffraction analysis. However, there are also some carbide inclusions too small to appear in a 500X micrograph, but visible in the electron micrographs, Figure 35. The number of the carbide inclusions can not be very large, because none are seen in any of the other electron micrographs. The structure contains some annealing twins, visible at 500X. One set of twins is also seen in Figure 35 A.

The structure of the material after straining to nominal 75 percent of fracture at the two strain rates and at ambient temperature are shown in Figures 33 B and 33 C. Since conditions other than strain rates for these two samples are very nearly alike, a direct comparison is possible.

The grains are elongated, as compared to the as-received sample, and a considerable number of slip planes have developed and are visible as lines. Most grains show two families of slip planes, each one oriented with respect to the direction of elongation at an angle somewhat less than 45°. The angle relationship of the lines, as well as their number, spacing, and distribution and any other parameter which can be evaluated by optical metallography, appear to be identical in the two samples.

Electron micrographs of specimens strained to nominal 75 percent of fracture strain at conventional and explosive strain rates are shown in Figures 36 A and 36 B respectively. Each picture shows a pattern of intersecting slip lines. In Figure 36 B, the one family of lines has degenerated into a micro-slip, relative to the other line family. This slight difference is, however, not considered significant. It should also be noted that none of the electron micrographs show visible precipitates or transformation products.

It is of interest to note that dislocations are visible in some of the electron micrographs. In Figure 36 B, slip lines are interrupted by a screw dislocation, and Figure 36A shows an assembly of three edge dislocations.

Structures of specimens prestrained at cryogenic temperatures are shown in Figure 34. The most obvious difference from the structures for prestrain at ambient temperature is that the lines within each family have increased in number and the grain surfaces show a somewhat stronger relief. It appears as if areas bounded between slip lines stand out as raised islands,indicating increased hardness in these areas. There is no typical difference discernible visually between the structures produced at the two strain rates.

The observation of areas of increased hardness indicates the possibility of a martensite-type transformation. This is in accordance with X-ray diffraction analysis, which has shown the presence of transformation products containing iron in the alpha - phase.

The electron micrographs, Figures 37 and 38, show again the two families of slip lines. The basic slip-line pattern is seen in Figure 38 A. In Figures 37 A and 37 B, it is seen that slip lines do not necessarily terminate at a solid obstruction (an inclusion or a carbide grain), but continue with little or no change in direction beyond the obstruction. A comparison with Figure 36 A may indicate a slightly more knobby surface texture. In Figure 38 B is finally seen the character of the grain boundaries, and the slip lines tend to fade away as they approach grain boundaries. In no case are precipitates or transformation products actually visible, neither in grain boundaries nor in slip lines.

4.1.2.2 X-Ray Diffraction Analysis

The measured and calculated data are listed in Table XIX. All specimens showed considerable change in microstress levels. The data for explosively strained specimens were constantly slightly less than those for the conventionally strained specimens. The residual stress levels were high and compressive in nature. The cryogenic explosively strained specimen showed a drastic change in lattice parameter. This is undoubtedly due to transformation rather than stress. The estimated accuracy in macrostress determinations is $\pm$ 4000 psi.

4.1.2.3 Mechanical Properties

Prestrain and mechanical properties data are given in Tables XX and XXI, and are plotted in Figures 39 through 42.

At ambient temperature, all three sets of strength data (yield, ultimate and notch) are higher at the explosive strain rate than at the conventional strain rate. At the cryogenic temperature, the situation is reversed; the strength data at explosive strain rates are lower than those obtained at conventional strain rates. (It is possible that an exception should be taken to the value for notch strength at explosive strain rate, highest prestrain ratio, and nominal -320^{o}F. The two values available for the notch strength differ considerably from each other, and it is not possible at this stage to determine which of the two values is the more correct one).

Ductility data (elongation and reduction of area) are, without exception, lower for explosive strain rates at ambient temperature. At cryogenic temperature, the situation is reversed for the elongation data which now are higher for the explosive strain rates. However, the reversal of trend is not extended to the reduction of area data which still show a lower value for explosive strain rates, and particularly so at the greater prestrain.

The ratios $\frac{N}{Y}$ and $\frac{N}{U}$ show completely mixed trends. At ambient temperature, $\frac{N}{Y}$ and $\frac{N}{U}$ are higher at the explosive strain rate.

In an attempt to discover unified trends that may exist, the data were converted to the true strain - true stress basis and plotted over strain rate in Figures 43 through 46. With these graphical presentations, the trends now become much more unified within the material investigated. Regardless of property, all curves show a strain rate effect, wholly or partly increasing with increasing strain rate. For some cases, the increase is monotonical from the lower end of the strain rate range to the upper end; in other cases, the raise is concentrated over a sub-interval within the entire range.

The sub-interval within which the essential raise takes place is in almost all cases located at the lower end of the interval, from 0.005 in/in/min to the vicinity of 3 in/in/min while the variation over the interval from 3 in/in/min to explosive strain rate is slight. In some cases, there is a decrease over said interval, resulting in a maximum located in the vicinity of 3 in/in/min.

This statement about strain rate effects, while essentially correct, is insufficient to explain the observations. It appears necessary also to consider the additional effects of factors other than just the strain rate, namely prestrain and temperature at prestraining.

Two conclusions can be drawn about the effects of these factors. They are:

a. The effects from the three factors are qualitatively additive, also with respect to sign.

b. There exists a ceiling for the combined effect.

With this general background, the curves, as found experimentally, can now be explained more in detail. This explanation is given in the following section.

4.1.2.4 Comments

AISI 301 stainless steel differs from the other test materials in that it is highly susceptible to phase change, being austenitic.

From the curves for the mechanical properties, it is seen that the ductility, yield and true ultimate increase sharply at a very moderate increase in strain rate, reaching a maximum and then declining. This would indicate that the delay in work-hardening, found for other materials, is much less for this material - if not entirely absent. Going to the cryogenic tests, it is seen that the increase in ductility is much less; in fact, for 100 percent prestrain, there is a decrease in ductility, while the yield and ultimate increase much more than at ambient temperature, indicating a still stronger work-hardening effect.

The general trend found previously is obviously modified strongly here by some other factor. This factor is the transformation from the gamma- to the alpha-phase.

Confirmation of this statement was found in the results from the X-ray diffraction tests. Conventionally strained material showed only a trace of transformation products, while explosively strained material showed an increase in the transformation products of approximately 30 percent. This increase is sufficient to account for a considerable increase in strength data.

It might be expected that the transformation products should be visible in the microscope. They are not, but this is explained by the fact that transformation products (ferrite, martensite, or pseudo-martensite) have the shape of platelets. If these platelets are formed in the slip planes and are oriented parallel to these planes, then it is obvious that their appearance is disguised by the general slip pattern.

A comparison between the microstructures for 75 percent prestrain ratio at -320°F with conventional as well as explosive strain rate (Figure 34) shows considerable similarity. The structures are largely martensitic with transformation having been initiated at mechanical slip planes rather than at grain boundaries (the normal nucleating points for transformation as the result of conventional quench and temper heat treatment). Extensive slip or twinning is shown with the same texture and orientation as that encountered in the austenitic material strained at ambient temperature. It is therefore concluded that the initial strain was in the same mode as that at ambient temperature. Subsequent transformation from austenite to martensite apparently took place after substantial slip had occurred in the austenite, since it is not likely that slip would occur in the martensite in a mixed martensitic-austenitic structure due to the large difference in strength between the two constituents. Where slip has taken place in two or three families of planes in a single grain, the strong martensite appears as raised islands in the structure with no evidence of internal slip inside the martensite. Thus, it would appear that the strain took place in the austenitic matrix until transformation occurred and locally reinforced the structure.

More martensite is present in the specimens subjected to explosive straining than in those which were conventionally strained. This determination was made by X-ray diffraction tests and was found for specimens strained at both ambient and cryogenic temperatures. The internal adaption by which strain is accommodated by the structure does not therefore appear to be different for the two types of strain application. Consequently, the increase in austenite-martensite transformation must be attributed to dynamic energy and stress relationships rather than to an altered strain mechanism.

The following explanation is offered for the data observed. The transformation of austenite to martensite involves a volume expansion, and in conventional straining the intragranular movements may be thought to be consecutive - that is, isolated movements consecutively consuming planes of weakness. This movement, along one plane at a time, does not alter the restraint to the transformation expansion, and thus transformation is retarded. In contrast, at sufficiently high strain rates, movement will occur along many planes at the same very short interval of time and also along two or more families of planes simultaneously. Under these conditions, it could be expected that the restraint preventing the transformation will be lost for a transient instant, and transformation will occur.

The increase in strength in the material strained at cryogenic temperatures was not found to be proportional to the amount of transformation which was induced, and was less for the material strained at the conventional rate. The measurement of the amount of transformation by X-ray diffraction which was employed in this investigation did not identify the transformation product, but the determination was made on the relative proportions of face-centered cubic austenite and body-centered cubic transformation products. These transformation products are often described as martensite, pseudo-martensite and ferrite-martensite. Since they are produced by strain, the specimens have high residual stress levels and consequently show line broadening in the X-ray diffraction traces, and line broadening could therefore not be employed as a method of monitoring for changes in the nature of the transformation products. This explanation provides a logical account for the inverse relationship between the amount of transformation which was induced and the mechanical strength properties.

4.1.3 17-7 PH Stainless Steel

4.1.3.1 Microstructure

This material has been studied extensively under a number of different combinations of conditions. It has been prestrained to 40 percent and 75 percent of fracture strain, at ambient temperature and at -320°F. Strained specimens have been tested unaged and aged. This applies to the ambient temperature prestraining as well as to the cryogenic prestraining.

A specimen from each test condition was carefully examined under the microscope and photographed. A representative selection of the photomicrographs are shown in Figures 47 through 49. No electron microscopy was performed.

As seen from the illustrations, the structure is characterized by somewhat elongated grains, generated by the rolling process. The rolling direction is further accentuated by carbides, located in the grain boundaries and mostly in the longitudinal grain boundaries, with an appearance like strings of pearls, and sometimes like continuous strings. Smaller and medium size black spots are caused by the etchant. The large grains show a directional texture oriented at 30° and 45° to the rolling direction. This texture is explained as an effect of surface flow caused by the polishing operation.

The most minute inspection of the photographs, not only those reproduced in this report but all the photographs available, fails to disclose any single feature that varies from specimen to specimen in such a manner that it would indicate a strain rate effect. The slight difference in the blackness of the grain boundaries is either an etching effect or an effect of the photographic reproduction. The difference in the clearness of the directional texture is an etching effect.

4.1.3.2 Mechanical Properties

Prestrain and mechanical properties data are given in Tables XXII through XXV, and are plotted in Figures 50 through 57.

In nearly all cases, the strength values are higher for the 3 in/in/min strain rate than for the explosive strain rate. One exception is the ultimate strength at ambient temperature for unaged material, where there is no appreciable difference between the two sets of values. For specimens prestrained at ambient temperature, the strength values of all three categories are higher after aging than for unaged specimens, and the differences between values for conventionally strained and for explosively strained specimens also tend to be higher generally for aged specimens.

The data for specimens prestrained at the cryogenic temperature show in broad terms a somewhat similar general picture, except for the fact that the curves for all three strength categories shrink together; that is, the difference between the values for 3 in/in/min strain rate and for explosive strain rate becomes very much smaller. This tendency becomes still more pronounced for aged specimens; in fact, the notch strength data for the two strain rates under these conditions could very well be connected by one single curve (see Figure 56).

The data for ductility - that is, for elongation and reduction of area - follow at least qualitatively the trend found for aluminum in that these values are higher for the explosive strain rate, but we do not find a quantitative difference comparable to the one found for the reduction of area of aluminum.

These remarks are valid for unaged specimens regardless of the prestraining temperature. A shift in the picture appears when the specimens are aged. For prestraining at ambient temperature, the gap between the curves begins to widen; in other words, the explosively prestrained material exhibits a somewhat superior ductility compared to the material prestrained at a lower strain rate. However, this effect is again drastically modified for specimens which are prestrained at cryogenic temperature and then aged (see Figure 57).

In this case, the superior ductility as evidenced by reduction of area is found at the lower strain rate. The difference is appreciable. However, the other criterion for ductility, elongation, shows a change in the opposite direction. Although the difference is small, the curve for the elongation of explosively strained specimens is located higher than the curve for specimens strained at 3 in/in/min.

In an attempt to discover more unified trends, the data were converted to the true strain - true stress basis. The data are plotted over strain rate in Figure 58 through 65. Of the two test conditions imposed on the material, the cryogenic prestraining temperature and the application of an aging treatment prior to mechanical testing, the cryogenic temperature has the greatest effect on trends.

At ambient temperature, the ductility, as evidenced by true fracture strain, increases very strongly with increase in the strain rate, at least above 3 in/in/min, and this is true for unaged as well as for aged specimens (see Figures 58 and 60). The greater the prestrain, the greater is the increase in ductility.

The yield strength increases strongly up to 3 in/in/min strain rate and stays approximately constant from here to the explosive strain rate. The true ultimate rises towards explosive strain rates, and somewhat faster for the aged specimens. The rate of rise is quite moderate. Yield as well as ultimate increases with increasing prestrain.

Notch strength increases rapidly at the lower strain rates (see Figures 59 and 61), and stays fairly constant beyond 3 in/in/min and up to the explosive strain rate. It varies significantly with prestrain. Notch strength ratios are independent of strain rate with only a small effect introduced by the prestrain.

At cryogenic temperatures, the most striking feature is a very rapid increase in ductility (see Figures 62 and 64), as evidenced by the true fracture strain. This rise begins at the low strain rate of 0.005 in/in/min and has, for a true prestrain of 37 - 38 percent of maximum, apparently reached its peak at or slightly beyond the strain rate of 3 in/in/min. At higher strain rates, it drops to almost the starting value. The drop is, however, restored by aging.

The governing factor here is apparently a combination of prestrain and strain rate. Within the available data, the most advantageous combination (without the use of aging) is 38 percent prestrain at 3 in/in/min strain rate. A lower or a higher prestrain, as well as a higher strain rate, produces less ductility.

It is concluded from these observations that increased strain rate and reduced prestraining temperature are equivalent factors - at least qualitatively. It is further concluded that the beneficial effect (high ductility) can be wholly or partly lost if the combined prestrain and strain rate exceeds a certain optimum value (here illustrated by 38 percent prestrain and 3 in/in/min strain rate). It is finally concluded (see Figure 64) that the loss by over-combining prestrain and strain rate can be eliminated by subsequent aging.

The effect of strain rate on yield at cryogenic temperatures is qualitatively as at ambient temperature; quantitatively it is very much higher. The effect is further increased by aging.

As to true ultimate, it appears at first sight (see Figure 62) as if there is no strain rate effect at all. This, however, is an illusion. An effect exists, only it is still invisible; but when the material is aged, then the inherent increase in ultimate becomes apparent and is higher, the higher the prestrain.

Notch strength (see Figures 63 and 65) displays a significant increase with increasing strain rate up to 3 in/in/min, and the effect of prestrain is significant. For aged material prestrained at cryogenic temperature, notch strength decreases with increased prestrain.

4.1.3.3 Comments

Despite the various combinations of test conditions, it has been possible to show that the material exhibits a rapid increase in ductility and a slow increase in strength with increased strain rate. In other words, there exists a delayed work-hardening effect.

Aging of specimens change the data quantitatively, but does not change the trend qualitatively.

The application of a cryogenic prestraining temperature is equivalent to a further increase in strain rate. A combination exists where the total effects of the two factors on the ductility have reached a maximum, and beyond this point the ductility decreases. The loss in ductility can be restored by aging.

The combination of an elevated strain rate with a cryogenic prestraining temperature exercises a strong delaying effect on the work-hardening. This delaying effect can, to a large extent, be eliminated by subsequent aging.

4.1.4 6Al-4V Titanium Alloy

4.1.4.1 Microstructure

This alloy has a heterogeneous alpha-beta structure, and it is a common observation that microstructural evidence of strain does not become apparent until large amounts of strain, i.e., 20 to 30 percent, have been introduced.

In the present cases, the amounts of strain that could be introduced in the uniaxial test specimens were limited by the occurrence of necking. It was necessary to reduce the largest applied prestrain to nominal 60 percent of maximum at fracture for as-received material, and 50 percent for solution-treated material, corresponding to approximately 7 percent engineering strain. The next lower prestrain range was selected at nominal 30 percent of maximum, corresponding to approximately 3 percent engineering strain.

With the previous remark in mind, it is not surprising that low values of strain were then not detectable by optical microscopy. No electron microscopy nor X-ray diffraction tests were performed on these samples. Examples of the photomicrographs obtained are shown in Figures 66 and 67. The only discernible difference in the material as-received and strained or solution-treated, strained, and aged is a small amount of grain elongation, which is due to strain rather than to strain rate.

4.1.4.2 Mechanical Properties

Prestrain and mechanical properties data are given in Tables XXIV and XXV, and are plotted in Figures 68 through 71.

Based on engineering data, all three stress values, yield, ultimate, and notch, increase gradually with increased prestrain and with increased strain rate. Ductility values are lower at increased prestrain, but the elongation is practically unaffected by strain rate, while reduction of area increases significantly at the explosive strain rate.

The variation pattern for the notch strength is very much like the pattern for yield and ultimate. Therefore, the ratios $\frac{N}{Y}$ and $\frac{N}{U}$ show very little variation with strain rate, and only a slight decrease with increased prestrain.

In the solution-treated condition, and aged after prestraining, the material exhibits a marked change in behavior pattern. At the conventional strain rate (3 in/in/min), all three stress values remain unchanged, but at the explosive strain rate, yield and ultimate decrease with increased prestrain while notch strength shows a slight increase. The ductility trends are practically unchanged, i.e., the reduction of area is significantly increased at the explosive strain rate while the elongation exhibits only negligible strain rate effect - if anything, a slight decrease. Notch strength ratios are practically unaffected.

The true-stress-strain presentations are shown in Figures 72 through 75.

The as-received material shows a considerable increase in ductility accompanied by a moderate increase in yield and ultimate. The gap between yield and ultimate varies very little with increased strain rate. These characteristics are the indicators for delayed work-hardening. The notch strength and associated ratios vary only insignificantly with prestrain and strain rate.

The properties are strongly prestrain-sensitive. Best ductility is obviously obtained by a moderate prestrain, located in the vicinity of 11 percent and definitely below 19 percent. The curves show an apparent improvement for 100 percent prestrain at explosive strain rate. It might, therefore, be expected to find an increase in ductility at explosive strain rate for higher prestrains, located somewhere between 19 percent and 100 percent. However, such prestrains could not be applied experimentally. The limit for the applied prestrain was imposed by necking of the specimens. Necking is not an unchangeable material property, but is influenced by the geometry of the system. In biaxially stressed systems, necking may be postponed. However, in the case of titanium, it has been found that visible necking may occur in dome forming, even at moderate deflections.

The solution-treated and aged specimens show similar trends to the as-received specimens. Ductility increases rapidly at increased strain rate, reaches a maximum at approximately 3 in/in/min strain rate and drops to a somewhat lower value at explosive strain rate. Best ductility is found with moderate prestrain. Ultimate drops sharply for increasing strain rates up to 3 in/in/min, and increases again to a still higher value at explosive strain rate. Yield is practically unaffected by strain rate. These variations are again evidence of delayed work-hardening. The delay is strong over the lower sub-interval of the strain rate range, from 0.005 to 3 in/in/min, but gradually disappears at the higher values up to the explosive strain rate.

4.1.4.3 Comments

No microstructural change was visible and could not be expected at the moderate prestrains applied.

As-received, as well as solution-treated and aged material, shows evidence of delayed work-hardening. The delay effect is concentrated over the lower end of the strain rate range, and the concentration is more pronounced for solution-treated material.

The work-hardening delay (increase in ductility without corresponding increase in the gap between yield and ultimate) is prestrain-sensitive. Strongest effect is found at moderate prestrains, in the vicinity of 12 percent of maximum (on the true-strain basis).

4.1.5 13V-11Cr-3Al Titanium Alloy

4.1.5.1 Microstructure

In making the photomicrographs, dark-field illumination was used which permitted better resolution than was possible with bright-field illumination. Unstrained material in the as-received and the aged condition is shown in Figure 76. Precipitate is clearly visible in the as-received condition, but obscured by the grain texture in the aged condition. Straining operations (see Figure 77) bring out an abundance of slip lines, criss-crossing in several directions (slip line families). Aging after straining (see Figure 78) seems to increase the density and contrast of the slip lines but, on the other hand, the precipitates appear perhaps slightly reduced in numbers. These differences are due to metallurgical factors - not to the applied strain and strain rate. Any visible effect of strain rate should be observed by comparison between Figure 77 A and 77 B, and between Figure 78 A and 78 B. However, even the closest examination does not reveal any such difference.

4.1.5.2 Mechanical Properties

Prestrain and mechanical properties data are given in Tables XXVIII and XXIX, and are plotted in Figures 79 through 82.

An examination of nearly all data for mechanical properties results in the observation that this material is generally strain-rate insensitive, at least within the strain-rate range investigated. This statement applies, nearly equally, to either one of the two conditions tested ("as-received" and "as-received and aged").

One apparent exception is the notch strength (Figure 79) where the values for explosive strain rates are considerably lower than for conventional strain rates. However, the data points for the explosive strain rate show an unusually large spread, and it is possible that the apparent difference may disappear with a repetition of the tests.

The only other discernible strain rate effect is on the reduction of area. This property seems to increase slightly at explosive strain rates, and more for aged than for as-received material.

The effect of the other variable - the amount of applied prestrain - is of some interest. The as-received material shows an increase in the stress values (yield and ultimate) (see Figure 79) and a decrease in elongation (with practically no variation in the reduction of area) at increased prestrain; in other words, an increased brittleness which is the normal behavior for a metal.

When aged (see Figures 81 and 82), the yield and ultimate stress values decrease, and the reduction of area increases rapidly while the elongation decreases slightly at increased prestrain indicating an improved ductility, contrary to what is normally found in a strained material.

The true stress-strain data are plotted in Figures 83 through 86. The as-received material shows a very slight increase in ductility accompanied by a slight increase in yield and ultimate with no appreciable change in the relative magnitude of these properties. The net effect of these observations is that the material is largely strain-rate insensitive, also with respect to work-hardening. There is some loss in notch strength and in the notch strength ratios $\frac{N}{Y}$ and $\frac{N}{U}$.

The aged material shows a large increase in ductility (true strain at fracture) over the interval from 0.005 to 3 in/in/min, accompanied by a moderate increase in ultimate and a slight decline in yield, indicating the presence of delayed work-hardening. Variations are slight on the remainder of the interval, up to the explosive strain rate, with decreasing ductility, slightly increasing ultimate, and near constant yield, indicating a slight increase in the work-hardening and slightly increased brittleness. There is a decided decrease in notch strength and in the notch strength ratios with increasing strain rate.

4.1.5.3 Comments

13V-11Cr-3Al titanium alloy, in the as-received as well as in the aged condition, is a strain-rate insensitive alloy. In the aged condition it shows delayed work-hardening with increased ductility over the lower end of the strain-rate interval (up to 3 in/in/min) and a slight reversal of this trend over the upper end of the interval up to the explosive strain rates.

5. CONCLUSIONS

From a survey of all data generated for the following materials, in the conditions indicated,

- 5456-0 Aluminum - prestrained at ambient temperature
- AISI 301 Stainless Steel - prestrained at ambient temperature and at -320°F
- 17-7 PH Stainless Steel - without and with aging, prestrained at ambient temperature and at -320°F
- 6Al-4V Titanium Alloy - without and with solution treatment and aging
- 13V-11Cr-3Al Titanium Alloy - without and with aging

some general conclusions can be drawn with respect to the mechanism of plastic metal deformation at high rates of flow (large strain rates) together with an estimate of the area of application of such general conclusions with modifications as required for specific cases.

Strain rate effects are a reality and are evidenced by variations in the mechanical properties. They are not visible by optical microscopy nor by electron microscopy with magnifications up to 30,000X.

It is of particular interest to note that the visible characteristics of microstructural damage caused by severe explosive loading and reported in the literature are absent in specimens subjected to the much lower loads normally associated with explosive forming.

The observed and measured changes in mechanical properties appear in most cases as an increase in ductility, accompanied by an increase, at a lower rate, in yield stress and true ultimate tensile stress, thus indicating a delay in the work-hardening that is induced.

The measurable changes in mechanical properties are analogous to the effects of the strain itself and of a lowering of the temperature during straining for the two stainless steel materials investigated. The effects of the three factors,

strain,
strain rate, and
temperature

appear to be qualitatively additive. However, there is an apparent ceiling for these effects, separately as well as collectively, and the material can be oversaturated with the combined strain, strain rate, and temperature effects. In such cases, it has been found that various mechanical properties reach their optimum values at intermediate strain rates and decrease again when higher strain rates are applied.

The observations are explained as an effect of the strain rate on the dislocations. High ductility is associated with the unobstructed motion of existing dislocations and generation of additional dislocations.

Each of these phenomena absorbs energy. The application of strain at a high rate provides instantaneously and simultaneously the necessary energy input throughout the mass to cause dislocations to be generated and to move in large numbers before too many obstructing slip planes have been formed.

Modifications of the general mechanism occur when additional sources of obstruction are introduced. Such additional obstacles may consist of phase transformation products or precipitates. The amount of obstruction presented by phase transformation products or precipitates depend on their number, size, shape, strength and location. For example, precipitates formed in grain boundaries have little effect, because grain boundaries in themselves are obstructions to dislocation movements. Small precipitates, as formed in 17-7 PH stainless steel, also have a very small effect, as observed in the large increase in the ductility of this material at increased strain rates. Conversely, platelets of martensite, formed in large quantities across the interior of the grains such as is the case with 301 stainless steel, present strong and numerous obstacles to substantially reduce the normal strain rate effects which otherwise would be expected. Similar observations were made by Williams (Ref. 46) and by Campbell and Duby (Ref. 52).

All observations indicate that there is no reason to expect microstructural injury to a metal from explosive forming within the strain rates investigated. The only cause for concern may be from the discovery of very high residual stresses as observed in low carbon steel. The high peak values approaching 100,000 psi may make the material susceptible to stress corrosion, and the wide distribution of the stresses may cause warpage during one-sided chemical milling or other metal removal operation.

6. RECOMMENDATIONS FOR CONTINUED WORK

a. In future work, less emphasis should be placed on optical microscopy.

b. Since dislocations can be made visible by electron microscopy, this technique should be applied to a study of the formation and motion of dislocations at various strain rates.

c. True stress-strain data should be generated in all tensile test procedures.

d. Microhardness traverses should be systematically employed.

e. For materials which do not show a "ceiling" within the range of strain rates investigated, the test program should be expanded to higher strain rates.

f. Biaxial tests should be continued with modified die configuration to allow for efficient control of strain components.

g. Residual stress investigations should be continued. For various materials, data should be generated for the prediction of stress patterns as functions of forming depth. Means should be developed for reduction of the residual stresses.

h. A study should be made of the reaction of welds to deformation with explosive strain rates.

REFERENCES

1. Anon., Strength of Metal Aircraft Elements, ANC-5, March 1955.

2. Fracture Testing of High Strength Sheet Materials, by the ASTM Committee on Fracture Testing of High-Strength Sheet Materials, ASTM Bull. No. 243, Jan. 1960, pp 29-39.

3. P. Ludwik, Uber den Einfluss der Deformationsgeschwindigkeit bei bleibenden Deformationen mit besonderer Beruecksichtigung der Nachwirkungserscheinigungen, Physikalische Zeitschrift, Vol. 10, 1909, pp 411-417.

4. L. Prandtl, Ein Gedankenmodell zur kinetischen Theorie der festen Koerper, Zeitschrift fur Angewandte Mathematik und Mechanik, Vol. 8, 1928, pp 85-106.

5. H. Deutler, Experimentelle Untersuchungen ueber die Abhaengigkeit der Zugspannungen von Verformungsgeschwindigkeit, Physikalische Zeitschrift, Vol. 33, 1932, pp 247-296.

6. Donald S. Clark, The Influence of Impact Velocity on the Tensile Characteristics of Some Aircraft Metals and Alloys, National Advisory Committee for Aeronautics, Technical Notes No. 868, October 1942.

7. D. S. Clark and D. S. Wood, The Tensile Impact Properties of Some Metals and Alloys, Transactions A. S. M., Vol. 42, 1950, pp 45-74.

8. Theodore von Kármán and Pol Duwez, The Propagation of Plastic Deformation in Solids, Journal of Applied Physics, Vol. 21, Oct. 1950, pp 987-994.

9. G. I. Taylor, Propagation of Earth Waves from an Explosion, British Official Report No. RC70, 1940.

10. G. I. Taylor, The Plastic Wave in a Wire Extended by an Impact Load, British Official Report No. RC329, 1942.

11. K. A. Rakhmatulin, Propagation of a Wave of Unloading, Prikladnaia Matematika i Mekhanika, Vol. 9, 1945, pp 91-100 (Russian).

12. G. S. Shapiro, Longitudinal Oscillation of Bars, Prikladnaia Matematika i Mekhanika, Vol. 10, 1946, pp 597-616 (Russian).

13. K. A. Rakhamatulin and G. S. Shapiro, On the Propagation of Plane Elastic-Plastic Waves, Prikladnaia Matematika i Mekhanika, Vol. 12, 1948, pp 369-374 (Russian).

14. L. E. Malvern, The Propagation of Longitudinal Waves of Plastic Deformation in a Bar of Material Exhibiting a Strain-Rate Effect, Journal of Applied Mechanics, Vol. 18, June 1951, pp 203-208.

15. J. E. Dorn, F. Hauser, and J. A. Simmons, Mathematical Theories of Plastic Deformation, First Technical Rept., 1 Apr. 1959, Series 133, Issue 1, Research Contr. supported by Convair, Div. of Gen. Dynamics, Minerals Research Lab., Inst. of Engrg. Research, Univ. of Calif., Berkeley, Calif.

16. A. Nadai and M. J. Manjoine, High-Speed Tension Tests at Elevated Temperatures, Part I, Proceedings ASTM, Vol. 40, 1940, pp 822-837.

17. A. Nadai and M. J. Manjoine, High-Speed Tension Tests at Elevated Temperatures, Parts II and III, Journal of Applied Mechanics, Transactions ASME, Vol. 63, 1941, pp A-77 - A91.

18. M. J. Manjoine, Influence of Rate of Strain and Temperature on Yield Stresses of Mild Steel, Journal of Applied Mechanics, Vol. 11, Dec. 1944, pp A211 - A218.

19. M. J. Manjoine, E. T. Wessel, and W. H. Pryle, Constant Head Rate Testing Machine with Instantaneous Speed Change, ASTM Bull. No. 226, Dec. 1957, pp 31-35 (TP219 - TP223).

20. Frederick Seitz, Jr., Andrew W. Lawson, and Park Miller, The Plastic Properties of Metals at High Rates of Strain, National Defense Research Committee, Rept. No. A-41, Prog. Rept. ASRD-495, Apr. 1942.

21. James Jamieson, Influence of Rate of Shear on Shearing Strength of Lead, Transactions ASME, Paper No. APM-56-7, pp 579-583.

REFERENCES (Cont.)

22. Glen N. Rardin, High Energy Rate Metal Forming, Interim Engr. Repts. No. 1 thru 8, Contr. No. AF 33(600)35543, Lockheed Aircraft Corporation.

23. Anon., Super Speed Metal Forming and Its Application in Today's Industries, Olin Mathieson Chemical Corporation, 1959.

24. Vasil Philipchuck, Metal Fabrication by Explosives, ASME Paper No. 60-MD-4, presented at the Design Engineering Conference, New York, May 23-26, 1960.

25. H. P. Tardif and W. H. Erickson, Explosive Metallurgy, The Canadian Mining and Metallurgical Bull. for June 1958, Montreal, pp 352-359.

26. Anon., Explosive Forming of Refractory Materials, Final Technical Rept., Chromalloy Corporation, 31 Dec. 1960, Contr. NOas 59-6265-C.

27. J. Hopkinson, Collected Scientific Papers, 1872, Vol. 11, p 316-ff.

28. B. Hopkinson, The Effects of Momentary Stresses in Metals, Proceedings Royal Society of London, 1905, Vol. A74, pp 498-506.

29. Sir Geoffrey Taylor, A. C. Whiffin, W. E. Carrington, and Marie L. V. Gayler, The Use of Flat Ended Projectiles For Determining Dynamic Yield Stress, Parts I, II, and III, Proceedings of the Royal Society of London, 1948, Vol. 194, Series A, 1038, p 289-ff.

30. A. F. C. Brown and N. G. D. Vincent, The Relationship Between Stress and Strain in the Tensile Impact Test, Proc. of the Inst. of Mech. Engrs., London, 1941, Vol. 145 (3), pp 126-134.

31. Behavior of Metals Under Impulsive Loads, by John S. Rinehart and John Pearson, American Society for Metals, Cleveland, Ohio, 1954.

32. Internat'l. Symposium on Stress Wave Propagation in Materials, edited by Norman Davis, sponsored by Office of Ordnance Research, U. S. Army, conducted by Dept. of Engrg. Mech., College of Engineering & Architecture, The Pennsylvania State Univ., Interscience Publ. Inc., New York & London, 1960.

33. Response of Metals to High Velocity Deformation, Proceedings of a Tech. Conf. sponsored by the Physical Metallurgy Committee of the Inst. of Metals Div., The Metallurgical Society, American Inst. of Mining, Metallurgical and Petroleum Engrs., Estes Park, Colorado, July 11-12, 1960. Edited by P. G. Shewman and V. F. Zackay, Interscience Publ. Inc., New York & London, 1961.

34. Metallographic Studies of Metals After Explosive Shock, by Cyril Stanley Smith, Transactions of the Metallurgical Society of AIME, Vol. 214, pp 574-589, 1958.

35. Hardness Plateaus and Twinning in Steel by Explosives with Lined Cavities, by Sampooran, Singh, N. R. Krishnaswamy, and A. Soundraraz, Journal of Applied Physics, Vol. 27, pp 617-620, 1956.

36. Study of Shock Propagation in Ferrous Metals, by Samuel Katz and R. E. Peterson, Stanford Research Institute, Final Rept. GU-863, 1955.

37. Hugoniot Equation of State of Aluminum and Steel from Oblique Shock Measurement, by Samuel Katz, D. G. Doran, and D. R. Curran, Journal of Applied Physics, Vol. 30, pp 568-576, 1959.

38. Investigation of the Effect of High Dynamic Pressures on the Metallurgical Properties of Iron and Titanium Base Alloys, by A. W. Hall, T. Matsuda, E. K. Henriksen, R. A. Rawe, and R. E. Herfert, 2nd Qrtrly Prog. Rept., 0485-01(02)QP, Contr. AF33(616)-8191, Aerojet-General Corporation, 15 July 1961 - 15 Oct. 1961.

39. Effect of Shock-Induced High Dynamic Pressures on Iron-Base Alloys, by Stephen M. Silverman, John E. Colgan, and Charles L. Wallace, 1st and 2nd Qrtrly Prog. Repts. No. PWA-2003 and PWA-2014, 1 May 1961 - 31 July 1961 and 1 Aug. 1961 - 31 Oct. 1961, Contr. AF33(616)-8190, Pratt & Whitney Aircraft, Div. of United Aircraft Corp.

40. E. K. Henriksen, Unpublished Memorandum, Aerojet-General Corp., 13 April 1959.

REFERENCES (Cont.)

41. E. K. Henriksen, Analysis of the Truing Process, in "Explosive Forming and Associated Programs", by M. Corney, A. Doherty, J. Edberg, A. Hall, E. K. Henriksen, I. Lieberman, and L. Zernow, Rept. No. 11, GWR 3567-04-603/664, Aerojet-General Corporation, Sept. 1959, pp 18-36.

42. E. K. Henriksen, Die Material Investigation, ibid., by I. Lieberman, A. E. Doherty, E. K. Henriksen, J. Edberg, C. H. Savage, J. L. Squier, and A. W. Hall, Rept. No. 12, GWR 3606-83-402, Aerojet-General Corporation, Dec. 1960, pp 14-29.

43. E. K. Henriksen, Study of Problems of Dome Sizing with Cylinders, ibid., by P. Barnett, A. E. Doherty, A. W. Hall, E. K. Henriksen, L. Knop, I. Lieberman, C. H. Savage, and L. Zernow, Rept. No. 3606-01QE-1, Aerojet-General Corporation, May 1960, pp 6-23.

44. P. C. Johnson, B. A. Stein, and R. S. Davis, Basic Parameters of Metal Behavior Under High Rate Forming, C-63080, Report to Watertown Arsenal Laboratories, Arthur D. Little Inc., Nov. 1961.

45. W. W. Wood, R. E. Goforth, D. L. Norwood, C. H. Cole, Jr., J. R. Russell, B. L. Scott and R. A. Ford, Sheet Metal Forming Technology, ASD Interim Report 7-871(1) and (2), Chance Vought Corporation, January-May 1962.

46. T. Williams, Some Metallurgical Aspects of Explosive Forming, Sheet Metal Industries, Vol. 39, No. 423, 1962, pp 487-494.

47. V. N. Krivobok and A. M. Talbot, Effect of Temperatures on the Mechanical Properties, Characteristics, and Processing of Austenitic Stainless Steels. Reprint from Copyrighted Proceedings of the American Society for Testing Materials, Vol. 50, 1950.

48. Daniel E. Strobecker, High Energy Rate Metal Working Bibliography, MEP 8006, North American Aviation, Inc., Columbus, Ohio.

49. J. R. Cotner and J. Weertman, Bibliography on High Speed Deformation of Materials, AF 29(601)-4343, Materials Science Dept., Northwestern University, 15 May 1961.

50. High Energy Rate Forming Bibliography, by ASTME Education Department, Paper No. SP60-187, American Society of Tool and Manufacturing Engineers.

51. C. T. Olofson and F. W. Boulger, Bibliography on Explosive Metal Working, DMIC Memo No. 51, Battelle Memorial Institute, Columbus, Ohio.

52. J. D. Campbell and J. Duby, The Yield Behavior of Mild Steel in Dynamic Compression, Proc. of the Royal Society, 1956, Vol. 236A, pp 24-40.

TABLE I

CHEMICAL COMPOSITION OF AISI 301 SHEET

Elements	Heat No. 44182 (1)	QQ-S-766 Specification Limits, %
Carbon	.08	0.15 Max.
Manganese	1.13	2.00 Max.
Silicon	.54	1.00 Max.
Nickel	8.84	6.00 Min.
Chromium	17.46	16.00 Min.
Phosphorus	.021	0.045 Max.
Sulphur	.017	0.035 Max.
Molybdenum	.14	
Copper	.20	

Note: (1) Procured from Affiliated Metal Products, Los Angeles, California.

TABLE II

CHEMICAL ANALYSIS OF 17-7PH STAINLESS STEEL SHEET

Elements	Heat No. 880437 (1) (%)	MIL-S-25043-B Specification Limits (%)
CARBON	.06	0.09 Max.
MANGANESE	.55	1.00 Max.
PHOSPHOROUS	.015	0.040 Max.
SULPHUR	.012	0.030 Max.
SILICON	.33	1.00 Max.
NICKEL	7.16	6.50 - 7.75
CHROMIUM	17.17	16.00 - 18.00
ALUMINUM	1.24	0.75 - 1.50

Note: (1) Procured from Affiliated Metal Products, Los Angeles, California

TABLE III

CHEMICAL ANALYSIS OF 6Al-4V TITANIUM ALLOY SHEET
- ANNEALED AND DESCALED -

Elements	Heat No. 3930274 (1) (%)	AMS 4911 Specification Limits (%)
CARBON	.032	0.10 Max.
NITROGEN	.009	0.05 Max.
ALUMINUM	6.15	5.50 - 6.75
IRON	.18	0.30 Max.
OXYGEN	.13	0.15 Max.
HYDROGEN	.004	0.015 Max.
VANADIUM	4.15	3.50 - 4.50

Note: (1) Procured from Republic Steel Corporation, Cleveland, Ohio

TABLE IV

CHEMICAL ANALYSIS OF 13V-11Cr-3Al TITANIUM ALLOY SHEET

- SOLUTION-TREATED AND DESCALED -

Elements	Heat No. 3960204 (1) (%)	AMS Draft 49A0 Specification Limits (%)
CARBON	.034	0.10 Max.
NITROGEN	.015	0.05 Max.
ALUMINUM	2.95	2.50 - 4.00
IRON	.38	0.35 Max.
OXYGEN	.11	0.10 - 0.17
CHROMIUM	11.50	10.0 - 12.0
VANADIUM	13.40	12.5 - 14.5
HYDROGEN		0.02 Max.

Note: (1) Procured from Republic Steel Corporation, Cleveland, Ohio

TABLE V

STRAIN DATA AND MECHANICAL PROPERTIES OF CONTROL AND STRAINED UNIAXIAL SPECIMENS

5456-0 ALUMINUM

Specimen No.	Specimen Type	FORMING CONDITIONS Temp. °F	Strain Rate in/in/min	Applied Strain % of Max	Measured Strain % El. in 2"	Actual Strain % of Max	Material Tested	MECHANICAL PROPERTIES Prop. Limit ksi	0.2% Yield Strength ksi	Ult. Tensile Strength ksi	% El. in 2"	% Red. of Area	E psi x 10^{-6}	Micro-Hardness Knoop
1B1L	Tensile Long						As Rec'd	20.1	22.2	50.6	21.5	32.9	9.8	
1B2L								20.5	22.2	50.4	21.0	32.2	9.8	
1B3L								18.1	22.0	50.3	20.5	33.3	9.8	
1B1LN	Notch Long									42.1				
1B2LN										42.1				
1B3LN										42.2				
1B1T	Tensile Trans.							20.7	22.5	50.5	23.5	32.7	9.6	
1B2T								20.2	22.4	50.6	21.5	33.5	9.7	
1B3T								21.0	22.5	50.7	21.5	31.5	10.0	
1B1TN	Notch Trans.									39.0				
1B2TN										39.1				
1B3TN										39.8				59.4
3B1	Fracture	Ambient	3	100	23.5									
3B2			3	100	22.0									
AVG.			3		22.7	100								
B6	Fracture		Expl.	100	28.5									
B8				100	29.0									
AVG.					28.7	100								
B1	Tensile		3	40	10.5	46.3	As Formed	40.7	48.2	54.9	13.0	27.7	9.6	
3B3			3	40	10.5	46.3		46.1	48.5	54.8	13.0	22.4	10.0	
4B1N	Notch		3	40	9.5	41.8				52.5				
4B2N			3	40	10.5	46.3				53.9				
B2	Micro		3	40	11.0	48.5								74.2

TABLE V (Cont.)

STRAIN DATA AND MECHANICAL PROPERTIES OF CONTROL AND STRAINED UNIAXIAL SPECIMENS

5456-O ALUMINUM

Specimen No.	Specimen Type	FORMING CONDITIONS			Measured Strain	Actual Strain	Material Tested	MECHANICAL PROPERTIES						
		Temp. °F	Strain Rate in/in/min	Applied Strain % of Max	% El. in 2"	% of Max		Prop. Limit ksi	0.2% Yield Strength ksi	Ult. Tensile Strength ksi	% El. in 2"	% Red. of Area	E psi x 10^-6	Micro-Hardness Knoop
4B2	Tensile	Ambient	3	75	16.0	70.5	As Formed	45.4	53.1	58.3	9.0	17.8	10.4	
4B3	↓	↓	3	75	15.5	68.4	↓	49.8	52.8	57.9	8.5	13.1	10.3	
3B2N	Notch		3	75	16.0	70.5				55.0				
3B3N	↓		3	75	17.0	75.0				56.1				
4B1	Micro		3	75	18.0	79.4								36.[illegible]
5B1	Tensile		Expl.	40	13.5	47.0		43.6	50.8	56.5	11.0	31.9	10.4	
5B2	↓		↓	40	13.5	47.0		42.1	50.4	56.3	12.0	36.2	10.5	
5B2N	Notch			40	13.5	47.0				54.3				
5B3N	↓			40	13.0	45.3				53.4				
7B3	Micro			40	14.0	48.8								75.1
B7	Tensile			75	19.0	66.2		39.1	53.1	57.9	11.0	16.7	10.1	
6B1				75	20.5	71.4		36.6	54.4	59.6	6.5	36.2	9.5	
6B3	↓			75	20.5	71.4		43.3	52.8	60.0	9.6	24.2	9.8	
6B2N	Notch			75	21.0	73.2				58.0				
6B3N	↓			75	20.0	69.7				57.2				
6B2	Micro	↓	↓	75	21.5	75.0	↓							58.9

TABLE VI

STRAIN DATA AND MECHANICAL PROPERTIES OF CONTROL AND STRAINED UNIAXIAL SPECIMENS

301 STAINLESS STEEL

Specimen No.	Specimen Type	FORMING CONDITIONS: Temp. °F	FORMING CONDITIONS: Strain Rate in/in/min	FORMING CONDITIONS: Applied Strain % of Max	Measured Strain % El. in 2"	Actual Strain % of Max	Material Tested	MECHANICAL PROPERTIES: Prop. Limit ksi	MECHANICAL PROPERTIES: 0.2% Yield Strength ksi	MECHANICAL PROPERTIES: Ult. Tensile Strength ksi	MECHANICAL PROPERTIES: % El. in 2"	MECHANICAL PROPERTIES: % Red. of Area	MECHANICAL PROPERTIES: E psi x 10⁻⁶	MECHANICAL PROPERTIES: Micro-Hardness [illegible]
1C1L	Tensile Long						As Rec'd	17.7	43.3	91.1	67.5	63.0	[illegible]	
1C2L								16.0	40.5	87.9	63.5	64.2	26.5	
1C3L								20.7	43.2	88.4	63.0	62.5	27.9	
1C1LN	Notch Long									84.2				
1C2LN										83.8				
1C3LN										84.0				
1C1T	Tensile Trans.							17.9	42.4	89.0	62.5	55.6	29.3	
1C2T								20.9	42.6	88.0	60.5	55.2	26.7	
1C3T								18.0	42.9	88.3	60.5	54.1	27.2	
1C1TN	Notch Trans.									77.5				
1C2TN										78.5				
1C3TN										76.3				[illegible]
3C1	Fracture	Ambient	3	100	56.0									
3C2			3	100	56.0									
AVG.			3		56.0	100								
C6	Fracture		Expl.	100	60.5									
C9			Expl.	100	60.0									
AVG.			Expl.		60.2	100								
15C2-2	Tensile		3	40	23.0	41.1	As Formed	66.1	96.0	109.0	31.0	52.6	28.4	
4C3-2			3	40	22.0	39.3		84.4	97.8	110.4	30.5	42.2	25.1	
4C1N	Notch		3	40	21.5	38.4				117.4				
4C2N			3	40	21.5	38.4				119.1				
4C2-2	Micro		3	40	21.0	37.5								277.5
4C1	Tensile		.03	75	45.0	80.4 *		63.1	123.9	129.5	19.0	43.3	22.2	
4C2			.03	75	45.0	80.4		72.1	126.2	131.5	19.0	41.8	22.8	
4C3			.03	75	45.0	80.4		77.1	127.8	131.8	18.0	46.3	21.9	
4C4			3	75	44.0	78.6		70.7	125.5	130.0	17.5	37.8	20.6	
4C5			3	75	41.5	74.1		75.0	123.0	127.6	20.5	44.3	22.9	

* 100 per cent for .03 in/in/min is taken as 56.0 as for 3 in/in/min.

TABLE VI (Cont.)

STRAIN DATA AND MECHANICAL PROPERTIES OF CONTROL AND STRAINED UNIAXIAL SPECIMENS

301 STAINLESS STEEL

Specimen No.	Specimen Type	FORMING CONDITIONS: Temp. °F	Strain Rate in/in/min	Applied Strain % of Max	Measured Strain % El. in 2"	Actual Strain % of Max	Material Tested	MECHANICAL PROPERTIES: Prop. Limit ksi	0.2% Yield Strength ksi	Ult. Tensile Strength ksi	% El. in 2"	% Red. of Area	E psi x 10^{-6}	Micro-Hardness Knoop
3C1N	Notch	Ambient	3	75	41.0	73.3	As Formed			144.0				
3C2N			3	75	40.0	71.5				144.0				
3C2-2	Micro		3	75	41.0	73.3								331.4
5C3	Tensile		Expl.	40	24.0	39.8		74.1	101.9	120.7	27.0	47.3	15.6	
5C4				40	25.0	41.5		88.0	109.9	118.9	26.5	42.5	12.1	
5C2N	Notch			40	25.5	42.3				131.4				
5C3N				40	24.5	40.7				127.0				
5C2	Micro			40	26.5	44.0								305.2
6C1	Tensile			75	42.5	70.6		85.1	134.8	139.5	14.0	43.0	22.6	
6C3				75	42.5	70.6		82.5	133.0	139.6	14.0	39.6	23.3	
6C3N	Notch			75	41.5	68.9				150.2				
C16				75	44.0	73.0				155.4				
6C2	Micro			75	43.0	71.4								359.0
15C1	Fracture	-320	.03	100	41.5									
15C2			.03	100	41.0									
AVG.					41.2	100								
1C1T-2			1.5	100	37.0									
1C2T-2			1.5	100	35.0									
AVG.					36.0	100								
17C2N			Expl.	100	40.0									
C24			Expl.	100	40.0									
AVG.					40.0	100								
15C1-2	Tensile		1.5	40	16.0	44.5	As Formed	117.5	143.2	171.6	14.5	34.0	20.3	
16C3-2			1.5	40	16.5	45.8		78.9	145.6	183.4	13.0	30.5	20.3	
16C1N	Notch		1.5	40	17.0	47.2				133.8				
16C4N			1.5	40	17.0	47.2				134.8				
16C3M	Micro		1.5	40	16.5	45.8								412.7

TABLE VI (Cont.)

STRAIN DATA AND MECHANICAL PROPERTIES OF CONTROL AND STRAINED UNIAXIAL SPECIMENS

301 STAINLESS STEEL

Specimen No.	Specimen No.	FORMING CONDITIONS Temp. °F	Strain Rate in/in/min	Applied Strain % of Max	Measured Strain % El. in 2"	Actual Strain % of Max	Material Tested ksi	MECHANICAL PROPERTIES Prop. Limit	0.2% Yield Strength ksi	Ult. Tensile Strength ksi	% El. in 2"	% Red. of Area	E psi x 10^{-6}	Micro-Hardness Knoop
16C1	Tensile	-320	.03	75	29.5	71.6	As Formed	126.7	230.5	233.0	4.5	31.0	24.4	
16C2			.03	75	31.0	75.2		112.4	231.5	234.2	4.5	27.9	24.6	
16C3			.03	75	30.5	74.0		112.1	-- (1)	238.6	4.5	26.2	24.2	
3C3			1.5	75	28.0	77.8		146.7	226.4	227.8	4.5	32.3	23.4	
15C3			1.5	75	28.0	77.8		156.5	226.3	226.8	4.5	30.8	22.0	
15C1N	Notch		1.5	75	29.0	80.5				130.2				
15C3N			1.5	75	24.0	66.7				139.5				
15C4N	Micro		1.5	75	28.5	79.2								458.2
20C1N	Tensile		Expl.	40	18.0	45.0		96.4	135.2	169.5	14.0	29.9	18.6	
20C2N				40	18.0	45.0		93.8	140.7	171.0	14.0	27.9	19.0	
20C3N	Notch			40	17.0	42.5				128.5				
20C4N				40	18.0	45.0				134.4				
19C4N	Micro			40	18.5	46.2								426.9
18C3N	Tensile			75	30.0	75.0		149.2	212.6	214.1	4.0	19.0	20.2	
C23				75	29.5	73.7		194.3	210.5	210.9	3.5	10.0	18.3	
19C1N	Notch			75	29.0	72.5				143.8				
19C2N				75	28.0	70.0				91.6				
18C4N	Micro			75	31.5	78.7								448.0

(1) Jaws slipped during Tensile Test.

TABLE VII

STRAIN DATA AND MECHANICAL PROPERTIES OF CONTROL AND STRAINED UNIAXIAL SPECIMENS

17-7 PH STAINLESS STEEL

Specimen No.	Specimen Type	FORMING CONDITIONS Temp. °F	Strain Rate in/in/min	Applied Strain % of Max	Measured Strain % El. in 2"	Actual Strain % of Max	Material Tested	MECHANICAL PROPERTIES Prop. Limit ksi	0.2% Yield Strength ksi	Ult. Tensile Strength ksi	% El. in 2"	% Red. of Area	E psi x 10^{-6}	Micro-Hardness Knoop
1D1L	Tensile Long						As Rec'd	18.9	38.5	139.9	29.5	45.1	28.2	
1D2L								19.5	38.8	141.2	30.0	46.1	26.2	
1D3L								19.7	39.1	139.5	29.5	49.1	27.1	
1D1LN	Notch Long									113.0				
1D2LN										110.9				
1D3LN										109.2				
1D1T	Tensile Trans.							21.8	41.8	134.7	28.5	47.4	27.4	
1D2T								19.8	40.7	135.3	30.0	42.2	27.7	
1D3T								21.0	40.7	135.1	30.0	45.9	27.2	
1D1TN	Notch Trans.									79.9				
1D2TN										81.3				
1D3TN										80.0				190.4
2D1L	Tensile Long						As Rec'd & Ht. Treated	79.0	181.8	196.8	10.5	34.3	29.0	
2D2L								72.6	177.4	193.7	10.5	38.9	29.3	
2D3L								81.1	177.0	192.7	10.5	38.9	29.3	
2D1LN	Notch Long									72.0				
2D2LN										119.9				
2D3LN										130.1				
2D1T	Tensile Trans.							61.9	173.1	192.8	9.5	25.6	29.6	
2D2T								71.9	174.4	192.0	9.5	27.9	30.2	
2D3T								67.8	179.3	195.6	9.5	22.0	30.2	
2D1TN	Notch Trans.									69.4				
2D2TN										94.1				
2D3TN										105.0				
3D1	Fracture	Ambient	3	100	33.0									
3D2			3	100	35.5									
AVG.			3		34.2	100								
D1			Expl.	100	59.5									
AVG.			Expl.		59.5	100								
D11	Tensile		3	40	13.0	38.0	As Formed	92.3	103.0	154.1	13.0	37.6	23.3	
D14			3	40	13.5	39.5		88.9	102.0	152.8	13.0	41.4	22.7	

TABLE VII (Cont.)

STRAIN DATA AND MECHANICAL PROPERTIES OF CONTROL AND STRAINED UNIAXIAL SPECIMENS

17-7 PH STAINLESS STEEL

Specimen No.	Specimen Type	FORMING CONDITIONS Temp. °F	Strain Rate in/in/min	Applied Strain % of Max	Measured Strain % El. in 2"	Actual Strain % of Max	Material Tested	MECHANICAL PROPERTIES Prop. Limit ksi	0.2% Yield Strength ksi	Ult. Tensile Strength ksi	% El. in 2"	% Red. of Area	E psi x 10^{-6}	Micro-Hardness Knoop
D13	Notch	Ambient	3	40	13.0	38.0	As Formed			125.6				
21D2			3	40	13.5	39.5				128.6				
16D3	Micro		3	40	13.5	39.5								312.0
4D1	Tensile		3	75	25.5	74.6		109.2	136.0	157.2	13.5	40.4	26.0	
4D3			3	75	25.5	74.6		109.6	138.8	159.6	14.0	36.6	26.1	
D18	Notch		3	75	25.0	73.1				165.6				
9D1			3	75	24.5	71.6				163.6				
4D2	Micro		3	75	26.5	77.5								361.0
5D2	Tensile		Expl.	40	24.0	40.3		71.7	96.6	159.6	16.5	41.3	21.9	
5D3				40	23.0	38.6		64.7	91.2	157.8	16.5	39.7	22.8	
5D1N	Notch			40	21.5	36.1				123.2				
5D2N				40	22.0	37.0				122.2				
5D1	Micro			40	27.0	45.4								344.5
6D1	Tensile			75	45.5	76.5		77.9	136.6	176.5	16.0	37.6	25.6	
6D2				75	45.0	75.7		75.1	143.1	181.6	14.0	40.7	24.4	
6D3				75	48.5	81.5		73.5	147.1	179.4	13.5	39.0	23.0	
6D1N	Notch			75	42.0	70.6				176.5				
6D3N				75	42.5	71.4				165.4				
D2	Micro			75	42.0	70.6								372.5
21D1	Tensile		3	40	13.0	38.0	As Formed & Aged	90.0	127.1	161.0	22.0	34.5	27.5	
D5			3	40	13.5	39.5		92.6	139.3	162.7	21.0	31.4	27.3	
21D3	Notch		3	40	13.0	38.0				125.2				
D6			3	40	13.0	38.0				132.6				
22D1	Micro		3	40	13.5	39.5								355.5
10D1	Tensile		3	75	26.0	76.0		151.3	196.4	196.4	9.0	27.9	25.6	
10D3			3	75	26.5	77.5		140.9	194.6	197.3	8.0	28.9	27.3	
9D3	Notch		3	75	24.5	71.6				163.6				
3D3			3	75	24.5	71.6				164.4				
10D2	Micro		3	75	26.0	76.0								417.8

TABLE VII(Cont.)

STRAIN DATA AND MECHANICAL PROPERTIES OF CONTROL AND STRAINED UNIAXIAL SPECIMENS

17-7 PH STAINLESS STEEL

Specimen No.	Specimen Type	FORMING CONDITIONS			Measured Strain	Actual Strain	Material Tested	MECHANICAL PROPERTIES						
		Temp. ^{o}F	Strain Rate in/in/min	Applied Strain % of Max	% El. in 2"	% of Max		Prop. Limit ksi	0.2% Yield Strength ksi	Ult. Tensile Strength ksi	% El. in 2"	% Red. of Area	E psi x 10^{-6}	Micro-Hardness Knoop
11D2	Tensile	Ambient	Expl.	40	22.5	37.8	As Formed & Aged	75.6	124.2	162.0	22.5	35.9	30.6	
11D3				40	21.5	36.2		79.0	128.0	156.9	21.0	33.5	27.7	
11D1N	Notch			40	21.0	35.3				116.3				
11D3N				40	22.0	37.0				118.6				
11D1	Micro			40	23.0	38.7								361.0
12D6	Tensile			75	40.5	68.1		113.0	173.7	188.3	13.0	34.8	26.8	
12D8				75	40.5	68.1		134.0	187.4	194.8	8.0	32.9	24.8	
12D2N	Notch			75	42.0	70.6				165.1				
12D3N				75	42.0	70.6				163.4				
26D2	Micro			75	46.5	78.1								434.2
1	Fracture	-320	3	100	16.0									
2			3	100	17.5									
3			3	100	21.0									
AVG.			3		18.2	100								
D31			Expl.	100	26.0									
17D2N			Expl.	100	26.0									
AVG.			Expl.		26.0	100								
16D2	Tensile		3	40	8.0	44.0	As Formed	119.3	157.5	218.7	10.5	26.2	22.1	
16D3			3	40	8.5	46.7		109.6	150.4	216.7	10.0	23.7	22.1	
16D1N	Notch		3	40	8.5	46.7				137.9				
16D4N			3	40	8.5	46.7				135.3				
16D1	Micro		3	40	9.0	49.5								451.6
15D1	Tensile		3	75	12.0	65.9		177.0	216.0	229.4	6.5	29.6	21.9	
15D3			3	75	12.5	68.7		180.5	219.1	233.9	6.0	18.7	22.5	
15D2N	Notch		3	75	11.0	60.5				150.3				
15D3N			3	75	11.0	60.5				143.5				
15D4N	Micro		3	75	11.5	63.2								441.0
24D3N	Tensile		Expl.	40	12.5	48.1		120.6	175.1	222.0	8.0	25.2	23.6	
24D4N				40	12.5	48.1		139.3	176.7	222.5	9.0	24.7	22.6	
25D4N	Notch			40	12.5	48.1				141.2				
25D3N				40	13.0	50.0				145.3				
24D1N	Micro			40	13.5	51.9								458.2

TABLE VII (Cont.)

STRAIN DATA AND MECHANICAL PROPERTIES OF CONTROL AND STRAINED UNIXIAL SPECIMENS

17-7 PH STAINLESS STEEL

Specimen No.	Specimen Type	FORMING CONDITIONS Temp. °F	Strain Rate in/in/min	Applied Strain % of Max	Measured Strain % El. in 2"	Actual Strain % of Max	Material Tested	MECHANICAL PROPERTIES Prop. Limit ksi	0.2% Yield Strength ksi	Ult. Tensile Strength ksi	% El. in 2'	% Red. of Area	E psi x 10^{-6}	Micro-Hardness Kroop
17D4N	Tensile	-320	Expl.	75	13.0	69.3	As Formed	156.1	240.5	247.3	3.5	17.9	25.3	
18D1N				75	18.0	69.3		169.2	240.9	246.4	3.5	15.8	23.5	
23D1N	Notch			75	19.0	73.1				131.9				
26D4N				75	19.0	73.1				132.8				
19D4N	Micro			75	20.0	77.0								500.0
22D1	Tensile		3	40	7.5	41.2	As Formed & Aged	175.0	222.5	260.0	8.5	12.2	22.7	
22D2			3	40	9.0	49.5		179.4	221.8	256.0	9.5	16.3	22.1	
22D2N	Notch		3	40	9.0	49.5				112.0				
22D4N			3	40	9.0	49.5				114.5				
16D3N	Micro		3	40	9.0	49.5								478.8
21D1X	Tensile		3	75	11.5	63.2		235.9	272.1	276.2	5.0	20.2	26.0	
21D2			3	75	11.5	63.2		215.6	269.5	281.3	5.0	18.5	25.0	
21D2N	Notch		3	75	10.0	55.0				119.6				
21D3N			3	75	11.0	60.5				87.7				
21D4N	Micro		3	75	12.0	65.9								481.2
25D1N	Tensile		Expl.	40	12.5	48.1		93.3	248.4	277.4	3.5	4.8	23.5	
25D2N				40	12.5	48.1		83.3	243.7	271.9	3.5	20.2	22.2	
23D2N	Notch			40	13.5	51.9				92.9				
23D4N				40	13.5	51.9				98.2				
24D2N	Micro			40	14.0	53.9								548.5
18D3N	Tensile			75	18.0	69.3		232.1	301.7	313.3	2.5	13.3	26.9	
26D2N				75	18.5	71.2		257.5	309.0	314.4	3.0	15.5	26.4	
20D1N	Notch			75	19.5	75.0				89.6				
19D3N				75	20.0	77.0				76.5				
20D2N	Micro			75	21.0	80.8								576.5

TABLE VIII

STRAIN DATA AND MECHANICAL PROPERTIES OF CONTROL AND STRAINED UNIAXIAL SPECIMENS

6Al-4V TITANIUM

Specimen No.	Specimen Type	FORMING CONDITIONS Temp. °F	Strain Rate in/in/min	Applied Strain % of Max	Measured Strain % El. in 2"	Actual Strain % of Max	Material Tested	MECHANICAL PROPERTIES Prop. Limit ksi	0.2% Yield Strength ksi	Ult. Tensile Strength ksi	% El. in 2"	% Red. of Area	E psi x 10^{-6}	Micro-Hardness Knoop
1E1L	Tensile Long						As Rec'd	128.2	140.2	147.3	12.0	24.1	15.9	
1E2L								120.3	138.6	145.5	13.5	29.5	16.2	
1E3L								126.2	139.4	146.2	12.5	26.6	16.2	
1E1LN	Notch Long									148.5				
1E2LN										149.7				
1E3LN										155.3				
1E1T	Tensile Trans.							129.5	147.2	153.1	14.0	31.1	17.6	
1E2T								135.7	146.9	151.6	14.5	31.7	17.6	
1E3T								132.1	146.8	151.5	14.5	32.5	17.6	
1E1TN	Notch Trans.									146.2				
1E2TN										154.7				
1E3TN										160.6				325.4
2E1L	Tensile Long						Sol.Treated & Aged	124.2	170.4	181.3	7.5	12.4	17.0	
2E3L								133.7	171.8	182.3	9.0	15.9	16.9	
2E4L								134.0	170.9	181.9	6.0	21.4	16.9	
2E1LN	Notch Long									150.7				
2E2LN										150.2				
2E3LN										134.2				
2E1TN	Tensile Trans.							144.3	171.0	182.9	9.0	28.4 / 27.3*	16.4	
2E2TN								142.3	171.1	182.4	8.0	19.6 / 19.7	16.4	
2E3TN								143.4	175.2	182.7	9.0	30.1 / [illegible]	16.5	
2E4TN	Notch Trans.									144.7				
2E5TN										136.8				
2E3TN														375.0

* From microscope measurements.

TABLE VIII (Cont.)

STRAIN DATA AND MECHANICAL PROPERTIES OF CONTROL AND STRAINED UNIAXIAL SPECIMENS

6Al-4V TITANIUM

Specimen No.	Specimen Type	FORMING CONDITIONS Temp. °F	Strain Rate in/in/min	Applied Strain % of Max	Measured Strain % El. in 2"	Actual Strain % of Max	Material Tested	MECHANICAL PROPERTIES Prop. Limit ksi	0.2% Yield Strength ksi	Ult. Tensile Strength ksi	% El. in 2"	% Red. of Area	E psi x 10^{-6}	Micro-Hardness Knoop
3E1	Fracture	Ambient	3	100	13.5									
3E2			3	100	14.5									
AVG.			3		14.0	100								
E1			Expl.	100	12.0									
E4				100	14.0									
E5				100	14.0									
AVG.					13.3	100								
13E 3	Tensile		3	30	4.0	28.6	As Formed	85.9	152.7	157.4	12.0	33.4 / 30.1*	16.3	
13E 4			3	30	4.0	28.6		129.1	157.7	161.6	9.0	28.3 / 32.0	16.5	
13E 5	Notch		3	30	4.0	28.6				150.9				
13E 8			3	30	3.5	25.0				154.6				
13E 7	Micro		3	30	4.5	32.2								326.1
4E1	Tensile		3	60	8.5	60.8		103.2	171.4	173.1	5.5	26.5	17.4	
4E3			3	60	8.5	60.8		115.3	171.5	171.5	6.5	25.4	17.1	
13E 9	Notch		3	60	6.0	42.9				159.0				
13E 11			3	60	6.0	42.9				159.1				
13E 10	Micro		3	60	7.0	50.0								316.6
5E1	Tensile		Expl.	30	4.0	30.1		101.4	161.7	164.8	10.5	36.0 / 32.8*	17.3	
7E1				30	4.0	30.1		114.2	164.5	164.9	10.0	34.5 / 31.7	17.3	
E12	Notch			30	3.5	26.3				161.7				
E15				30	3.5	26.3				165.2				
5E2	Micro			30	3.0	22.6								287.4
6E2	Tensile			60	8.5	64.0		106.6	170.4	171.2	7.5	29.2	17.4	
6E3				60	6.0	45.2		106.6	164.8	165.4	8.5	32.0	17.5	
6E4				60	6.0	45.2		-- (1)	167.7	167.9	8.5	32.0	18.4	
E7	Notch			60	6.0	45.2				164.3				
E8				60	6.0	45.2				156.6				
E9				60	7.0	52.7				163.2				
E6	Micro			60	6.5	48.9								287.4

* From microscope measurements.

(1) Jaws slipped during tensile test.

TABLE VIII (Cont.)

STRAIN DATA AND MECHANICAL PROPERTIES OF CONTROL AND STRAINED UNIAXIAL SPECIMENS

6Al-4V TITANIUM

Specimen No.	Specimen Type	FORMING CONDITIONS: Temp. °F	Strain Rate in/in/min	Applied Strain % of Max	Measured Strain % El. in 2"	Actual Strain % of Max	Material Tested	MECHANICAL PROPERTIES: Prop. Limit ksi	0.2% Yield Strength ksi	Ult. Tensile Strength ksi	% El. in 2"	% Red. of Area	E psi x 10^{-6}	Micro-Hardness Knoop
14E5	Fracture Sol. Tr.	Ambient	3	100										
14E6			3	100										
AVG.			3			100								
9E3			Expl.	100	4.0									
10E1				100	10.5									
14E1				100	7.0									
AVG.					7.2	100								
14E4	Tensile		3	50	2.5	38.5	Sol. Tr., Formed, & Aged	134.0	170.8	180.9	8.5	28.5 / 35.2*	16.3	
14E8			3	50	2.5	38.5		136.5	171.3	182.6	7.0	22.3 / 30.0	16.6	
14E9	Notch		3	50	2.5	38.5				142.6				
14E10			3	50	2.5	38.5				143.3				
14E11			3	50	2.5	38.5				138.5				
14E12	Micro		3	50	2.5	38.5								— —
12E2	Tensile		Expl.	50	3.0	41.7		135.6	164.9	176.1	7.5	36.3 / 32.0*	17.0	
12E3				50	3.0	41.7		125.9	165.1	174.4	5.5	21.9 / 23.1	16.5	
10E3	Notch			50	3.0	41.7				132.8				
11E2				50	3.0	41.7				152.8				
11E1	Micro			50	3.5	48.6								358.6

* From microscope measurements.

TABLE IX

STRAIN DATA AND MECHANICAL PROPERTIES OF CONTROL AND STRAINED UNIAXIAL SPECIMENS

13V-11Cr-3Al TITANIUM

Specimen No.	Specimen Type	FORMING CONDITIONS: Temp. °F	Strain Rate in/in/min	Applied Strain % of Max	Measured Strain % El. in 2"	Actual Strain % of Max	Material Tested	MECHANICAL PROPERTIES: Prop. Limit ksi	0.2% Yield Strength ksi	Ult. Tensile Strength ksi	% El. in 2"	% Red. of Area	E psi x 10^{-6}	Micro-Hardness Knoop
1F1L	Tensile Long						As Rec'd	123.0	132.4	133.9	20.5	44.4	14.5	
1F2L								123.8	132.4	133.9	20.5	44.1	14.2	
1F3L								123.8	132.2	134.0	21.0	41.6	14.3	
1F1LN	Notch Long									158.5				
1F2LN										158.1				
1F3LN										163.1				
1F1T	Tensile Trans.							133.2	140.0	142.2	15.5	37.8	15.3	
1F2T								132.8	139.5	141.8	14.0	38.7	15.4	
1F3T								130.0	139.1	141.5	14.5	42.3	15.5	
1F1TN	Notch Trans.									169.1				
1F2TN										170.3				
1F3TN										168.9				319.2
2F1L	Tensile Long						As Rec'd & Aged	126.4	136.8	146.4	13.5	23.8	14.6	
2F2L								114.2	138.9	146.9	11.5	14.6	15.0	
2F3L								99.4	136.8	147.1	14.0	23.8	15.3	
2F1LN	Notch Long									139.1				
2F2LN										163.0				
2F3LN										158.8				
2F1T	Tensile Trans.							127.1	146.6	155.2	7.5	14.5	16.5	
2F2T								129.7	149.7	155.7	8.0	13.5	16.4	
2F3T								120.5	144.6	152.0	7.0	11.4	16.3	
2F1TN	Notch Trans.									152.9				
2F2TN										167.7				
2F3TN										163.6				362.0

TABLE IX (Cont.)

STRAIN DATA AND MECHANICAL PROPERTIES OF CONTROL AND STRAINED UNIAXIAL SPECIMENS

13V-11Cr-3Al TITANIUM

Specimen No.	Specimen Type	FORMING CONDITIONS Temp. °F	Strain Rate in/in/min	Applied Strain % of Max	Measured Strain % El. in 2"	Actual Strain % of Max	Material Tested	MECHANICAL PROPERTIES Prop. Limit ksi	0.2% Yield Strength ksi	Ult. Tensile Strength	% El. in 2"	% Red. of Area		E psi x 10^-6	Micro-Hardness Knoop
4F2	Fracture	Ambient	3	100	10.5										
10F2			3	100	9.0										
AVG.			3		9.75	100									
F11			Expl.	100	9.0										
6F1				100	7.0										
AVG.					8.0	100									
8F1	Tensile		3	50	3.5	35.9	As Formed	156.9	157.7	157.7	8.0	42.6	38.7*	15.2	
8F2			3	50	3.5	35.9		155.2	157.3	157.3	8.0	37.7	35.9	15.8	
9F2	Notch		3	50	3.5	35.9				176.3					
11F3			3	50	3.5	35.9				172.8					
4F3	Micro		3	50	4.0	41.1									304.3
F16	Tensile		Expl.	50	3.0	37.5		138.8	154.9	154.9	8.5	40.0	38.6*	15.1	
F19				50	3.0	37.5		141.8	155.6	155.6	10.5	41.0	39.6	15.1	
F14	Notch			50	4.0	50.0				141.3					
F17				50	3.5	43.7				173.1					
F18	Micro			50	3.5	43.7									337.6
13F3	Tensile		3	50	3.5	43.7	As Formed & Aged	115.8	130.5	136.2	4.5	32.9	33.5*	12.9	
14F2			3	50	3.5	43.7		110.9	129.0	133.8	4.3	32.3	30.0	13.2	
9F3	Notch		3	50	3.0	37.5				112.3					
11F2			3	50	4.0	50.0				114.6					
4F3A	Micro		3	50	4.0	50.0									339.8
F21	Tensile		Expl.	50	3.0	37.5		112.8	128.6	138.2	4.5	31.1	31.4*	12.8	
F22				50	3.0	37.5		114.4	130.3	138.6	4.5	32.8	33.4	12.7	
F26	Notch			50	4.0	50.0				102.3					
F28				50	3.5	43.7				101.2					
F27	Micro			50	4.0	50.0									354.6

* From microscope measurements

TABLE X

DETERMINATION OF EXPLOSIVE STRAIN RATES BY HIGH-SPEED PHOTOGRAPHY

MATERIAL	SPECIMEN NO.	STRAIN in/in.	FRAME RATE Fr/Milisec	FRAMES To Fracture	STRAIN RATE in/in/sec
5456-0 ALUMINUM	B12	.30	9	~ 18	~ 150
	B11	.30	12	~ 34	~ 106
AISI 301 STAINLESS STEEL	C19	.60	8.5	< 50	> 102
	C20	.63	10	< 60	> 105
	C17	.605	12	< 60	> 121
17-7 PH STAINLESS STEEL	D21	.65	9.5	~ 40	~ 154
	D22	.57	13	< 43	> 172
6Al-4V TITANIUM	7E2	.16	10.5	< 32	> 52.5
	E19	.17	12	~ 20	~ 102
6Al-4V Sol. Tr.	14E2	.08	8	~ 12	~ 53.4
13V-11Cr-3Al TITANIUM	F31	.07	9	~ 12	~ 52.5
	F29	.07	12	< 30	> 28

TABLE XI

FILM MEASUREMENT DATA - SPECIMEN 7B3N

	Frame No.	Film Reading, F				Shoulder Length S (in.)	Gage Length (From Fig. 12) (in.)	Strain (in/in)	Time * (μ sec)
		1	2	3	Avg.				
	1	159	156	160	158				0
	2	159	158	160	159	3.14	2.000	.000	.0893
	3	159	158	160	159	3.14	2.000	.000	.1786
	4	160	159	159	159	3.14	2.000	.000	.2679
Detonation →	5	161	160	159	160	3.16	2.014	.007	.3572
	6	163	162	160	162	3.19	2.033	.016	.4465
	7	165	162	163	163	3.21	2.048	.024	.5358
	8	166	163	164	164	3.23	2.060	.030	.6251
	9	168	166	166	167	3.25	2.074	.037	.7144
	10	168	170	170	169	3.32	2.121	.060	.8037
	11	171	170	170	170	3.34	2.135	.062	.8930
	12	175	172	174	174	3.42	2.192	.096	.9823
	13	176	177	177	177	3.47	2.228	.114	1.0716
	14	178	177	179	178	3.49	2.244	.122	1.1609
	15	180	181	181	181	3.55	2.291	.145	1.2502
	16	179	181	179	180	3.53	2.275	.137	1.3395
	17	184	182	186	184	3.60	2.330	.165	1.4288
	18	183	183	184	183	3.58	2.315	.157	1.5181
	19	184	187	186	186	3.64	2.364	.132	1.6074
	20	185	183	186	185	3.62	2.348	.174	1.6967

TABLE XI (Cont.)

FILM MEASUREMENT DATA - SPECIMEN 7B3N

Frame No.	Film Reading, F				Shoulder Length S (in.)	Gage Length (From Fig. 12) (in.)	Strain (in/in)	Time * (μ sec)
	1	2	3	Avg.				
21	188	186	190	188	3.68	2.399	.199	1.7860
22	186	187	188	187	3.66	2.381	.190	1.8753
23	188	184	191	188	3.68	2.399	.199	1.9646
24	190	188	189	189	3.69	2.408	.204	2.0539
25	190	188	190	189	3.69	2.408	.204	2.1432
26	188	189	186	188	3.68	2.399	.199	2.2325
27	189	189	191	190	3.71	2.426	.213	2.3218
28	192	190	191	191	3.73	2.444	.222	2.4111
29	194	193	195	194	3.79	2.501	.250	2.5004
30	194	195	193	194	3.79	2.501	.250	2.5897
31	192	196	194	194	3.79	2.501	.250	2.6790
32	193	196	197	196	3.82	2.533	.266	2.7683
33	196	195	193	195	3.80	2.512	.256	2.8576
34	194	195	197	195	3.80	2.512	.256	2.9469
35	194	195	197	195	3.84	2.554	.277	3.0362
36	193	199	199	197	3.77	2.482	.241	3.1255
37	192	193	194	193	3.77	2.482	.241	3.2148
38	192	193	195	193	3.77	2.482	.241	3.3041
39	193	194	196	194	3.79	2.501	.250	3.3934
40	194	195	196	195	3.80	2.512	.256	3.4827

TABLE XI (Cont.)

FILM MEASUREMENT DATA - SPECIMEN 7B3N

	Frame No.	Film Reading, F				Shoulder Length S (in.)	Gage Length (From Fig. 12) (in.)	Strain (in/in)	Time* (μ sec)
		1	2	3	Avg.				
	41	195	192	191	193	3.77	2.482	.241	3.5720
	42	191	196	200	196	3.82	2.534	.267	3.6613
	43	194	191	200	195	3.80	2.512	.256	3.7506
	44	193	196	199	196	3.82	2.534	.267	3.8399
	45	193	189	199	194	3.79	2.501	.250	3.9292
	46	193	195	197	195	3.80	2.512	.256	4.0185
	47	192	193	196	194	3.79	2.501	.250	4.1078
	48	198	196	205	200	3.90	2.622	.311	4.1971
	49	203	198	200	200	3.90	2.622	.311	4.2864
	50	195	201	201	199	3.88	2.598	.299	4.3757
	51	194	200	195	196	3.82	2.534	.267	4.4650
Fracture →	52	193	203	198	198	3.86	2.576	.288	4.5543
	53	200	205	201	202	3.93	2.657	.328	4.6436

* The framing rate was 11,200 frames/sec, or 0.0893 μsec/frame.

TABLE XII

SHOULDER LENGTHS AND GAGE LENGTHS
FOR EXPLOSIVELY STRAINED
UNIAXIAL 5456-0 ALUMINUM SPECIMENS

(Values Plotted in Figure 12)

Specimen No.	Shoulder Length (in.)	Gage Length (in.)	Condition After Straining
Original - All Specimens	3.14	2.00	
5B3N	3.50	2.26	Uniform elongation
5B2N	3.52	2.27	
5B1	3.52	2.27	
5B2	3.54	2.27	
7B3	3.55	2.28	
5B1N	3.56	2.31	
B7	3.67	2.38	
6B3N	3.67	2.40	
6B1	3.71	2.41	
6B3	3.71	2.41	
6B2N	3.70	2.42	
6B2	3.72	2.43	
6B5	3.72	2.43	Necked
B13	3.81	2.51	Uniform elongation
B10	3.82	2.55	
B6	3.86	2.57	Fracture
7B3N	3.86	2.58	
B8	3.87	2.58	
B11	3.88	2.60	
B12	3.88	2.60	
7B2N	3.89	2.61	
5B3	3.93	2.62	
6B1N	3.93	2.63	
B9	3.92	2.64	

TABLE XIII

STRAIN DATA AND MECHANICAL PROPERTIES OF STRAINED BIAXIAL SPECIMENS

5456-0 ALUMINUM

Conventional Strain Rate

SPECIMEN NO.	SPECIMEN TYPE	STRAIN RATE in/in/min	SPECIMEN DIRECTIONALITY WITH ROLL	STRAIN LONG. WITH SPECIMEN % El.	STRAIN TRANS. WITH SPECIMEN % El.	SPECIMEN THICKNESS AFTER STRAINING In.	MECHANICAL PROPERTIES: PROP. LIMIT ksi	0.2% YIELD STRENGTH ksi	ULT. TENSILE STRENGTH ksi	% EL. in 2"	% RED. OF AREA	E psi x 10^{-6}
BB40	Tensile	0.86	Trans.	10	-1	.091	39.9	45.7	54.0	12.0	24.1	10.4
BB44	Tensile	0.86	Trans.	10	-1	.091	39.6	46.1	56.5	13.5	25.0	10.6
BB42	Tensile	0.86	Trans.	10	-2	.090	39.9	47.7	56.3	11.5	21.7	11.7
BB41	Notch	0.86	Trans.	10	-2	.090			53.4			
BB43	Notch	0.94	Trans.	11	-1	.090			53.3			
BB45	Tensile	0.60	Long.	2	7	.090	31.5	40.3	54.3	13.5	24.3	9.5
BB46	Tensile	0.69	Long.	0	8	.090	28.8	39.2	54.4	13.5	27.4	9.6
BB4	Micro	0.69		6	8							
BB50	Tensile	0.51	Trans.	6	0	.090	34.7	41.3	54.6	16.5	24.0	9.7
BB54	Tensile	0.60	Trans.	7	0	.090	34.8	41.5	54.1	13.5	27.8	9.8
BB55	Notch	0.69	Trans.	8	0	.090			50.2			
BB59	Notch	0.60	Trans.	7	0	.090			50.5			
BB56	Tensile	0.69	Trans.	8	0	.090	36.9	42.6	54.6	12.5	24.2	9.5
BB58	Tensile	0.69	Trans.	8	0	.090	35.6	42.4	54.6	15.0	25.1	9.7
BB51	Notch	0.86	Trans.	10	1	.089			50.6			
BB53	Notch	0.69	Trans.	8	0	.090			50.6			
BB52	Tensile	0.51	Trans.	6	1	.089	34.4	41.4	54.0	13.5	24.9	9.5
BB57	Notch	0.60	Trans.	7	1	.089			50.8			
BB5	Micro	0.86		-2	10							

TABLE XIV

STRAIN DATA AND MECHANICAL PROPERTIES OF STRAINED BIAXIAL SPECIMENS

5456-0 ALUMINUM

Explosive Strain Rate

SPECIMEN NO.	SPECIMEN TYPE	STRAIN (1) RATE in/in/min	SPECIMEN DIRECTIONALITY WITH ROLL	STRAIN (2) LONG. WITH SPECIMEN % El.	STRAIN (2) TRANS. WITH SPECIMEN % El.	SPECIMEN THICKNESS AFTER STRAINING In.	MECHANICAL PROPERTIES					
							PROP. LIMIT ksi	0.2% YIELD STRENGTH ksi	ULT. TENSILE STRENGTH ksi	% EL. in 2"	% RED. OF AREA	E psi x 10-6
BB1 BB5	Tensile Tensile	EXPL.	Trans. Trans.			.076 .078	33.1 30.1	46.7 46.3	56.9 61.4	7.0 7.5	30.6 10.0	10.7 10.6
BB6 BB10	Tensile Tensile		Trans. Trans.		14	.077 .078	38.7 39.7	47.2 48.6	57.2 59.4	7.5 8.0	20.9 14.4	11.7 9.4
BB3 BB8	Tensile Tensile		Trans. Trans.	14	16	.078 .080	23.4 33.9	41.0 46.5	56.6 57.7	7.5 7.0	22.4 21.6	10.2 9.2
BB2 BB4	Notch Notch		Trans. Trans.			.080 .075			53.6 55.7			
BB7 BB9	Notch Notch		Trans. Trans.			.081 .083			54.7 53.5			
BB BB	Micro Micro											
BB11 BB18	Tensile Tensile		Trans. Trans.			.085 .085	34.2 29.1	44.8 43.8	57.3 55.9	11.0 10.0	27.1 25.2	10.6 11.7
BB12 BB17	Notch Notch		Trans. Trans.			.088 .087			52.8 54.1			
BB14 BB15	Tensile Tensile		Long. Long.	14		.088 .089	37.0 35.0	48.5 50.1	58.3 58.7	12.5 10.0	24.8 13.1	8.9 -
BB13 BB16	Notch Notch		Long. Long.			.079 .075			55.7 56.5			
BB BB	Micro Micro											

(1) See Figure 22.

(2) Values recorded where photogrid permitted measurement.

TABLE XIV (Cont.)

STRAIN DATA AND MECHANICAL PROPERTIES OF STRAINED BIAXIAL SPECIMENS

5456-O ALUMINUM

Explosive Strain Rate

SPECIMEN No.	SPECIMEN TYPE	STRAIN RATE (1) in/in/min	SPECIMEN DIRECTIONALITY WITH ROLL	STRAIN (2) LONG. WITH SPECIMEN % El.	STRAIN (2) TRANS. WITH SPECIMEN % El.	SPECIMEN THICKNESS AFTER STRAINING In.	MECHANICAL PROPERTIES PROP. LIMIT ksi	0.2% YIELD STRENGTH ksi	ULT. TENSILE STRENGTH ksi	% EL. in 2"	% RED. OF AREA	E psi x 10^{-6}
BB20 BB21 BB22	Tensile Tensile Tensile	EXPL.	Trans. Trans. Trans.	18 16 13	30 23 18	.062 .065 .077	39.0 35.7 36.6	52.4 51.3 49.0	62.0 59.7 56.0	7.5 8.0 6.0	16.9 16.4 30.5	10.2 7.3 7.6
BB19 BB23	Notch Notch		Trans. Trans.	18 10	12	.075 .077			53.8 53.0			
BB24 BB25	Tensile Tensile		Long. Long.	10 3	8 5	.082 .087	28.0 34.0	46.1 48.0	60.7 59.4	8.0 9.0	24.5 22.7	10.5 11.0
BB BB BB	Micro Micro Micro											

(1) See Figure 22.

(2) Values recorded where photogrid permitted measurement.

TABLE XV

BIAXIAL STRAIN RATE DATA

5456-0 Aluminum
Explosive Strain Rate

Switch No.	Switch Height (in.)	Height Increment dZ (in.)	Time (μsec)	Time Increment dt (μsec)	Total Defl. to Center of Height Increment Z (in.)	Strain Rate (in/in/sec)	Velocity of Blank (ft/sec)
1	3.579		0				
		0.677		0.24	0.709	26	235
2	2.902		0.24				
		0.987		0.19	1.541	103	433
3	1.915		0.43				
		0.910		0.19	2.490	153	399
4	1.005		0.62				
		0.960		0.34	3.425	124	235
5	0.045		0.96				
AVERAGE						86	343

TABLE XVI

X-RAY DIFFRACTION DATA FOR 5456-0 ALUMINUM

Load (Stress) System	Specimen Identification	Condition Tested	Strain Rate	Applied Prestrain in % of Max. Strain at Fracture		Microstress Half-Height Width θ°	Lattice Parameter Å	Residual Stress psi	Phase Present
				Nominal	Actual				
No Load	-	As-Received	--	-	-	1.10	4.0740	--	Al-Mg Solid Solution Primary Phase
Uniaxial	4B1	Prestrained	Conv.	75	79.4	1.28	4.0751	+ 1080	
	6B2		Expl.	75	75	1.38	4.0756	+ 1570	

Biaxial:

Dome No.	Reference Point	Location	Strain Rate	Strain Component in %		Microstress Half-Height Width θ°	Lattice Parameter Å	Residual Stress psi	Phase Present
				Longitudinal to Roll	Transverse to Roll				
12	1	Center of Bottom	Expl.	0	10	1.62	4.0767	+ 2650	Al-Mg Solid Solution Primary Phase
	2	Longitudinal Axis of bottom, at center of half circle	Expl.	34	24	1.20	4.0792	+ 5180	
	3	End of bottom, at formed radius	Expl.	-	-	1.30	4.0796	+ 5200	
19	4	Near center of bottom	Expl.	6	-	1.35	4.0736	-	
	5	End of bottom, at formed radius	Expl.	-	-	1.18	4.0793	+ 5190	
21	6	Center of Bottom	Expl.	2	21	1.25	4.0764	+ 2350	
	7	Same location	Expl.	2	21	1.33	4.0747	+ 100	
	8	End of bottom, at formed radius	--	-	-	1.25	4.0795	+ 5200	

TABLE XVII

INTENSITIES OF "d-SPACINGS" FOR BIAXIALLY STRAINED ALUMINUM

Miller Indices	DOME NO. 12			DOME NO. 19		DOME NO. 21			
	Reference Points								
h k l	1	2	3	4	5	6	7	8	Theoretical
1 1 1	O.S.*	24	24	106	84	142	0.5	36	100
2 0 0	O.S.	O.S.	173	O.S.	O.S.	206	O.S.	194	47
2 2 0	199	O.S.	O.S.	O.S.	O.S.	142	O.S.	O.S.	22
3 1 1	96	65	55	77	74	118	82	58	24
2 2 2	24	--	2	10	7	12	17	5	7
4 0 0	36	12	19	26	24	17	34	14	2

* Off scale intensity reading.

TABLE XVIII

PRESTRAIN AND MECHANICAL PROPERTIES DATA

5456-0 ALUMINUM

(From Table V and Figures 29 and 30)

Strain Rate	Pre Strain %	Yield Strength ksi	Ultimate Strength ksi	Elongation %	Red. of Area %	Notch-Strength Ratio N/Y	Notch-Strength Ratio N/U	Notch Strength Ultimate ksi
0	0	22.5	50.6	22.2	32.6	1.75	.78	39.3
CONV.	10.5	48.2	54.9	13.0	27.7			
	10.5	48.5	54.8	13.0	22.4			
	9.5							52.5
	10.5							53.9
	16.0	53.1	58.3	9.0	17.8			
	15.5	52.8	57.9	8.5	18.1			
	16.0							55.0
	17.0							56.1
EXPL.	13.5	50.8	56.5	11.0	31.9			
	13.5	50.4	56.3	12.0	36.1			
	13.5							54.3
	1[illegible] 0							53.4
	19.0	53.1	57.9	11.0	26.7			
	20.5	54.4	59.6	8.5	36.2			
	21.0							58.0
	20.0							57.2
		STRENGTH VALUES FROM CURVES						
CONV.	10.5	48.3	54.8			1.10	.97	53.2
	16.0	53.1	58.2			1.04	.95	55.3
EXPL.	13.5	50.6	56.4			1.07	.96	54.0
	20.0	53.5	59.0			1.07	.97	57.3

TABLE XIX

X-RAY DIFFRACTION DATA FOR 301 STAINLESS STEEL

Load (Stress) System	Specimen Identification	Condition Tested	Temperature	Strain Rate	Applied Prestrain in % of Max. Strain at Fracture		Microstress Half-Height Width θ^{o}	Lattice Parameter Å	Residual Stress psi	Components Found	
					Nominal	Actual				Austenite (γ-component	Martensite
No Load	--	As-Received	--	--	--	--	1.20	3.58984	--	--	--
Uniaxial	3C2-2	As Prestrained	Ambient	Conv.	75	73.3	1.90	3.58786	-46,390	--	5-10%
	6C2		Ambient	Expl.	75	71.4	1.70	3.58588	-92,800	--	5-10%
	15C4N		$-320^{o}F$	Conv.	75	79.2	1.90	3.58786	-46,390	38%	62%
	18C4N		$-320^{o}F$	Expl.	75	78.7	1.80	3.6000	-238,000*	23%	77%

* Transformation has taken place indicating large L.P. changes.

TABLE XX

PRESTRAIN AND MECHANICAL PROPERTIES DATA

301 STAINLESS STEEL
Prestrained at Ambient

(From Table VI and Figures 39 and 40)

Strain Rate	Pre Strain %	Yield Strength ksi	Ultimate Strength ksi	Elongation %	Red. of Area %	Notch-Strength Ratio N/Y	Notch-Strength Ratio N/U	Notch Strength Ultimate ksi
0	0	42.6	88.6	61.2	55.0	1.82	0.88	77.6
CONV.	23.0	96.0	109.0	31.0	52.6			
	22.0	97.8	110.4	30.5	42.2			
	21.5							117.4
	21.5							119.1
	45.0	123.9	129.5	19.0	43.3			
	45.0	126.2	131.5	19.0	41.8			
	45.0	127.8	131.8	18.0	46.3			
	44.0	125.5	130.0	17.5	37.8			
	41.5	123.0	127.6	20.5	44.3			
	41.0							144.0
	40.0							144.0
EXPL.	24.0	101.9	120.7	27.0	47.3			
	25.0	109.9	118.9	26.5	42.5			
	25.5							131.4
	24.5							127.0
	42.5	134.8	139.5	14.0	43.0			
	42.5	133.0	139.6	14.0	39.6			
	41.5							150.2
	44.0							155.4
		STRENGTH VALUES FROM CURVES						
CONV.	25.0	100.0	112.5			1.23	1.09	123.0
	40.0	120.0	126.0			1.19	1.14	143.0
EXPL.	25.0	107.0	121.0			1.21	1.07	129.0
	40.0	130.0	137.0			1.15	1.09	150.0

TABLE XXI

PRESTRAIN AND MECHANICAL PROPERTIES DATA

301 STAINLESS STEEL
Prestrained at -320° F

From Table VI and Figures 41 and 42

Strain Rate	Pre Strain %	Yield Strength ksi	Ultimate Strength ksi	Elong-ation %	Red. of Area %	Notch-Strength Ratio N/Y	N/U	Notch Strength Ultimate ksi
0	0	42.6	88.6	61.2	55.0	1.82	0.88	77.6
CONV.	16.0	143.2	171.6	14.5	34.0			
	16.5	145.6	183.4	13.0	30.5			
	17.0							133.8
	17.0							134.8
	29.5	230.5	233.0	4.5	31.0			
	31.0	231.5	234.2	4.5	27.9			
	30.5	---	238.6	4.5	26.2			
	28.0	226.4	227.8	4.5	32.3			
	28.0	226.3	226.8	4.5	30.8			
	29.0							130.2
	24.0							139.5
EXPL.	18.0	135.2	169.5	14.0	29.9			
	18.0	140.7	171.0	14.0	27.9			
	17.0							128.5
	18.0							134.4
	30.0	212.6	214.1	4.0	19.0			
	29.5	210.5	210.9	3.5	10.0			
	29.0							143.8
	28.0							91.6
		STRENGTH VALUES FROM CURVES						
CONV.	15.0	137.0	170.0			0.93	0.75	127.0
	28.0	221.0	227.0			0.52	0.51	115.0
EXPL.	15.0	121.0	156.0			1.02	0.79	123.0
	28.0	200.0	207.0			0.60	0.58	120.0

TABLE XXII

PRESTRAIN AND MECHANICAL PROPERTIES DATA

17-7 PH STAINLESS STEEL
Prestrained at Ambient

(From Table VII and Figures 50 and 51)

Strain Rate	Pre Strain %	Yield Strength ksi	Ultimate Strength ksi	Elongation %	Red. of Area %	Notch-Strength Ratio N/Y	Notch-Strength Ratio N/U	Notch Strength Ultimate ksi
0	0	41.1	135.0	29.5	45.2	1.95	0.60	80.4
CONV.	13.0	103.0	154.1	18.0	37.6			
	13.5	102.0	150.8	18.0	41.4			
	13.0							125.6
	13.5							128.6
	25.5	136.0	157.2	13.5	40.4			
	25.5	138.8	159.6	14.0	36.6			
	25.0							165.6
	24.5							163.6
EXPL.	24.0	96.6	159.6	16.5	41.3			
	23.0	91.2	157.8	16.5	39.7			
	21.5							123.2
	22.0							122.2
	45.5	136.6	176.5	16.0	37.6			
	45.0	143.1	181.6	14.0	40.7			
	48.5	147.1	179.4	13.5	39.0			
	42.0							176.5
	42.5							165.4
		STRENGTH VALUES FROM CURVES						
CONV.	13.0	102.0	152.0			1.25	0.84	127.0
	25.0	136.0	158.0			1.21	1.04	165.0
EXPL.	25.0	97.0	165.0			1.34	0.79	130.0
	40.0	139.0	175.0			1.29	0.95	166.0

TABLE XXIII

PRESTRAIN AND MECHANICAL PROPERTIES DATA

17-7 PH STAINLESS STEEL
Prestrained at Ambient and Aged

(From Table VII and Figures 52 and 53)

Strain Rate	Pre Strain %	Yield Strength ksi	Ultimate Strength ksi	Elong-ation %	Red. of Area %	Notch-Strength Ratio $\frac{N}{Y}$	Notch-Strength Ratio $\frac{N}{U}$	Notch Strength Ultimate ksi
CONV.	13.0	127.1	161.0	22.0	34.5			
	13.5	139.3	162.7	21.0	31.4			
	13.0							125.2
	13.0							132.6
	26.0	196.4	196.4	9.0	27.9			
	26.5	194.6	197.3	8.0	28.9			
	24.5							163.6
	24.5							164.4
EXPL.	22.5	124.2	162.0	22.5	35.9			
	21.5	128.0	156.9	21.0	33.5			
	21.0							116.3
	22.0							118.6
	40.5	173.7	188.3	13.0	34.8			
	40.5	187.4	194.8	8.0	32.9			
	42.0							165.1
	42.0							163.4
		STRENGTH VALUES FROM CURVES						
CONV.	13.0	132.0	161.0			0.97	0.80	128.0
	24.5	187.0	192.0			0.88	0.85	164.0
EXPL.	23.0	129.0	161.0			0.94	0.75	121.0
	40.0	179.0	190.0			0.89	0.84	160.0

TABLE XXIV

PRESTRAIN AND MECHANICAL PROPERTIES DATA

17-7 PH STAINLESS STEEL
Prestrained at $-320^{\circ}F$

(From Table VII and Figures 54 and 55)

Strain Rate	Pre Strain %	Yield Strength ksi	Ultimate Strength ksi	Elongation %	Red. of Area %	Notch-Strength Ratio N/Y	Notch-Strength Ratio N/U	Notch Strength Ultimate ksi
0	0	41.1	135.0	29.5	45.2	1.95	0.60	80.4
CONV.	8.0	157.5	218.7	10.5	26.2			
	8.5	150.4	216.7	10.0	23.7			
	8.5							137.9
	8.5							135.3
	12.0	216.0	229.4	6.5	29.6			
	12.5	219.1	233.9	6.0	18.7			
	11.0							150.3
	11.0							143.5
EXPL.	12.5	175.1	222.0	8.0	25.2			
	12.5	176.7	222.5	9.0	24.7			
	12.5							141.2
	13.0							145.3
	18.0	240.5	247.3	3.5	17.9			
	18.0	240.9	246.4	3.5	15.8			
	19.0							131.9
	19.0							132.8
		STRENGTH VALUES FROM CURVES						
CONV.	8.0	148.0	215.0			0.91	0.62	134.0
	11.0	195.0	227.0			0.75	0.65	147.0
EXPL.	13.0	180.0	224.0			0.79	0.63	142.0
	18.0	241.0	247.0			0.56	0.54	134.0

TABLE XXV

PRESTRAIN AND MECHANICAL PROPERTIES DATA

17-7 PH STAINLESS STEEL
Prestrained at $-320^{o}F$ and Aged

(From Table VII and Figures 56 and 57)

Strain Rate	Pre Strain %	Yield Strength ksi	Ultimate Strength ksi	Elong-ation %	Red. of Area %	Notch-Strength Ratio N/Y	Notch-Strength Ratio N/U	Notch Strength Ultimate ksi
CONV.	7.5	222.5	260.0	8.5	12.2			
	9.0	221.8	256.0	9.5	16.3			
	9.0							112.0
	9.0							114.5
	11.5	272.1	276.2	5.0	20.2			
	11.5	269.5	281.3	5.0	18.5			
	10.0							119.6
	11.0							87.7
EXPL.	12.5	248.4	277.4	3.5	4.8			
	12.5	243.7	271.9	8.5	20.2			
	13.5							92.9
	13.5							98.2
	18.0	301.7	313.3	2.5	13.3			
	18.5	309.0	314.4	3.0	15.5			
	19.5							89.6
	20.0							76.5
		STRENGTH VALUES FROM CURVES						
CONV.	9.0	233.0	263.0			0.49	0.43	113.0
	10.5	257.0	273.0			0.40	0.37	102.0
EXPL.	13.5	257.0	282.0			0.37	0.34	96.0
	18.0	302.0	312.0			0.28	0.28	86.0

TABLE XXVI

PRESTRAIN AND MECHANICAL PROPERTIES DATA

6Al-4V TITANIUM

(From Table VIII and Figures 68 and 69)

Strain Rate	Pre Strain %	Yield Strength ksi	Ultimate Strength ksi	Elongation %	Red. of Area %	Notch-Strength Ratio N/Y	Notch-Strength Ratio N/U	Notch Strength Ultimate ksi
0	0	147.0	152.1	14.3	31.8	1.05	1.01	153.8
CONV.	4.0	152.7	157.4	12.0	33.4			
	4.0	157.7	161.6	9.0	28.3			
	4.0							150.9
	3.5							154.6
	8.5	171.4	173.1	5.5	26.5			
	8.5	171.5	171.5	6.5	25.4			
	6.0							159.0
	6.0							159.1
EXPL.	4.0	161.7	164.8	10.5	36.0			
	4.0	164.5	164.9	10.0	34.5			
	3.5							161.7
	3.5							165.2
	8.5	170.4	171.2	7.5	29.2			
	6.0	164.8	165.4	8.5	32.0			
	6.0	167.7	167.9	8.5	32.0			
	6.0							164.3
	6.0							156.6
	7.0							163.2
		STRENGTH VALUES FROM CURVES						
CONV.	3.0	153.2	157.8			1.00	0.97	152.7
	6.0	162.4	165.1			0.98	0.96	159.0
EXPL.	3.0	159.0	161.8			1.02	1.00	162.0
	6.0	166.2	166.8			0.97	0.96	160.7

TABLE XXVII

PRESTRAIN AND MECHANICAL PROPERTIES DATA

6Al-4V TITANIUM
Solution Treated, Prestrained, and Aged

(From Table VIII and Figures 70 and 71)

Strain Rate	Pre Strain %	Yield Strength ksi	Ultimate Strength ksi	Elong- ation %	Red. of Area %	Notch-Strength Ratio N/Y	N/U	Notch Strength Ultimate ksi
0	0	172.4	182.7	8.7	26.0	0.81	0.77	140.7
CONV.	2.5	170.8	180.9	8.5	28.5			
	2.5	171.3	182.6	7.0	22.3			
	2.5							142.6
	2.5							143.3
	2.5							138.5
EXPL.	3.0	164.9	176.1	7.5	36.3			
	3.0	165.1	174.4	5.5	21.9			
	3.0							132.8
	3.0							152.8
		STRENGTH VALUES FROM CURVES						
CONV.	2.5	171.0	181.7			0.83	0.78	141.5
EXPL.	3.0	165.0	175.2			0.86	0.81	142.8

TABLE XXVIII

PRESTRAIN AND MECHANICAL PROPERTIES DATA

13V-11Cr-3Al TITANIUM

(From Table IX and Figures 79 and 80)

Strain Rate	Pre Strain %	Yield Strength ksi	Ultimate Strength ksi	Elongation %	Red. of Area %	Notch-Strength Ratio N/Y	Notch-Strength Ratio N/U	Notch Strength Ultimate ksi
0	0	139.5	141.8	14.7	39.6	1.22	1.20	169.4
CONV.	3.5	157.7	157.7	8.0	42.6			
	3.5	157.3	157.3	8.0	37.7			
	3.5							176.3
	3.5							172.8
EXPL.	3.0	154.9	154.9	8.5	40.0			
	3.0	155.6	155.6	10.5	41.0			
	4.0							141.3
	3.5							173.1
		STRENGTH VALUES FROM CURVES						
CONV.	1.5	147.2	148.3			1.16	1.15	171.5
	3.5	157.5	157.5			1.11	1.11	174.5
EXPL.	1.5	147.5	148.1			1.11	1.11	164.5
	3.0	155.2	155.2			1.03	1.03	159.9

TABLE XXIX

PRESTRAIN AND MECHANICAL PROPERTIES DATA

13V-11Cr-3Al TITANIUM
Prestrained and Aged

(From Table IX and Figures 81 and 82)

Strain Rate	Pre Strain %	Yield Strength ksi	Ultimate Strength ksi	Elong-ation %	Red. of Area %	Notch-Strength Ratio N/Y	Notch-Strength Ratio N/U	Notch Strength Ultimate ksi
0	0	147.0	154.3	7.5	13.1	1.10	1.05	161.4
CONV.	3.5	130.5	136.2	4.5	32.9			
	3.5	129.0	133.8	4.3	32.3			
	3.0							112.3
	4.0							114.6
EXPL.	3.0	128.6	138.3	4.5	31.1			
	3.0	130.3	138.6	4.5	32.8			
	4.0							102.3
	3.5							101.2
		STRENGTH VALUES FROM CURVES						
CONV.	1.5	139.6	146.0			0.98	0.94	137.5
	3.0	132.2	137.5			0.86	0.83	113.5
EXPL.	1.5	138.1	146.8			0.99	0.94	137.5
	3.0	129.5	138.4			0.88	0.82	113.5

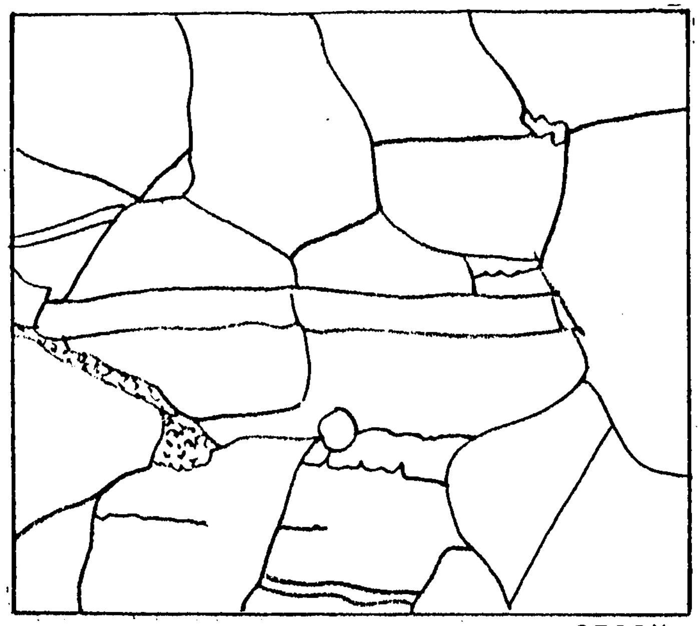

2500X

FIGURE 1. EXPLOSIVELY LOADED 1020 STEEL SHOWING TWINS CROSSING A GRAIN BOUNDARY WITHOUT DIRECTIONAL CHANGE (AFTER EICHELBERGER, REF. 32)

235X

FIGURE 2. EXPLOSIVELY LOADED 1050 STEEL SHOWING TWINS CROSSING BOUNDARIES BETWEEN FERRITE AND PEARLITE GRAINS (AFTER TARDIFF, CLAISSE, AND CHOLLET, REF. 33)

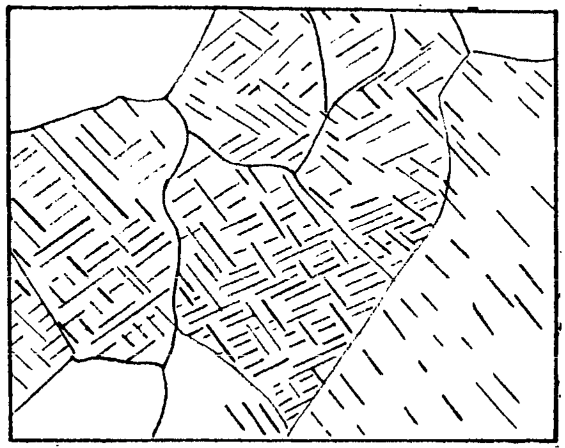

235X

FIGURE 3. COLUMBIUM SHOCKED AT 430 KILOBARS SHOWING TWINS CROSSING GRAIN BOUNDARIES (AFTER DEITER, REF. 33)

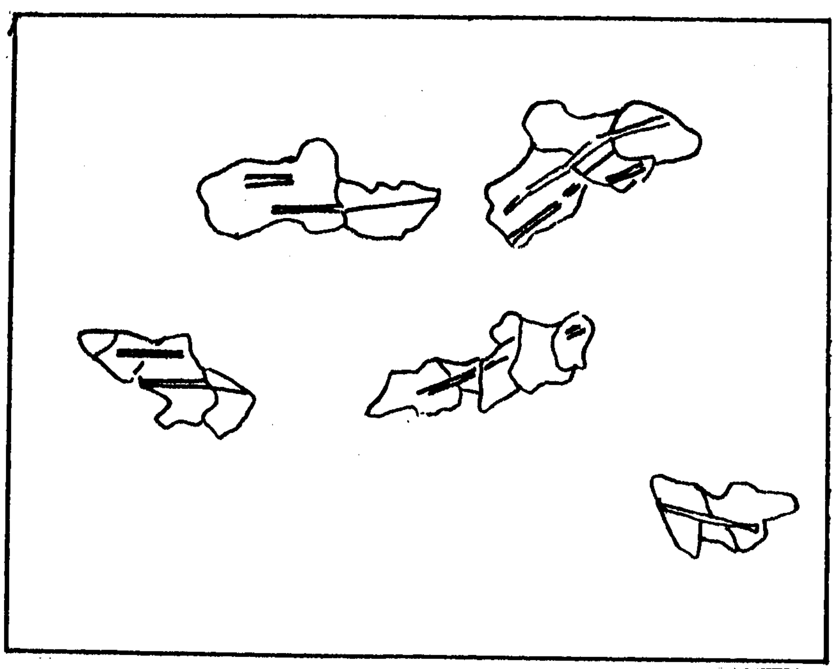

500X

FIGURE 4. 1020 STEEL, SHOCK LOADED BY DRIVER PLATE AT 183.5-188.5 KILOBARS, SHOWING TWINS CROSSING GRAIN BOUNDARIES (AFTER HALL ET AL. REF. 38)

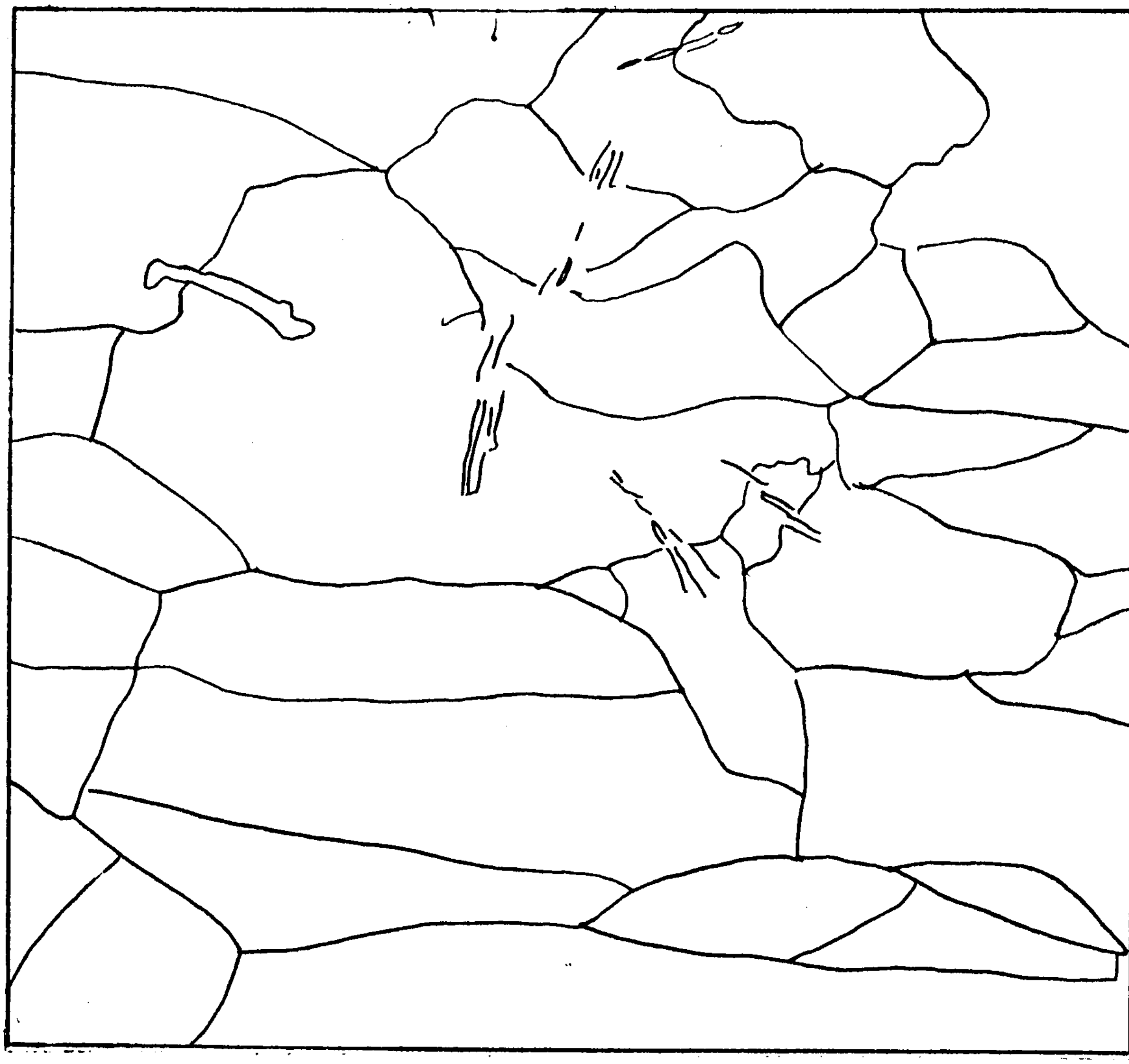

1000X

FIGURE 5. EXPLOSIVELY LOADED HIGH NICKEL STEEL (UDIMET A) SHOWING TWINS CROSSING GRAIN BOUNDARIES (AFTER SILVERMAN ETAL, REF. 39)

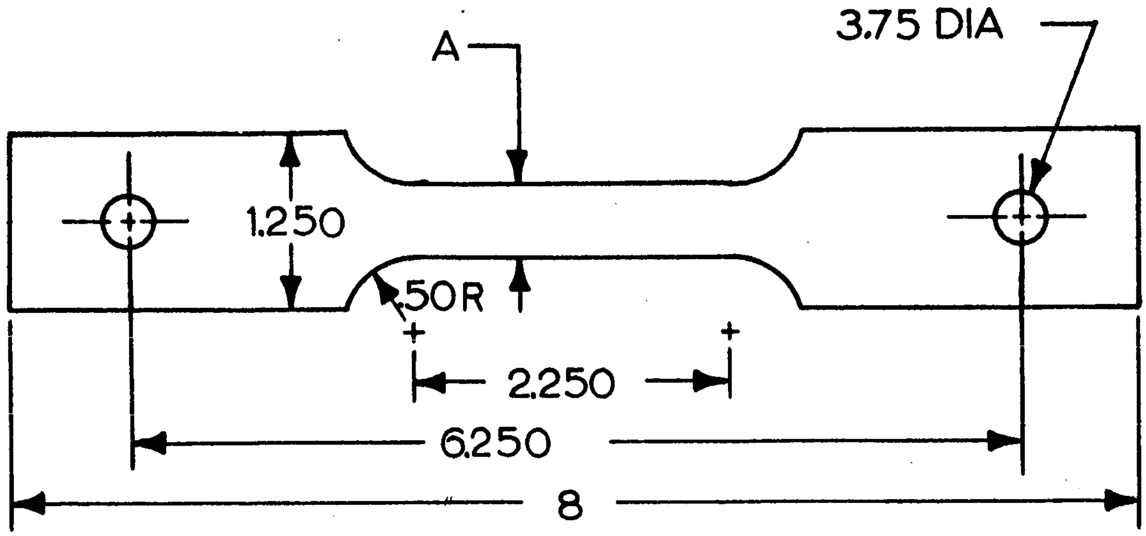

DIM A	MATERIAL
.750	5456-0 ALUMINUM
.750	301 S.S.
.600	301 S.S. STRAINED AT - 320°F
.750	17-7PH S.S.
.560	17-7PH S.S. STRAINED AT - 320°F
.750	6 Al - 4 V TITANIUM
.560	6 Al - 4 V TITANIUM SOLUTION TREATED
.540	13V-11Cr-3Al
.500	STANDARD FLAT TENSILE SPECIMEN

FIGURE 6. SPECIMEN CONFIGURATION FOR UNIAXIAL STRAINING AND STANDARD TENSILE TESTING

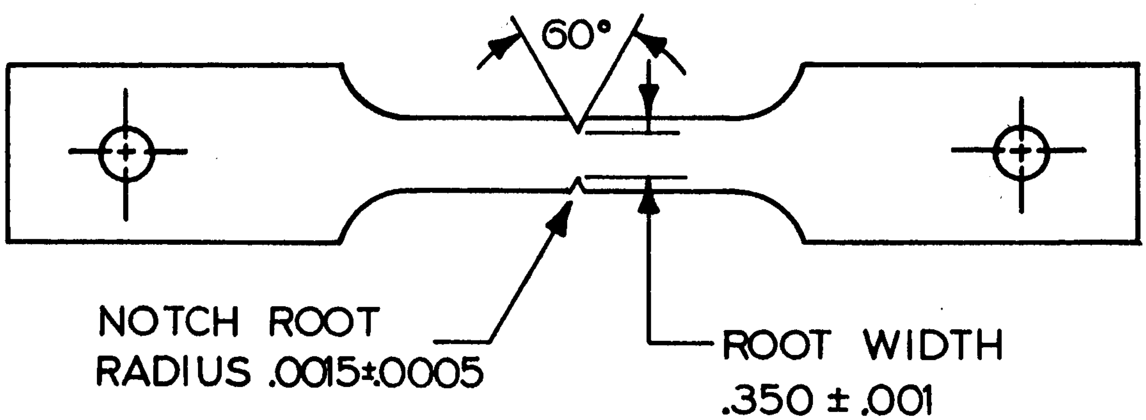

FIGURE 7. EDGE NOTCH TENSILE SPECIMEN

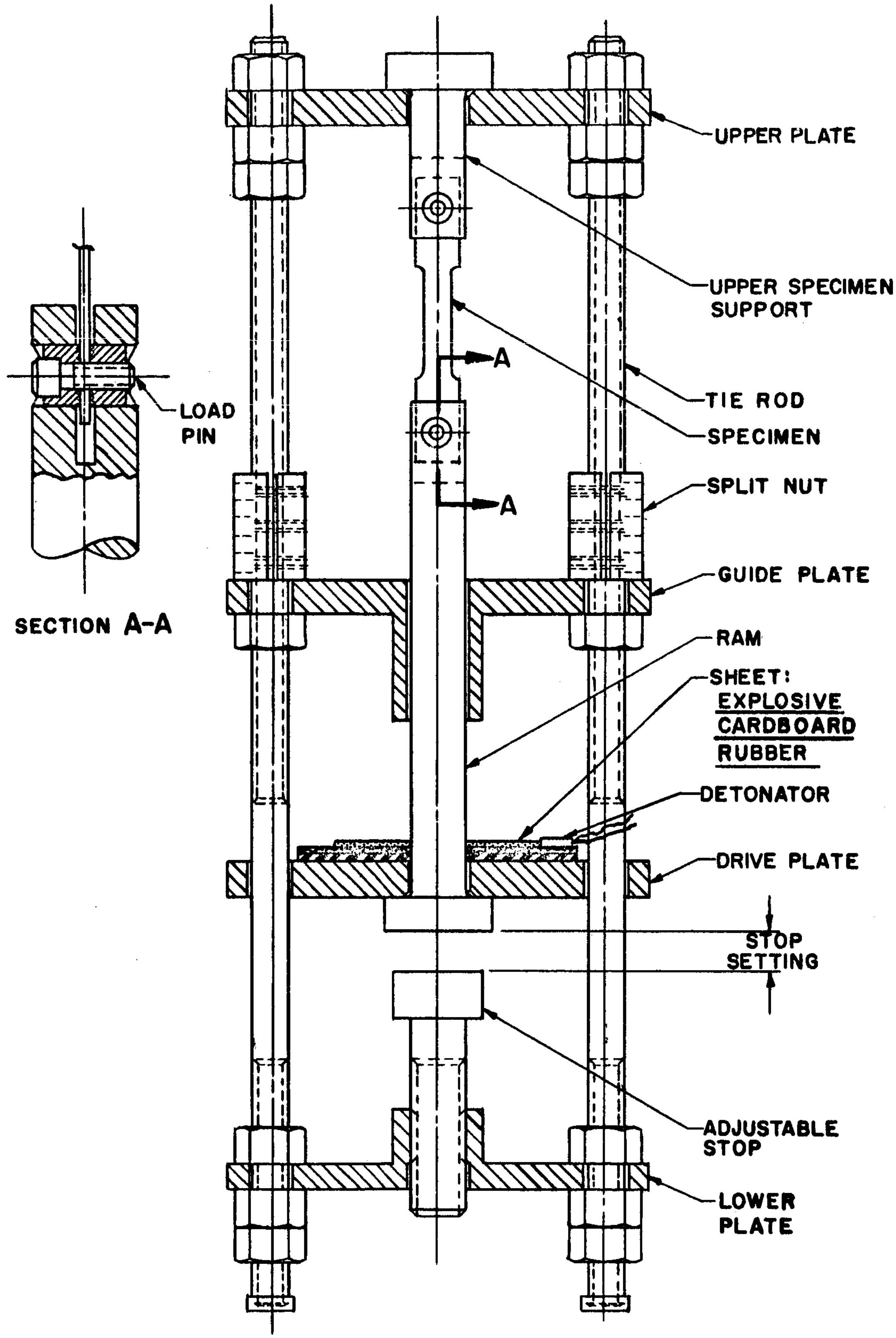

FIGURE 8. DYNAMIC TEST FIXTURE

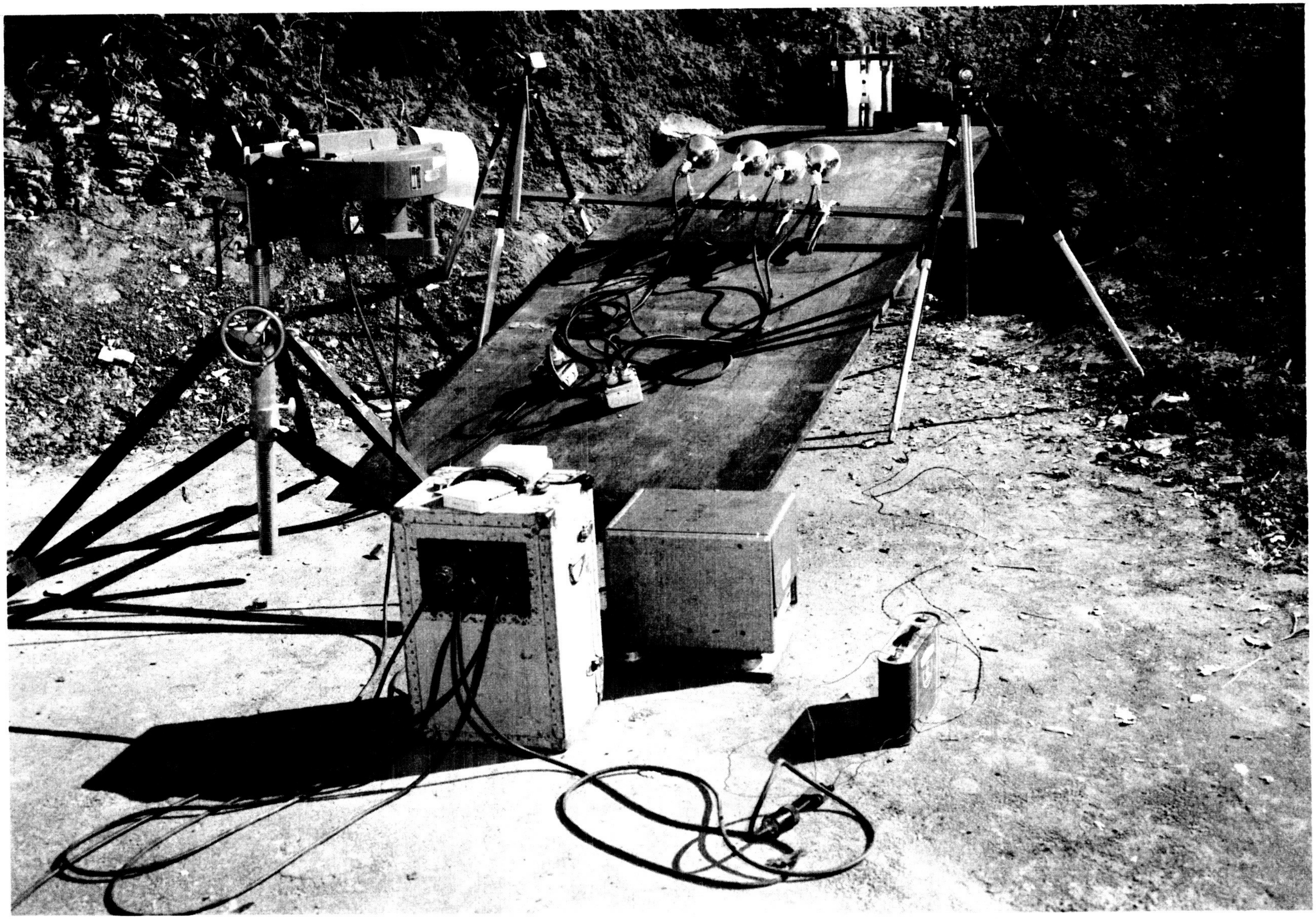

FIGURE 9. HIGH-SPEED PHOTOGRAPHY EQUIPMENT SETUP EMPLOYED FOR DETERMINATION OF EXPLOSIVE STRAIN RATE

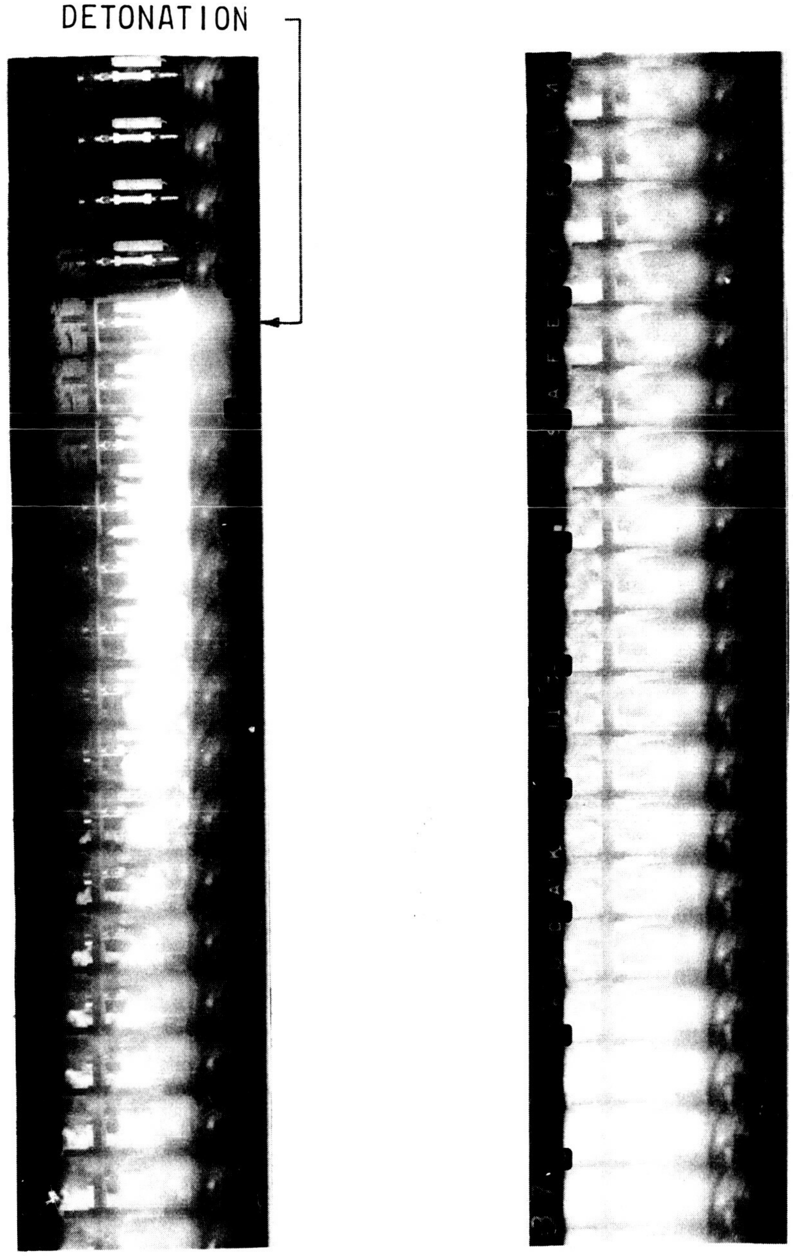

FIGURE 10. FASTAX FILM RECORD OF AISI 301 STAINLESS STEEL SPECIMEN 7C1 STRAINED TO FRACTURE. OBSCURATION CAUSED BY DETONATION PRODUCTS.

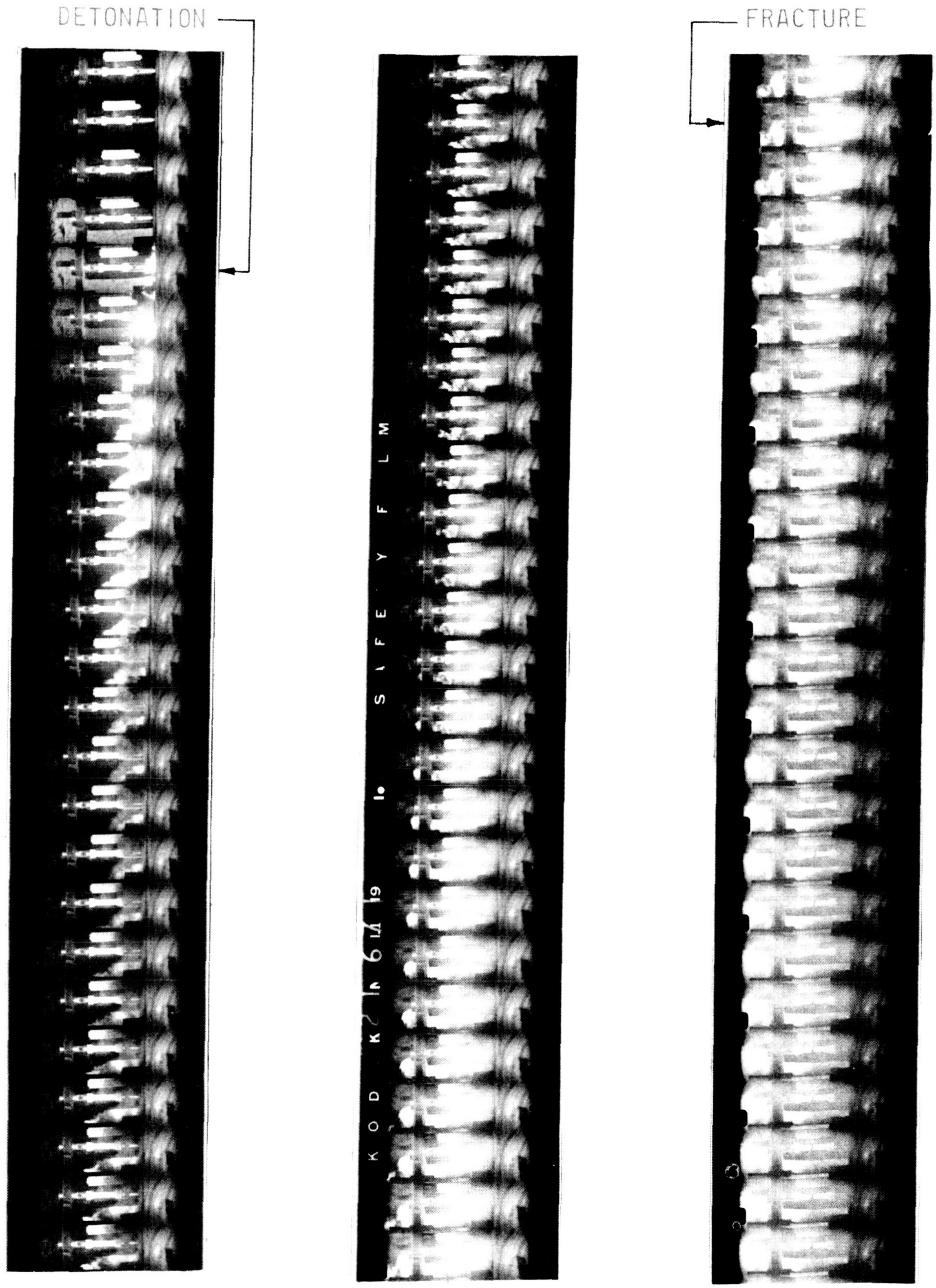

FIGURE 11. FASTAX FILM RECORD OF 5456-0 ALUMINUM SPECIMEN 7B3N EXPLOSIVELY STRAINED TO FRACTURE.

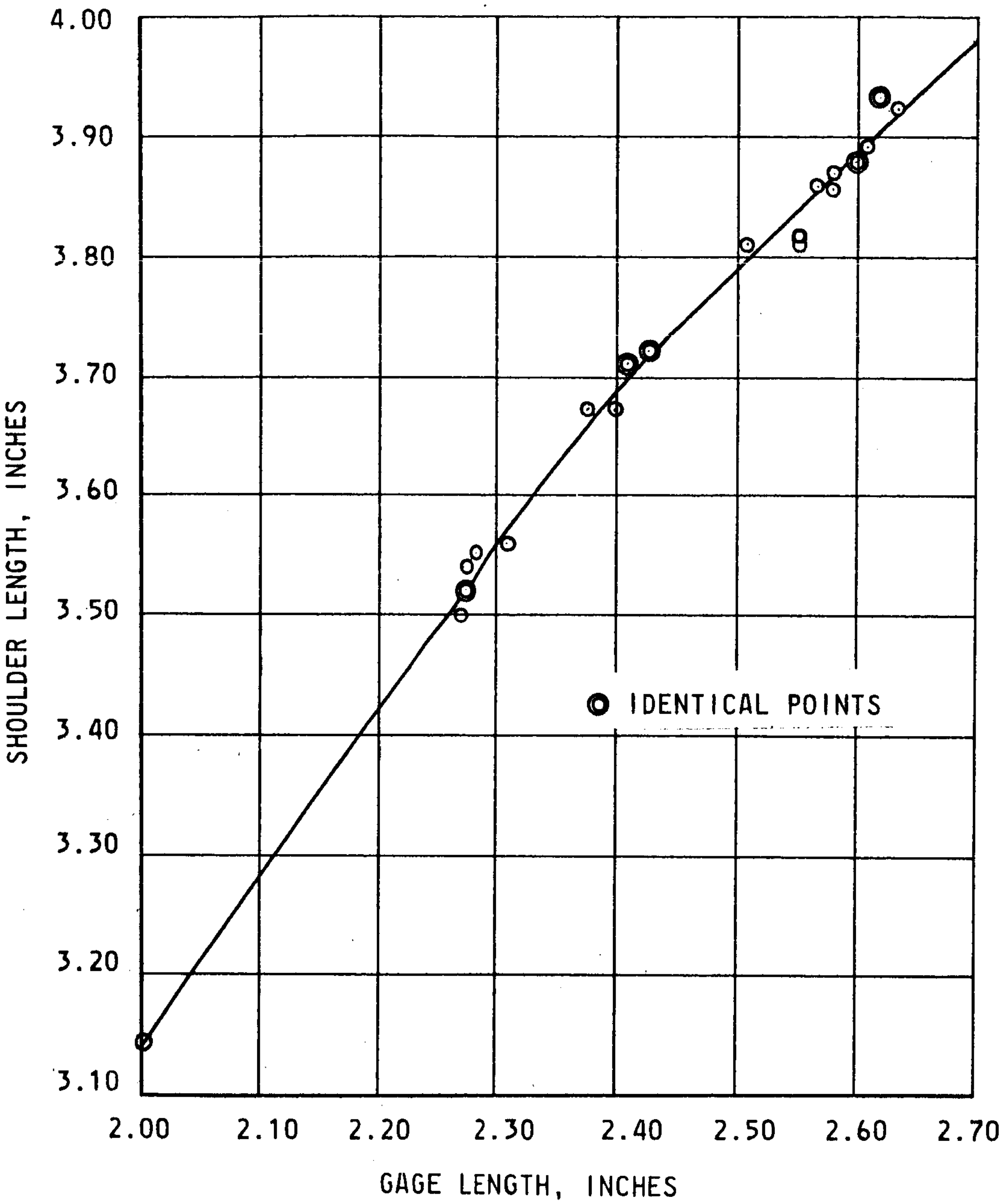

FIGURE 12 SHOULDER LENGTH V/S GAGE LENGTH FOR EXPLOSIVELY STRAINED TENSILE SPECIMENS 5456-O ALUMINUM.

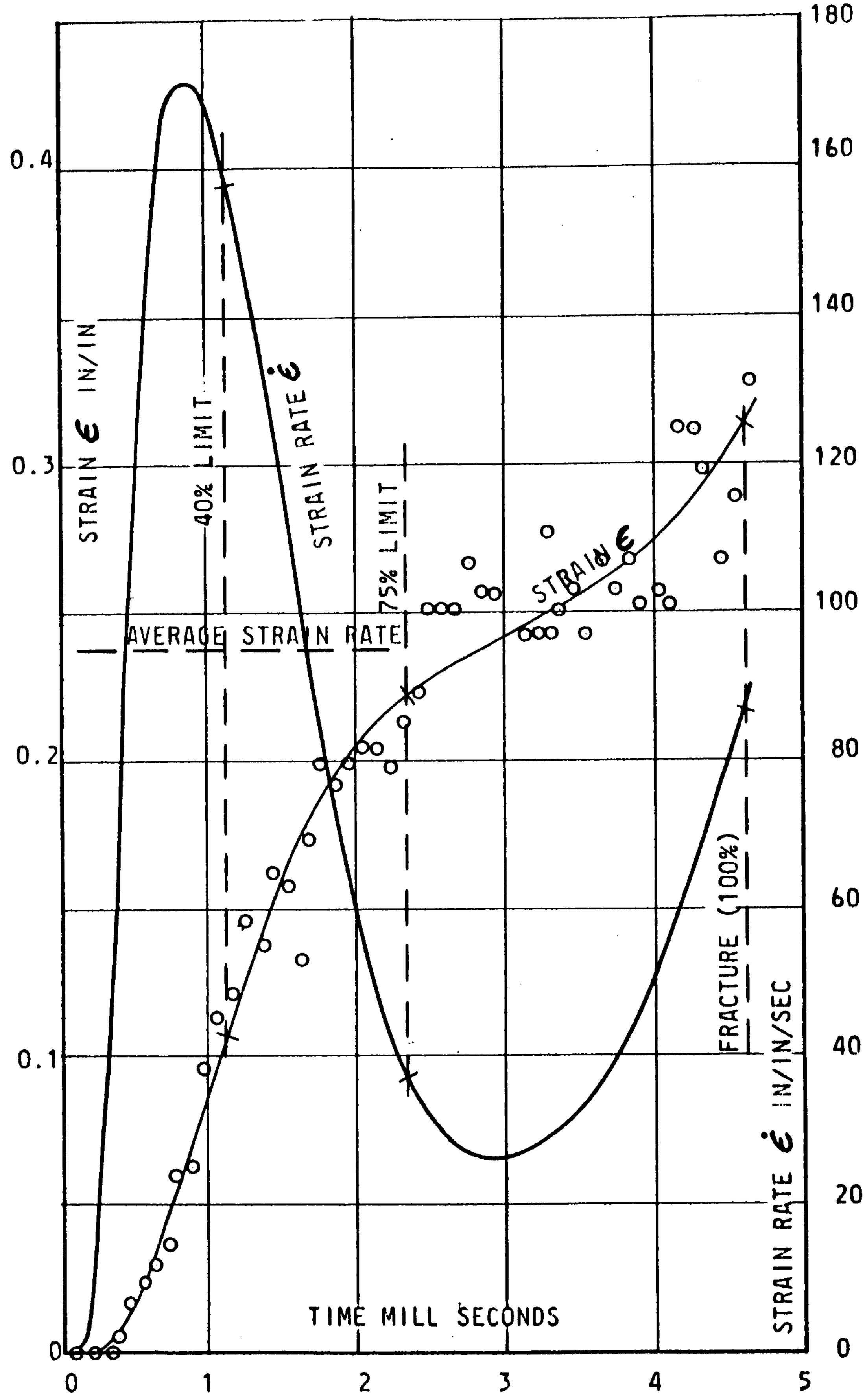

FIGURE 13. STRAIN-TIME RELATIONSHIP AND STRAIN RATE VARIATION IN UNIAXIAL TESTING

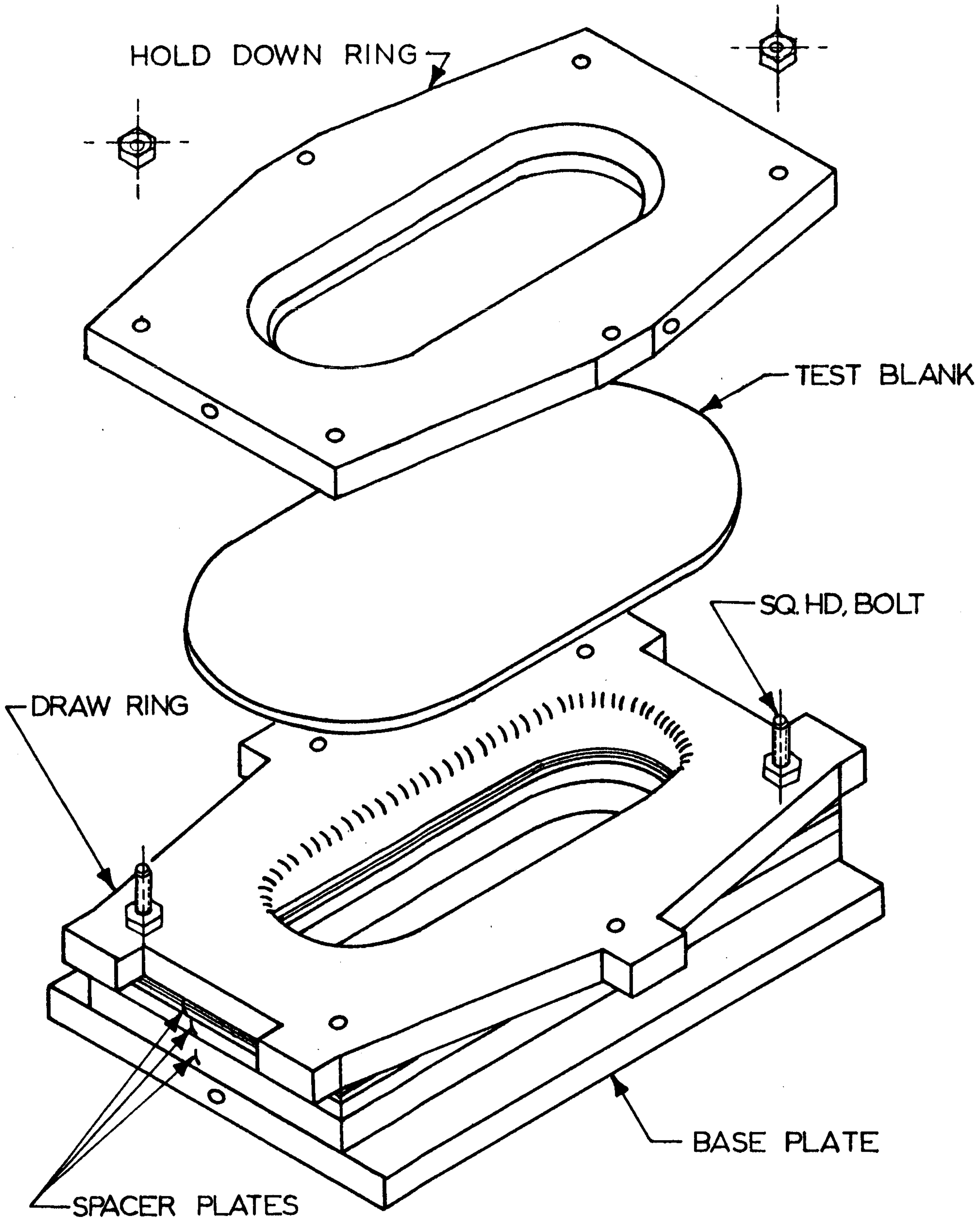

FIGURE 14. ELONGATED DOME DIE

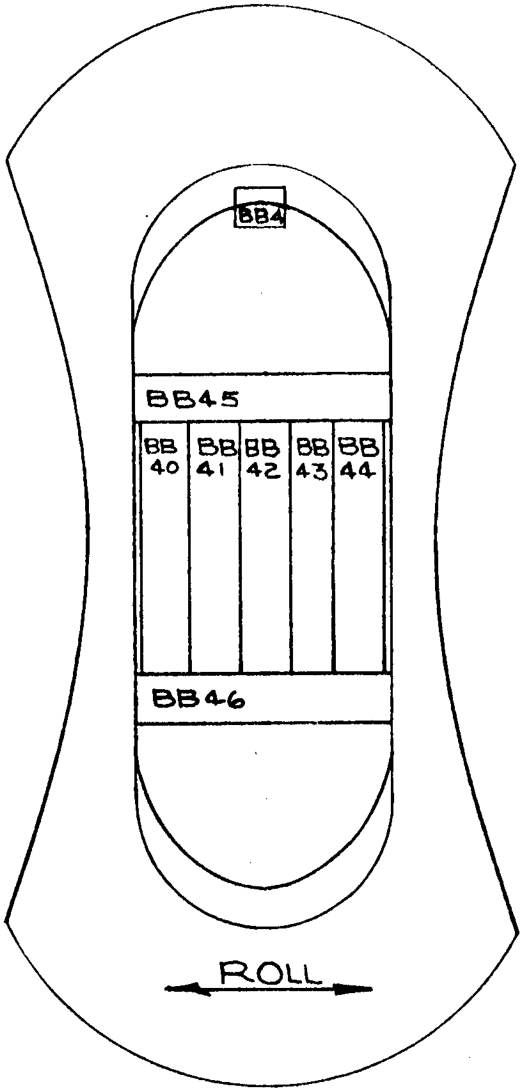

SPECIMEN NO.	DIRECTION	SPECIMEN TYPE
BB4		Micro
BB40	Trans.	Tensile
BB41	Trans.	Notch
BB42	Trans.	Tensile
BB43	Trans.	Notch
BB44	Trans.	Tensile
BB45	Long.	Tensile
BB46	Long.	Tensile

Elongation is 2% to -2% longitudinal to the rolling direction and 7% to 11% transverse to the rolling direction.

FIGURE 15. LOCATIONS OF SPECIMENS TAKEN FROM CONVENTIONALLY FORMED DOME NO. 4

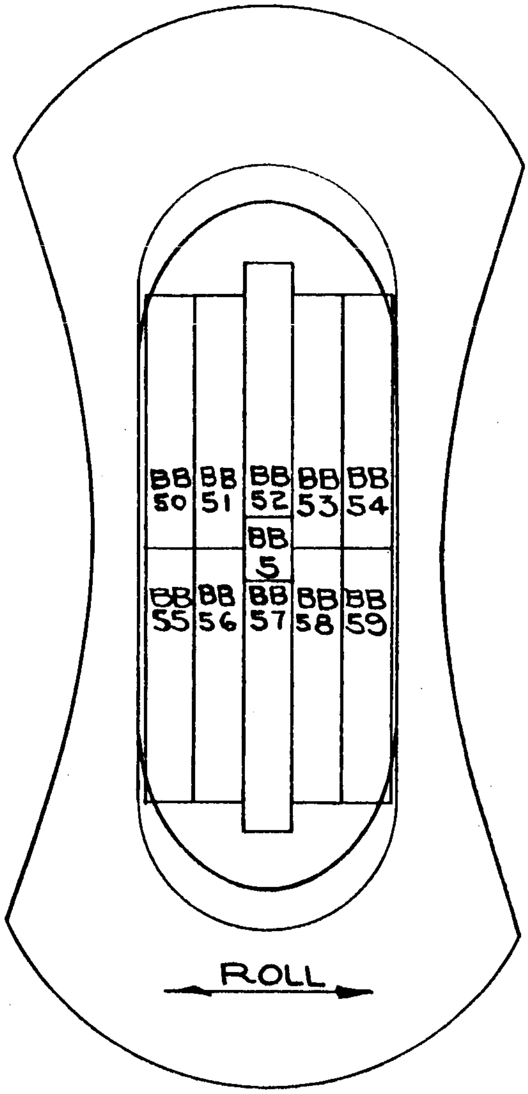

SPECIMEN NO.	DIRECTION	SPECIMEN TYPE
BB5		Micro
BB50	Trans.	Tensile
BB51		Notch
BB52		Tensile
BB53		Notch
BB54		Tensile
BB55		Notch
BB56		Tensile
BB57		Notch
BB58		Tensile
BB59		Notch

Elongation is 1% to -2% longitudinal to the rolling direction and 6% to 10% transverse to the rolling direction.

FIGURE 16. LOCATIONS OF SPECIMENS TAKEN FROM CONVENTIONALLY FORMED DOME NO. 5

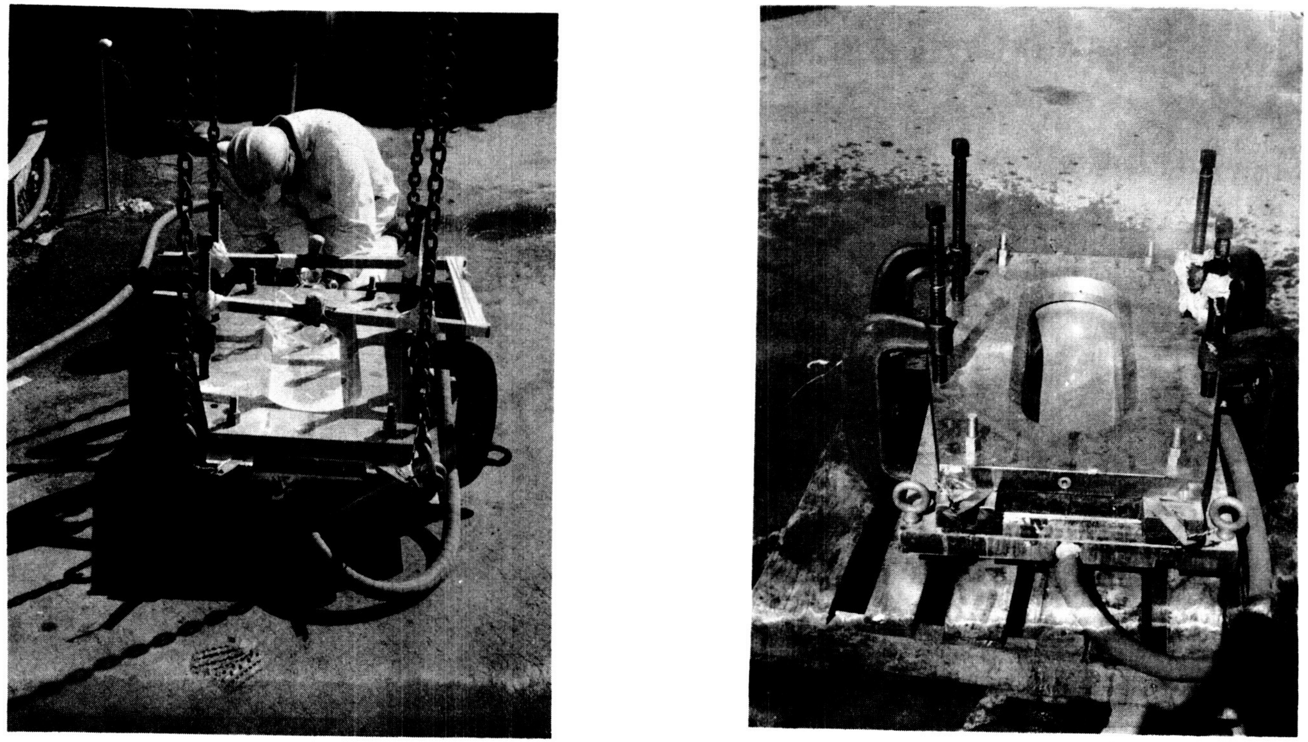

A B

FIGURE 17. EXPLOSIVE FORMING SETUP FOR ELONGATED DOME DIE

(A) BEFORE FORMING

(B) AFTER FORMING

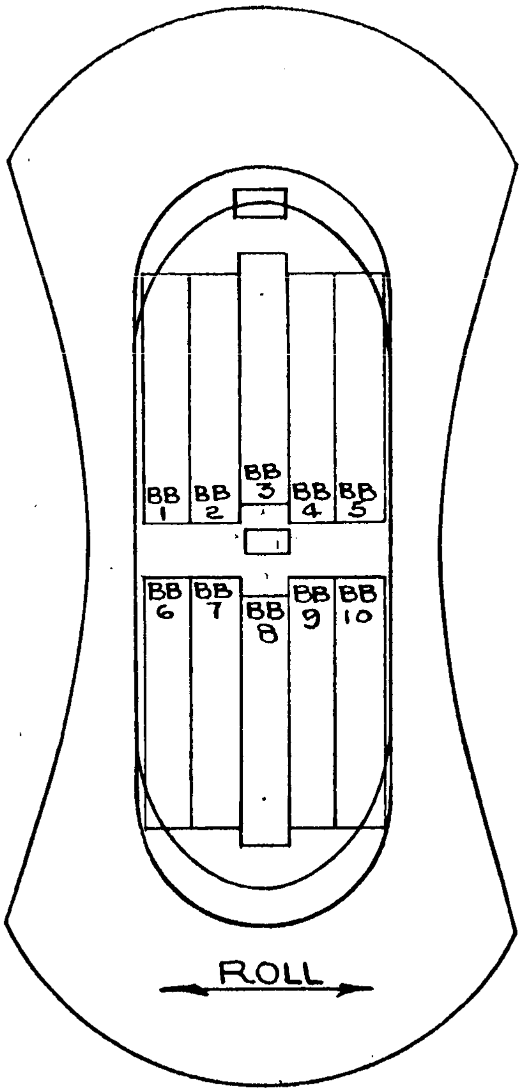

DOME NO. 21

SPECIMEN NO.	DIRECTION	SPECIMEN TYPE
BB1	Trans.	Tensile
BB2		Notch
BB3		Tensile
BB4		Notch
BB5		Tensile
BB6		Tensile
BB7		Notch
BB8		Tensile
BB9		Notch
BB10		Tensile

Elongation is 14% to 16% longitudinal to the rolling direction and up to 10% transverse to the rolling direction.

FIGURE 18. LOCATIONS OF SPECIMENS TAKEN FROM EXPLOSIVELY FORMED DOME NO. 21

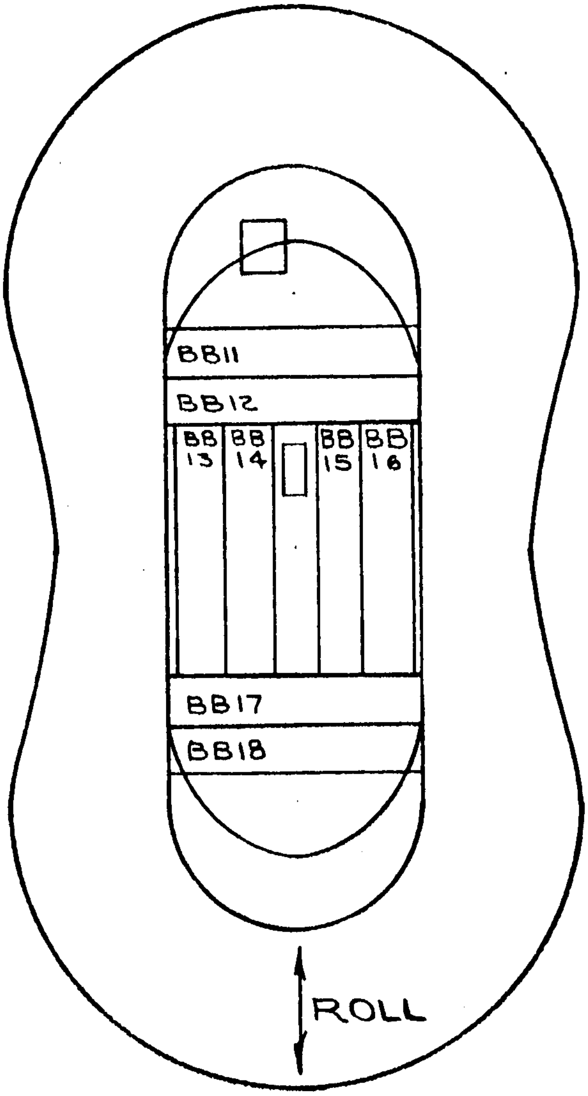

DOME NO. 19

SPECIMEN NO.	DIRECTION	SPECIMEN TYPE
BB11	Trans.	Tensile
BB12	Trans.	Notch
BB13	Long.	Notch
BB14	Long.	Tensile
BB15	Long.	Tensile
BB16	Long.	Notch
BB17	Trans.	Notch
BB18	Trans.	Tensile

Elongation is 10% to 15% longitudinal to the rolling direction. No elongation transverse to the rolling direction could be determined due to obscured grid marks.

FIGURE 19. LOCATIONS OF SPECIMENS TAKEN FROM EXPLOSIVELY FORMED DOME NO. 19

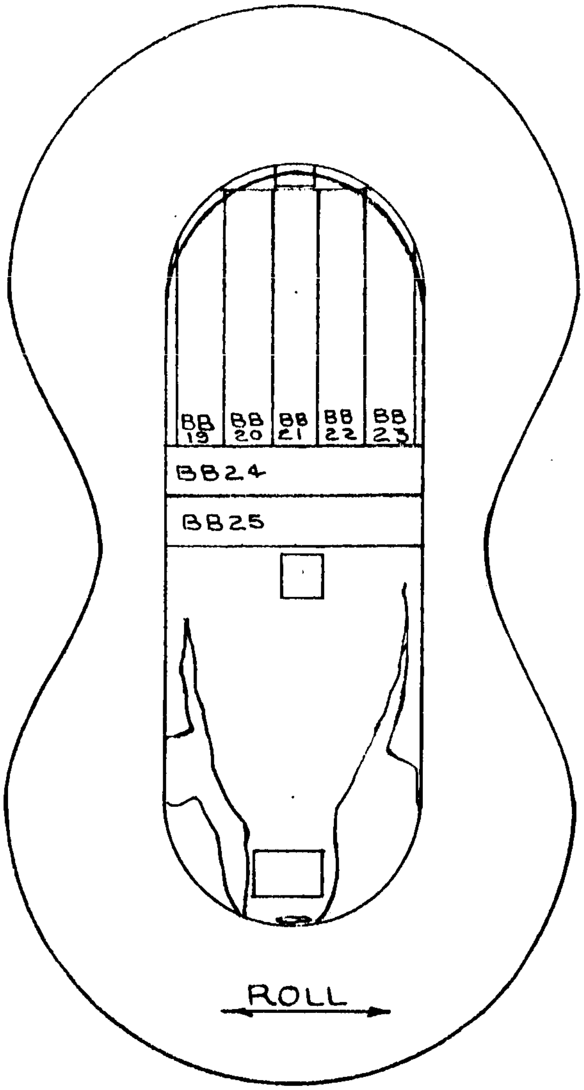

DOME NO. 12

SPECIMEN NO.	DIRECTION	SPECIMEN TYPE
BB19	Trans.	Notch
BB20	Trans.	Tensile
BB21	Trans.	Tensile
BB22	Trans.	Tensile
BB23	Trans.	Notch
BB24	Long.	Tensile
BB25	Long.	Tensile

Elongation is 16% to 34% longitudinal to the rolling direction and 15% to 20% transverse to the rolling direction.

FIGURE 20. LOCATIONS OF SPECIMENS TAKEN FROM EXPLOSIVELY FORMED DOME NO. 12

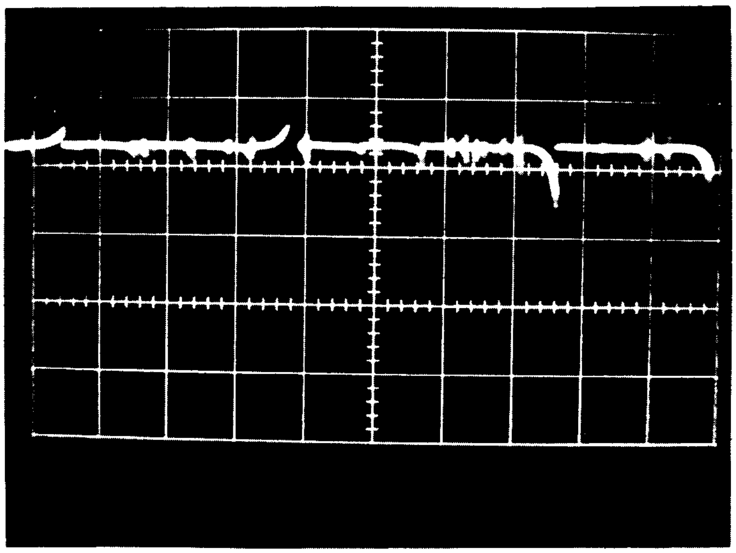

FIGURE 21. OSCILLOGRAM SHOWING PULSES GENERATED BY PIN SWITCHES

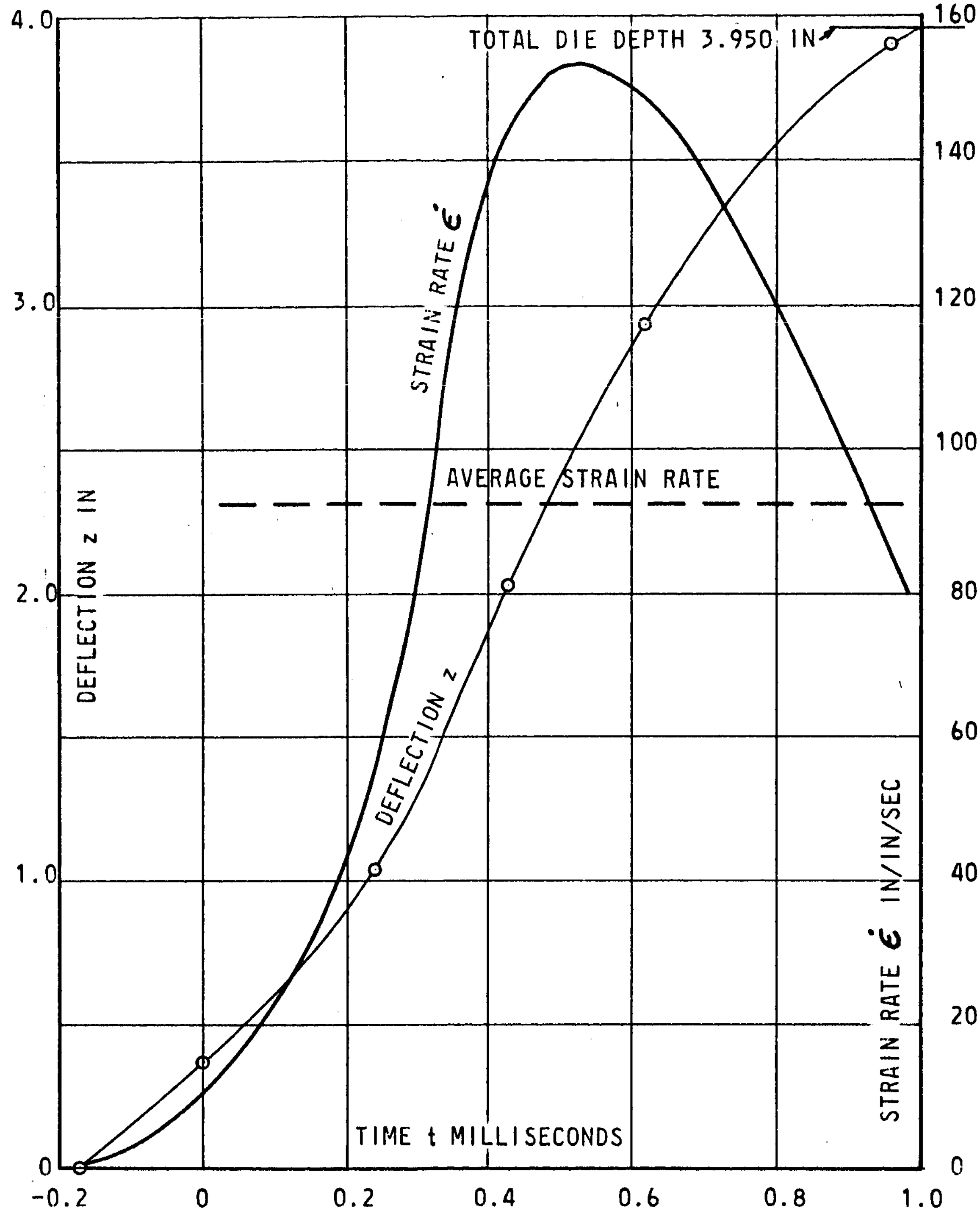

FIGURE 22. DEFLECTION-TIME RELATIONSHIP AND STRAIN RATE VARIATION IN BIAXIAL EXPLOSIVE FORMING

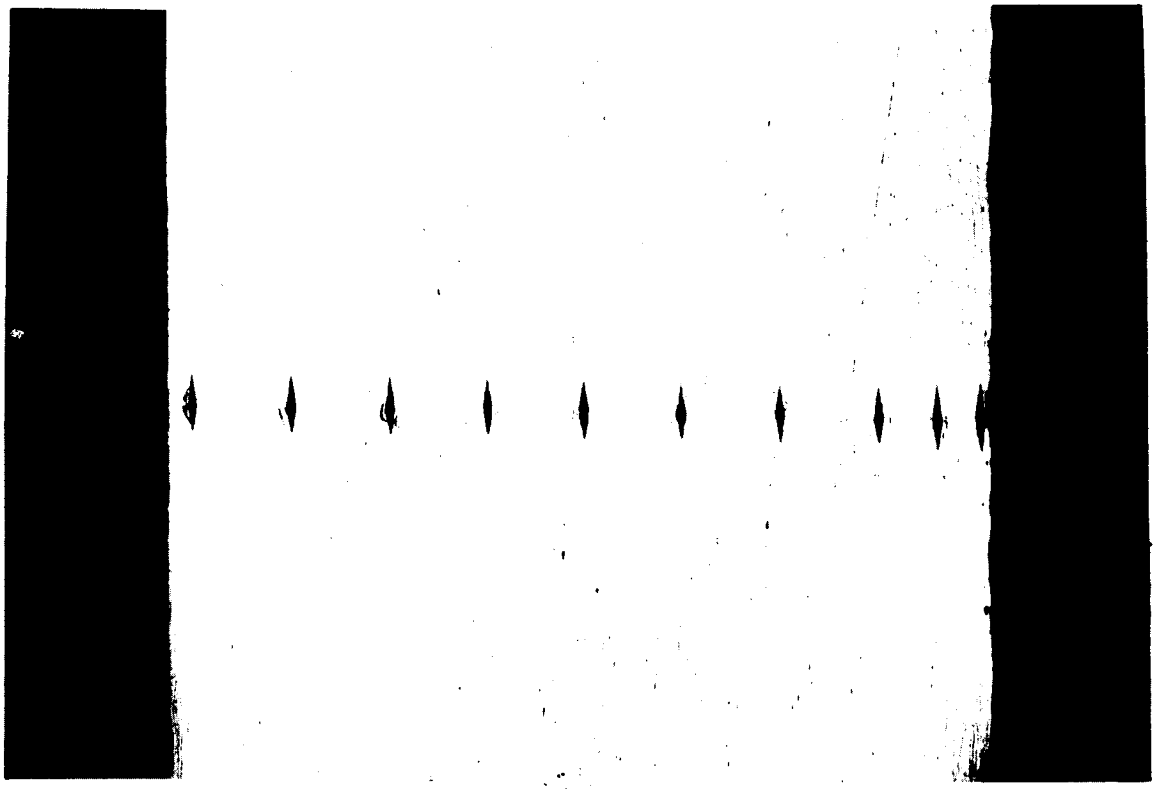

FIGURE 23. PHOTOMACROGRAPH OF MICROHARDNESS TRAVERSE - 6Al-4V TITANIUM - SPECIMEN 11E1

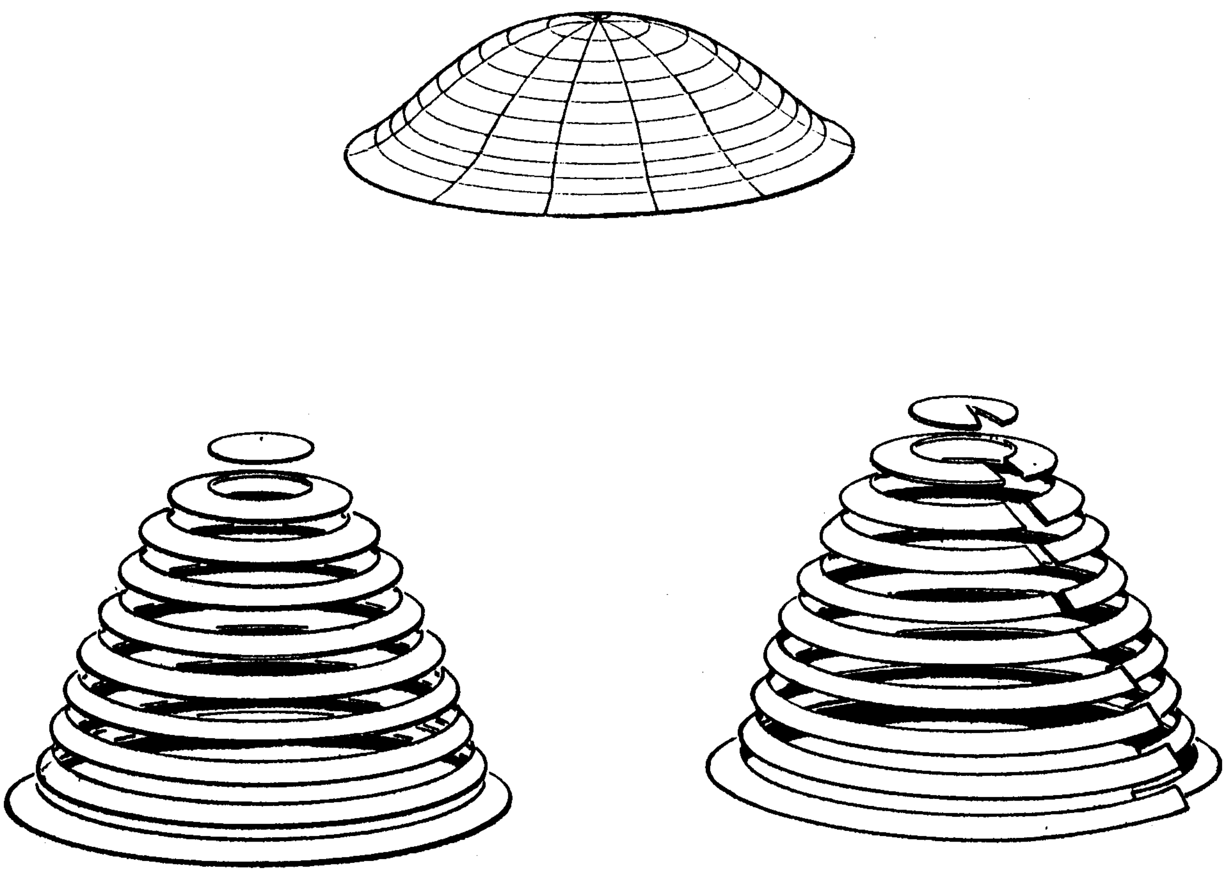

FIGURE 24. TWO-STAGE SECTIONING METHOD FOR INVESTIGATION OF RESIDUAL STRESSES IN DOMES

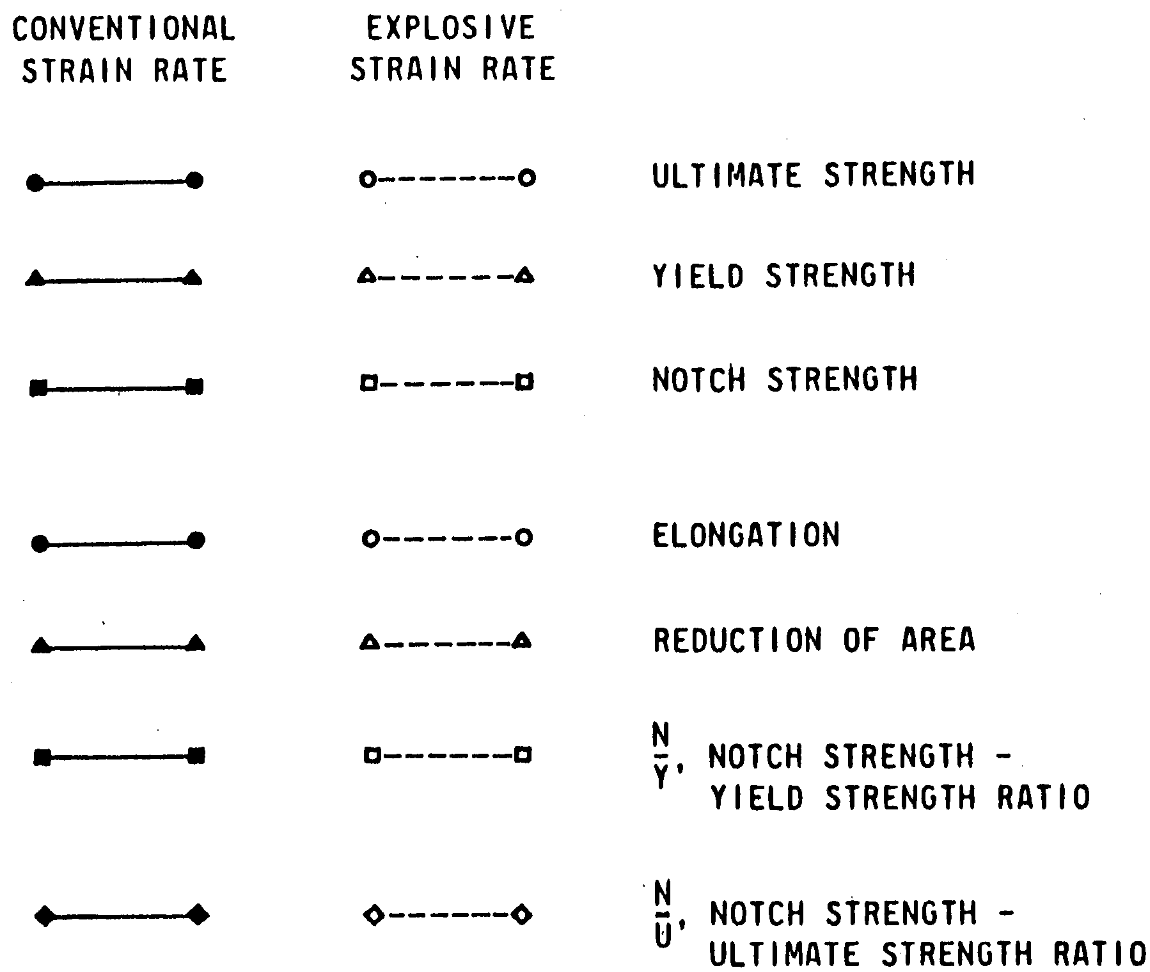

FIGURE 25. SYMBOLS USED ON MECHANICAL PROPERTIES CHARTS

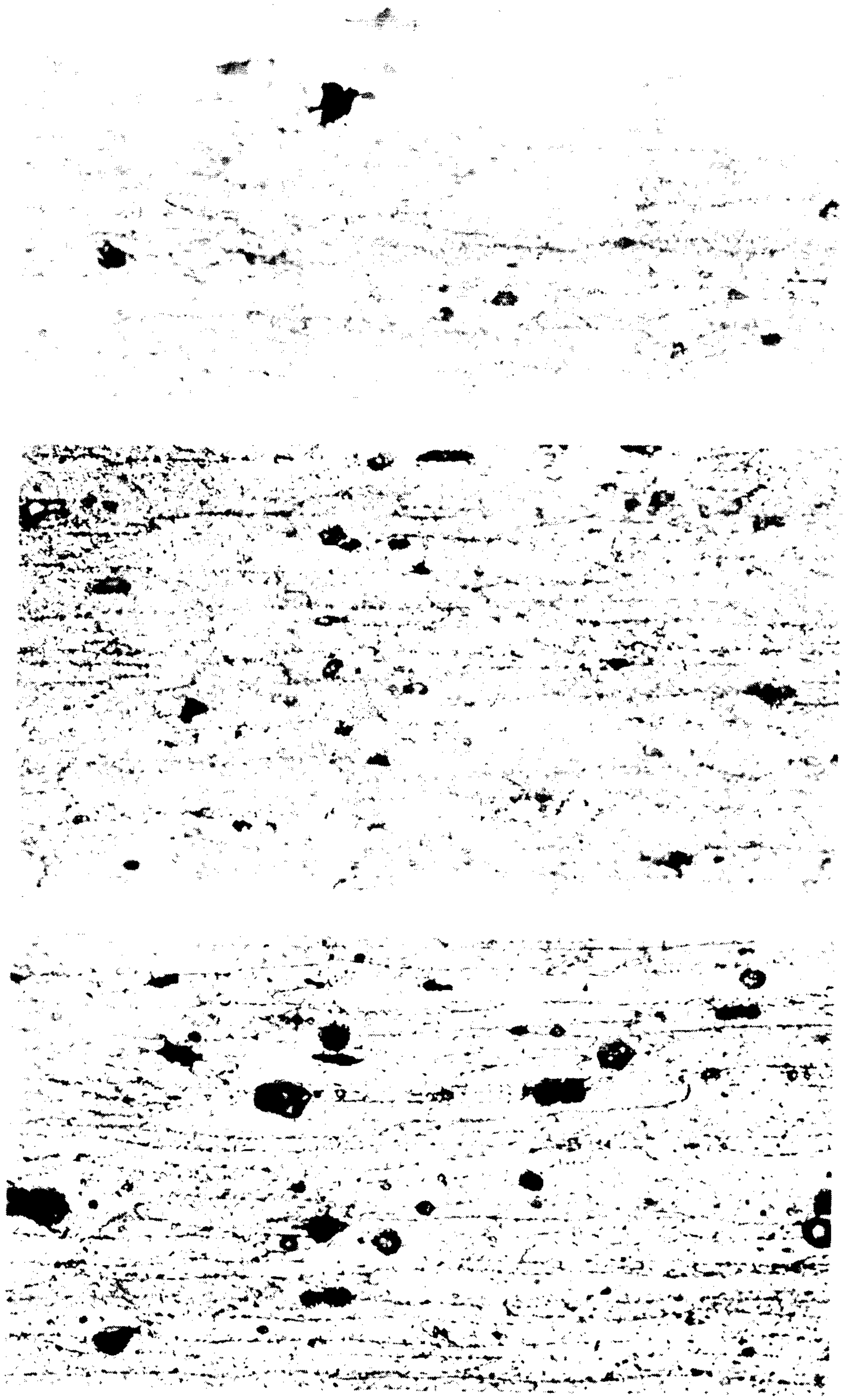

A

B

C

500X

FIGURE 26. 5456-0 ALUMINUM STRAINED AT NOMINAL ROOM TEMPERATURE
(A) AT 3 in/in/min TO NOMINAL 75% OF FRACTURE STRAIN
(B.) EXPLOSIVELY TO NOMINAL 75% OF FRACTURE STRAIN
(C) EXPLOSIVELY TO 34% BIAXIAL STRAIN
KELLER'S ETCH

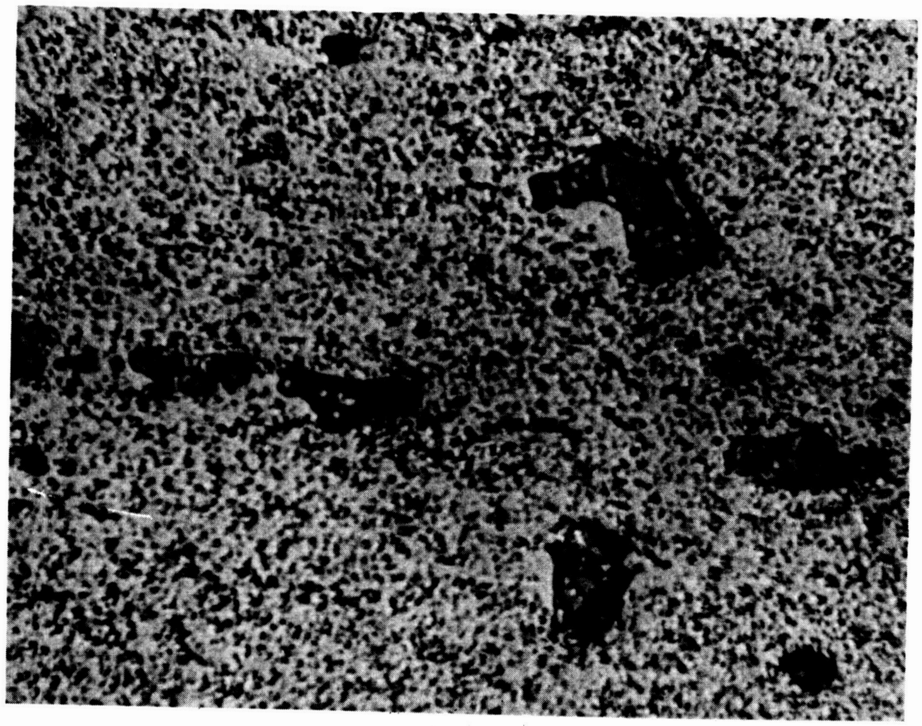

A

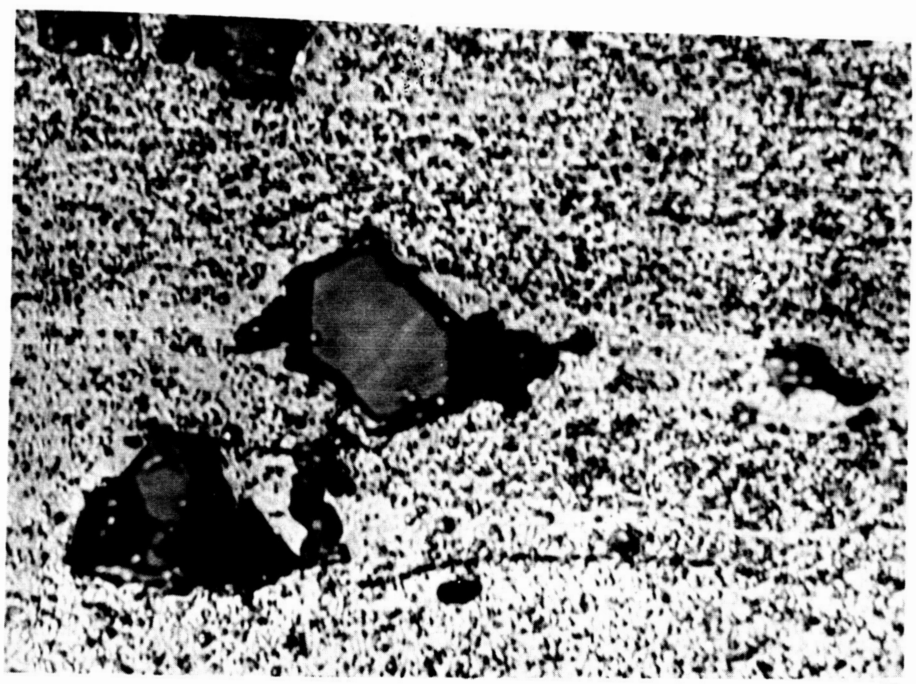

B

2000X

FIGURE 27. 5456-O ALUMINUM
(A) AS RECEIVED (UNSTRAINED)
(B) STRAINED EXPLOSIVELY AT NOMINAL ROOM TEMPERATURE TO NOMINAL 75% OF FRACTURE STRAIN

KELLER'S ETCH

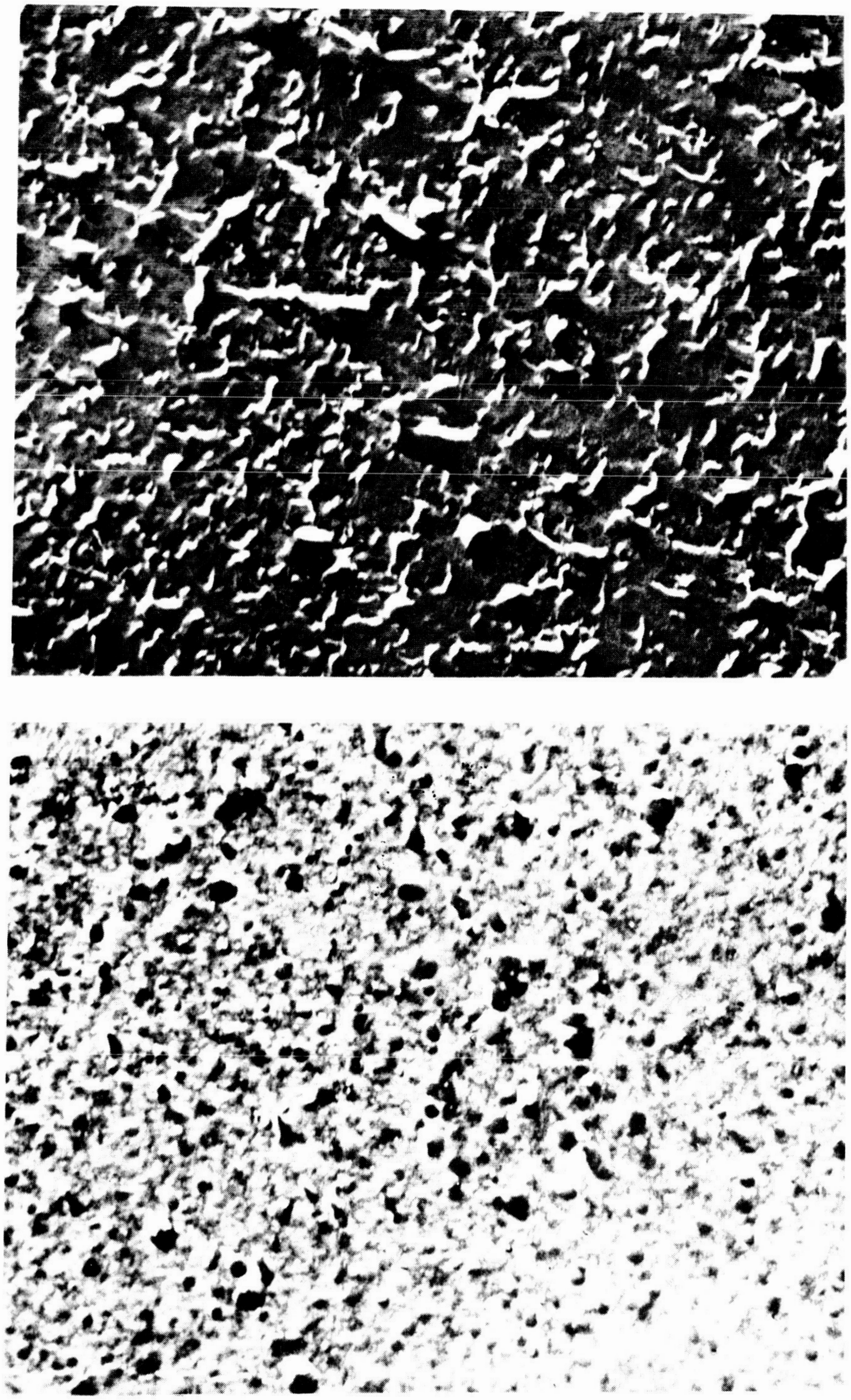

A

B

25,000X

FIGURE 28. 5456-O ALUMINUM STRAINED AT NOMINAL ROOM TEMPERATURE TO NOMINAL 75% OF FRACTURE STRAIN
(A) AT 3 in/in/min
(B) EXPLOSIVELY KELLER'S ETCH

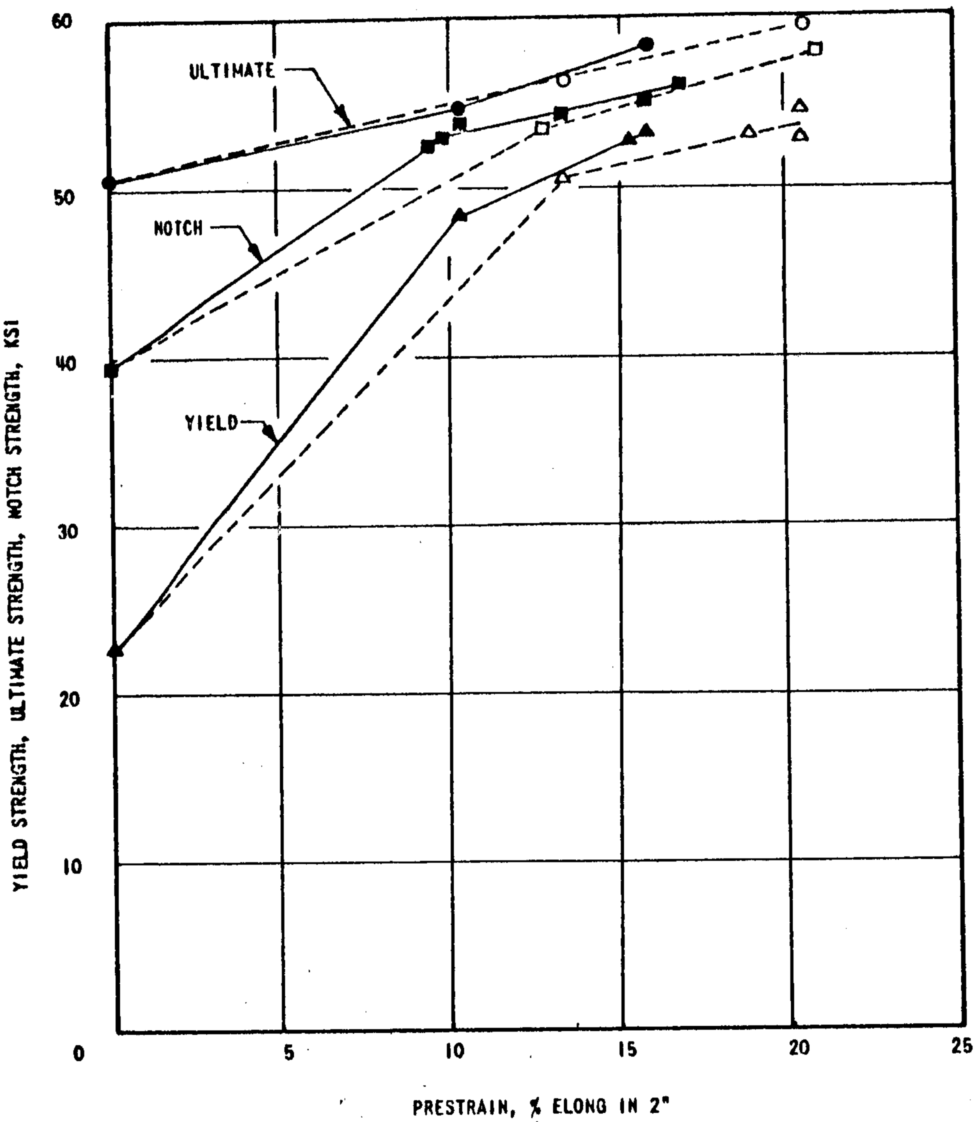

FIGURE 29. MECHANICAL PROPERTIES OF 5456-0 ALUMINUM AFTER VARIOUS PRESTRAINS AT NOMINAL ROOM TEMPERATURE

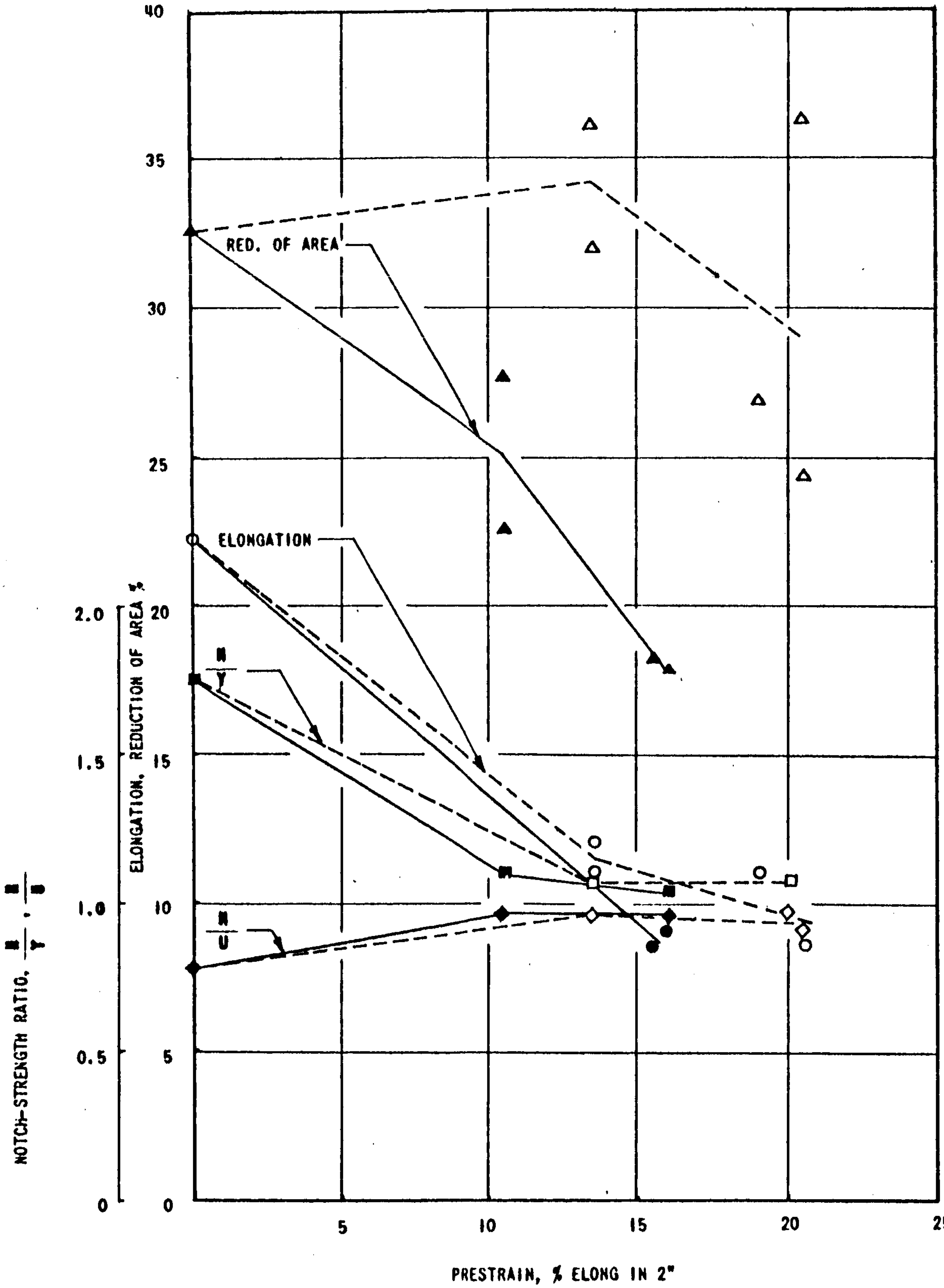

FIGURE 30. MECHANICAL PROPERTIES OF 5456-O ALUMINUM AFTER VARIOUS PRESTRAINS AT NOMINAL ROOM TEMPERATURE

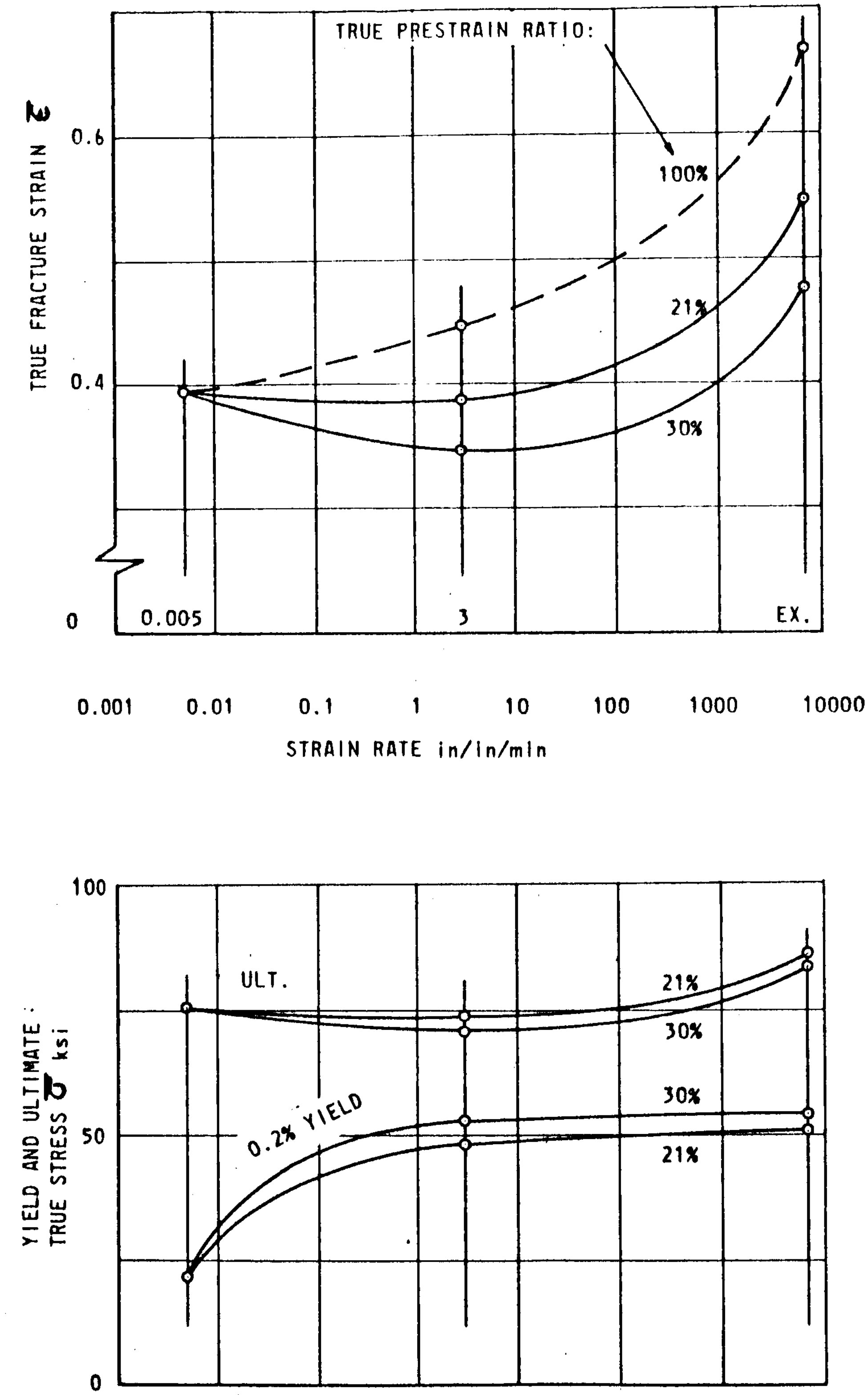

FIGURE 31. TRUE STRESS-STRAIN DATA FOR 5456-0 ALUMINUM AFTER VARIOUS PRESTRAINS AT NOMINAL ROOM TEMPERATURE

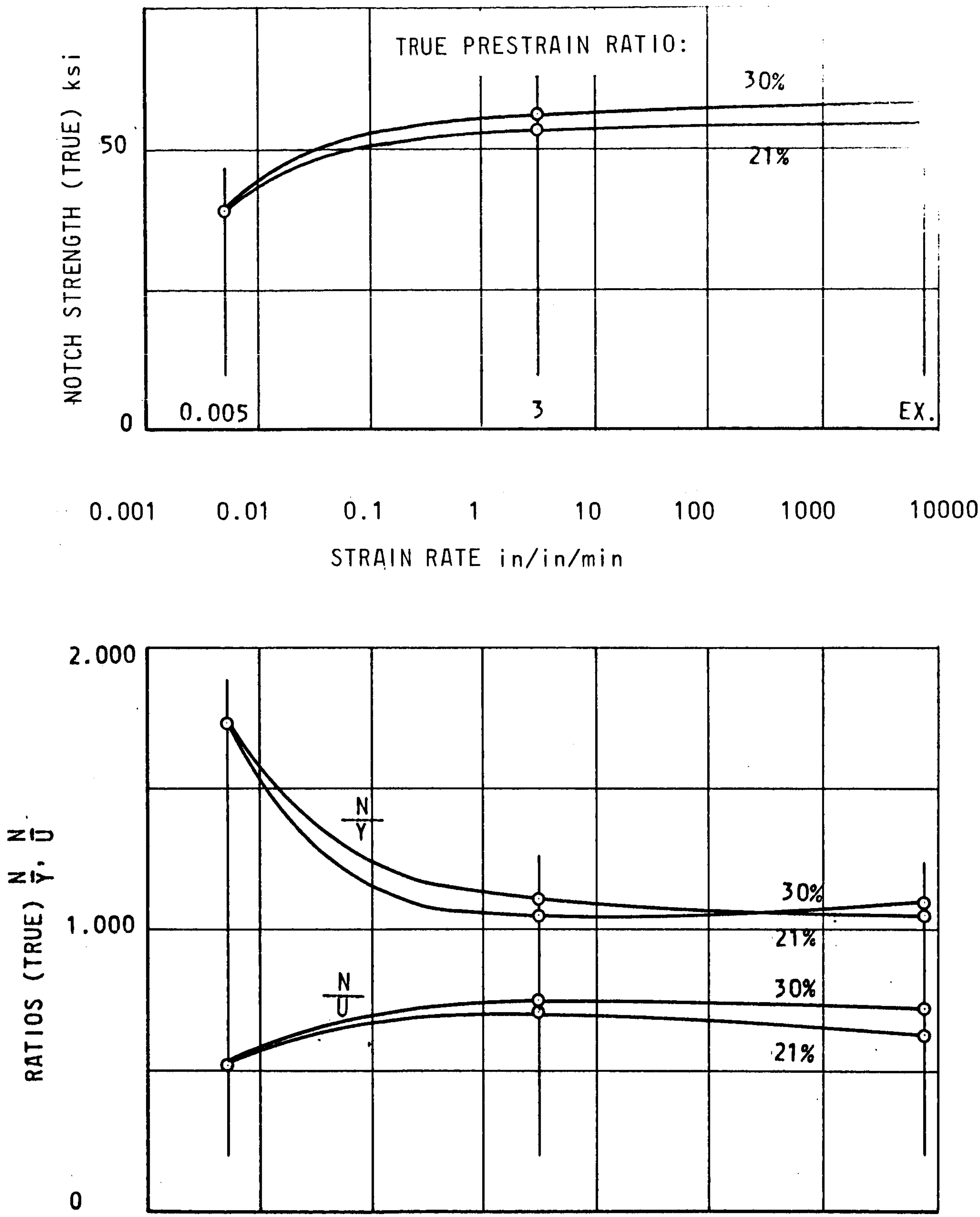

FIGURE 32. NOTCH STRENGTH (TRUE) DATA FOR 5456-0 ALUMINUM AFTER VARIOUS PRESTRAINS AT NOMINAL ROOM TEMPERATURE

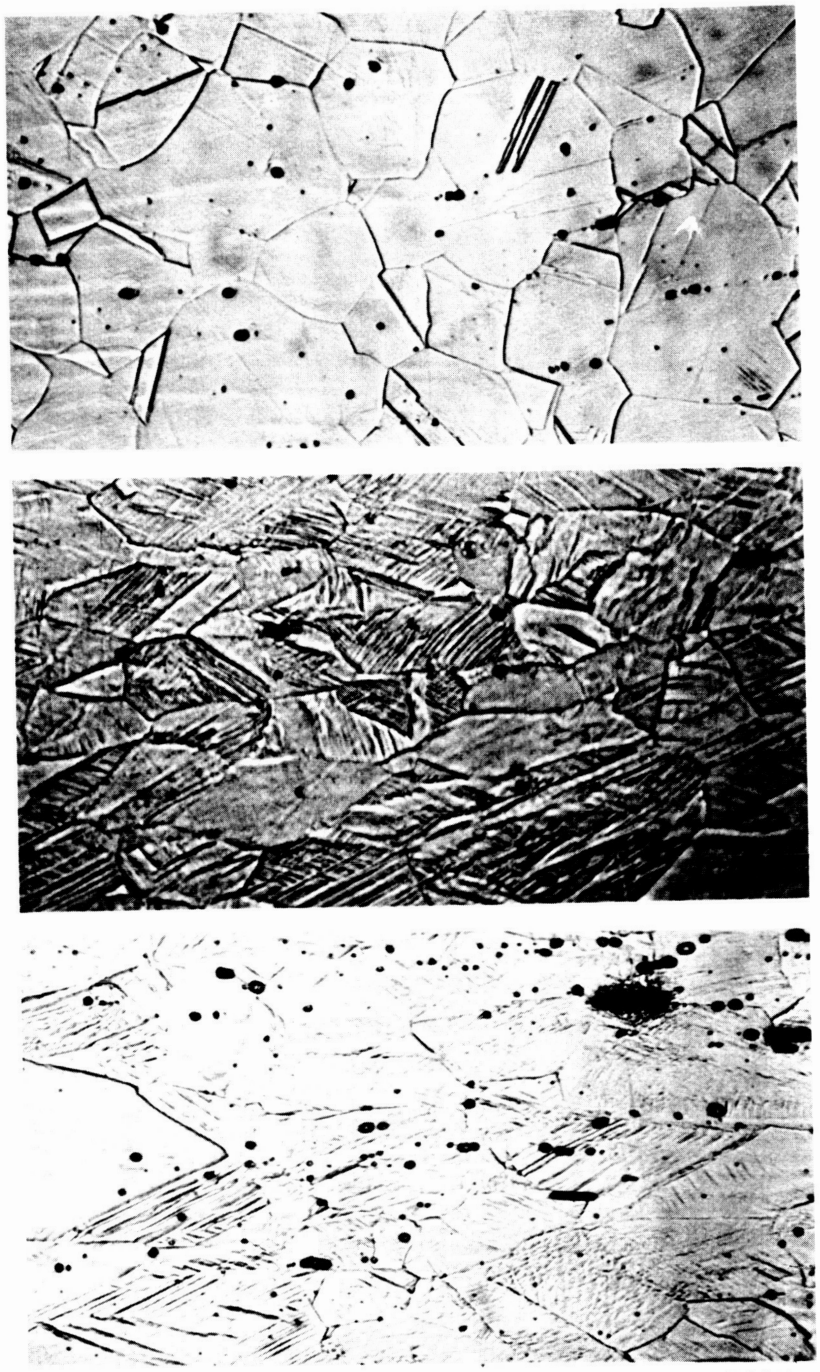

A

B

C

500X

FIGURE 33. AISI 301 STAINLESS STEEL
(A) AS RECEIVED (UNSTRAINED)
ETCHANT: 20% HF, 50% HNO_3
(B) STRAINED AT 3 in/in/min AT NOMINAL ROOM TEMPERATURE TO NOMINAL 75% OF FRACTURE STRAIN
(C) STRAINED EXPLOSIVELY AT NOMINAL ROOM TEMPERATURE TO NOMINAL 75% OF FRACTURE STRAIN
ETCHANT: AMMONIUM PERSULFATE (ELECTROLYTIC)

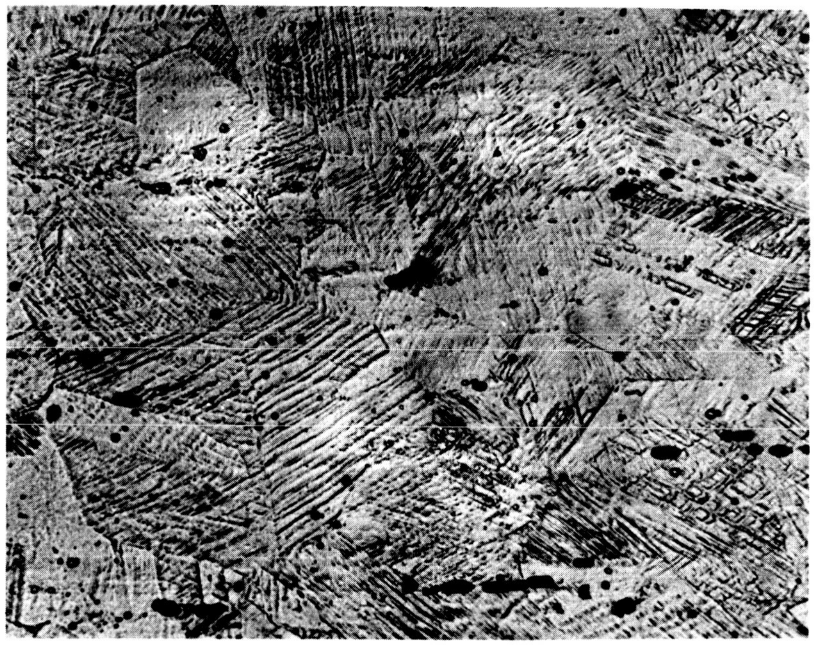

A

B

500X

FIGURE 34. AISI 301 STAINLESS STEEL STRAINED AT NOMINAL -320°F TO NOMINAL 75% OF FRACTURE STRAIN
(A) AT 3 in/in/min
(B) EXPLOSIVELY
ETCHANT: AMMONIUM PERSULFATE (ELECTROLYTIC)

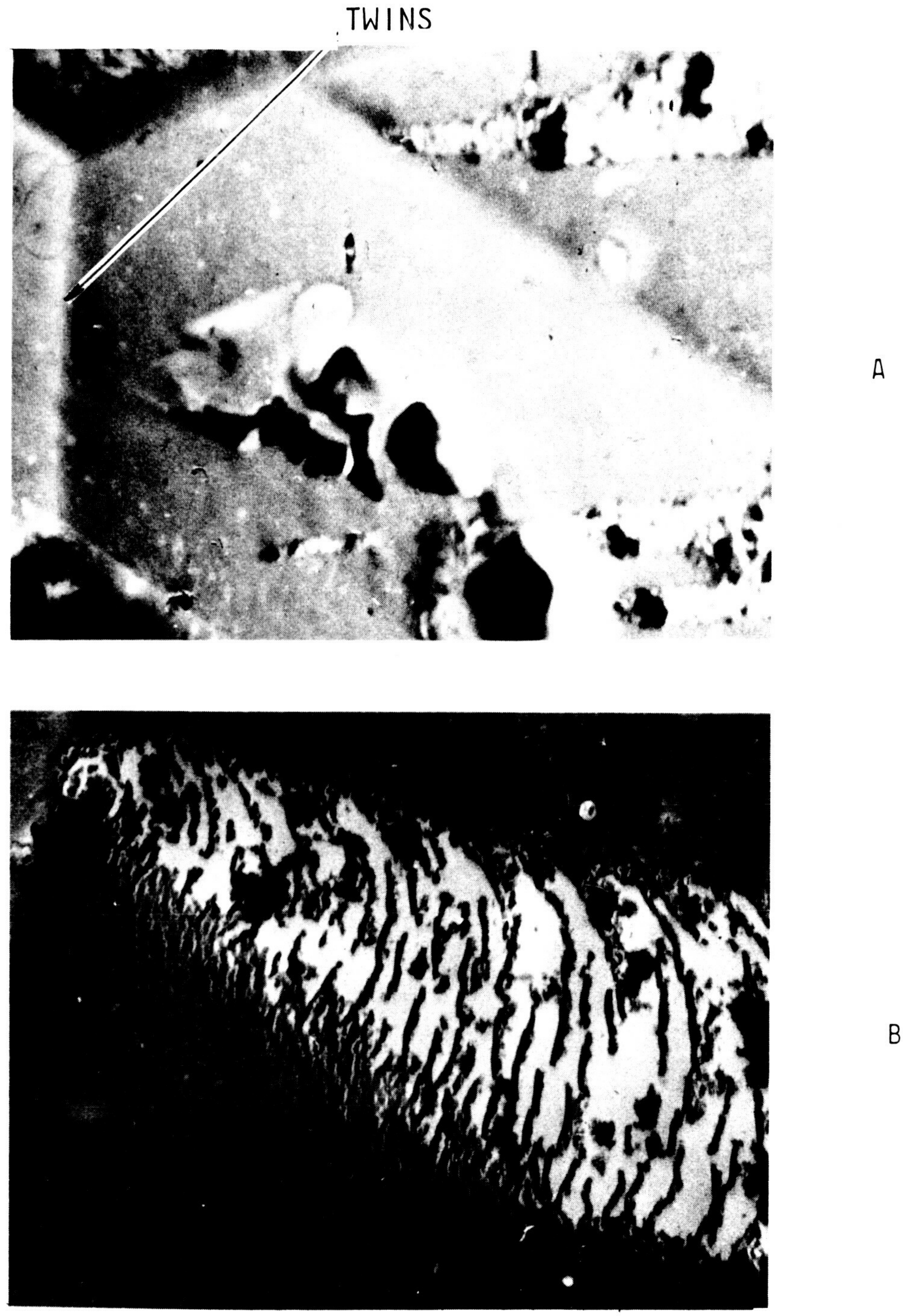

20,000X

FIGURE 35. AISI 301 STAINLESS STEEL AS RECEIVED
ETCHANT: 20% HF, 50% HNO_3

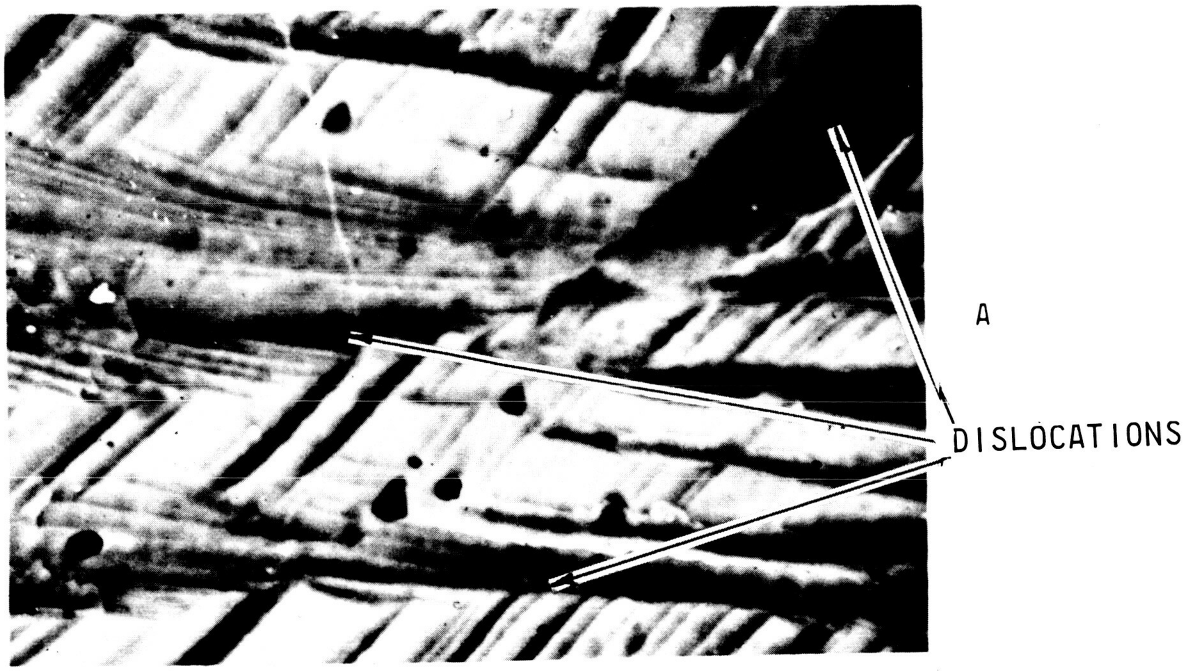

12,000X

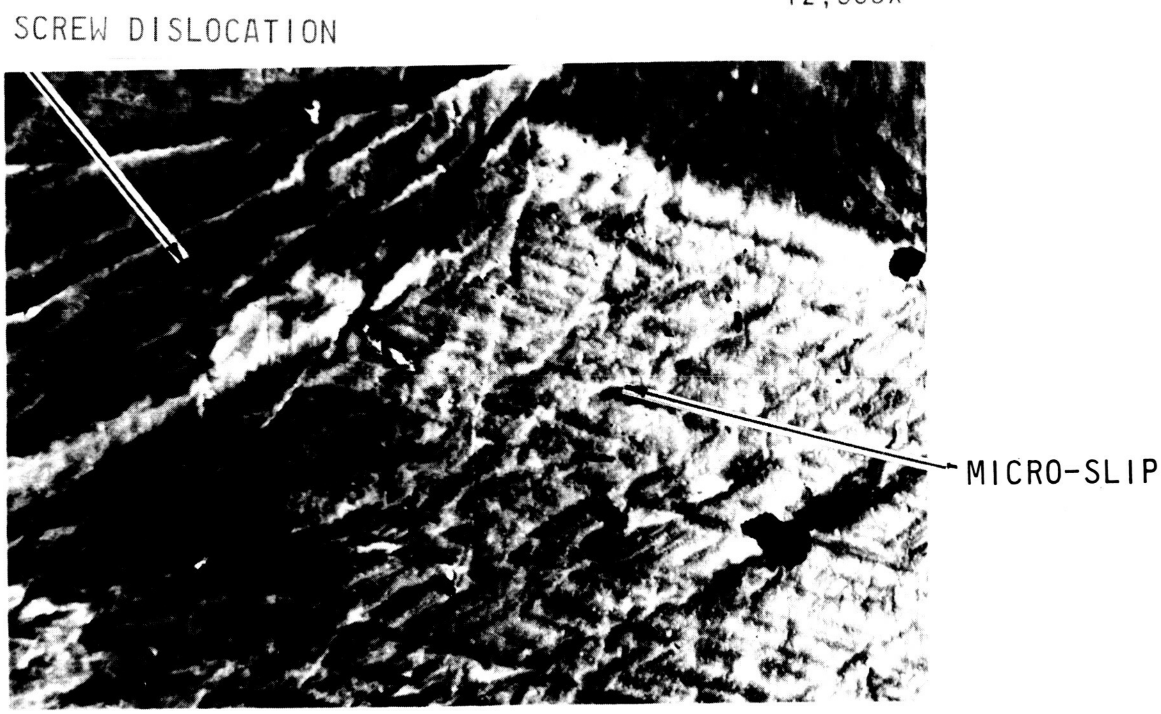

15,000X

FIGURE 36. AISI 301 STAINLESS STEEL STRAINED AT NOMINAL ROOM TEMPERATURE TO NOMINAL 75% OF FRACTURE STRAIN
(A) AT 3 in/in/min
(B) EXPLOSIVELY
ETCHANT: 20% HF, 50% HNO_3

A

B

30,000X

FIGURE 37. AISI 301 STAINLESS STEEL STRAINED EXPLOSIVELY AT NOMINAL -320°F
(A) TO NOMINAL 75% OF FRACTURE STRAIN
(B) TO NOMINAL 40% OF FRACTURE STRAIN
ETCHANT: 20% HF, 50% HNO_3

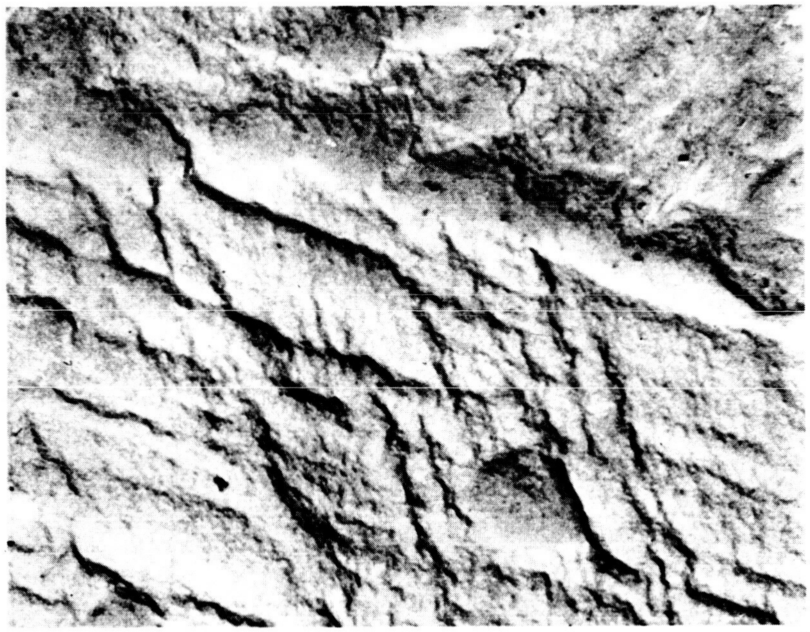

A

10,000X

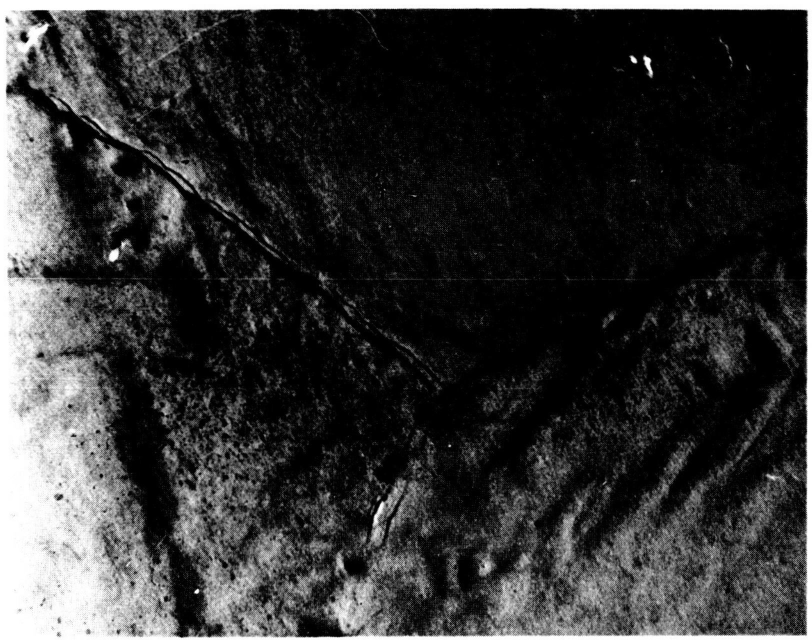

B

30,000X

FIGURE 38. AISI 301 STAINLESS STEEL STRAINED EXPLOSIVEL AT NOMINAL -320°F TO NOMINAL 75% OF FRACTURE STRAIN ETCHANT: 20% HF, 50% HNO_3

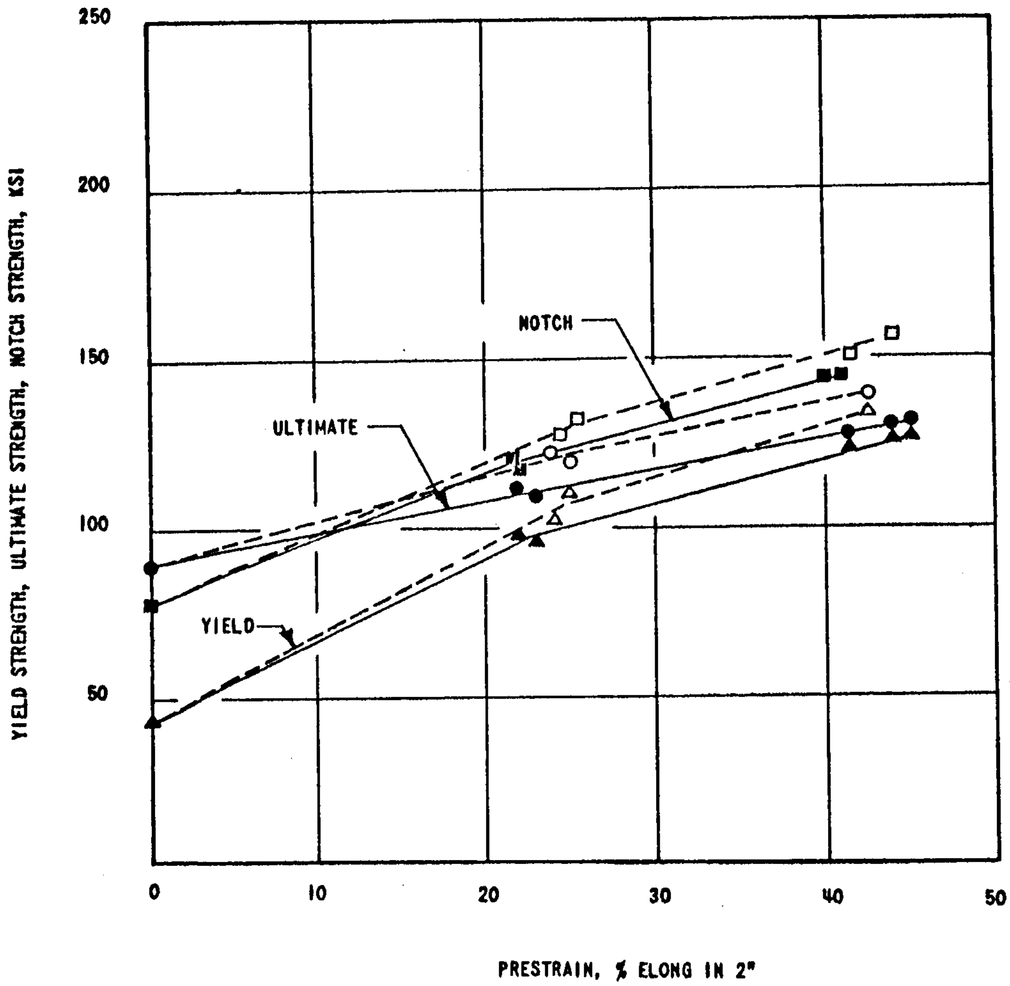

FIGURE 39. MECHANICAL PROPERTIES OF AISI 301 STAINLESS STEEL AFTER VARIOUS PRESTRAINS AT NOMINAL ROOM TEMPERATURE

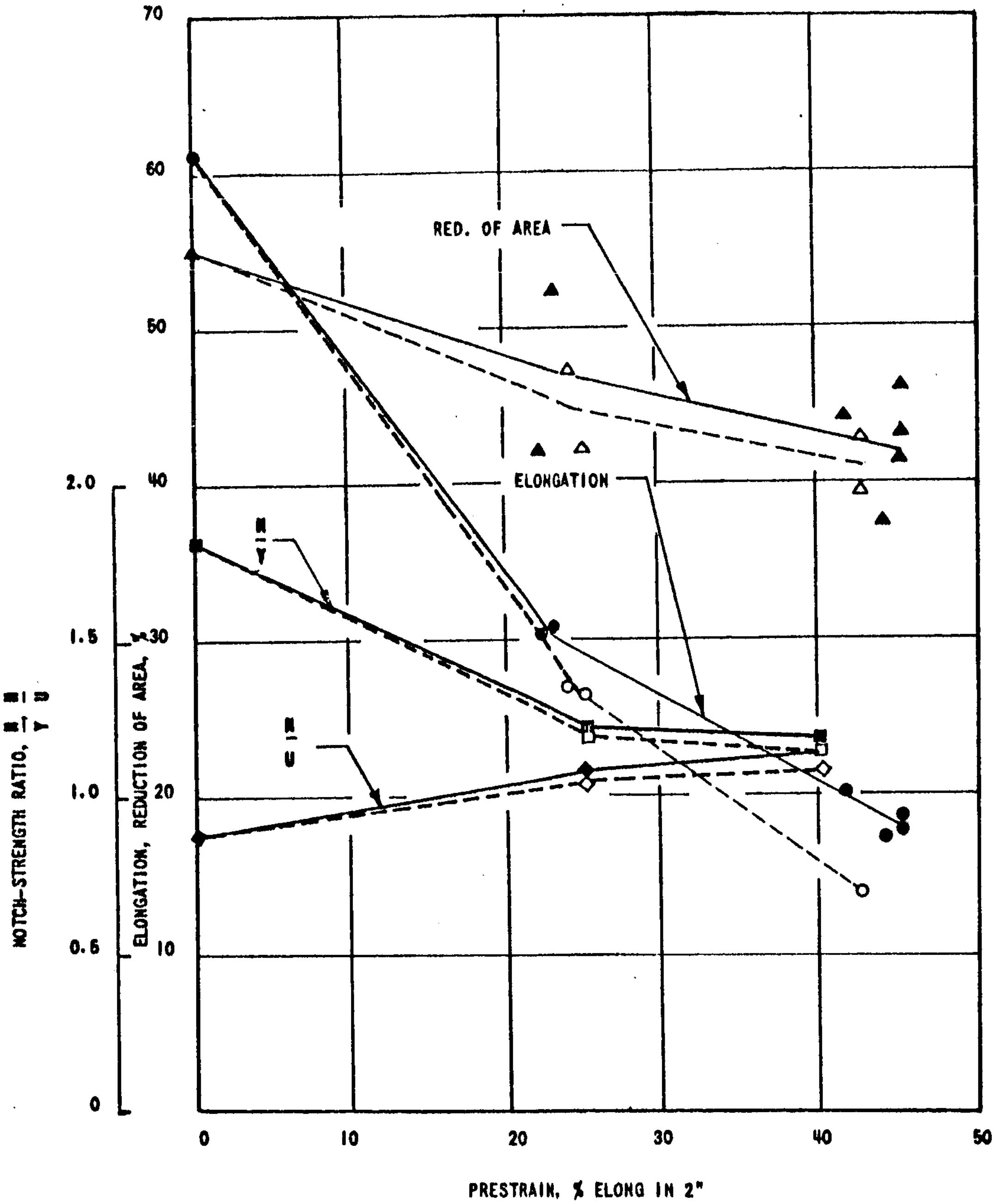

FIGURE 40. MECHANICAL PROPERTIES OF AISI 301 STAINLESS STEEL AFTER VARIOUS PRESTRAINS AT NOMINAL ROOM TEMPERATURE

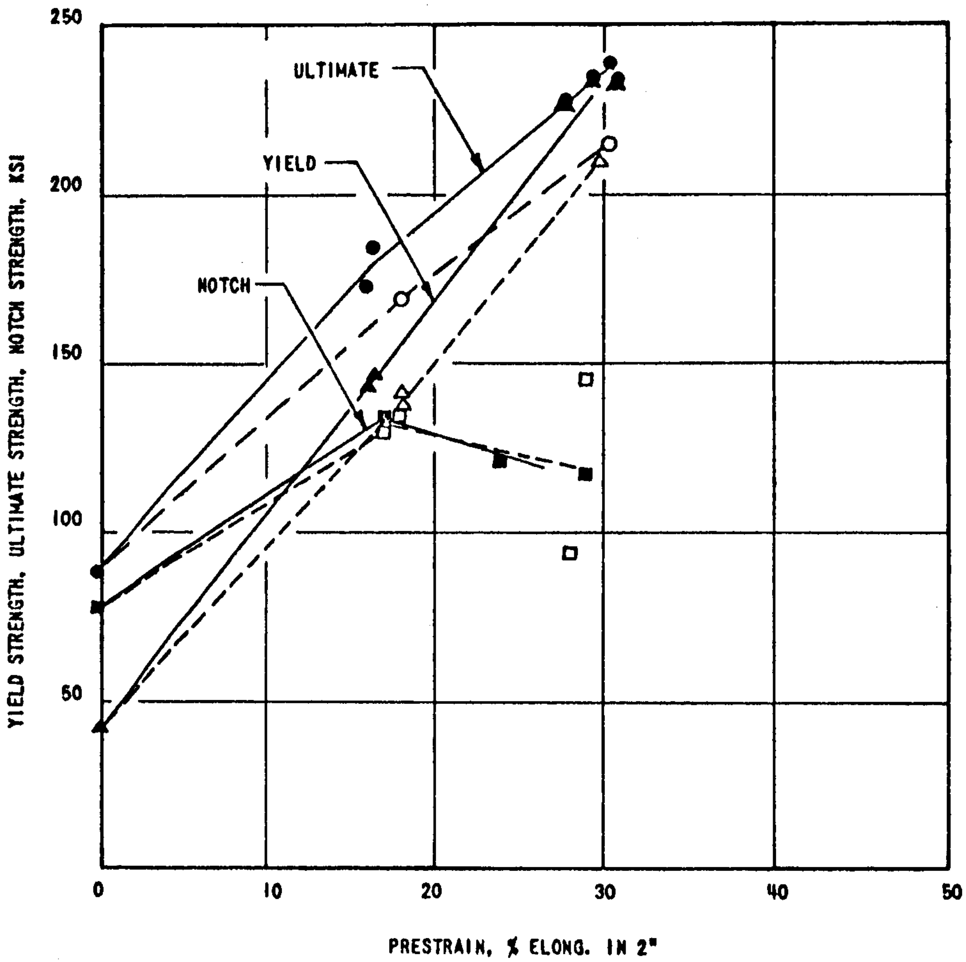

FIGURE 41. MECHANICAL PROPERTIES OF AISI 301 STAINLESS STEEL AFTER VARIOUS PRESTRAINS AT NOMINAL -320°F

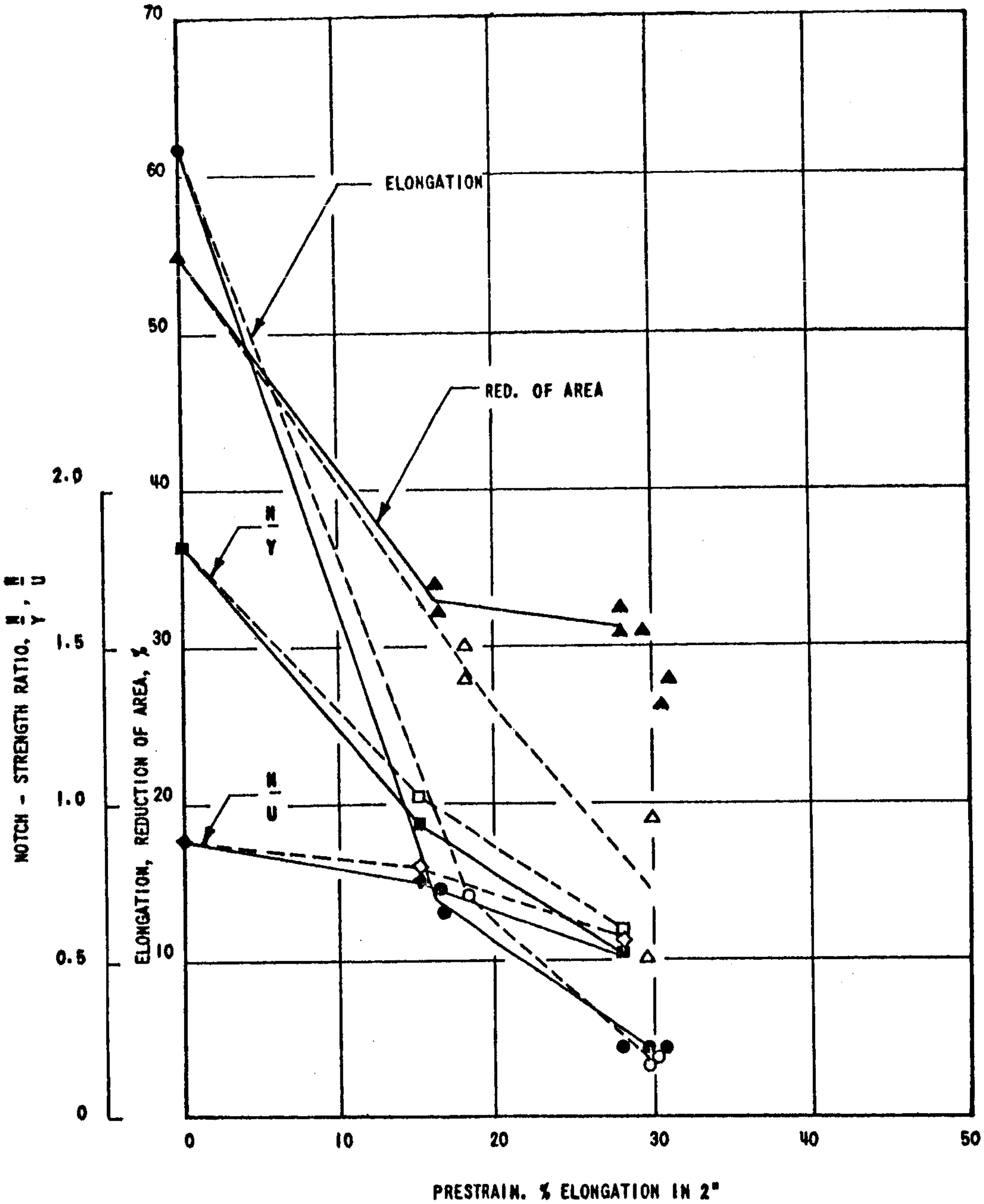

FIGURE 42. MECHANICAL PROPERTIES OF AISI 301 STAINLESS STEEL AFTER VARIOUS PRESTRAINS AT NOMINAL -320°F

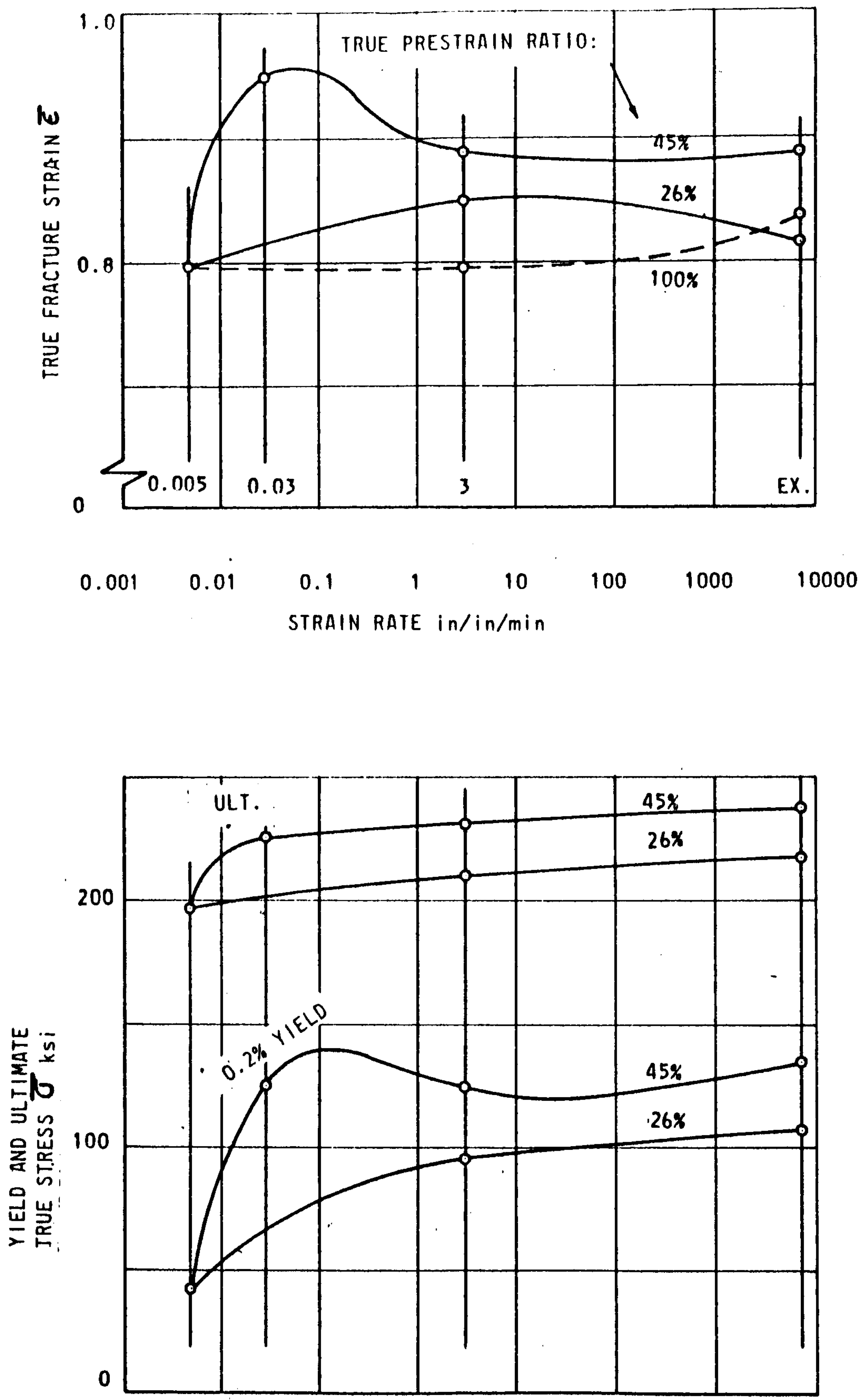

FIGURE 43 TRUE STRESS-STRAIN DATA FOR 301 STAINLESS STEEL AFTER VARIOUS PRESTRAINS AT NOMINAL ROOM TEMPERATURE

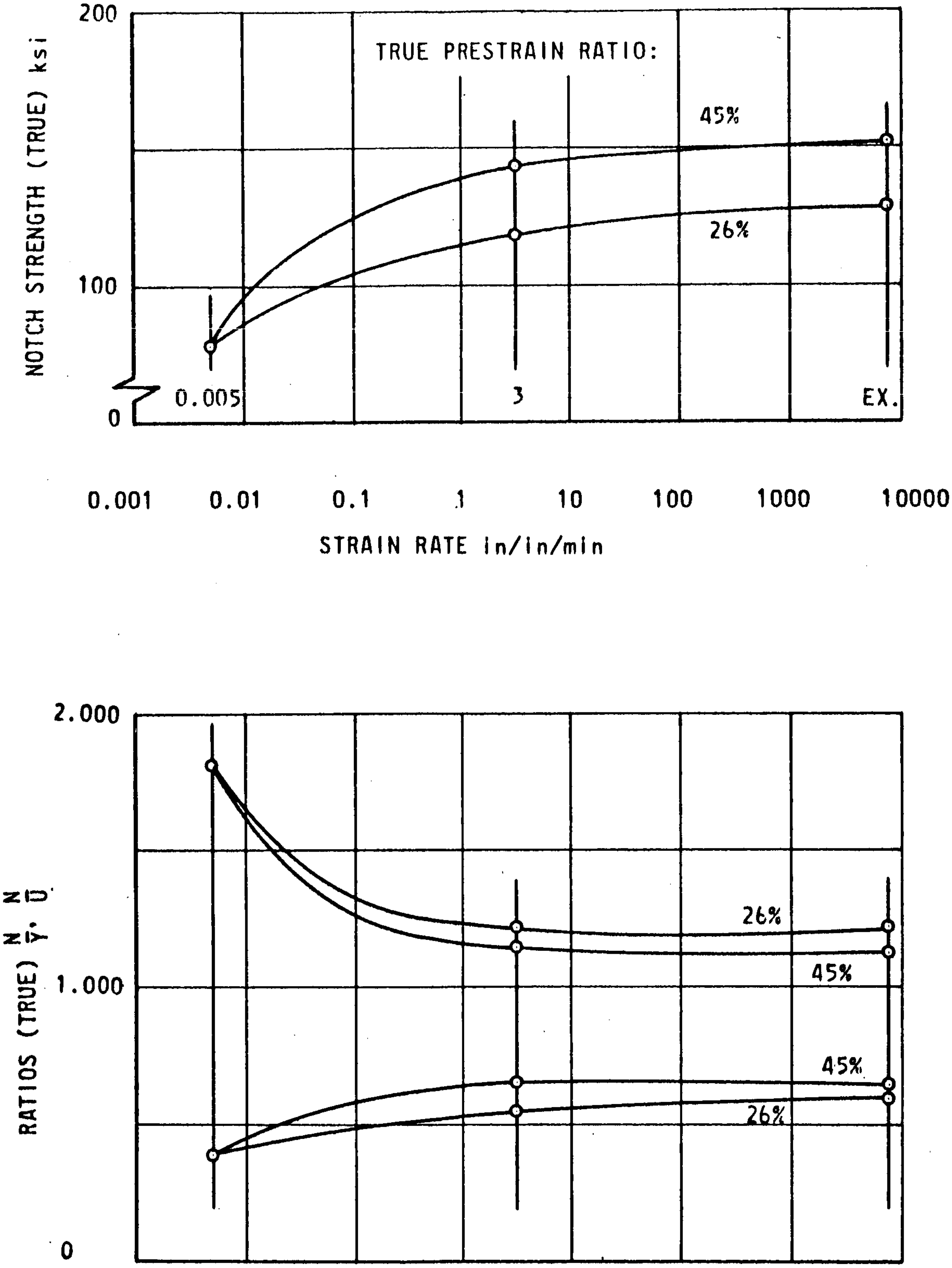

FIGURE 44. NOTCH STRENGTH (TRUE) DATA FOR 301 STAINLESS STEEL AFTER VARIOUS PRESTRAINS AT NOMINAL ROOM TEMPERATURE.

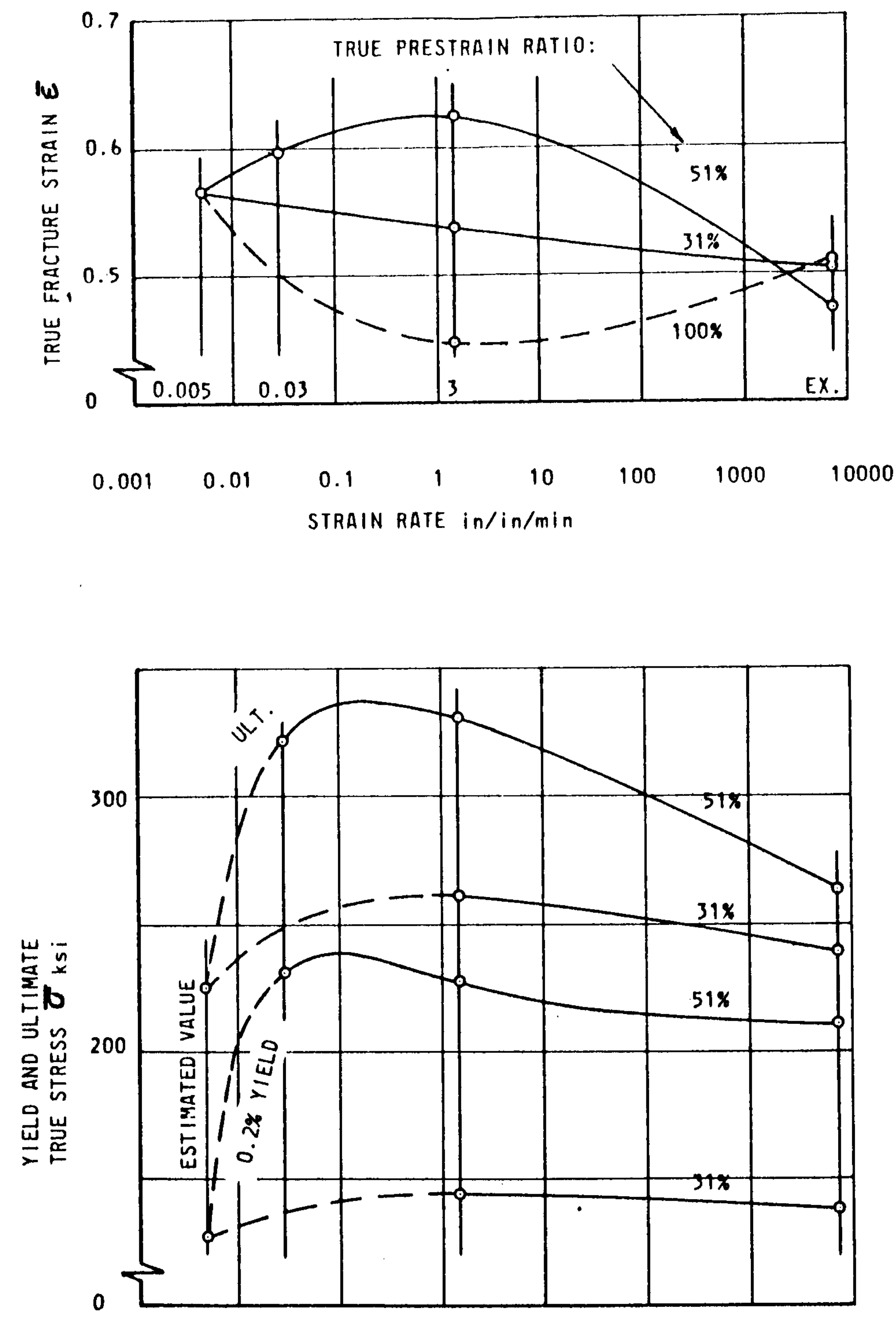

FIGURE 45 TRUE STRESS-STRAIN DATA FOR 301 STAINLESS STEEL AFTER VARIOUS PRESTRAINS AT NOMINAL -320°F

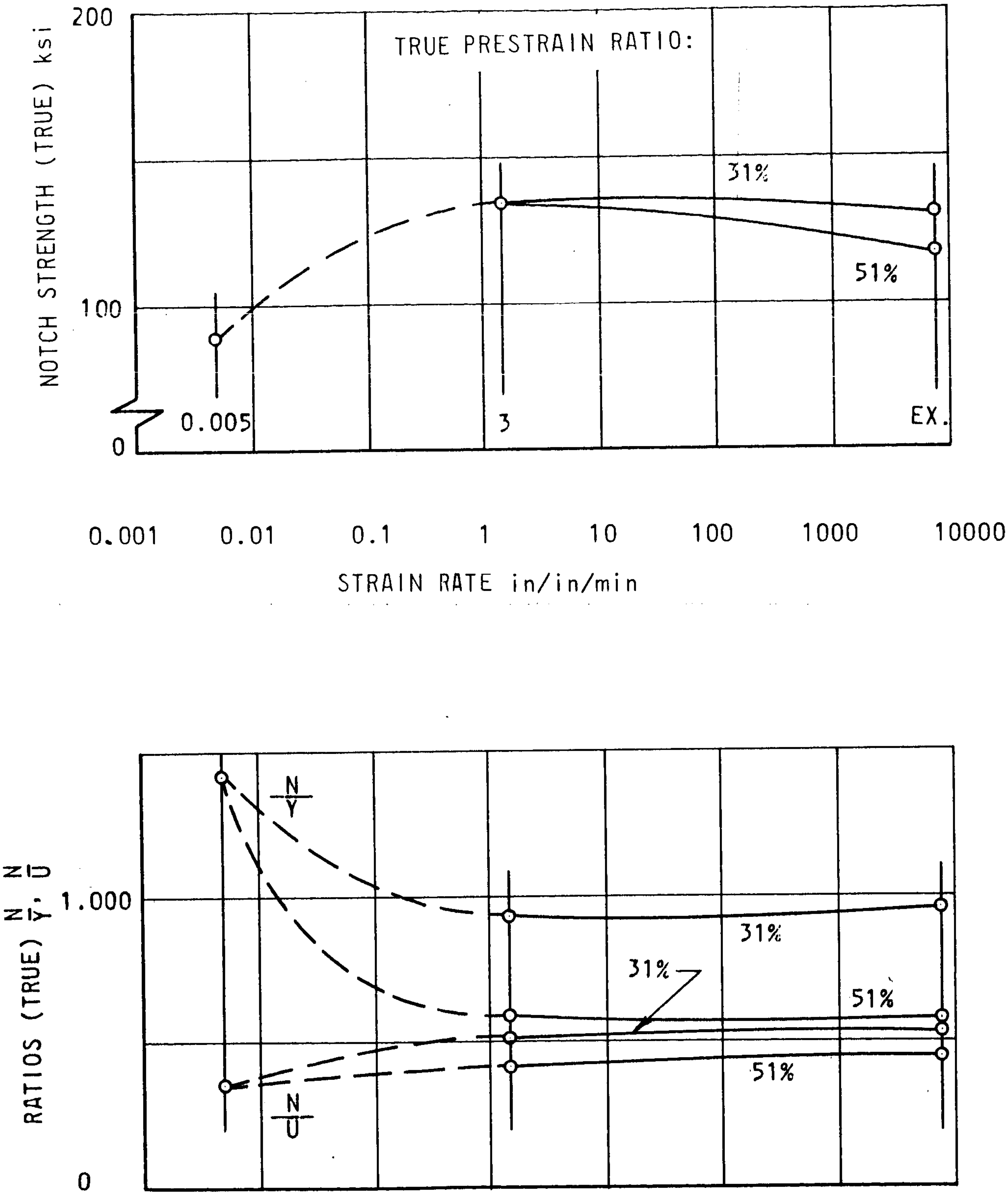

FIGURE 46. NOTCH STRENGTH (TRUE) DATA FOR 301 STAINLESS STEEL AFTER VARIOUS PRESTRAINS AT NOMINAL -320°F

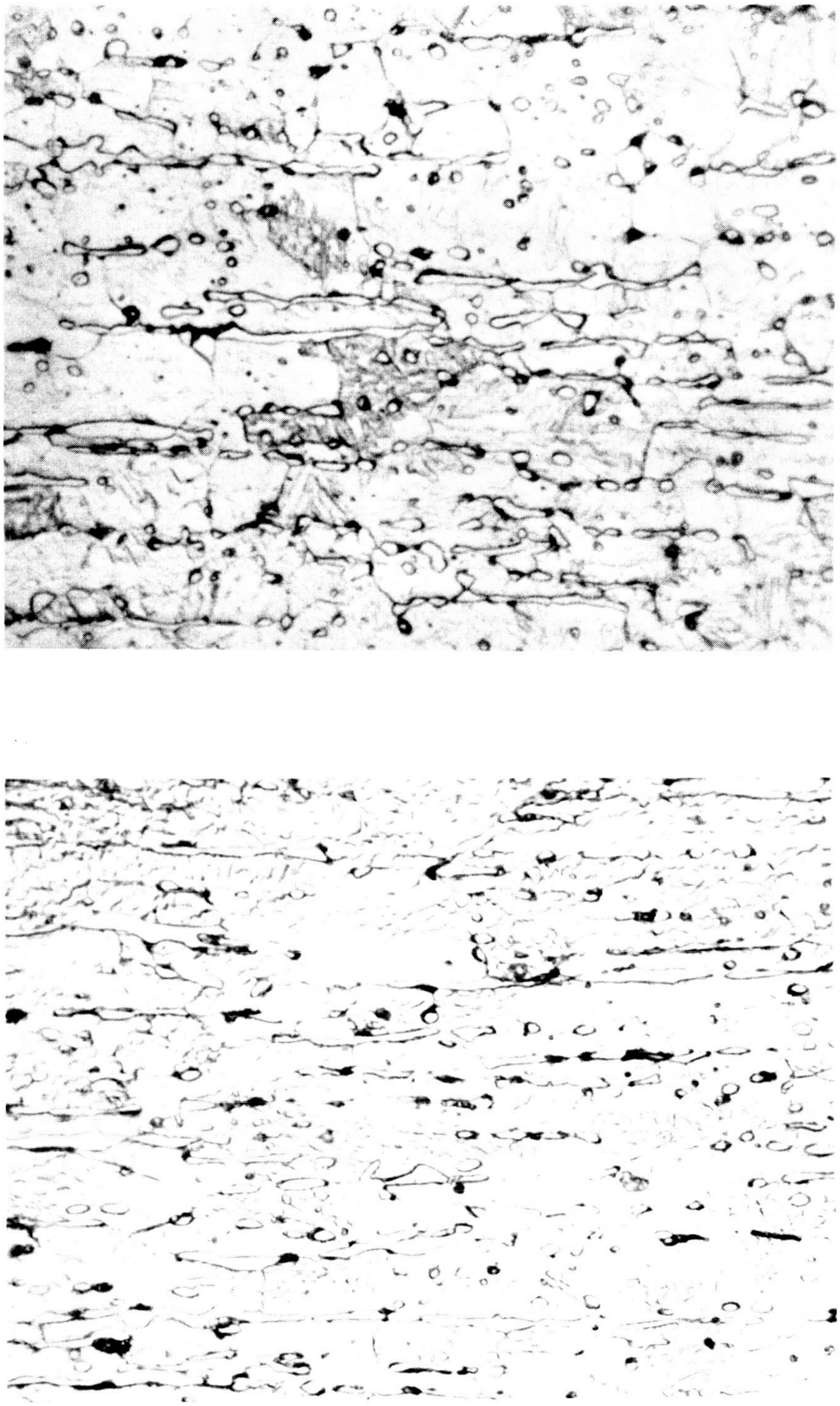

A

B

1000X

FIGURE 47. 17-7 PH STAINLESS STEEL
(A) AS RECEIVED (UNSTRAINED)
(B) STRAINED EXPLOSIVELY AT NOMINAL ROOM TEMPERATURE TO NOMINAL 75% OF FRACTURE STRAIN

ETCHANT: 20% HF, 50% HNO_3

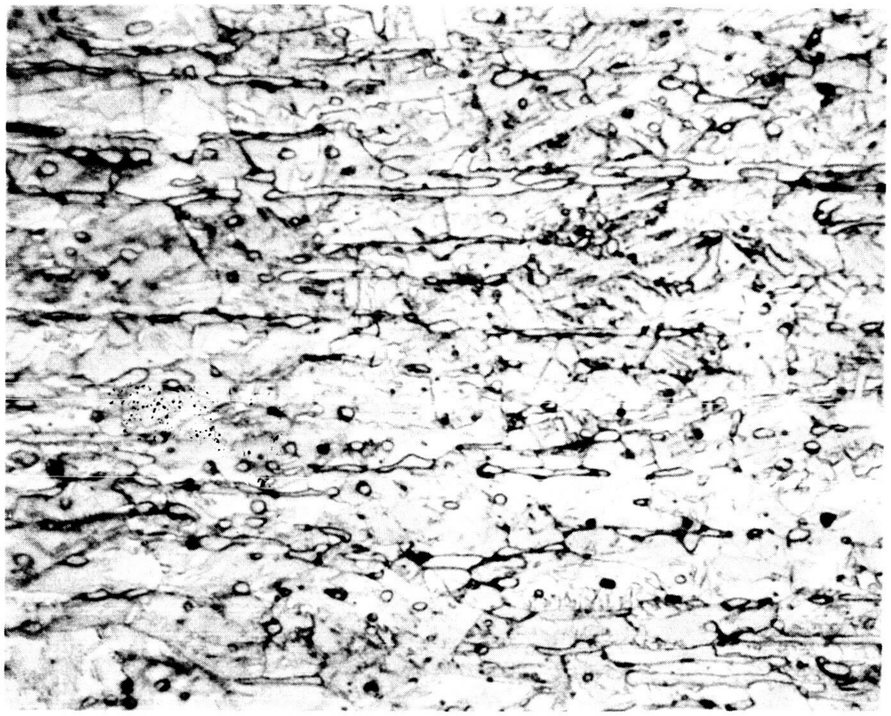

A

B

1000X

FIGURE 48. 17-7 PH STAINLESS STEEL STRAINED AT NOMINAL ROOM TEMPERATURE TO NOMINAL 75% OF FRACTURE STRAIN
(A) AT 3 in/in/min AND AGED
(B) EXPLOSIVELY AND AGED
ETCHANT: 20% HF, 50% HNO_3

1000X

FIGURE 49. 17-7 PH STAINLESS STEEL STRAINED EXPLOSIVELY AT NOMINAL -320°F TO NOMINAL 75% OF FRACTURE STRAIN AND AGED ETCHANT: ARMCO

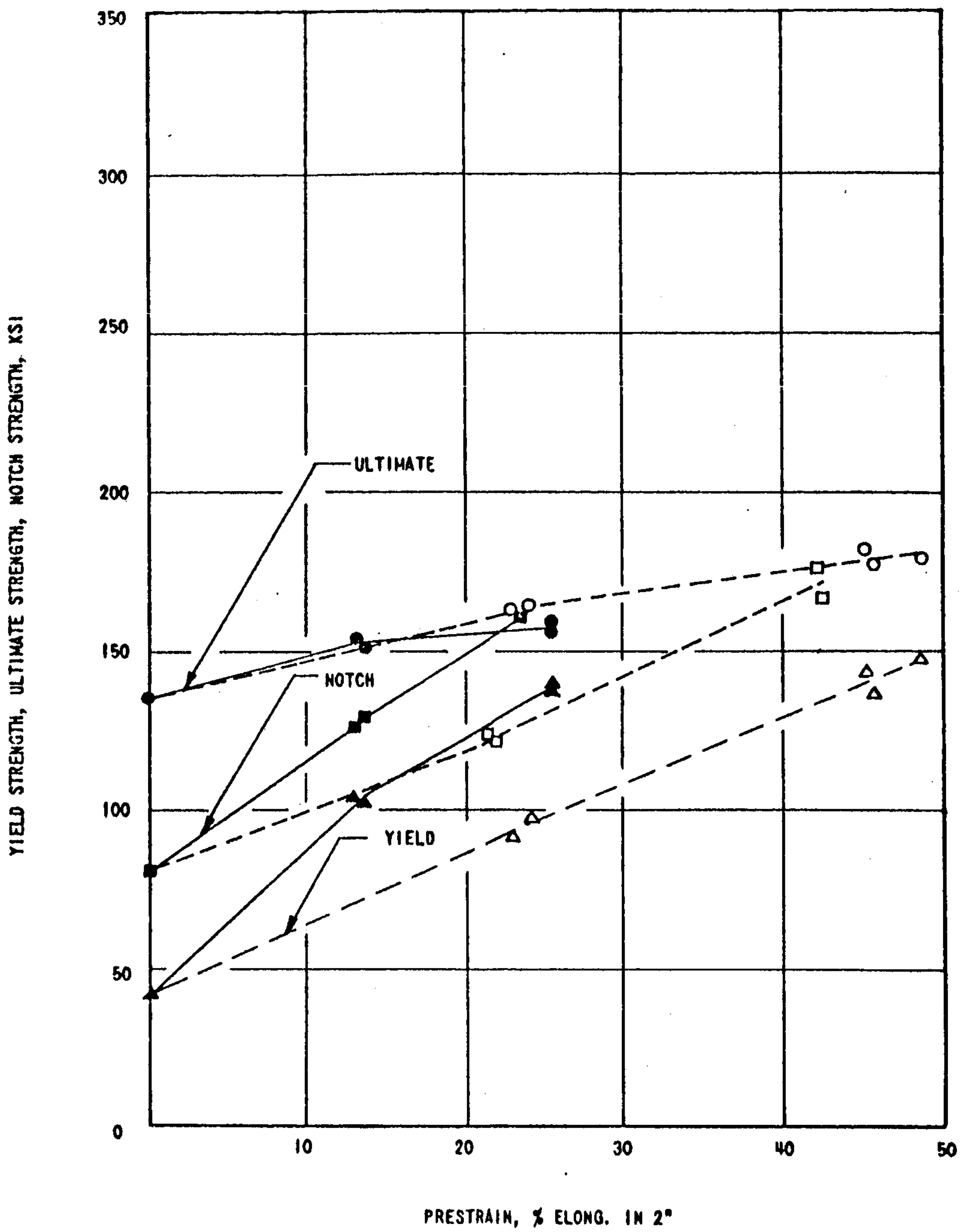

FIGURE 50. MECHANICAL PROPERTIES OF 17-7 PH STAINLESS STEEL AFTER VARIOUS PRESTRAINS AT NOMINAL ROOM TEMPERATURE

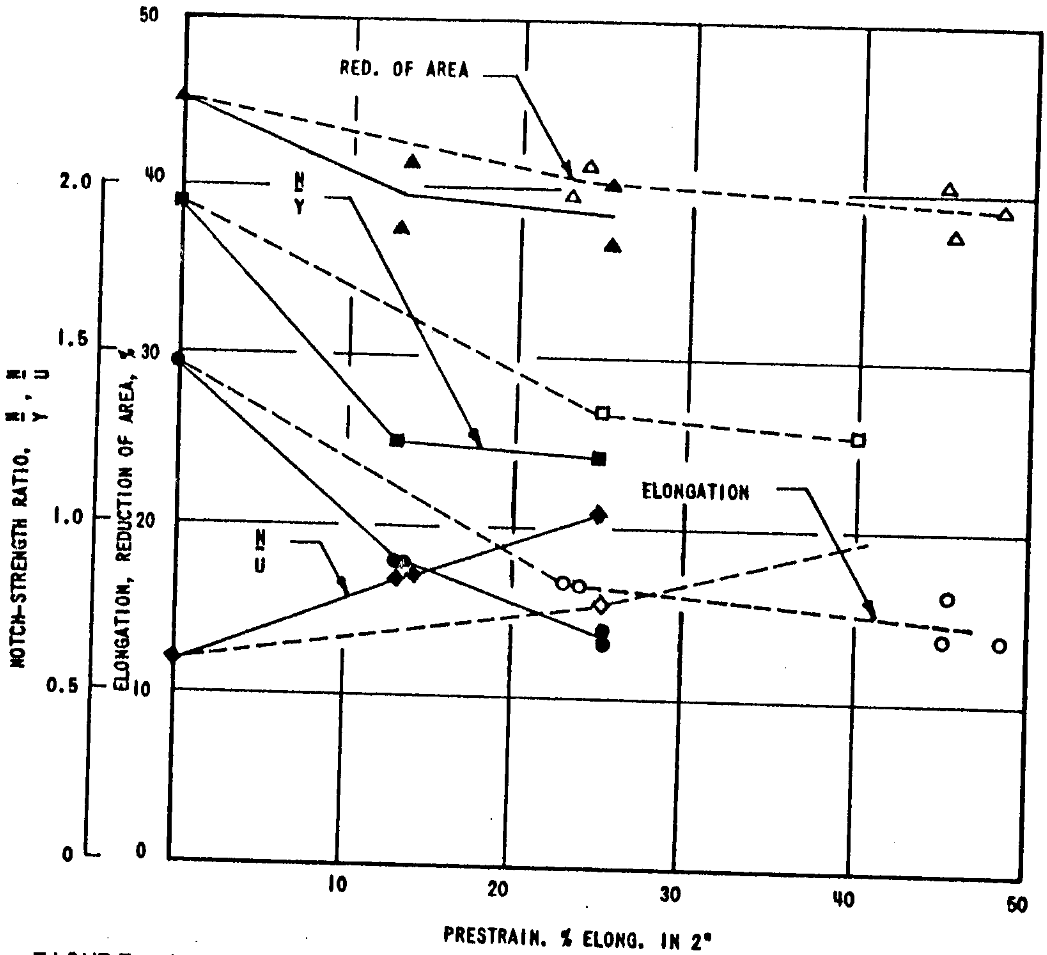

FIGURE 51. MECHANICAL PROPERTIES OF 17-7 PH STAINLESS STEEL AFTER VARIOUS PRESTRAINS AT NOMINAL ROOM TEMPERATURE

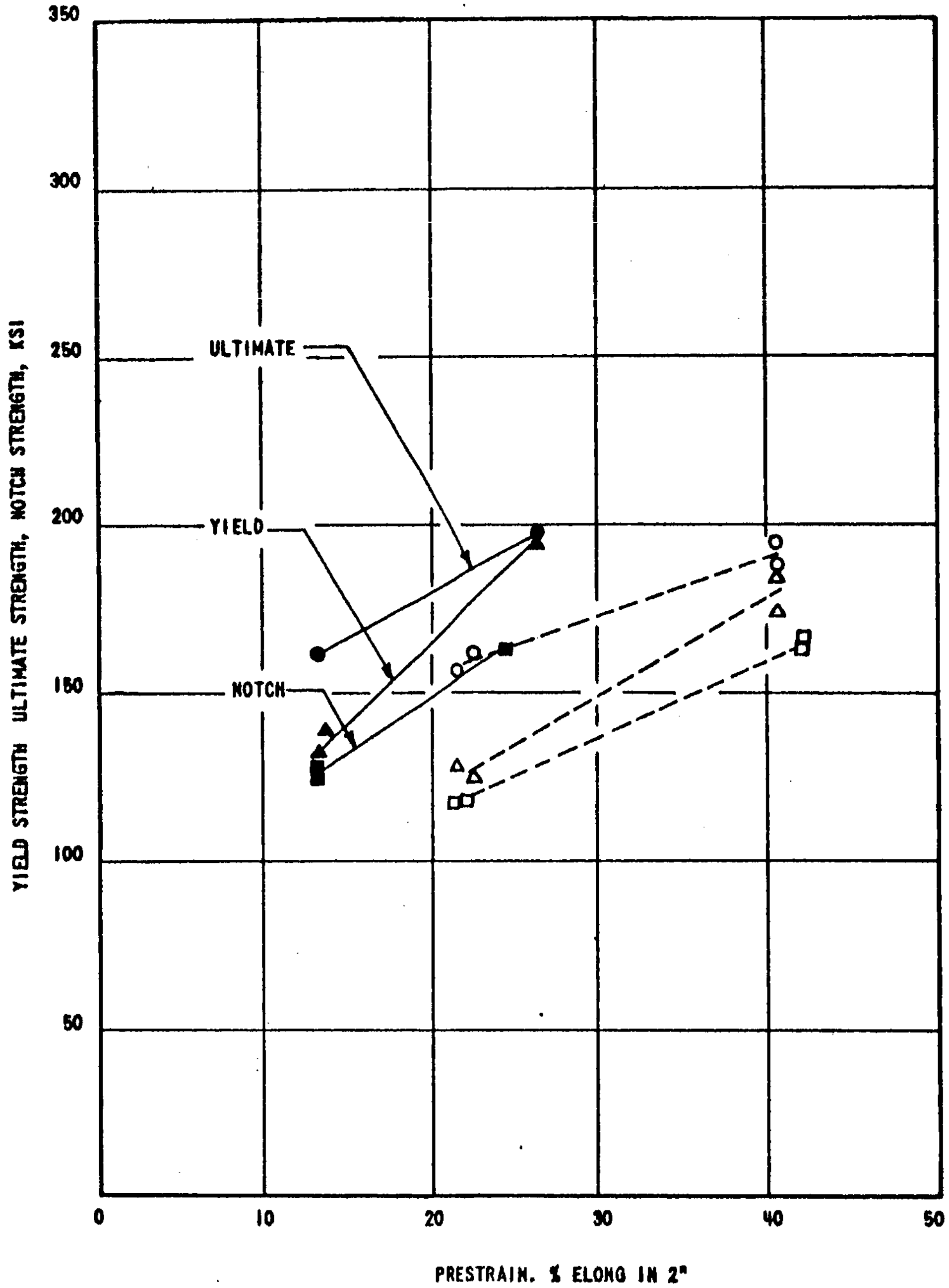

FIGURE 52. MECHANICAL PROPERTIES OF 17-7 PH STAINLESS STEEL AFTER VARIOUS PRESTRAINS AT NOMINAL ROOM TEMPERATURE AND AGING

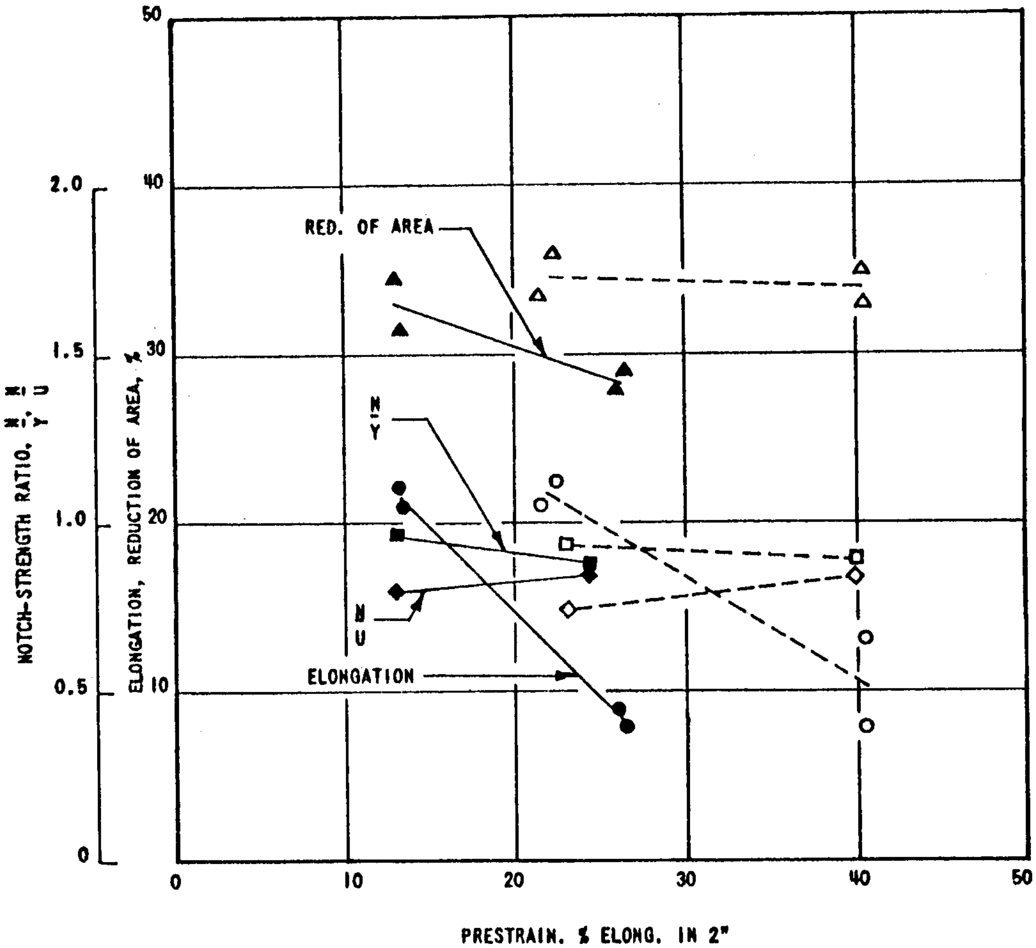

FIGURE 53. MECHANICAL PROPERTIES OF 17-7 PH STAINLESS STEEL AFTER VARIOUS PRESTRAINS AT NOMINAL ROOM TEMPERATURE AND AGING

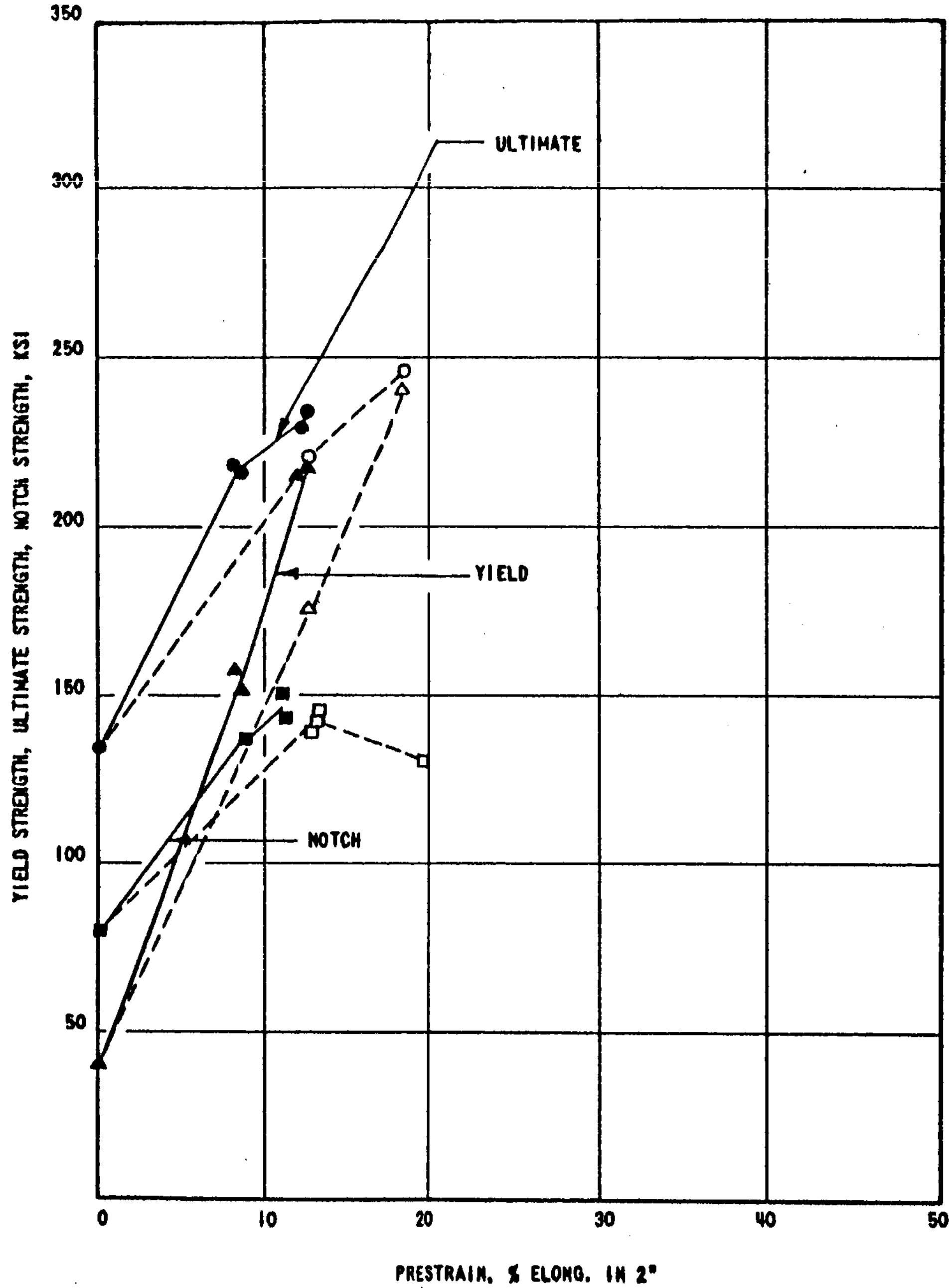

FIGURE 54. MECHANICAL PROPERTIES OF 17-7 PH STAINLESS STEEL AFTER VARIOUS PRESTRAINS AT NOMINAL -320°F

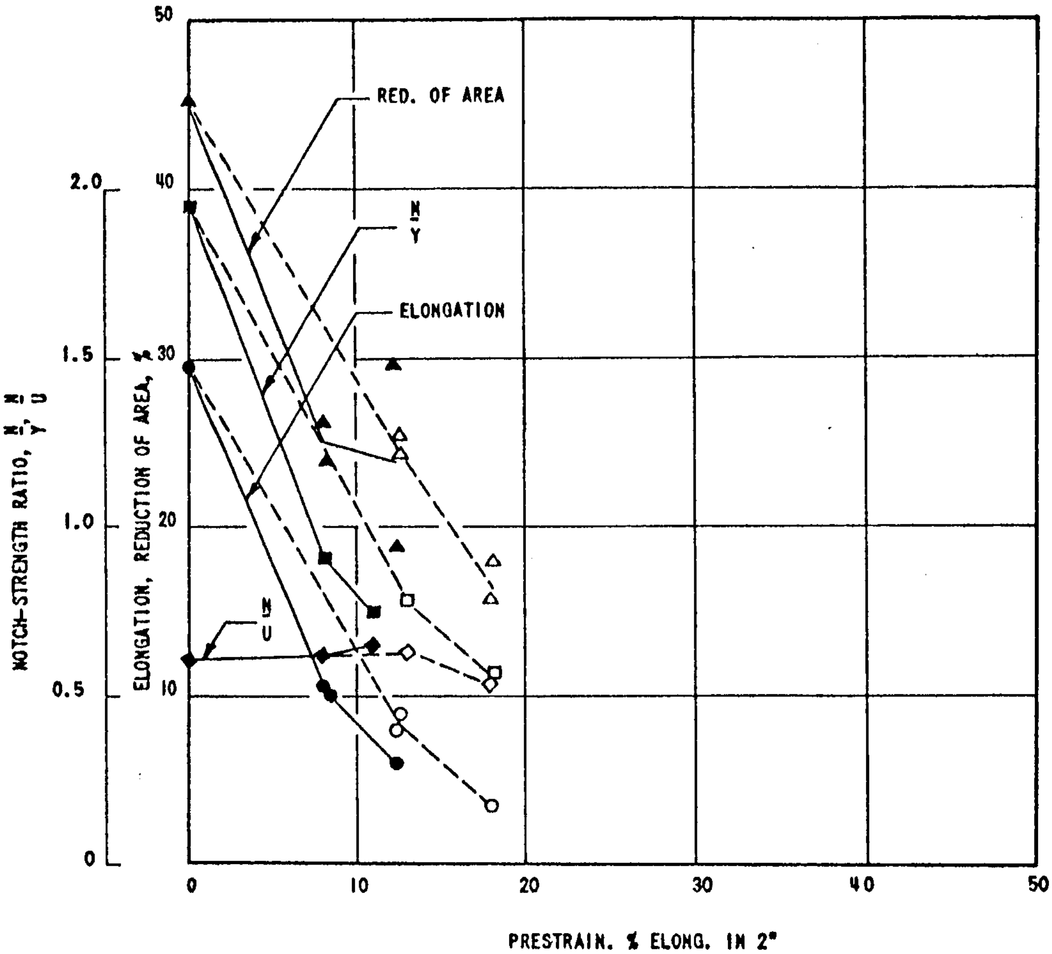

FIGURE 55. MECHANICAL PROPERTIES OF 17-7 PH STAINLESS STEEL AFTER VARIOUS PRESTRAINS AT NOMINAL -320°F

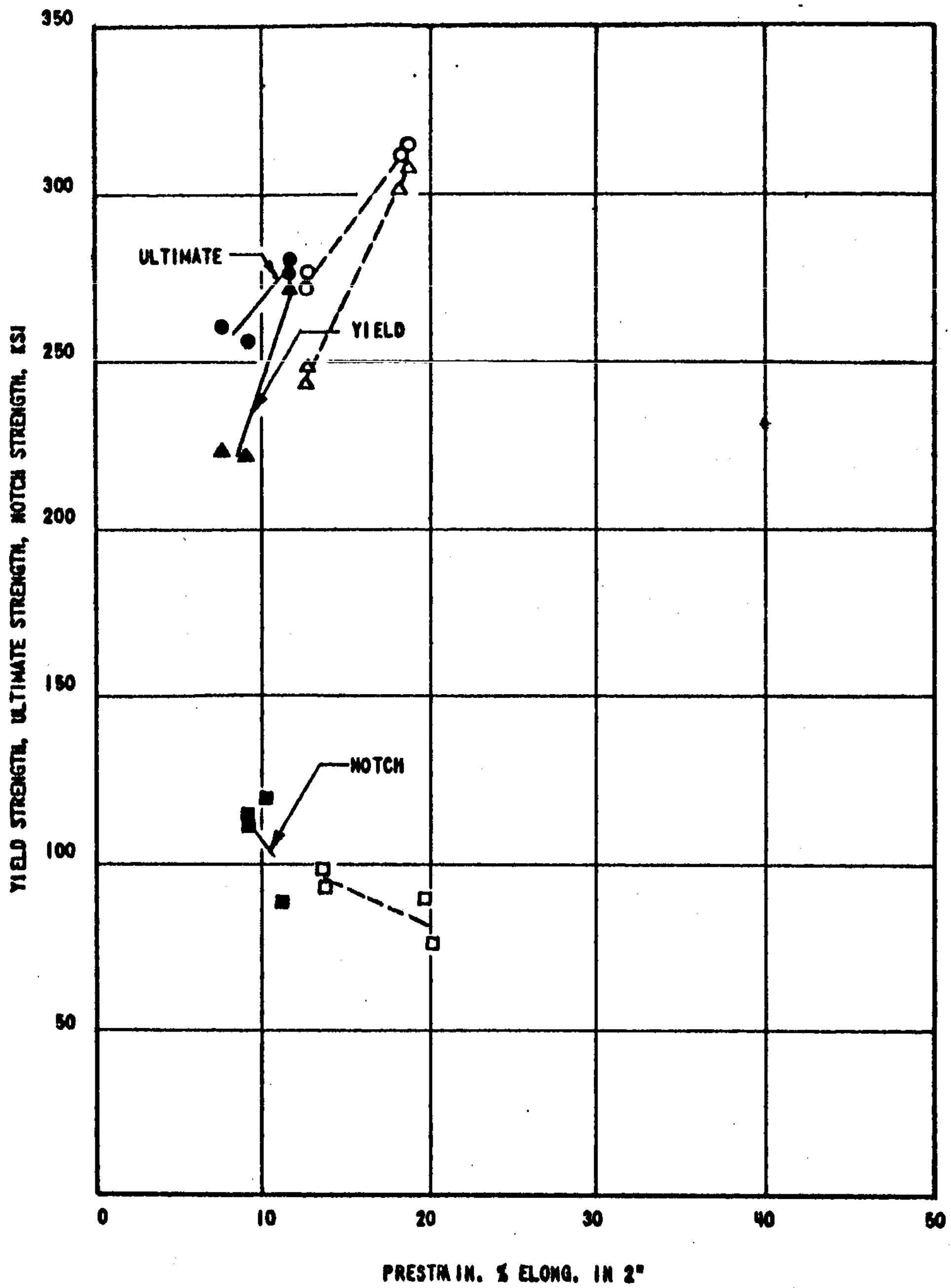

FIGURE 56. MECHANICAL PROPERTIES OF 17-7 PH STAINLESS STEEL AFTER VARIOUS PRESTRAINS AT NOMINAL -320°F AND AGING

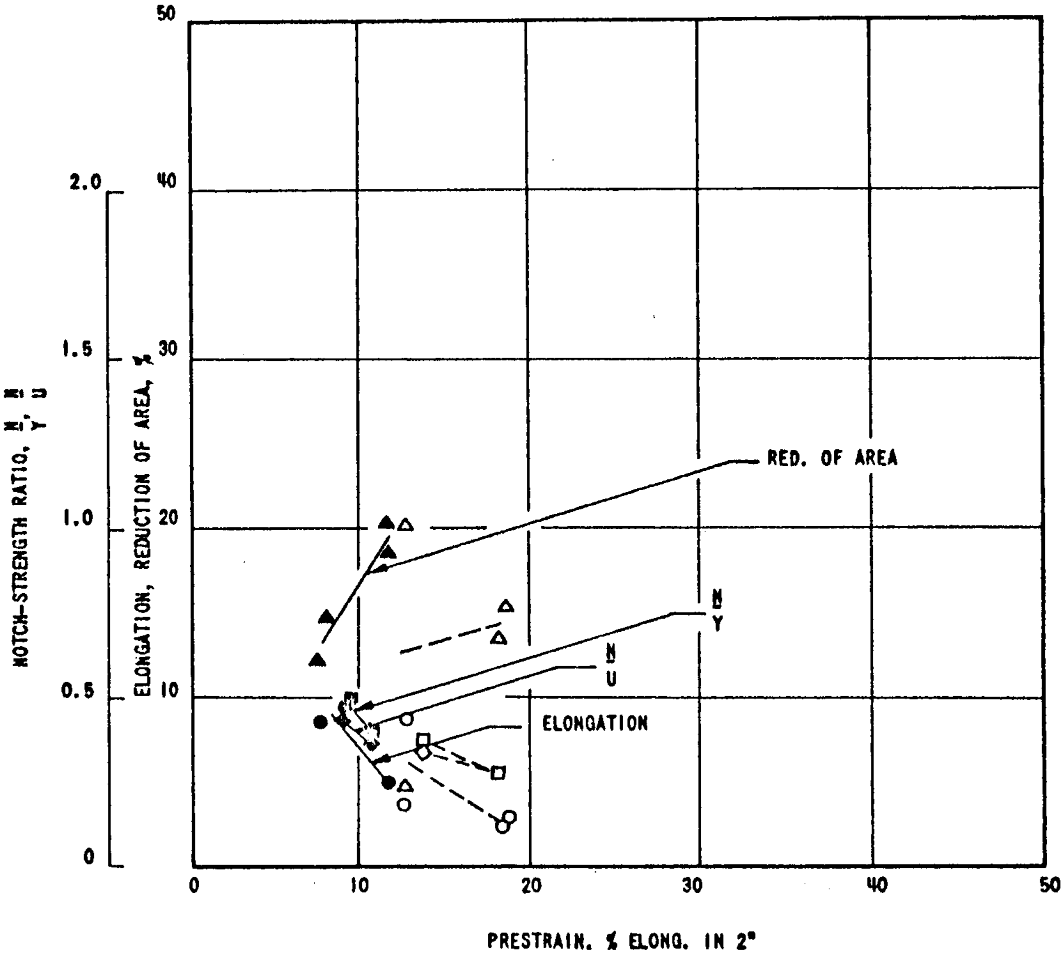

FIGURE 57. MECHANICAL PROPERTIES OF 17-7 PH STAINLESS STEEL AFTER VARIOUS PRESTRAINS AT NOMINAL -320°F AND AGING

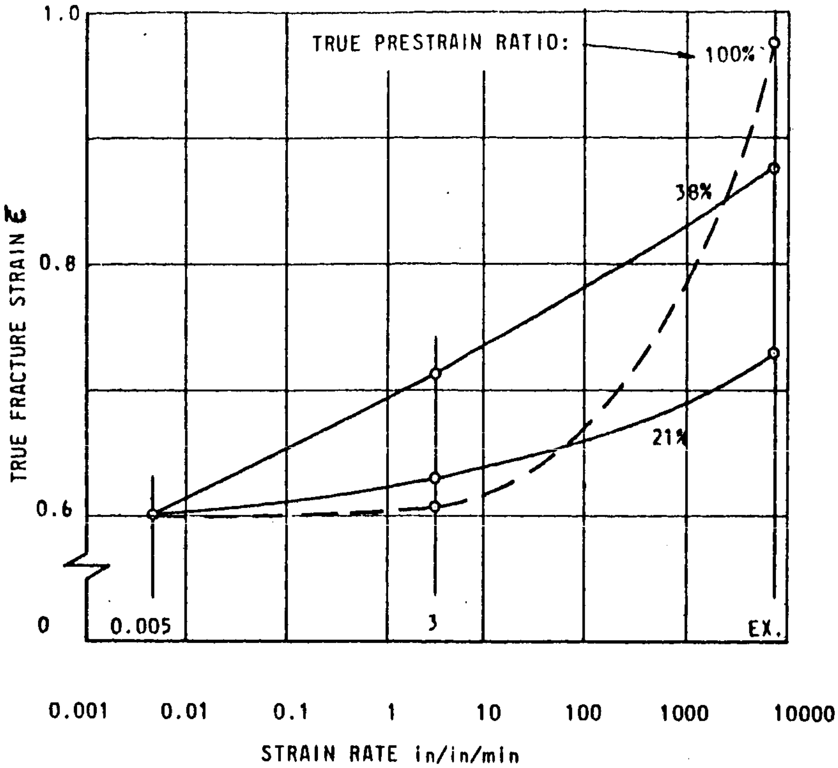

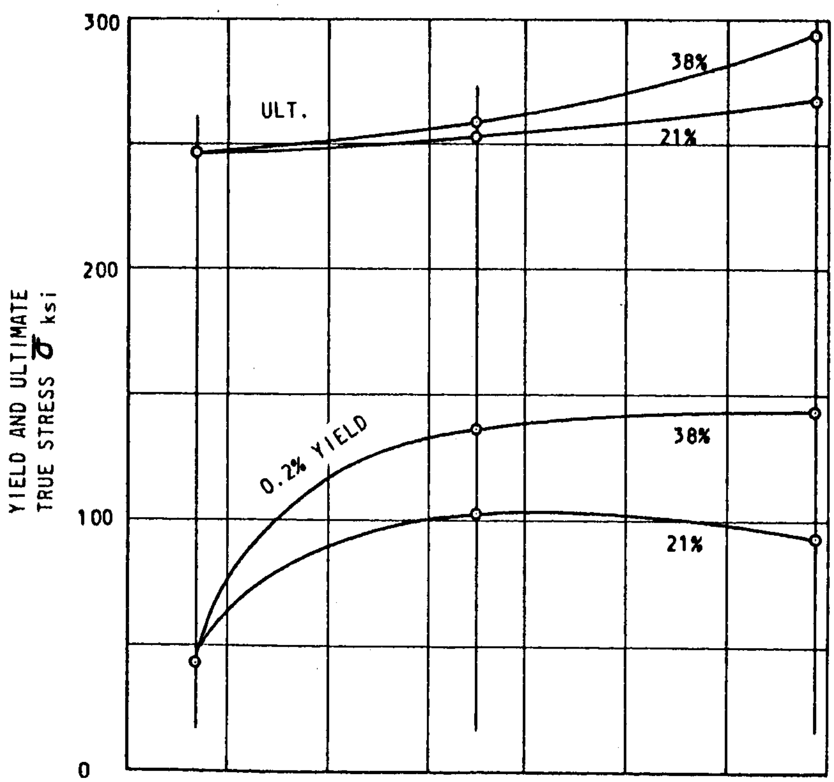

FIGURE 58 TRUE STRESS-STRAIN DATA FOR 17-7 PH STAINLESS STEEL AFTER VARIOUS PRESTRAINS AT NOMINAL ROOM TEMPERATURE

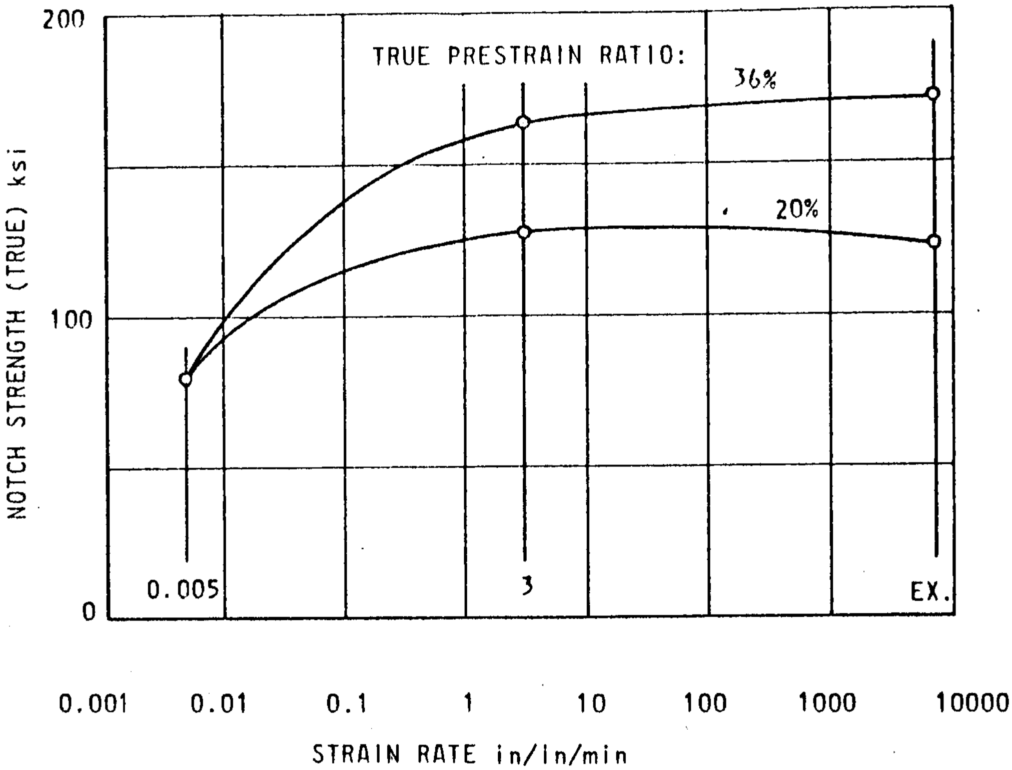

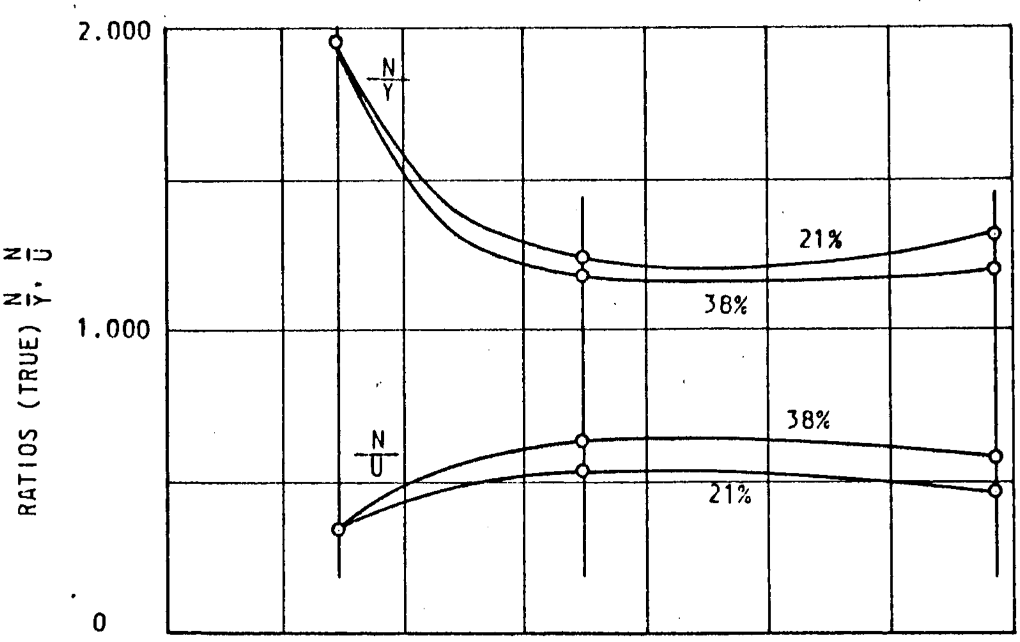

FIGURE 59. NOTCH STRENGTH (TRUE) DATA FOR 17-7 PH STAINLESS STEEL AFTER VARIOUS PRESTRAINS AT NOMINAL ROOM TEMPERATURE

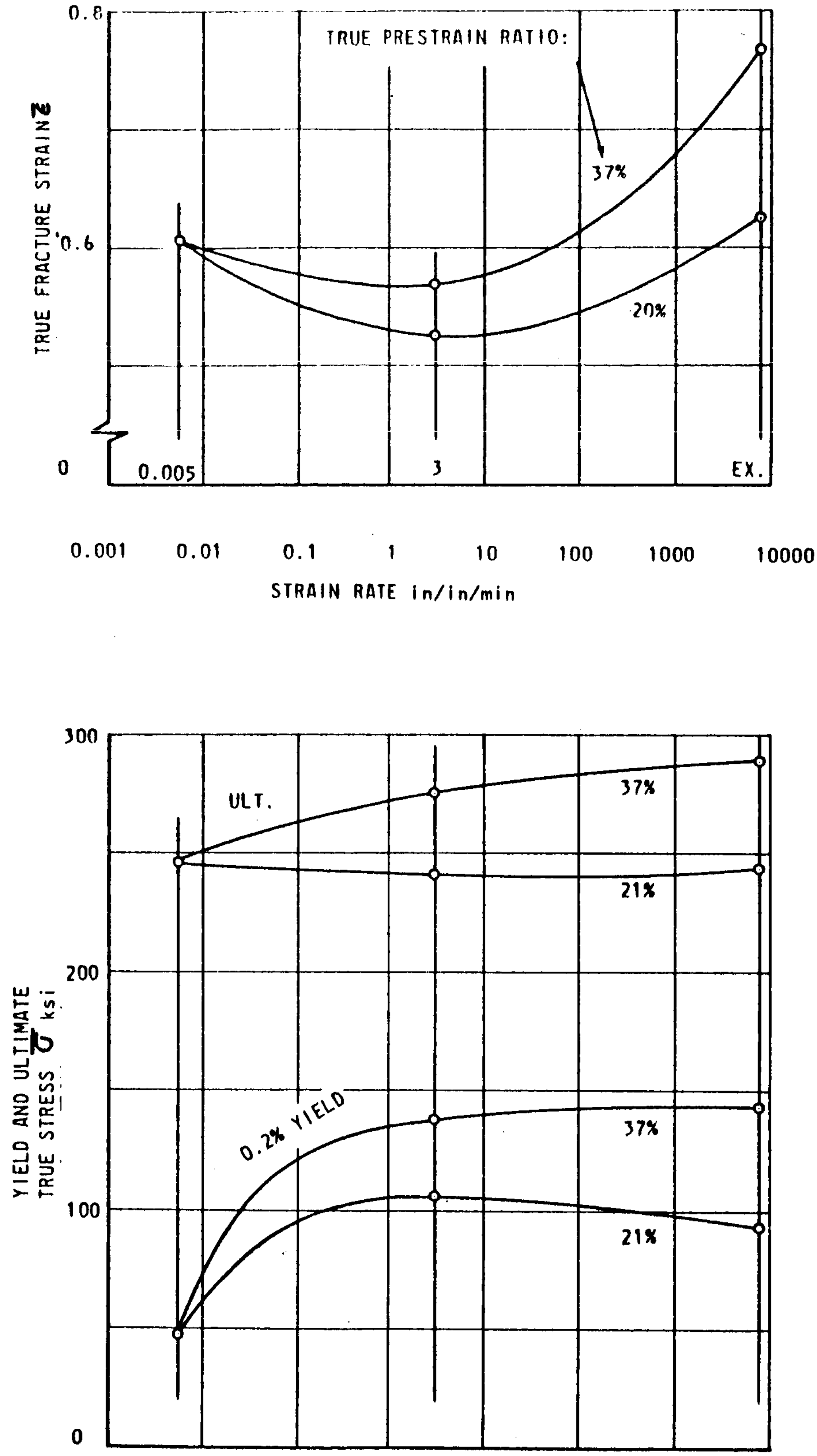

FIGURE 60 TRUE STRESS-STRAIN DATA FOR 17-7 PH STAINLESS STEEL AFTER VARIOUS PRESTRAINS AT NOMINAL ROOM TEMPERATURE AND AGING

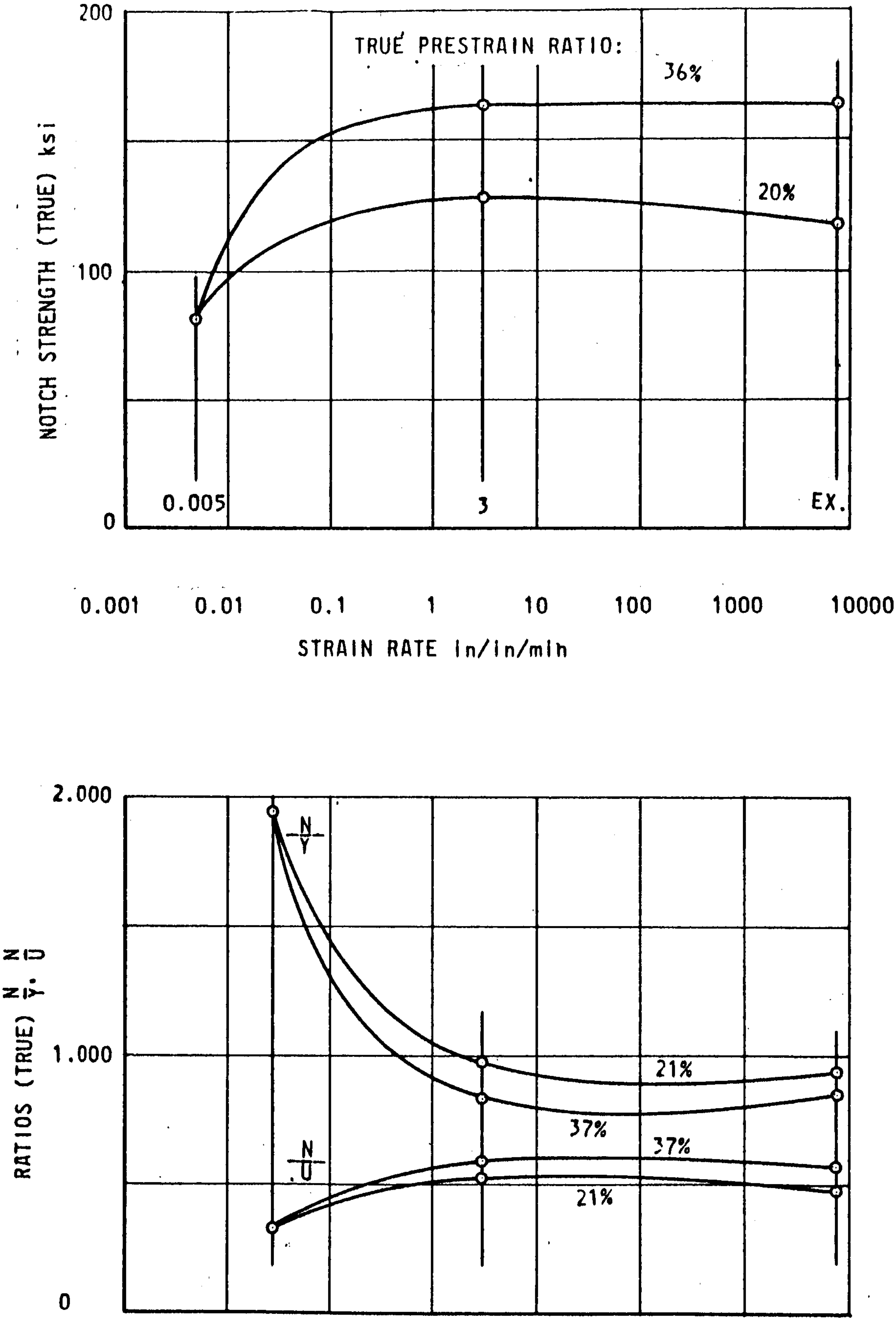

FIGURE 61. NOTCH STRENGTH (TRUE) DATA FOR 17-7 PH STAINLESS STEEL AFTER VARIOUS PRESTRAINS AT NOMINAL ROOM TEMPERATURE AND AGING

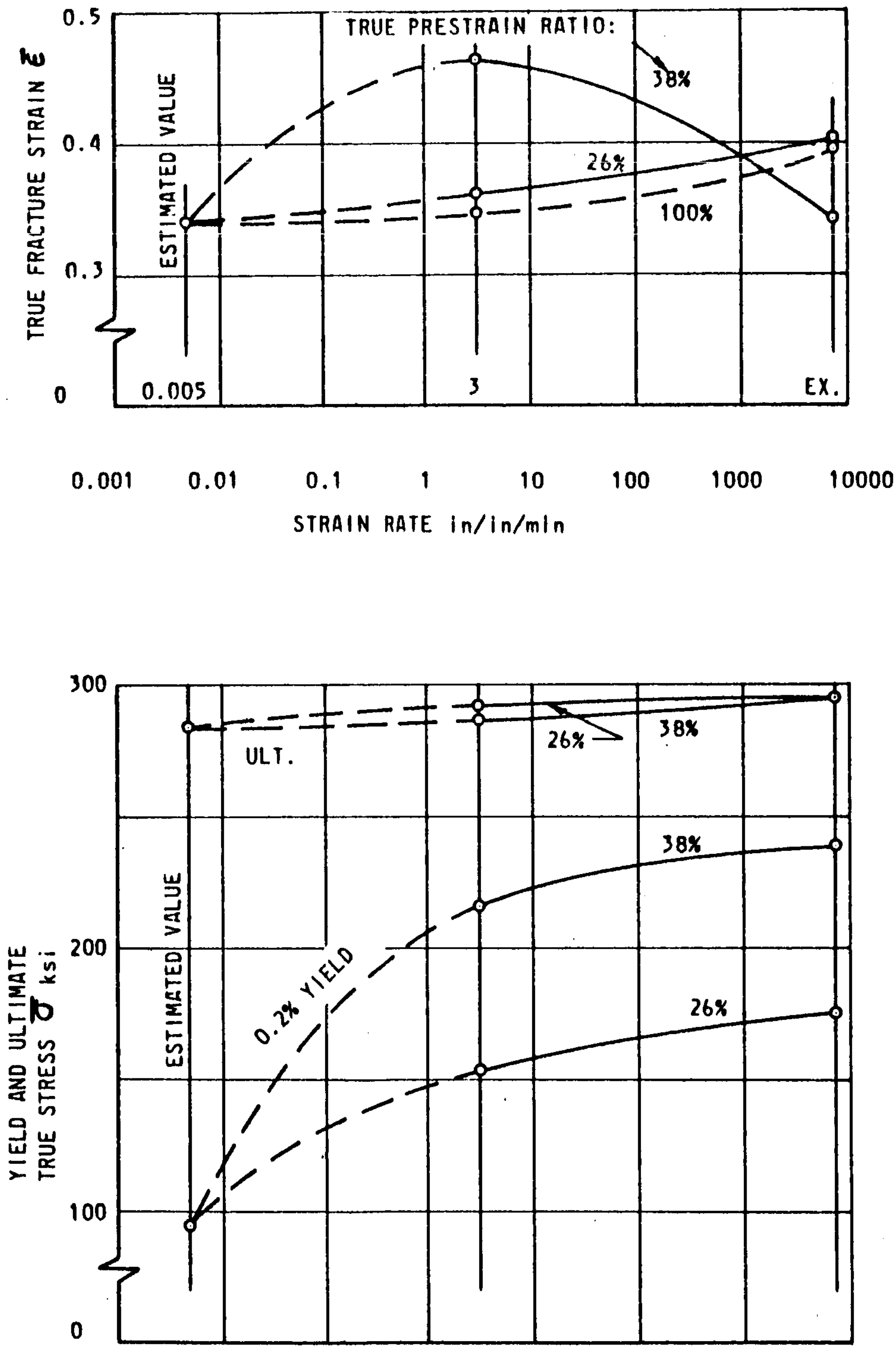

FIGURE 62 TRUE STRESS-STRAIN DATA FOR 17-7 PH STAINLESS STEEL AFTER VARIOUS PRESTRAINS AT NOMINAL -320°F

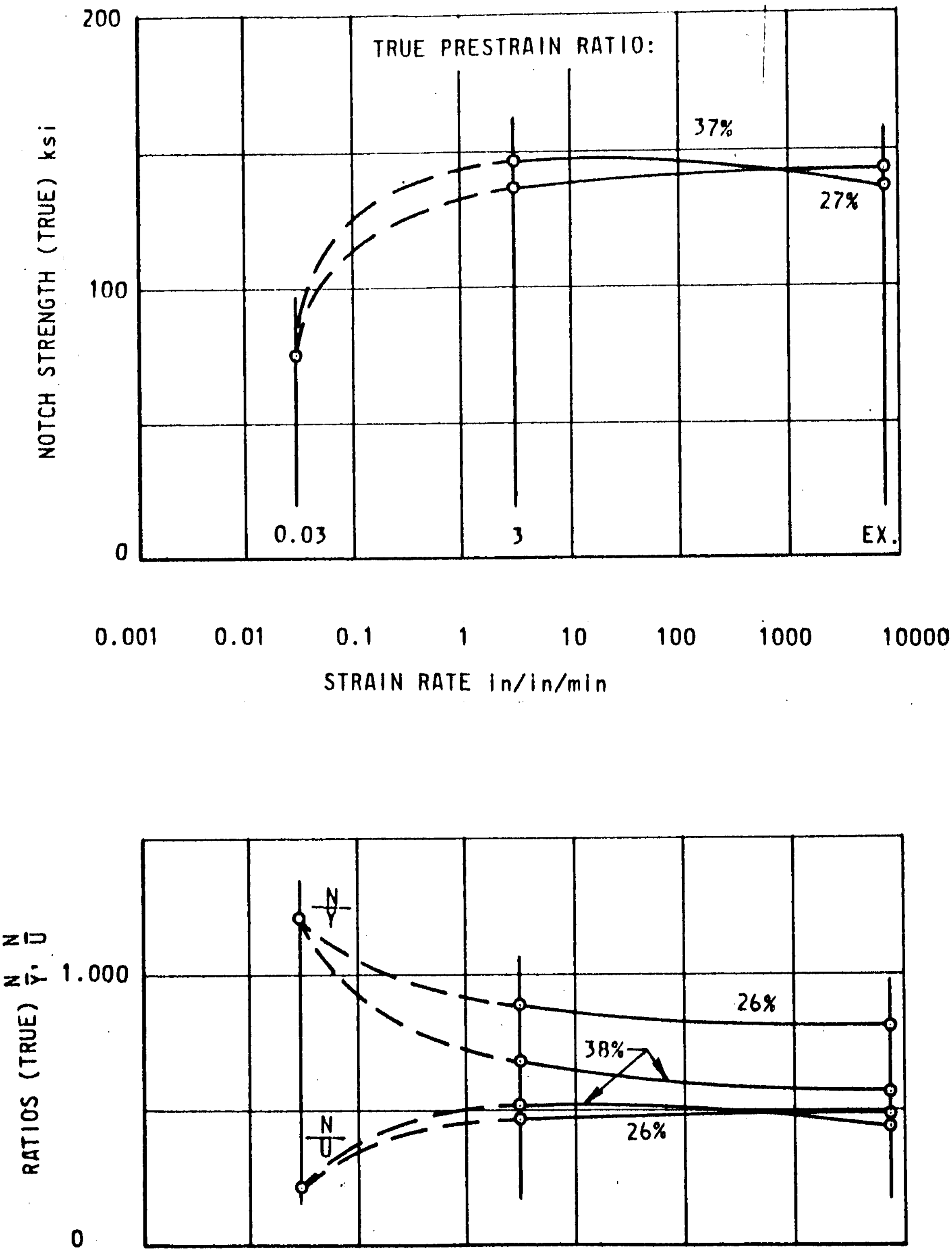

FIGURE 63. NOTCH STRENGTH (TRUE) DATA FOR 17-7 PH STAINLESS STEEL AFTER VARIOUS PRESTRAINS AT NOMINAL -320°F

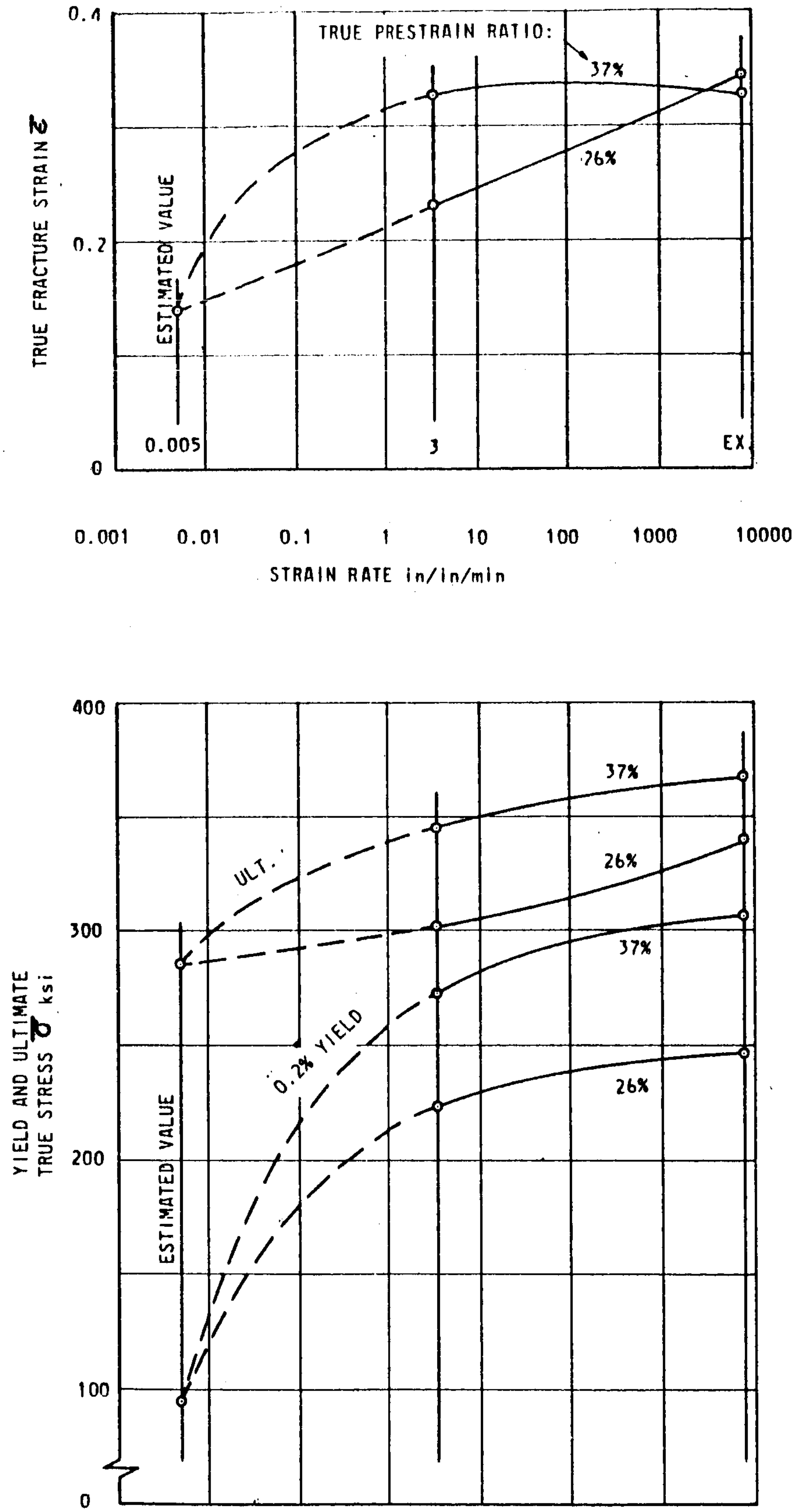

FIGURE 64 TRUE STRESS-STRAIN DATA FOR 17-7 PH STAINLESS STEEL AFTER VARIOUS PRESTRAINS AT NOMINAL -320°F AND AGING

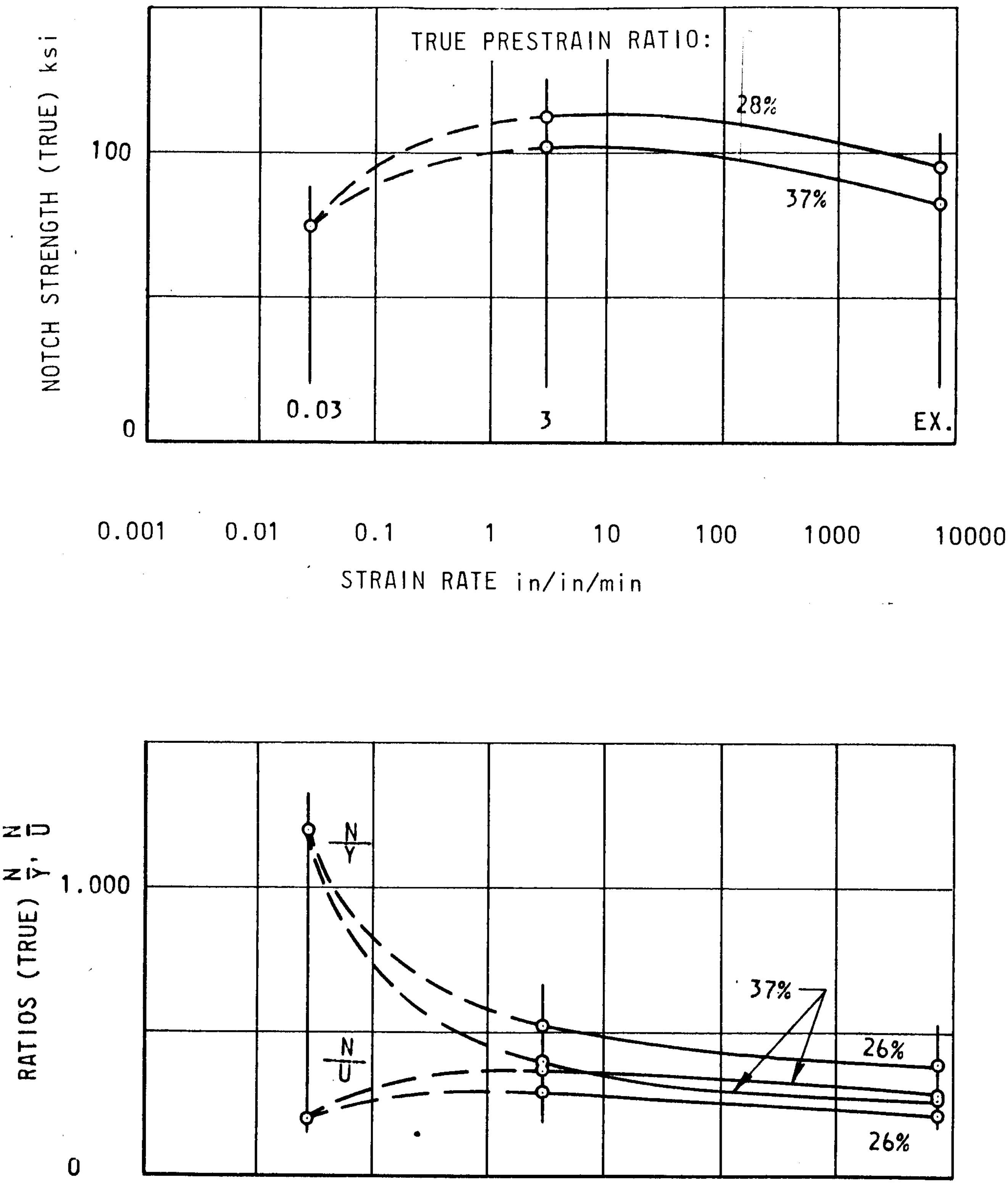

FIGURE 65. NOTCH STRENGTH (TRUE) DATA FOR 17-7 PH STAINLESS STEEL AFTER VARIOUS PRESTRAINS AT NOMINAL -320°F AND AGING

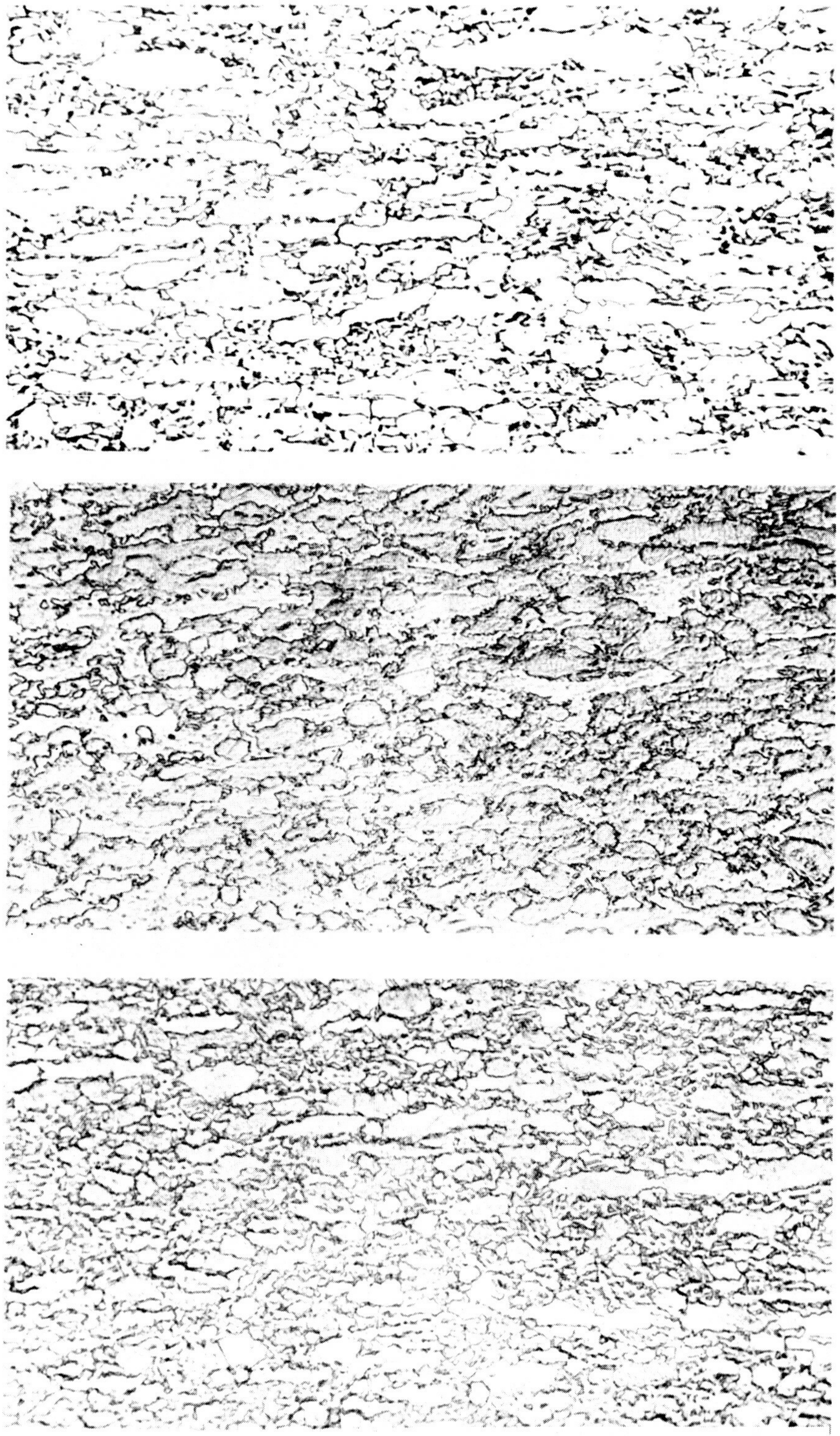

A

B

C

500X

FIGURE 66. 6Al-4V TITANIUM ALLOY
(A) AS RECEIVED (UNSTRAINED)
(B) STRAINED AT 3 in/in/min AT NOMINAL ROOM TEMPERATURE TO NOMINAL 60% OF FRACTURE STRAIN
(C) STRAINED EXPLOSIVELY AT NOMINAL ROOM TEMPERATURE TO NOMINAL 60% OF FRACTURE STRAIN KROLL'S ETCH

A

B

500X

FIGURE 67. 6Al-4V TITANIUM ALLOY SOLUTION TREATED
(A) AND AGED (UNSTRAINED)
(B) STRAINED EXPLOSIVELY AT NOMINAL ROOM TEMPERATURE TO NOMINAL 40% OF FRACTURE STRAIN AND AGED

KROLL'S ETCH

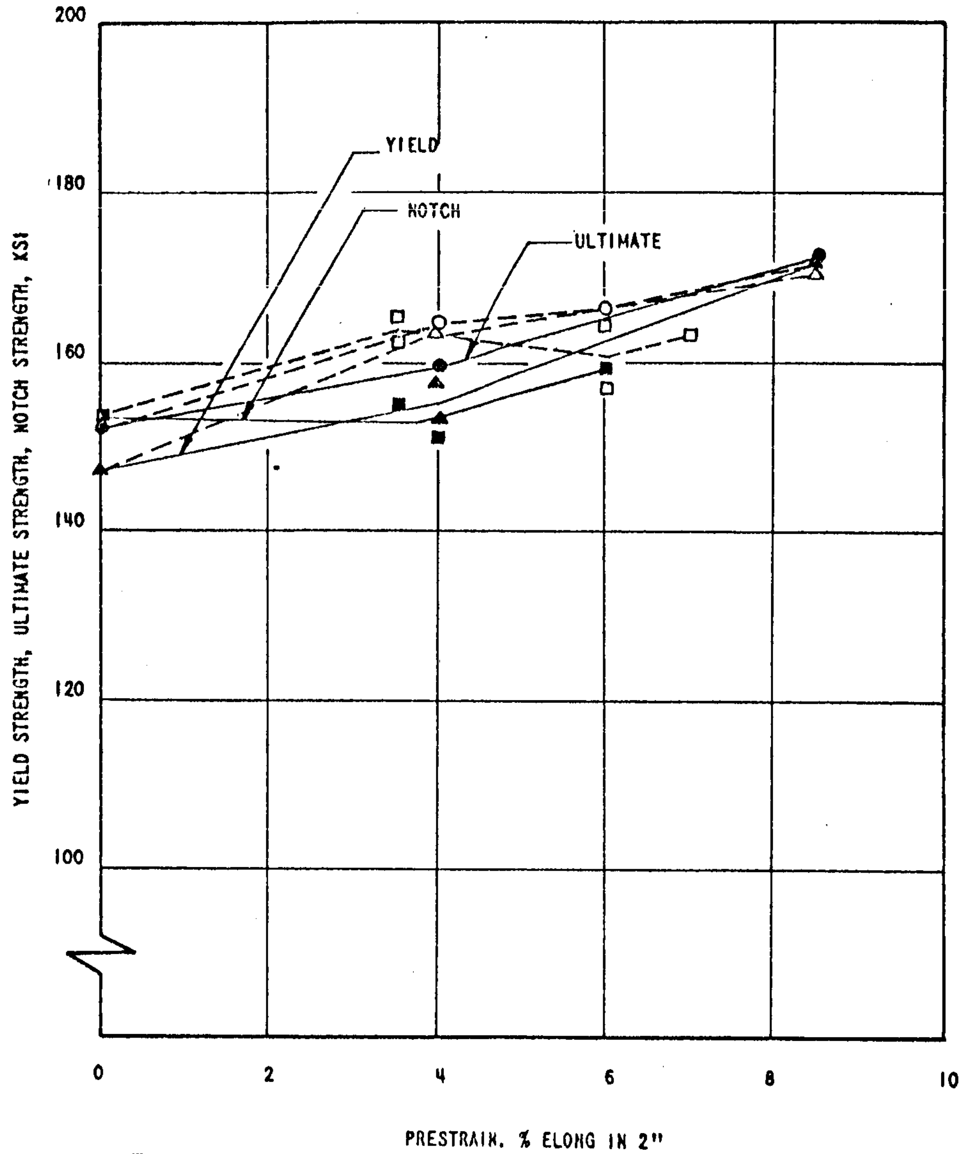

FIGURE 68. MECHANICAL PROPERTIES OF 6Al-4V TITANIUM ALLOY AFTER VARIOUS PRESTRAINS AT NOMINAL ROOM TEMPERATURE

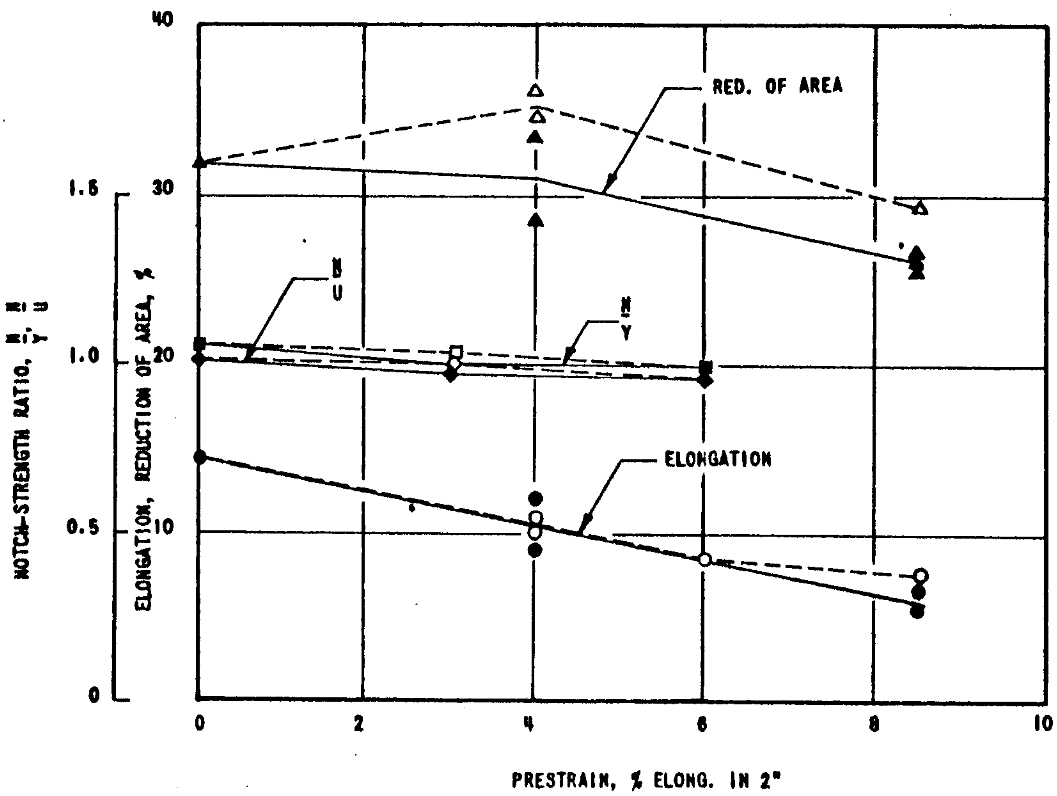

FIGURE 69. MECHANICAL PROPERTIES OF 6Al-4V TITANIUM ALLOY AFTER VARIOUS PRESTRAINS AT NOMINAL ROOM TEMPERATURE

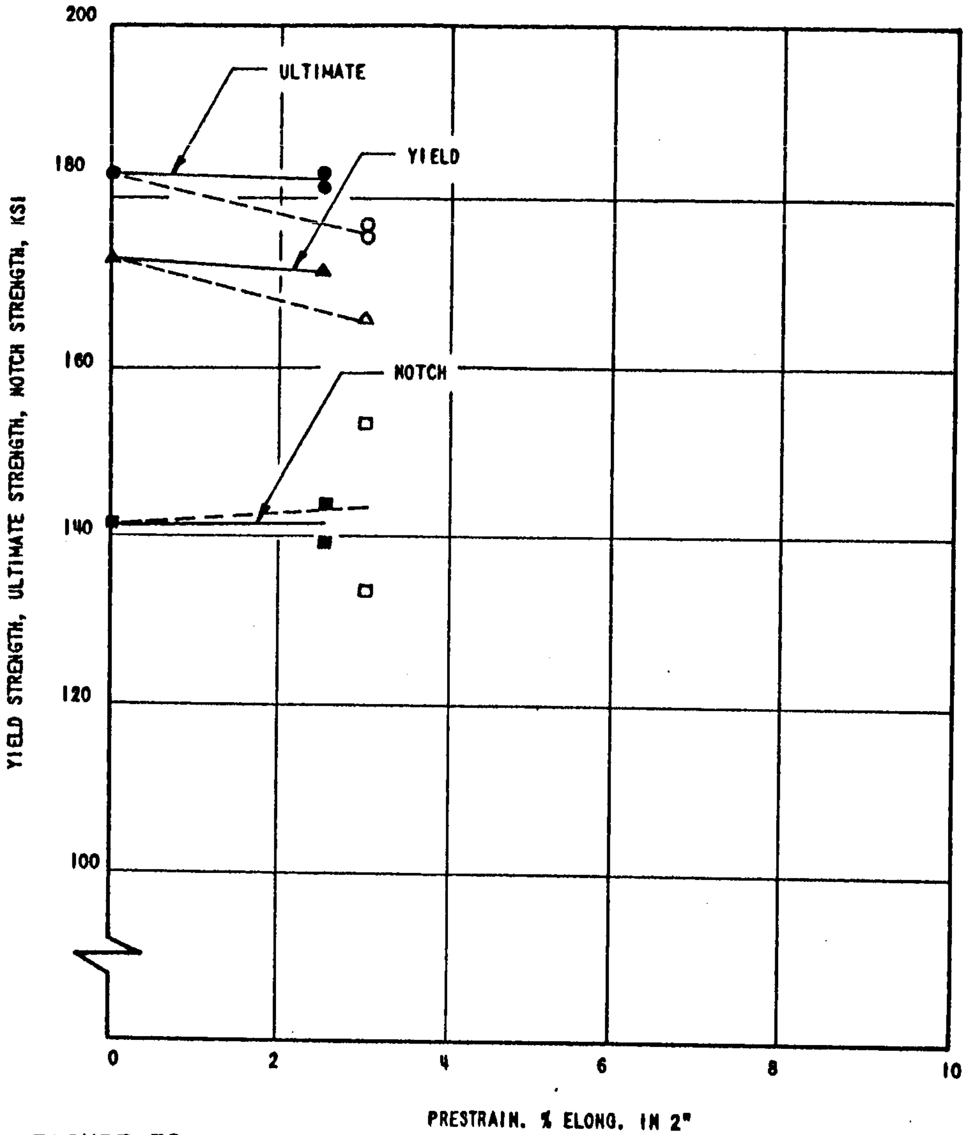

FIGURE 70. MECHANICAL PROPERTIES OF 6Al-4V TITANIUM ALLOY AFTER VARIOUS PRESTRAINS AT NOMINAL ROOM TEMPERATURE AND AGING

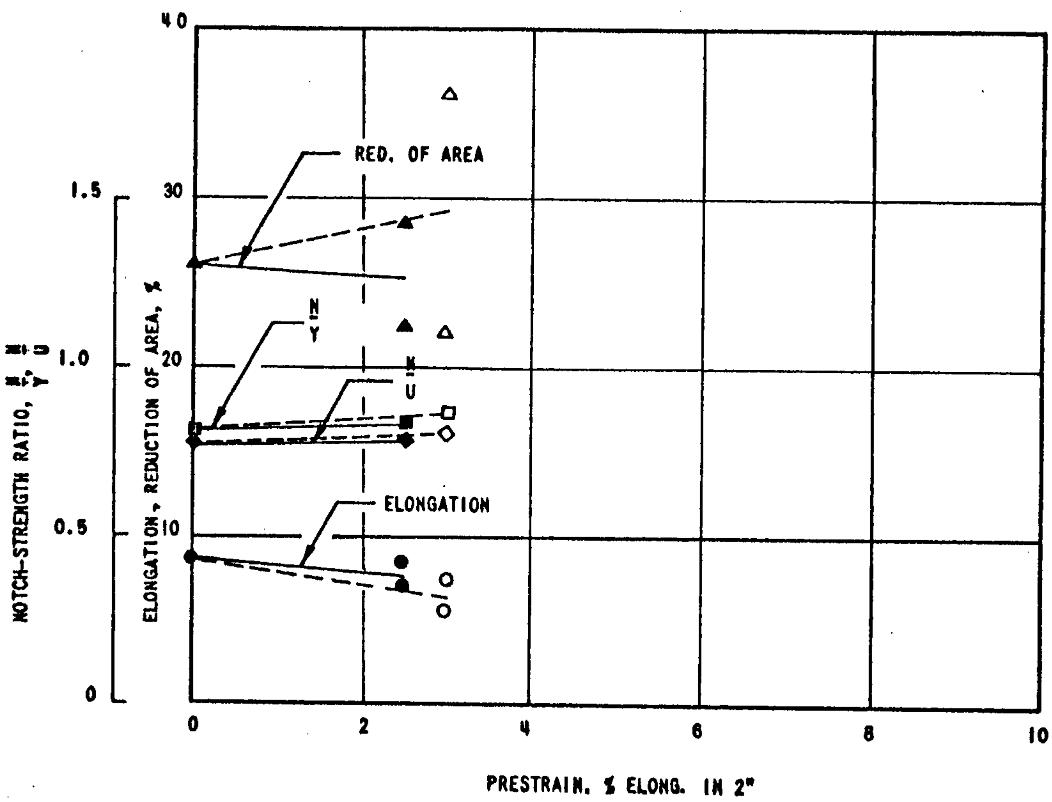

FIGURE 71. MECHANICAL PROPERTIES OF 6Al-4V TITANIUM ALLOY AFTER VARIOUS PRESTRAINS AT NOMINAL ROOM TEMPERATURE AND AGING

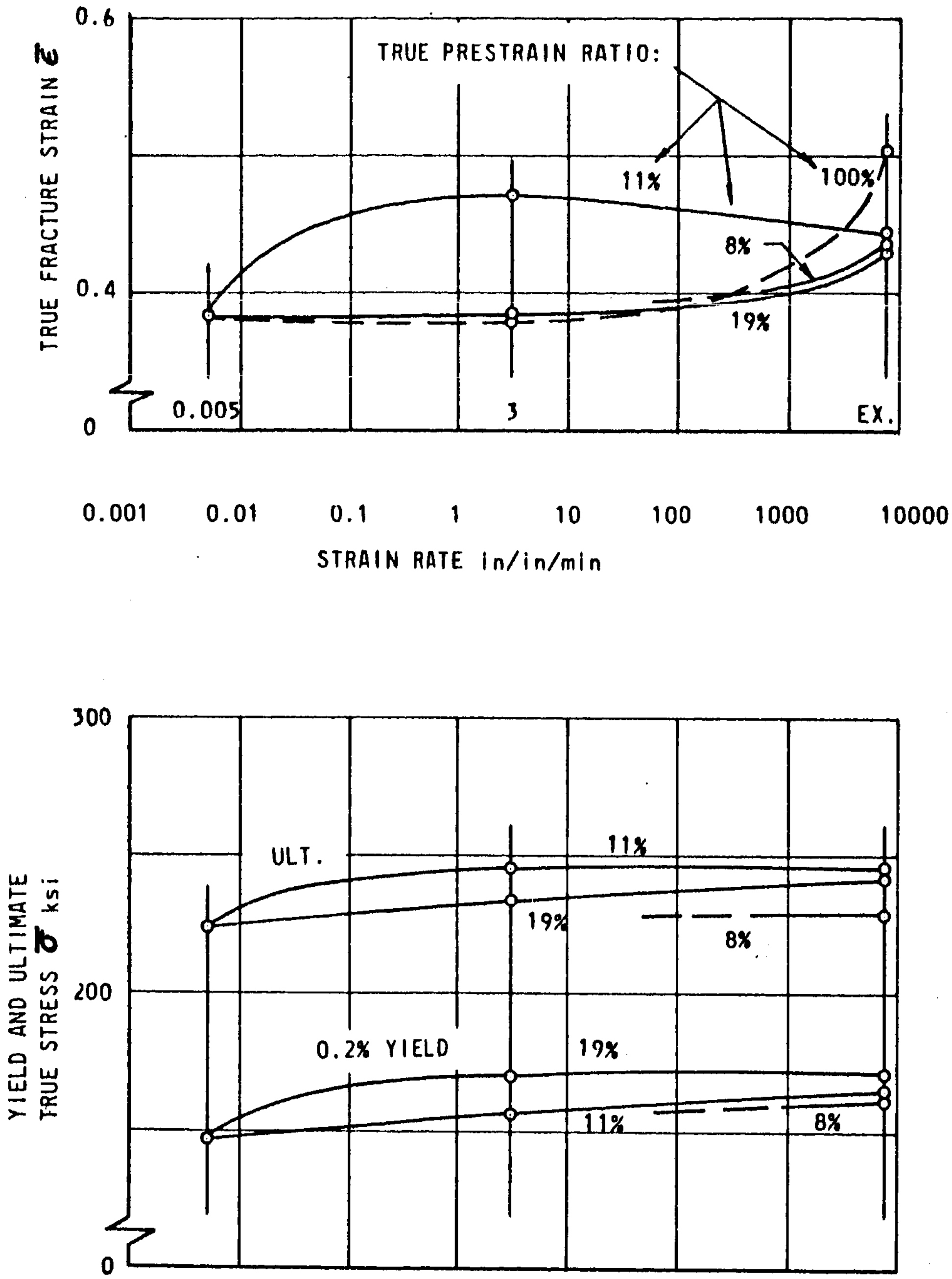

FIGURE 72 TRUE STRESS-STRAIN DATA FOR 6Al-4V TITANIUM AFTER VARIOUS PRESTRAINS AT NOMINAL ROOM TEMPERATURE

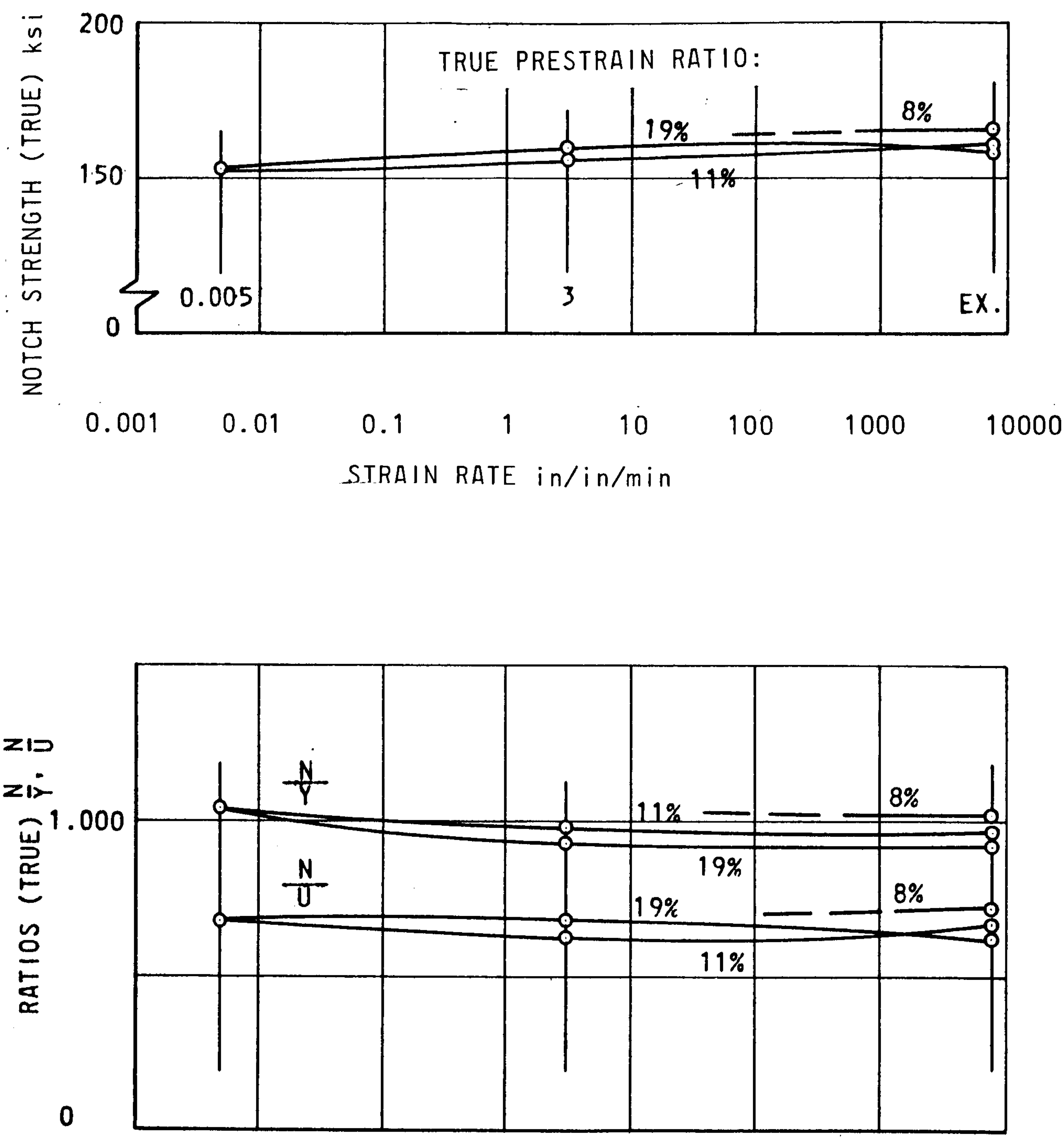

FIGURE 73. NOTCH STRENGTH (TRUE) DATA FOR 6Al-4V TITANIUM AFTER VARIOUS PRESTRAINS AT NOMINAL ROOM TEMPERATURE

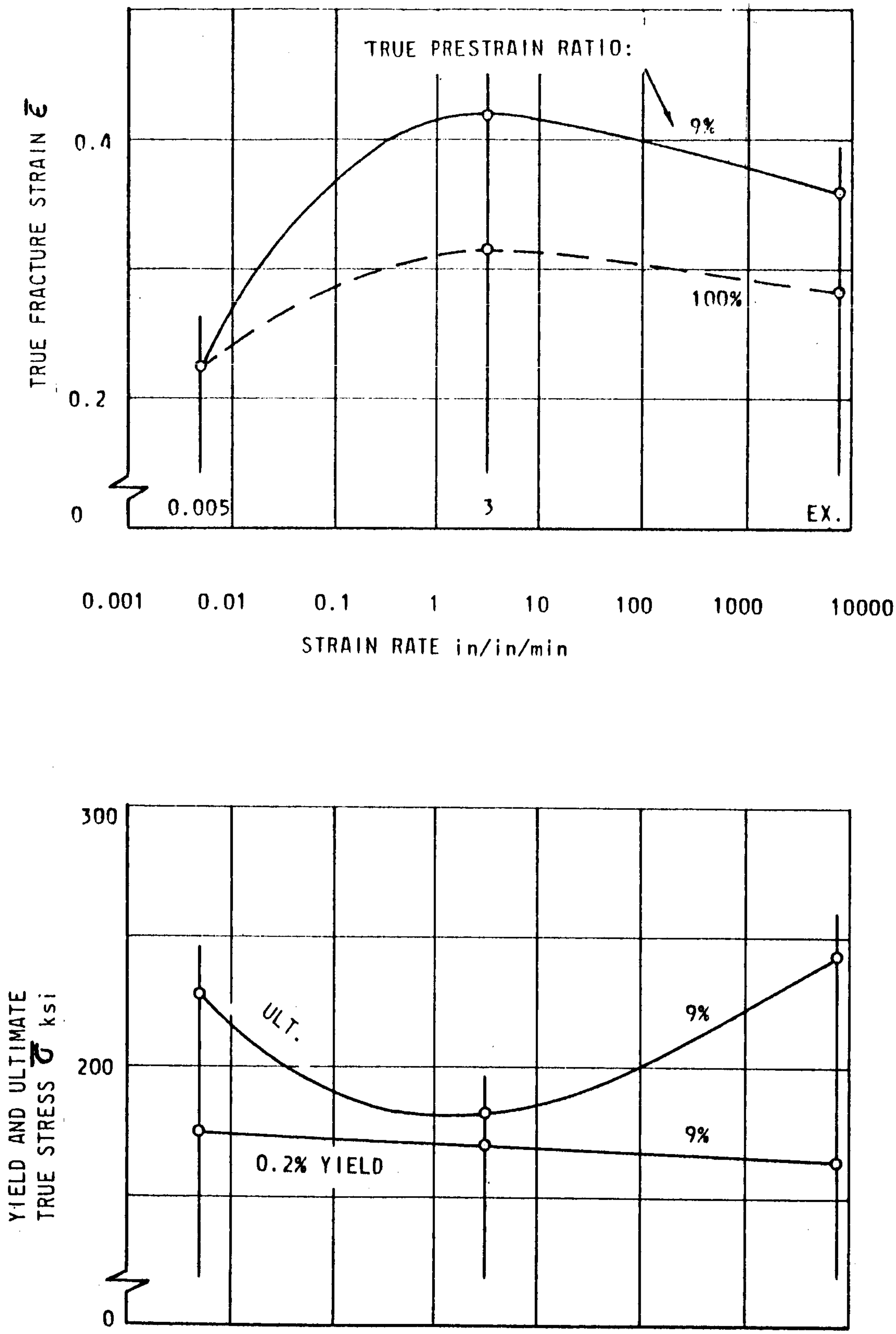

FIGURE 74 TRUE STRESS-STRAIN DATA FOR 6Al-4V TITANIUM AFTER VARIOUS PRESTRAINS AT NOMINAL ROOM TEMPERATURE AND AGING

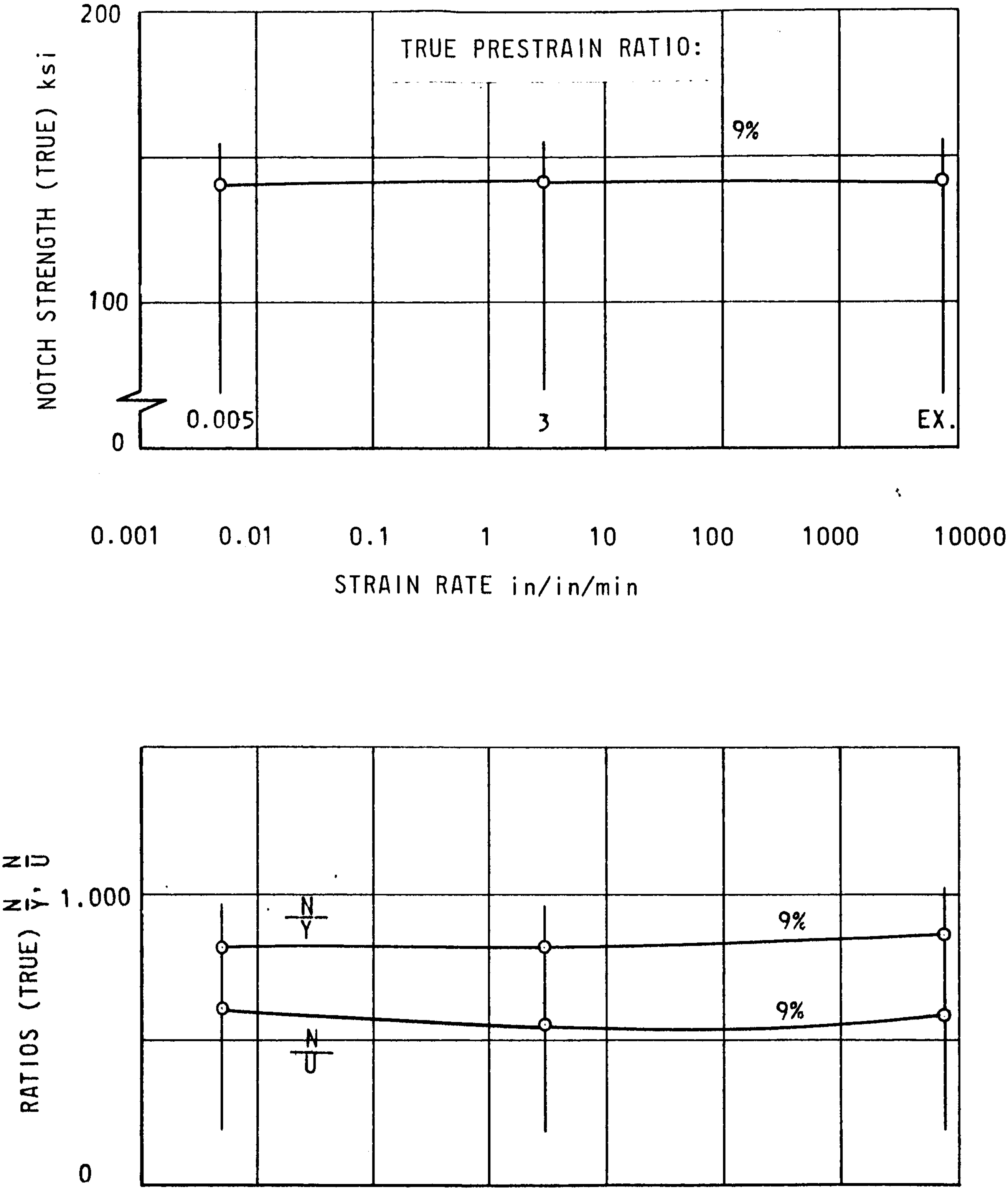

FIGURE 75. NOTCH STRENGTH (TRUE) DATA FOR 6Al-4V TITANIUM AFTER VARIOUS PRESTRAINS AT NOMINAL ROOM TEMPERATURE AND AGING

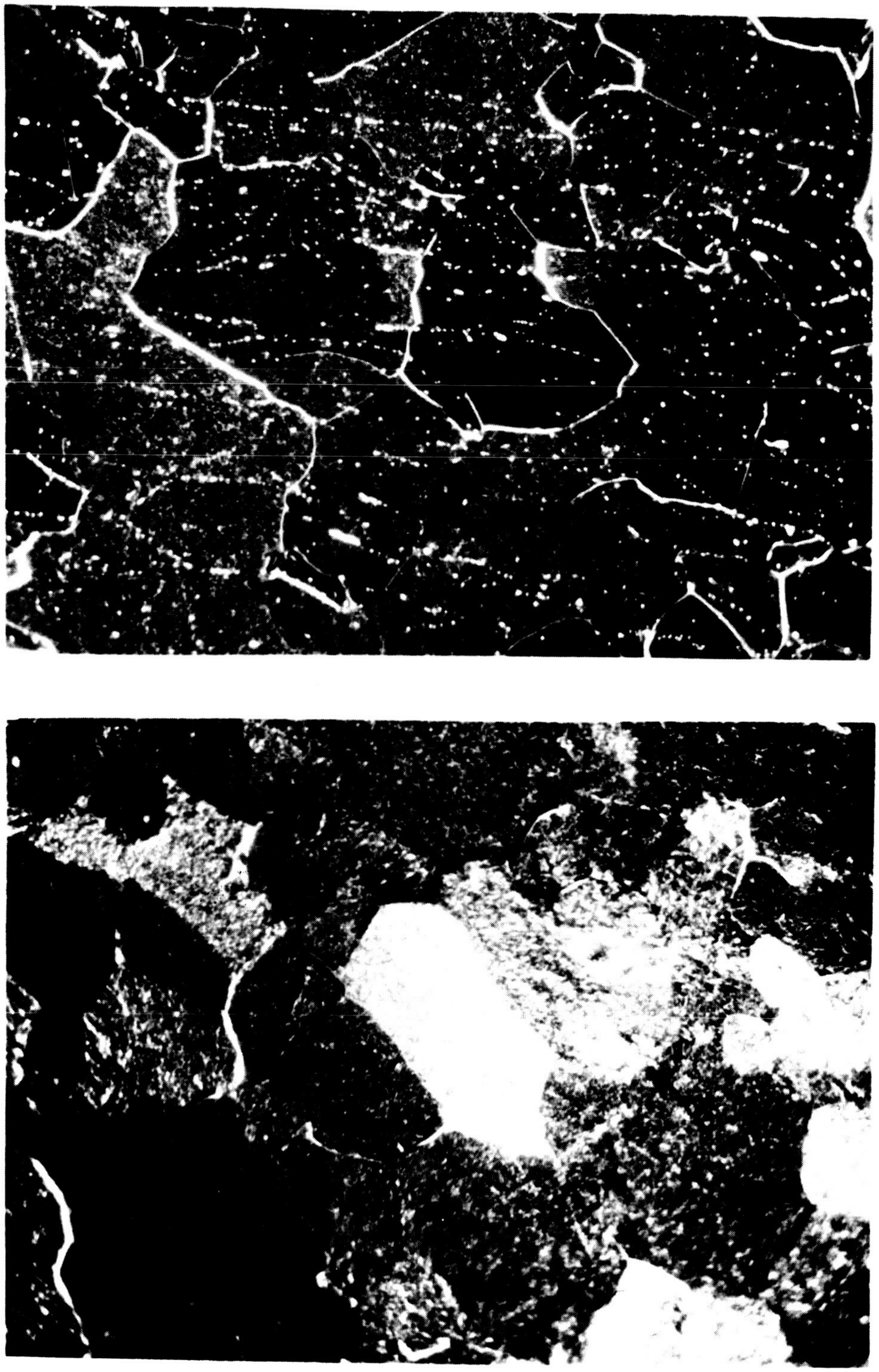

A

B

DARK-FIELD ILLUMINATION 250X

FIGURE 76. 13V-11Cr-3Al TITANIUM ALLOY (UNSTRAINED)
(A) AS RECEIVED
(B) AS RECEIVED AND AGED KROLL'S ETCH

A

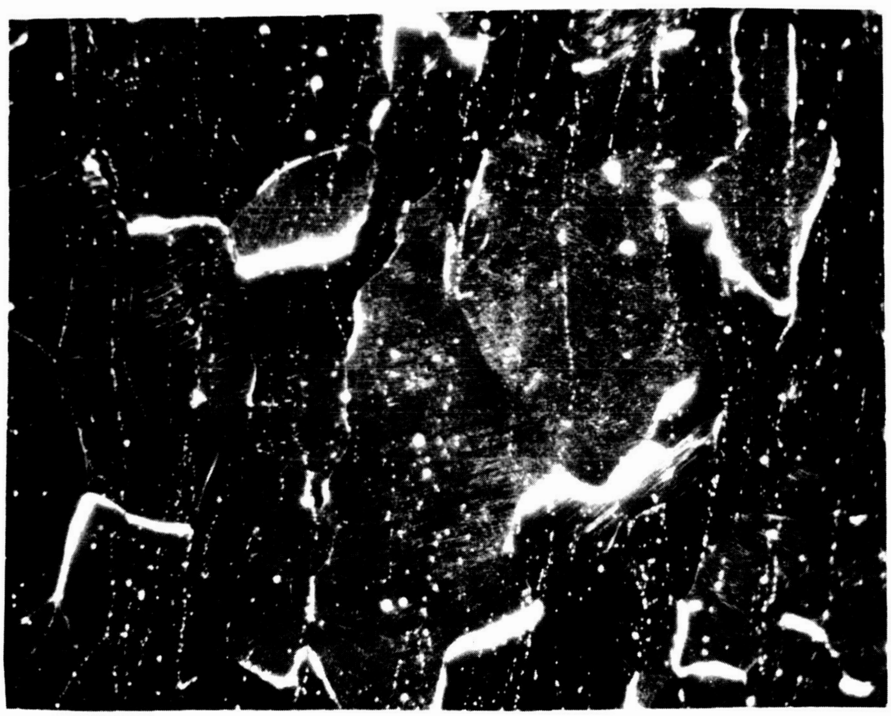

B

DARK-FIELD ILLUMINATION 250X

FIGURE 77. 13V-11Cr-3Al TITANIUM ALLOY STRAINED AT NOMINAL ROOM TEMPERATURE TO NOMINAL 50% OF FRACTURE STRAIN
(A) AT 3 in/in/min
(B) EXPLOSIVELY KROLL'S ETCH

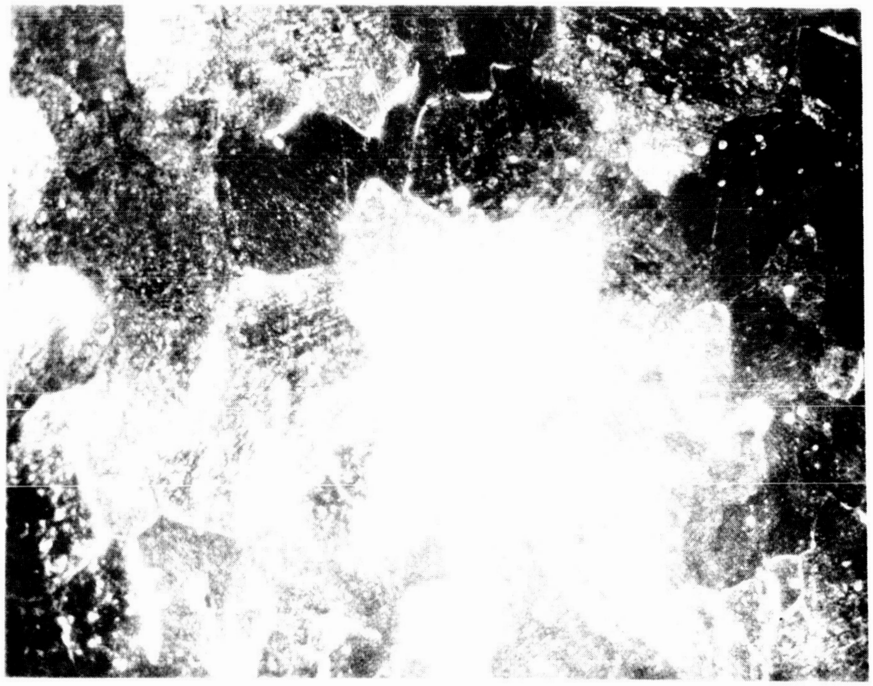

A

B

DARK-FIELD ILLUMINATION 250X

FIGURE 78. 13V-11Cr-3Al TITANIUM ALLOY STRAINED AT NOMINAL ROOM TEMPERATURE TO NOMINAL 50% OF FRACTURE STRAIN
(A) AT 3 in/in/min AND AGED
(B) EXPLOSIVELY AND AGED KROLL'S ETCH

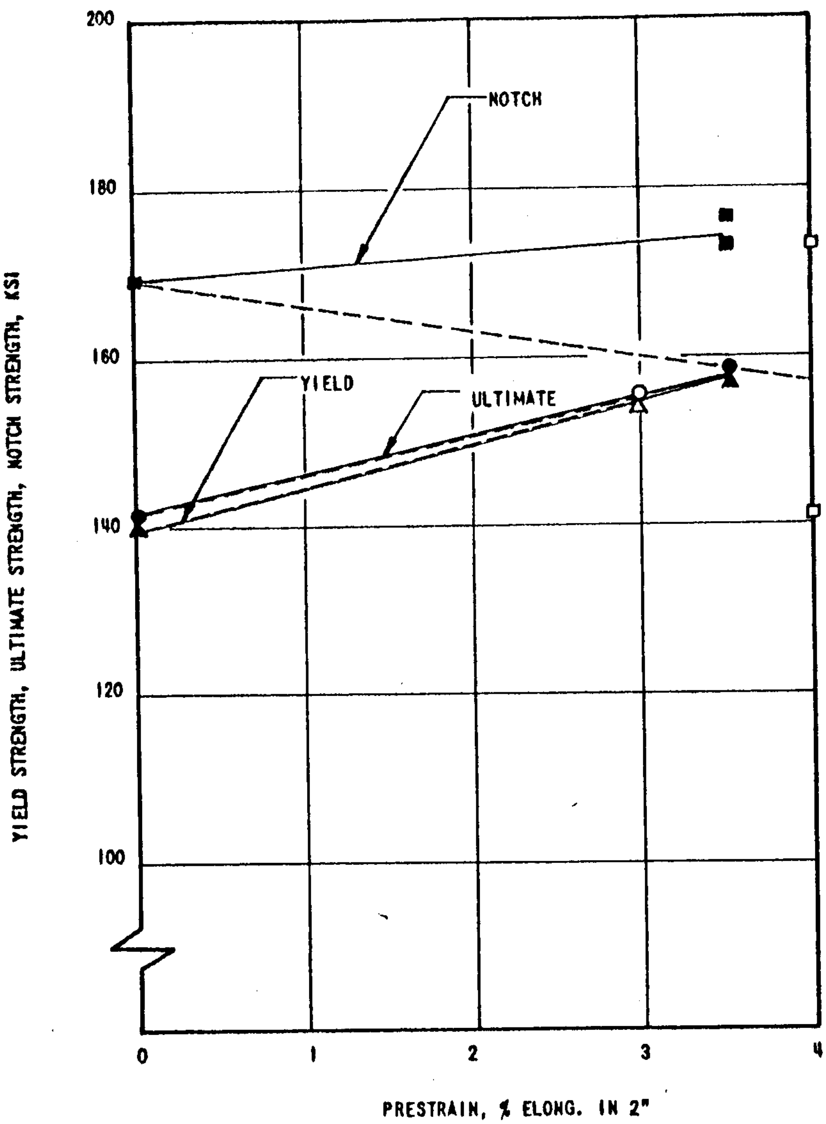

FIGURE 79. MECHANICAL PROPERTIES OF 13V-11Cr-3Al TITANIUM ALLOY AFTER VARIOUS PRESTRAINS AT NOMINAL ROOM TEMPERATURE

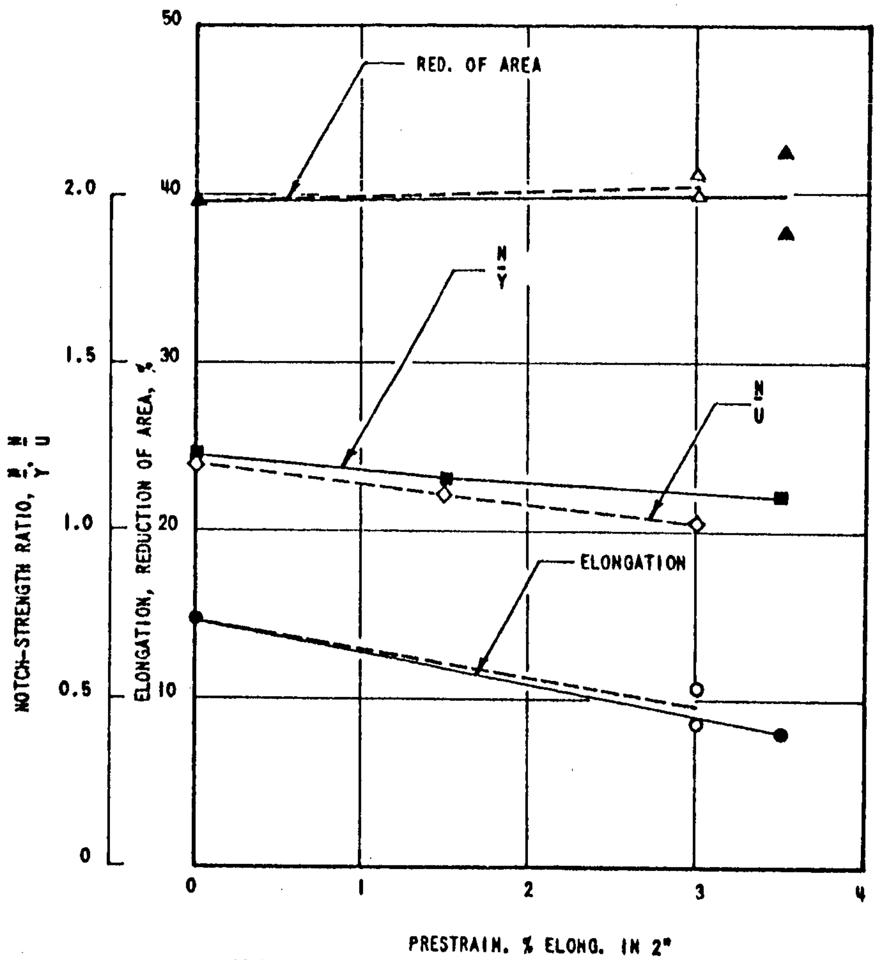

FIGURE 80. MECHANICAL PROPERTIES OF 13V-11Cr-3Al TITANIUM ALLOY AFTER VARIOUS PRESTRAINS AT NOMINAL ROOM TEMPERATURE

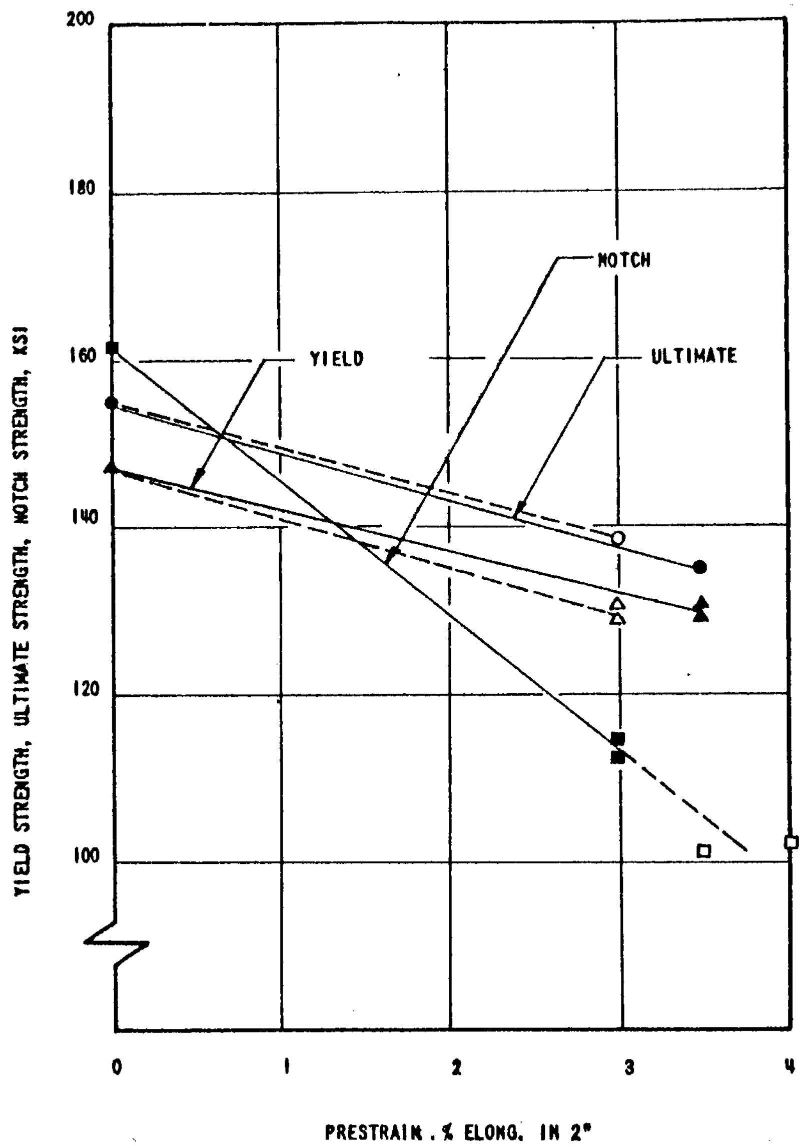

FIGURE 81. MECHANICAL PROPERTIES OF 13V-11Cr-3Al TITANIUM ALLOY - AFTER VARIOUS PRESTRAINS AT NOMINAL ROOM TEMPERATURE AND AGING

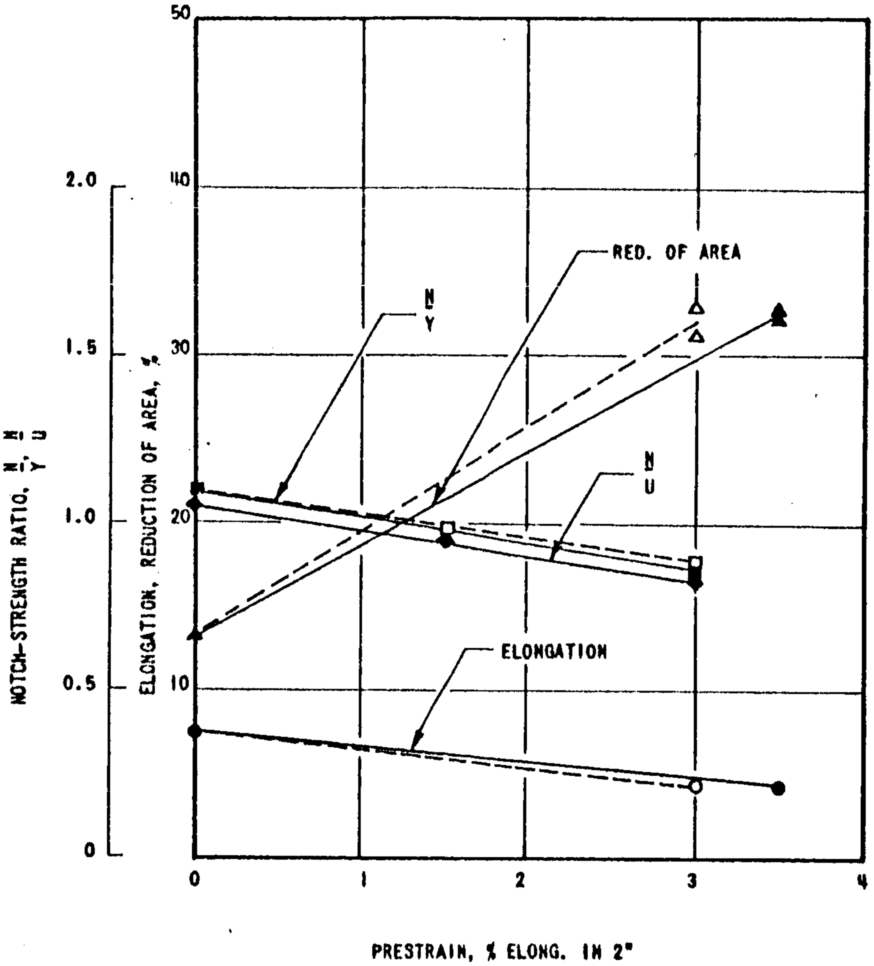

FIGURE 82. MECHANICAL PROPERTIES OF 13V-11Cr-3Al TITANIUM ALLOY - AFTER VARIOUS PRESTRAINS AT NOMINAL ROOM TEMPERATURE AND AGING

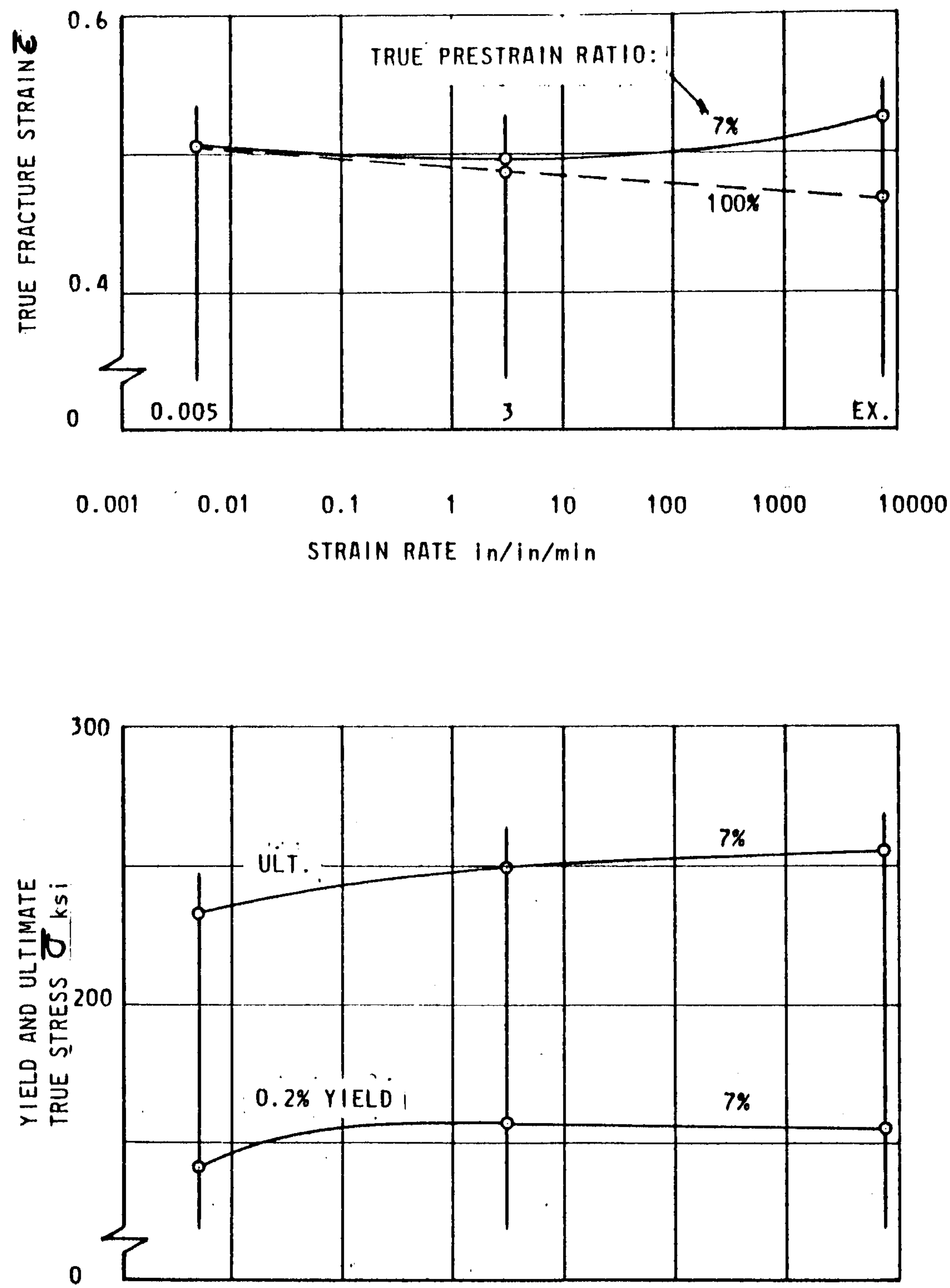

FIGURE 83 TRUE STRESS-STRAIN DATA FOR 13V-11Cr-3Al TITANIUM AFTER VARIOUS PRESTRAINS AT NOMINAL ROOM TEMPERATURE

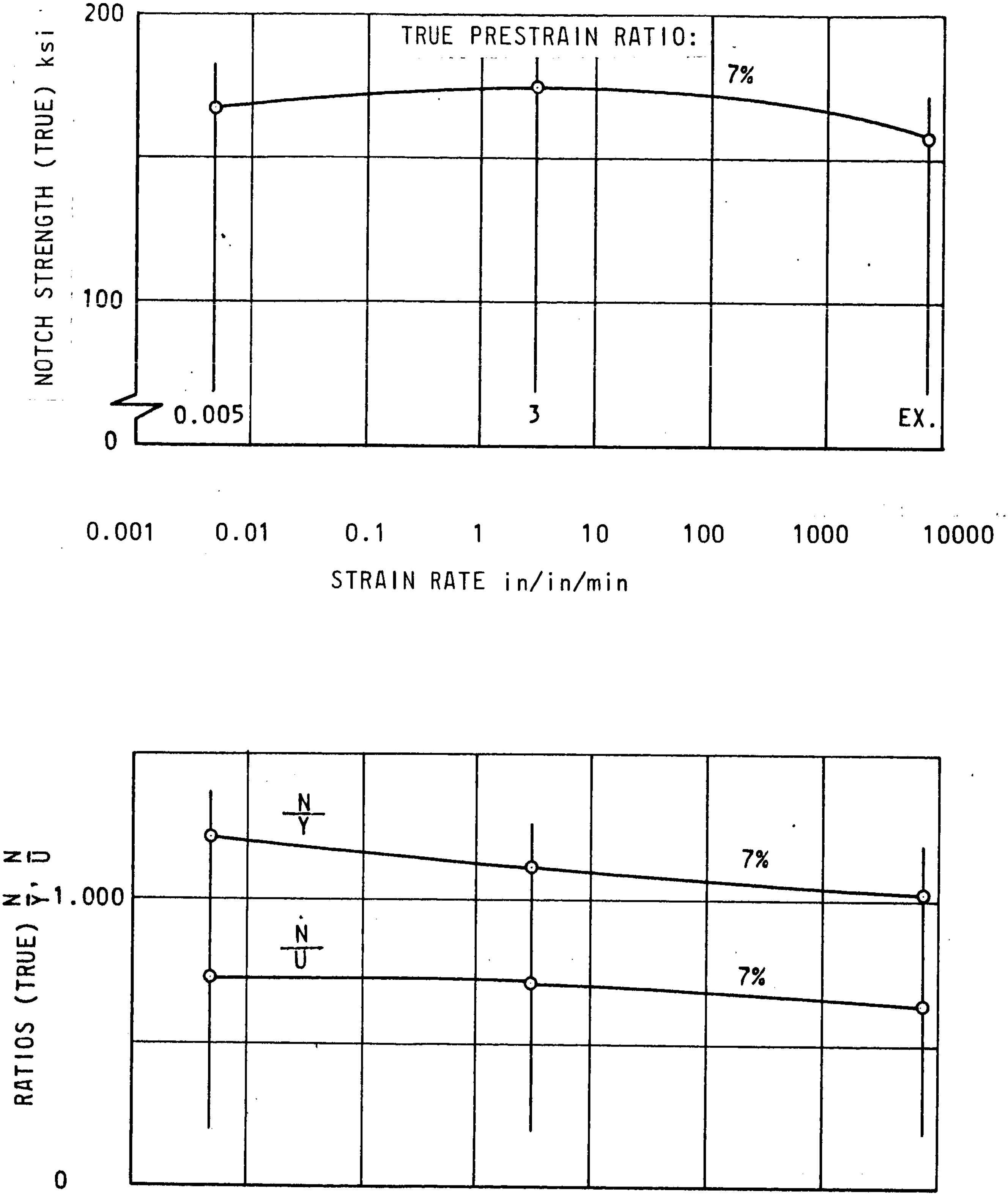

FIGURE 84. NOTCH STRENGTH (TRUE) DATA FOR 13V-11Cr-3Al TITANIUM AFTER VARIOUS PRESTRAINS AT NOMINAL ROOM TEMPERATURE

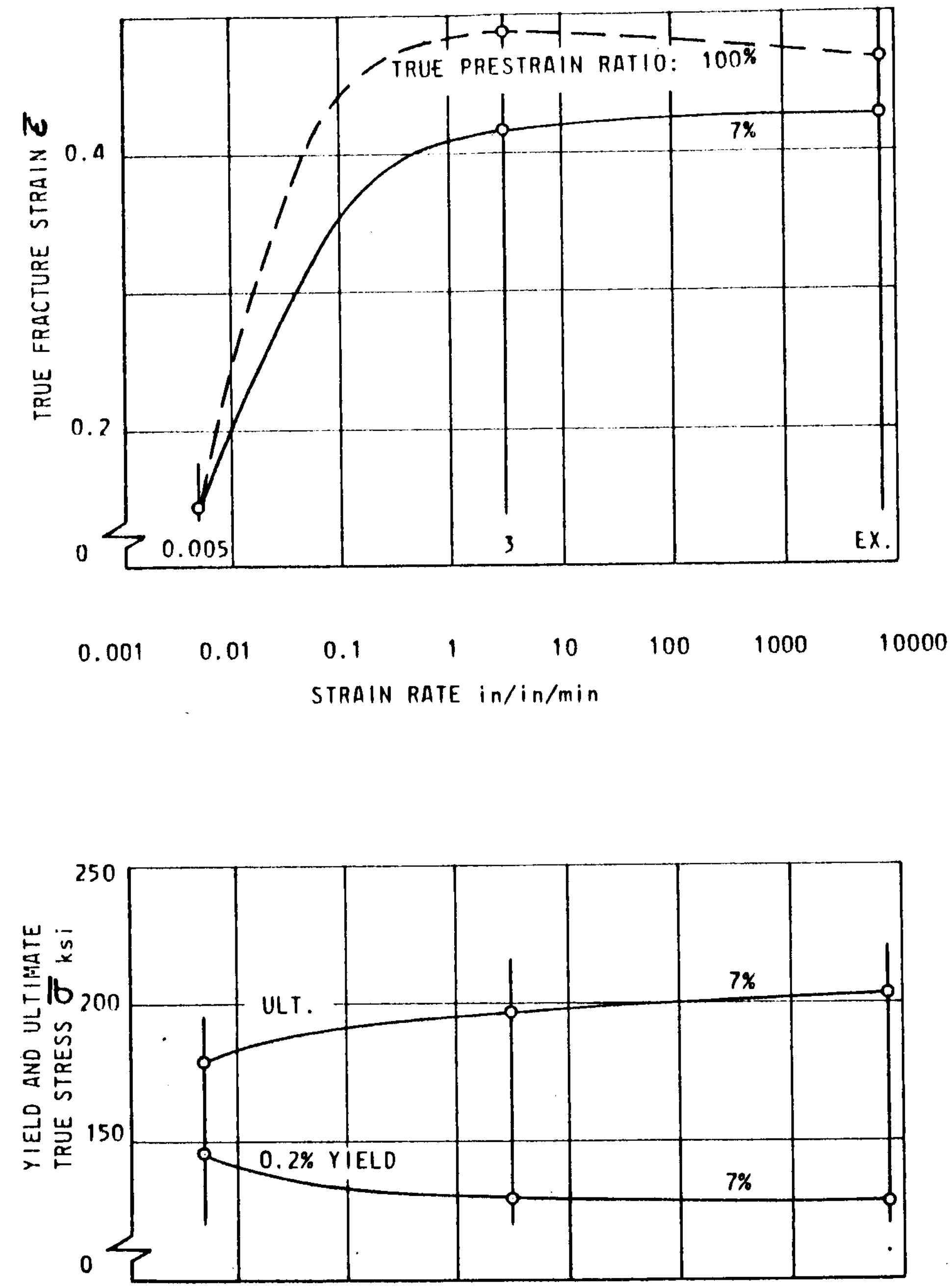

FIGURE 85 TRUE STRESS-STRAIN DATA FOR 13V-11Cr-3Al TITANIUM AFTER VARIOUS PRESTRAINS AT NOMINAL ROOM TEMPERATURE AND AGING

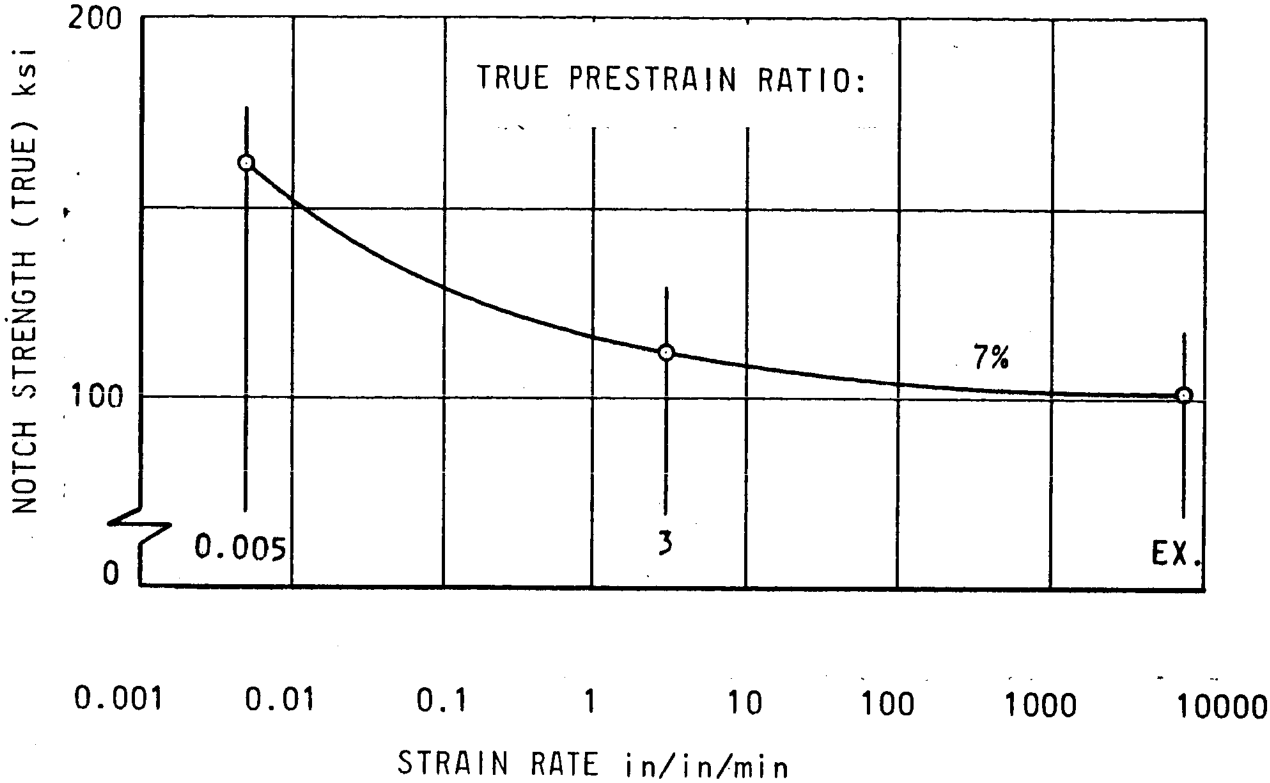

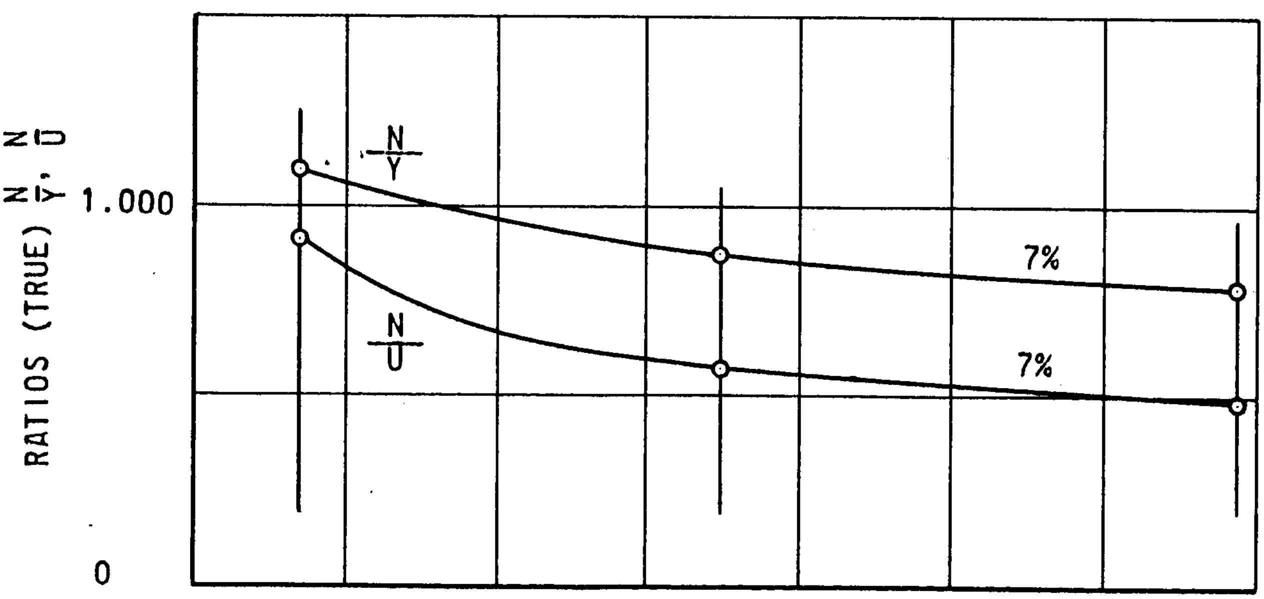

FIGURE 86. NOTCH STRENGTH (TRUE) DATA FOR 13V-11Cr-3Al TITANIUM AFTER VARIOUS PRESTRAINS AT NOMINAL ROOM TEMPERATURE AND AGING

APPENDIX A

LITERATURE SURVEY

A1 - Discussion of Clark and Wood Data Related to High Strain Rate Application.

A2 - British Investigations.

A3 - Data from Westinghouse.

A4 - Extract from "Behavior of Metals Under Impulsive Loads", by John S. Rinehart and John Pearson.

APPENDIX A1

DISCUSSION OF CLARK AND WOOD DATA RELATED TO HIGH STRAIN RATE APPLICATION

Compiled and presented for quick reference from Donald S. Clark: "The Influence of Impact Velocity on The Tensile Characteristics of Some Aircraft Metals and Alloys," NACA TECHNICAL NOTES No. 868, October 1942, and D. S. Clark and D. S. Wood: "The Tensile Properties of Some Metals and Alloys," TRANSACTIONS OF THE A.S.M., Volume 42, 1950.

I. INTRODUCTION

Explosive forming has focused attention on the formability of materials at high strain rates.

Some observations indicate that various materials under forming conditions involving high strain rates show greater formability than when they are formed by conventional, low strain rate methods.

Explosive forming is now being increasingly applied for the forming of materials which are considered difficult to form with conventional methods. Any gain in formability, resulting from an application of a high strain rate process, is therefore a highly desirable feature.

A search for data for clarification of this subject has been undertaken, and some results are accumulated in this technical memorandum.

II. CHARACTER OF INFORMATION ON DYNAMIC LOADING

Most of the available research on effects of dynamic loading has been dictated by the need of designers, and is consequently emphasizing the changes, if any, in elastic limit, proportionality limit, yield point, ultimate strength, and total energy absorption. Recent and present research also attempt to provide a physical explanation for the observed phenomena, and a mathematical analysis thereof.

Unlike other forming methods, the explosive forming process can control the amount of energy applied to the workpiece, practically without upper limits, and the absolute values for the pertinent stress levels are, therefore, in themselves of less significance to this process.

One fundamental problem with regard to explosive forming is posed by the need for predicting amount of deformation which the material will endure before fracture.

The type of data needed are those pertaining to elongation and reduction of area at high strain rates.

Data for reduction of area has the great advantage of being independent of an arbitrary gage length. They are also applicable to the construction of true-stress-strain diagrams. They are, therefore, intrinsically more valuable for the present purpose than elongation data.

A comprehensive collection of the desired type of data has been found in the following two publications:

a. Donald S. Clark: "The Influence of Impact Velocity on the Tensile Characteristics of Some Aircraft Metals and Alloys," NACA TECHNICAL NOTES No. 868, October 1942, briefly referred to as "D. S. Clark 1942".

b. D. S. Clark and D. S. Wood: "The Tensile Impact Properties of Some Metals and Alloys," TRANSACTIONS OF THE A.S.M., Volume 42, 1950, pp. 45-74, briefly referred to as "Clark and Wood 1950".

From these publications, static and dynamic data have been extracted for the pertinent stresses, elongation and reduction of area, the impact velocity applied, and, where available, the critical impact velocity.

The data are presented graphically in the Data Sheets of this memorandum.

The experimental data from "D. S. Clark 1942" do not exceed 150 ft. per second impact velocity. The data from "Clark and Wood 1950" go up to 200 ft. per second. When the highest impact velocity listed in the Data Sheets is below 150 or 200 ft. per second respectively, it means that this velocity is identical with the critical velocity.

NOTE OF CAUTION: In some cases, with regard to the aluminum alloys, the grades and heat-treat conditions used by the investigators are not necessarily identical with the standardized grades and conditions currently available today. The author has, wherever possible, attempted to list the nearest equivalent from today's standard grades and conditions. The aluminum alloys tested have, generally, less elongation than their nearest present day equivalents.

III. FUNDAMENTAL THEORY

A. SOME DEFINITIONS

When a limited part of a body is forced to change its shape, for example, by the application of an external force, it is said to be strained.

The strain will first appear where the force is applied, but it is not confined to this limited locality. It will spread over a greater part of the body, and this process of spreading of the strain is called strain propagation.

Strain propagation is a process that requires time. We can therefore speak of the strain propagation velocity.

When a point, or a small portion of a body, is set into motion instantaneously with a velocity v_1, then the condition is called impact loading. As the velocity increases instantaneously from zero to v_1, then the stress at the same point will change from zero to a value σ_1, and this change will also take place instantaneously.

The strain and stress can be in tension or in compression, or in shear. Explosive forming is mostly concerned with tensile strains, at least for the time being, and this memorandum deals exclusively with data for tensile impact loading.

The available experimental data were determined for prismatic rods of considerable, but finite length. They are, however, applicable also to other cases of strain and stress, just as results from the static tensile test are applicable to a variety of stress systems by proper modification.

B. ELASTIC STRAIN

For strains within the elastic limit, the propagation relation was stated by Thomas Young in 1807.

The formula reads

$$\varepsilon_1 = \frac{v_1}{c_o} \tag{1}$$

or in words:

When the end of a long prismatic bar is suddenly set in motion with a constant velocity v_1, then an elastic strain ε_1 will be created and will travel lengthwise through the bar as a strain wave with a propagation velocity c_o.

A basic conclusion to be drawn from (1) is that the elastic strain is proportional to the velocity by which it is generated.

A compatible set of dimensions for formula (1) may be as follows:

ε_1	inches per inch	$\left(\frac{\text{inch}}{\text{inch}}\right)$
v_1	feet per second	$\left(\frac{\text{feet}}{\text{sec.}}\right)$
c_o	feet per second	$\left(\frac{\text{feet}}{\text{sec.}}\right)$

The propagation velocity c_o is given by the formula

$$c_o = \sqrt{\frac{E}{\rho}} \tag{2}$$

where E is the modulus of elasticity and ρ is the mass density of the material.

A compatible set of dimensions for formula (2) may be as follows:

c_o inches per second $\left(\frac{\text{inch}}{\text{sec.}}\right)$

E pounds per square inch $\left(\frac{\text{lbs.}}{\text{inch}^2}\right)$

ρ pounds-second^2 per inch^4 $\left(\frac{\text{lbs. sec.}^2}{\text{inch}^3\ \text{inch}}\right)$

<u>NOTE OF CAUTION</u>: The dimensions quoted for E and ρ for use in (2) are those most commonly used. They result in the dimension inches per second for c_o.

If c_o is determined in this manner, its value must be divided by 12 in order to give it in feet per second, which is the most commonly used dimension for velocities of the type discussed here. Impact velocity data listed in this appendix are given in feet per second.

C. PLASTIC STRAIN

It follows from (2) that $\mathcal{E}_1$ may exceed the elastic range if v_1 becomes large enough, in absolute measure as well as in relation to c_o. If and when this happens, (1) and (2) are not valid any more.

Theodore von Kármán has shown that the propagation velocity c of a plastic strain, and the relation between a plastic strain $\mathcal{E}_1$ and the impact velocity v_1 by which it is generated, can be calculated when the stress-strain curve is known.

A stress-strain curve for a material is shown in Figure 1. A is an arbitrary point beyond the elastic range. The strain $\mathcal{E}_1$ in A is a plastic strain. The slope of the tangent to the curve in A is $\frac{d\sigma}{d\mathcal{E}}$.

The relation between an impact velocity v_1 and the plastic strain ε, which it generates, is given by

$$v_1 = \int_0^{\varepsilon_1} \sqrt{\frac{\frac{d\sigma}{d\varepsilon}}{\rho}}\, d\varepsilon \qquad (3)$$

and the propagation velocity c of this particular plastic strain is given by

$$c = \sqrt{\frac{\frac{d\sigma}{d\varepsilon}}{\rho}} \qquad (4)$$

A compatible set of dimensions for formulae (3) and (4) may be as follows:

σ pounds per square inch $\left(\frac{\text{lbs.}}{\text{inch}^2}\right)$

ε inches per inch $\left(\frac{\text{inch}}{\text{inch}}\right)$

ρ pounds-second^2 per inch^4 $\left(\frac{\text{lbs. sec.}^2}{\text{inch}^3\ \text{inch}}\right)$

hence:

v and c inches per second $\left(\frac{\text{inch}}{\text{sec.}}\right)$

Several important conclusions can be drawn from (3) and (4).

It is seen from (4) that the strain propagation velocity c is now associated with the slope $\frac{d\sigma}{d\varepsilon}$ of the tangent to the stress-strain curve.

Within the elastic range we have

$$E = \frac{d\sigma}{d\varepsilon} \qquad (5)$$

When (5) is substituted into (4), we get

$$c = \sqrt{\frac{\frac{d\sigma}{d\varepsilon}}{\rho}} = \sqrt{\frac{E}{\rho}} = c_o$$

and when (5) and (4) are substituted into (3), we get

$$v_1 = \int_o^{\varepsilon_1} \sqrt{\frac{\frac{d\sigma}{d\varepsilon}}{\rho}} \, d\varepsilon = \int_o^{\varepsilon_1} c_o \quad d\varepsilon = c_o \int_o^{\varepsilon_1} \quad d\varepsilon = c_o \varepsilon_1$$

This shows that (5) applied to (3) and (4) brings us back to (1) and (2).

The conclusion is therefore that (3) and (4) are actually generalizations of (1) and (2), and not merely supplementary to them, or in other words, (3) and (4) are valid over the whole range of elastic and plastic strain, while (1) and (2) are contained in (3) and (4) and represent special modifications of them, which are valid only within the elastic range.

From (3) it is concluded that the plastic strain ε_1 increases with increasing impact velocity v_1, as in the case of elastic strain, with the difference, however, that there is no direct proportionality.

It is further concluded, from (4), that the variation of the propagation velocity c follows the variation of the $\frac{d\sigma}{d\varepsilon}$. A glance at a stress-strain diagram, such as the one illustrated in Figure 1, shows that $\frac{d\sigma}{d\varepsilon}$ is decreasing with increasing ε, and that $\frac{d\sigma}{d\varepsilon}$ reaches the value zero at point B, corresponding to the ultimate strength. From this observation, it follows:

a. that a plastic strain propagates slower than an elastic strain.

b. that larger plastic strains propagate slower than smaller plastic strains, and, finally

c. that the plastic strain propagation velocity may become zero.

The zero value for c is reached at the point of ultimate stress; the strain at this point is designated $\mathcal{E}_m$. The corresponding impact velocity v_m is calculated from

$$v_m = \int_0^{\mathcal{E}_m} \sqrt{\frac{\frac{d\sigma}{d\mathcal{E}}}{\rho}}\, d\mathcal{E} \qquad (6)$$

and is known as <u>the critical impact velocity</u>.

THE CRITICAL VELOCITY CAN BE VISUALIZED AS THE IMPACT VELOCITY, AT WHICH THE PLASTIC STRAIN DOES NOT PROPAGATE ALONG THE ROD. CONSEQUENTLY, SINCE THE STRAIN IS TENSILE, THE ROD MUST BREAK INSTANTANEOUSLY AT THE POINT OF IMPACT.

The von Kármán theory, as first published* is based on the simplifying approximations that the static and the dynamic stress-strain curves are identical. Expressed in a different wording, this means that the shape of the stress-strain curve does not depend on the strain rate. There can, however, be no doubt that a strain rate effect exists in a great many cases.

Another limitation, also set forth in the original publication, is that the theory is not fully valid for materials with a definite yield point. The stress-strain curves for such materials have a region where the curve is not concave towards the strain axis, and this fact, or rather the discontinuity imposed by the yielding mechanism, is not taken into account by the original theory.

Apart from these limitations, the experimental investigations have shown an unusually satisfactory agreement between theory and test results, in spite of approximations and experimental difficulties.

---

* Theodore von Kármán and Pol Duwez, "The Propagation of Plastic Deformation in Solids", <u>Journal of Applied Physics</u>, Vol. 21, Oct. 1950, pp. 987-994.

IV. EXPERIMENTAL PROCEDURE

The data listed in this memorandum are based on tensile tests with round test coupons. The dimensions of the test coupons are shown in Figures (2) to (5).

For the testing, one end of a coupon was held in a dynamometer, while the other end was exposed to an impact of constant velocity. The constancy of the impact velocity was secured by the large mass of the flywheel in the impact testing machine. The response of the dynamometer was amplified and recorded by means of a cathode-ray oscilloscope and camera.

The force-time diagrams for the dynamometer end obtained in this manner are not entirely identical with the force-time diagrams that represent the conditions at the impact end of the test specimen. The dynamometer load is delayed in relation to the impact load because the load is transferred by a wave action. The dynamometer reading may also be affected by one or several wave reflections. These modifying factors depend on the properties of the material tested. The determining parameter was found to be the ratio of the static elastic limit to the static ultimate strength.

Three different types of diagrams were obtained. With a very low ratio parameter, between 0 and 0.25, the diagrams would be of the type shown in Figure 6. When the ratio parameter is medium, that is, between approximately 0.25 and 0.6, the diagram takes the shape shown in Figure 7. When finally the ratio parameter is large, between 0.6 and 1.0, the diagrams will look like Figure 8.

In each of the three cases, corrections can be made for the modifications caused by the wave transmission,and the final data for the dynamic stresses occurring at the impact end can be calculated for each impact velocity tested. Elongations and area reductions were measured directly from the broken test coupons in the conventional manner.

When the final data are plotted over impact velocity, the resulting graphs can, by their characteristic appearance, be grouped into three classifications.

V. DYNAMIC CLASSIFICATION OF MATERIALS

The various materials tested differ widely in their dynamic response to impact loading.

The critical velocity varies from 50 ft. per second (measured for cold-rolled copper) to 490 ft. per second (calculated for Stainless Steel 302, as-received).

The decrease in elongation and reduction of area above the critical velocity may be gradual and continuous, as shown in Figures 9 and 11, or it may appear as a sudden drop, as shown in Figure 10. The most important feature is the pattern of variation of elongation over the velocity range from zero (static testing) up to the critical velocity. The curves for area reduction are very similar to the curves for elongation. For each of the three classes, the curve defined a practical dynamic elongation.

All the materials tested can be divided into three classes, according to whether they show constant, increasing, or scattered dynamic elongation.

A. CLASS 1 - CONSTANT DYNAMIC ELONGATION

Examples of this pattern are shown in Figures 9 and 10. The elongation is constant over the dynamic range up to the critical velocity, where it starts to decrease, either gradually or suddenly.

The practical critical velocity is the one where the elongation begins to decrease.

The practical dynamic elongation is taken as the constant value over the dynamic range.

It should be noted that the velocity data are not converted to strain rate data. In tests of this type, the strain rate varies non-uniformly over the length of the test specimen. The determination of strain rate data requires tests of an entirely different character.

B. CLASS 2 - INCREASING DYNAMIC ELONGATION

This pattern is shown in Figure 11. The elongation increases progressively with impact velocity up to a maximum. This maximum corresponds to the critical velocity. Beyond this maximum, the elongation decreases gradually.

The practical dynamic elongation is taken as the maximum value.

C. CLASS 3 - SCATTERED DYNAMIC ELONGATION

An example of this pattern is shown in Figure 12. In the example, the critical velocity is above the highest tested velocity of 200 feet per second and does not appear in the graph. The calculated critical velocity is 226 feet per second.

The elongation shows a moderate, and somewhat scattered, variation over the dynamic range. The variation is too great for the material to come in Class 1, and it is not regular enough to bring it into Class 2.

The practical dynamic elongation is taken as the average value over the dynamic range.

VI. GENERAL CONCLUSIONS AND TRENDS

A. ULTIMATE STRENGTH

The general rule is that the ultimate strength is higher under impact load than under static load. The rule is not quite exclusive. Out of eighty-one (81), seventy-three (73) followed the rule, while eight (8) only showed a different behavior.

The eight exceptions are:

Clark 1942:	U.T.S. psi Static	Dynamic
Dowmetal J, extruded	44,500	-06%
Steel, SAE X4130, QT to 30 R_C	187,500	-19%
Steel, SAE X4130, QT to 37 R_C	210,000	-18%

Clark 1942: (Cont.)	U.T.S. psi Static	Dynamic
Stainless Steel M286, QT at 900°F	215,000	-21%
Steel, 6140, QT to 35 R_C	190,000	-3.6%
Clark & Wood 1950:		
Steel, SAE 1095, QT at 900°F	176,500	-3%
Steel, NE 9445, aust'd to 52 R_C	282,100	-6%
Steel, NE 9445, QT to 52 R_C	275,000	-1%

The Dowmetal is an extruded grade. All other light alloys, including seven magnesium samples, showed a gain in ultimate tensile stress under impact load.

The common feature for the steels listed is that they are treated to conditions of high strength. However, other high-strength steels have been found with equally high strength properties, which show higher ultimate strength under dynamic load than under static load.

It does not appear justified to draw general conclusions from these eight observations. It appears most likely that they represent a few exceptions from the general rule, which is that dynamic ultimate strength is higher than static ultimate strength.

B. DEFORMATION (ELONGATION AND REDUCTION OF AREA)

The dominating rule is that the dynamic deformation is greater than the static deformation, and it makes no significant difference whether the deformation is defined by elongation or by reduction of area. The rule is somewhat less exclusive than the corresponding result found for ultimate tensile stress.

Out of eighty-one (81) cases, sixty-eight (68) cases showed greater dynamic deformation (up to 260% over the static value, observed for Zamac), and 13 cases showed less dynamic deformation (to 89% below the static value, for Dow O). The 13 exceptions are:

Clark 1942:

Dowmetal M	Elongation	static	14.02	dynamic	5.3%
SAE 1020, hot rolled	"	"	34.2	"	30.4%
SAE X4130, annealed	"	"	33.9	"	27.8%
Stainless M286, QT at 900°F	"	"	21.0	"	17.5%
Stainless 303, as-received	"	"	70.8	"	52.5%

Clark & Wood 1950:

Ingot iron	Elongation	static	25.7	dynamic	16.2%
SAE 1015, annealed	Reduction	static	69.0	dynamic	63.0%
SAE 1045, spheroidized	Elongation	static	23.6	dynamic	21.7%
SAE 1095, high annealed	Reduction	static	23.0	dynamic	19.0%
Stainless 302, as-received	Elongation	static	58.5	dynamic	46.6%
Dowmetal M	"	"	6.0	"	1.1%
Dowmetal M^x	"	"	11.5	"	7.0%
Dow O	"	"	3.8	"	0.4%

These exceptions form a fairly clear picture. It appears that within the range of metals investigated, only the magnesium alloys and the high ductile ferrous materials are adversely affected by dynamic loading. For the magnesium alloys, the loss in ductility is severe; for the ductile steels the loss is moderate.

C. YIELD STRENGTH

Data for yield strength are only available from "D. S. Clark 1942" and cover 21 cases, comprising carbon steels up to SAE 1035, alloy steels (including stainless steels) in various heat-treat conditions, aluminum, magnesium alloys (Dowmetal), copper and copper alloys.

In every case without exceptions, the dynamic yield strength is higher than the static yield strength. The gain ranges from 1.1% (for SAE 4130 steel, quenched and tempered to 37 R_C, ultimate tensile strength

210,000 psi) and up to 216% (for SAE 1020 steel, hot rolled).

D. ENERGY ABSORPTION

The dominating rule is that the energy absorption in dynamic deformation is greater than in static deformation.

Only eight (8) cases do not follow the rule. They are:

Clark 1942:	Dynamic Energy Absorption	
Ingot iron, annealed	down	39%
SAE X4130, annealed	down	3.9%
Stainless M286, QT at 700°F	down	9.2%
Stainless M286, QT at 900°F	down	40%
Dowmetal M	down	41%
Clark & Wood 1950:		
SAE 1095, spheroidized	down	5%
Stainless 302, as-received	down	3%
Dowmetal M^x	down	8%

The data indicates a confirmation of the previously found trend, namely that a few highly ductile materials lose some ductility under dynamic loading conditions.

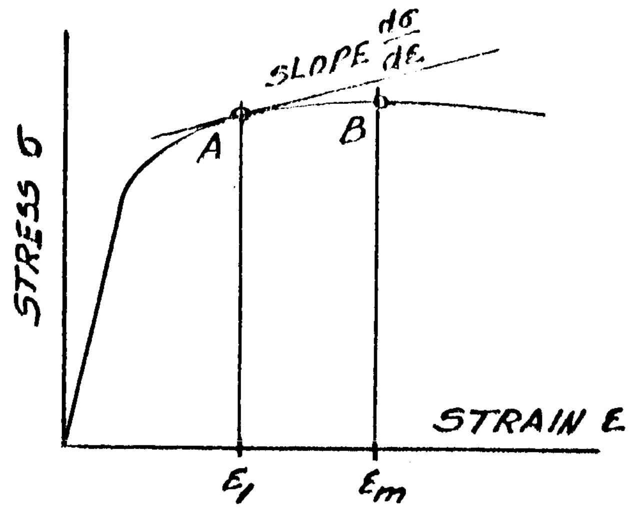

Figure A1-1 Conventional Stress - Strain Diagram.

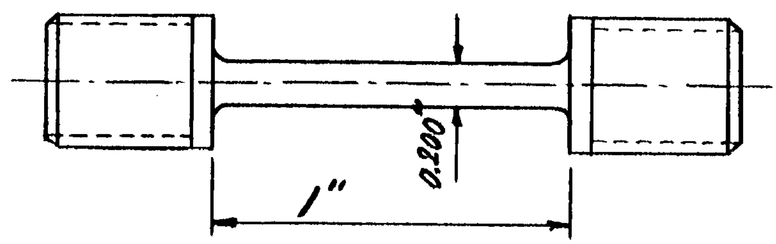

Figure A1-2 Tensile Test Specimen. D. S. Clark 1942.

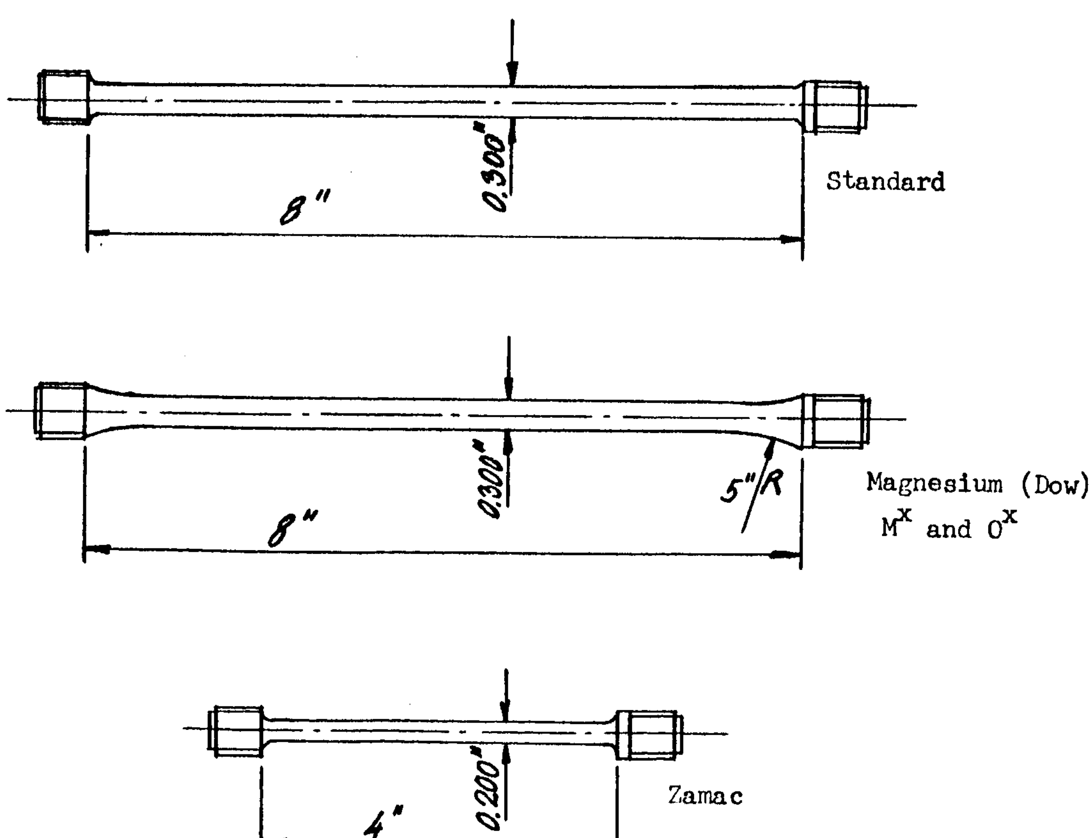

Figures A1-3 - A1-5 Tensile Test Specimens. Clark and Wood 1950.

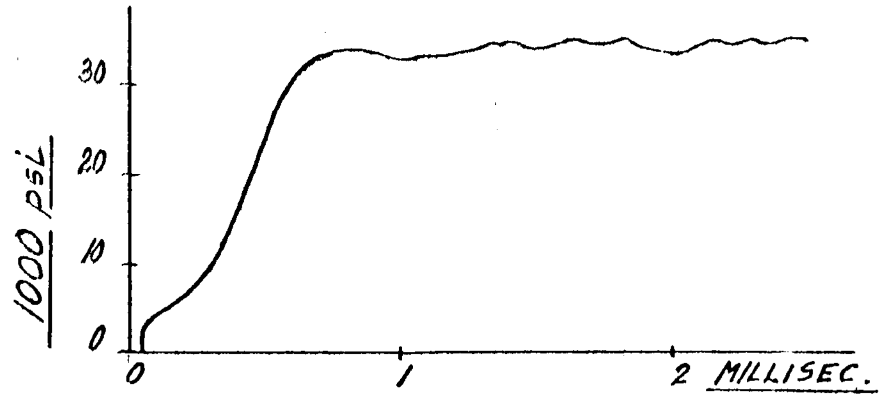

Low ratio parameter. Annealed Copper.

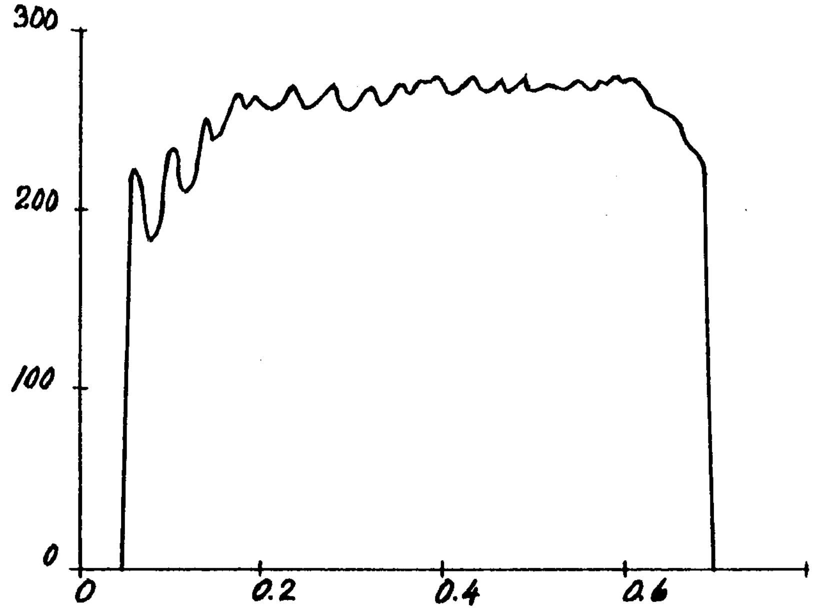

Medium ratio parameter. Austempered steel SAE 2345.

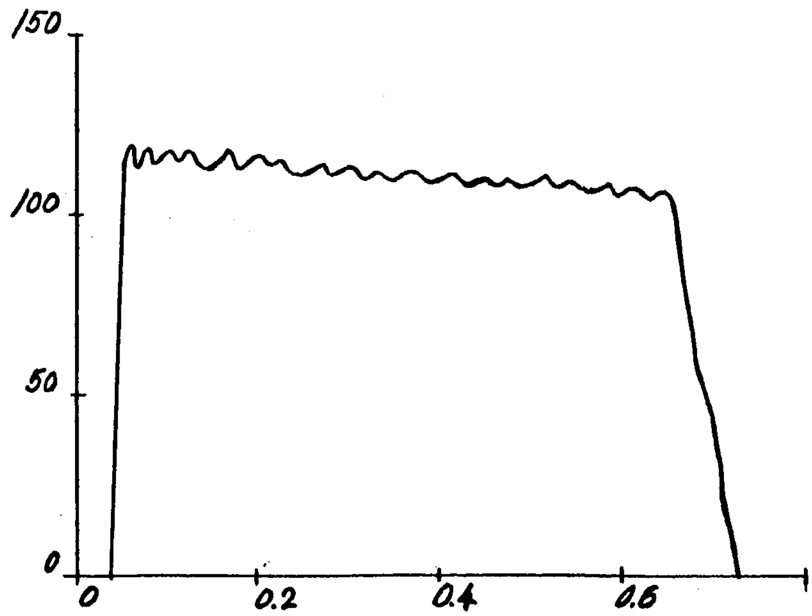

Large ratio parameter. Cold rolled steel SAE 1020.

Figures A1-6 - A1-8 . Recorded, Stress-Time Diagrams.

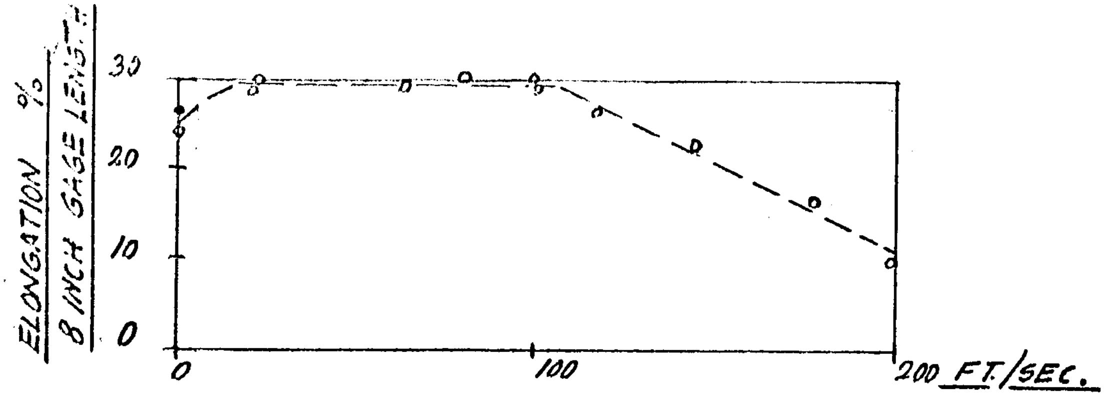

Class 1. SAE 1015 Steel, annealed.

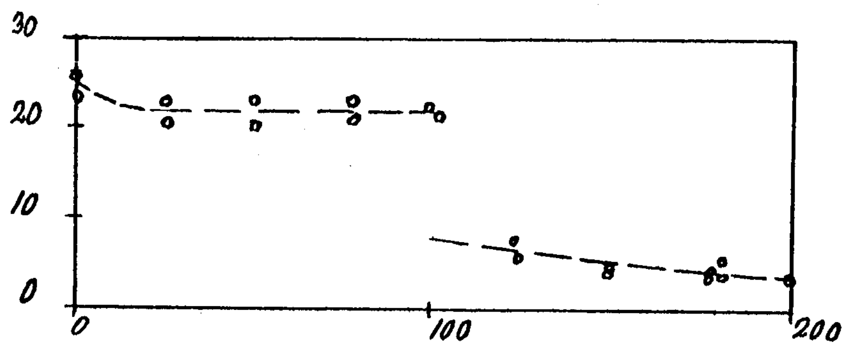

Class 1. SAE 1045 Steel, quenched at 1500°, spheroidized at 1300°.

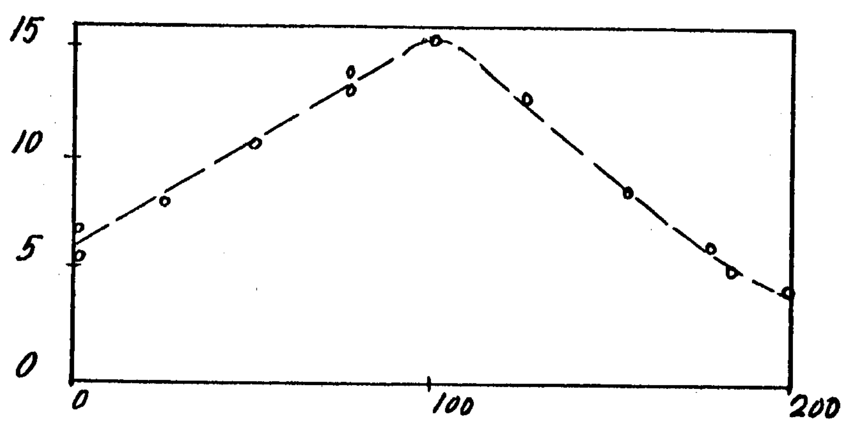

Class 2. SAE 1022 Steel, cold rolled.

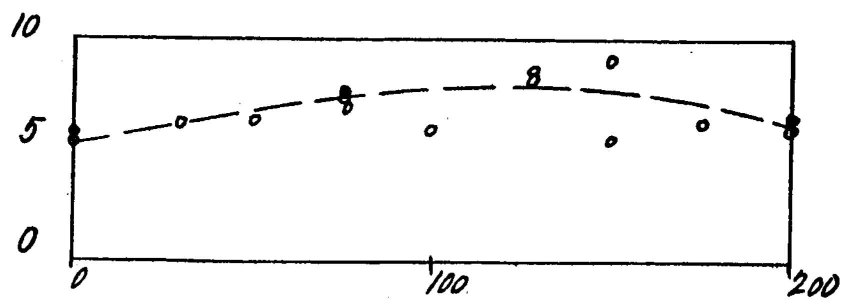

Class 3. SAE 2345 Steel, quenched and tempered to 52 R_c.

Figures A1-9 - A1-12 Elongation vs. Velocity Curves..

STATIC AND DYNAMIC DEFORMATION IN TENSILE TESTING

CARBON AND LOW ALLOY STEELS

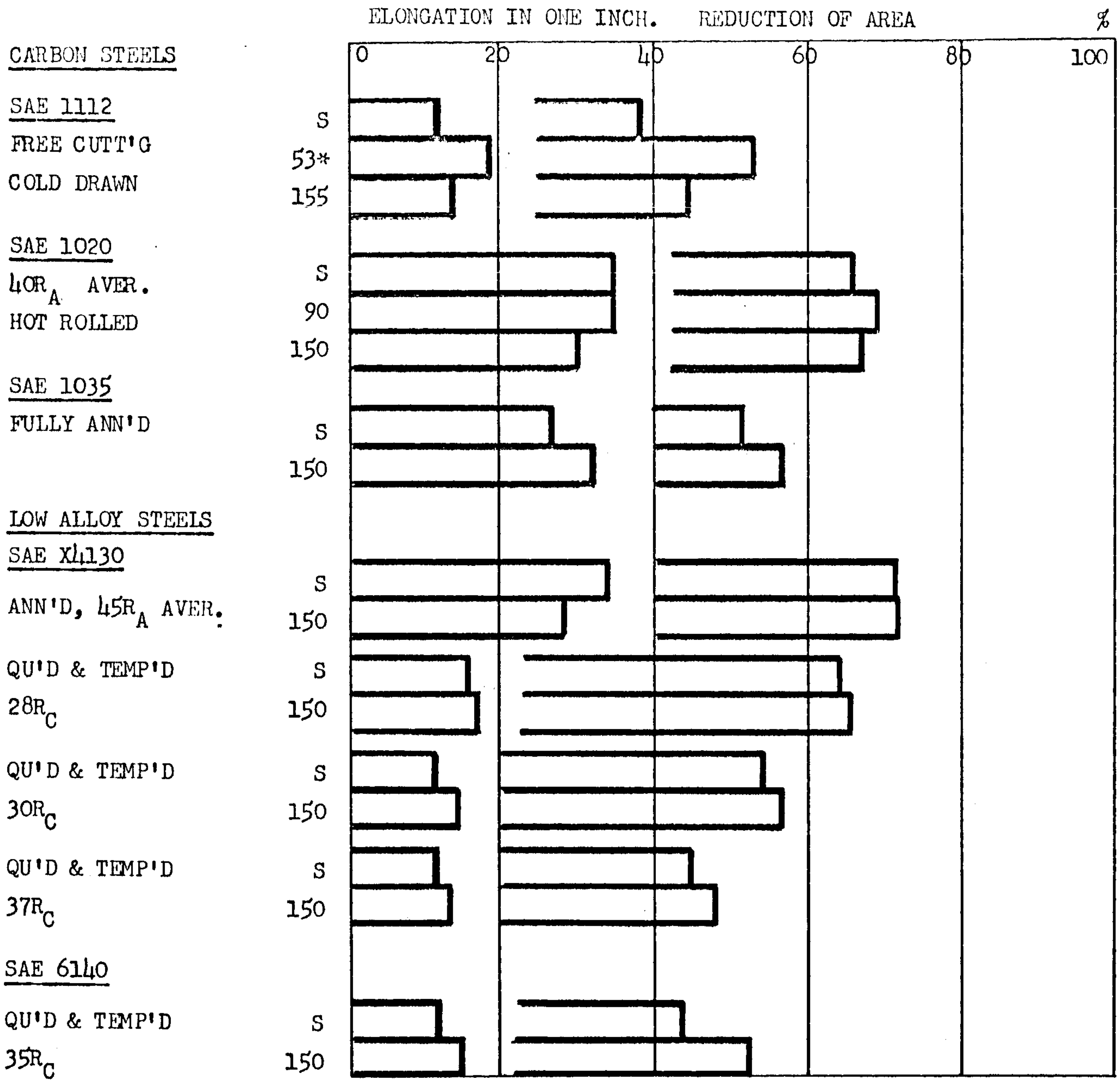

After D. S. Clark 1942 *Impact Velocity Feet/Second

STATIC AND DYNAMIC DEFORMATION IN TENSILE TESTING

STAINLESS STEELS

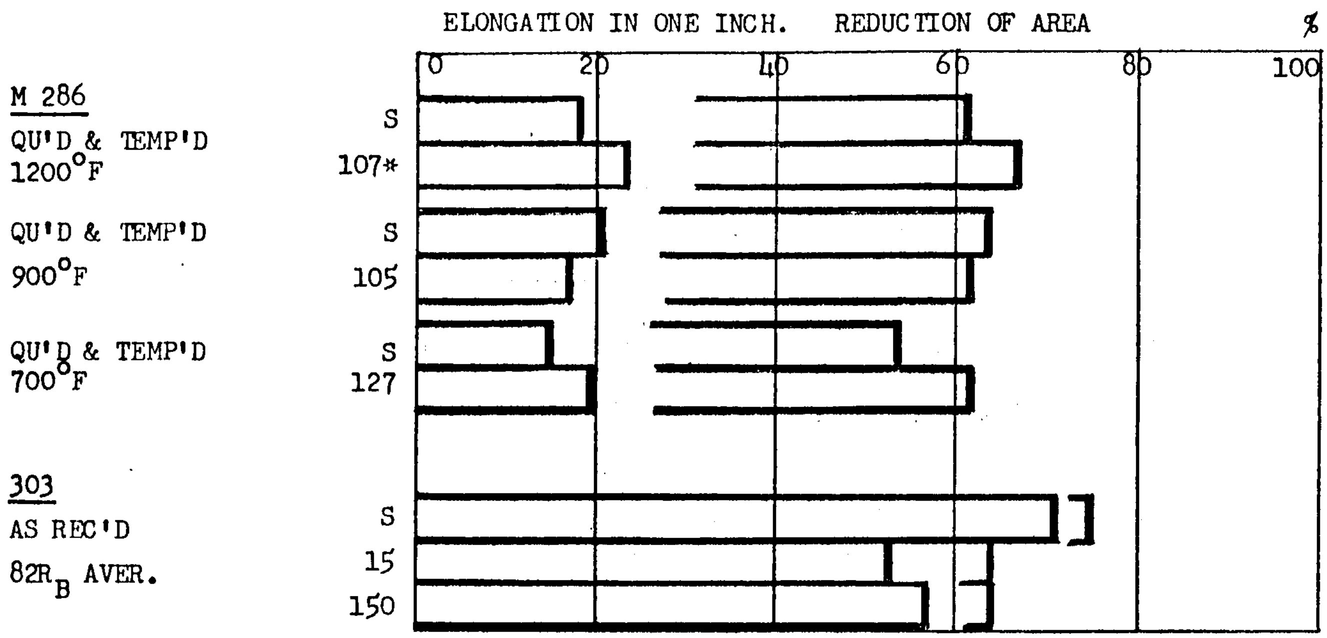

After D. S. Clark 1942 *Impact Velocity Feet/Second

STATIC AND DYNAMIC DEFORMATION IN TENSILE TESTING

COPPER MATERIALS

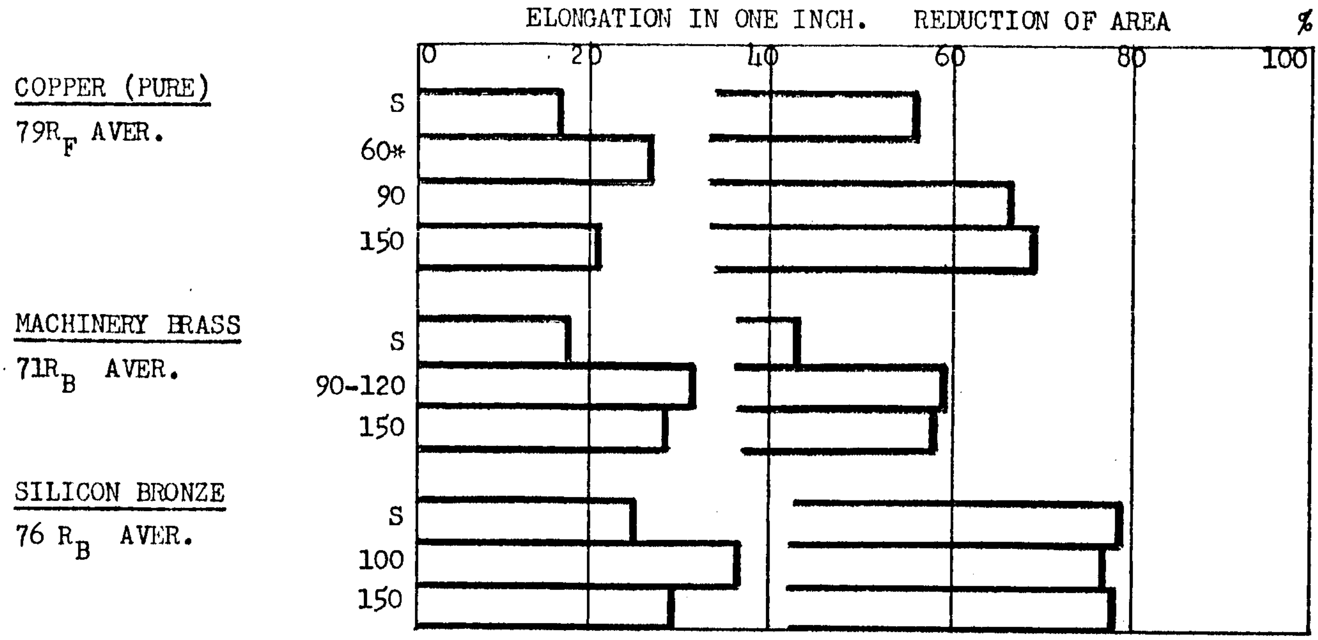

After D. S. Clark 1942 *Impact Velocity Feet/Second

STATIC AND DYNAMIC DEFORMATION IN TENSILE TESTING

ALUMINUM AND MAGNESIUM MATERIALS

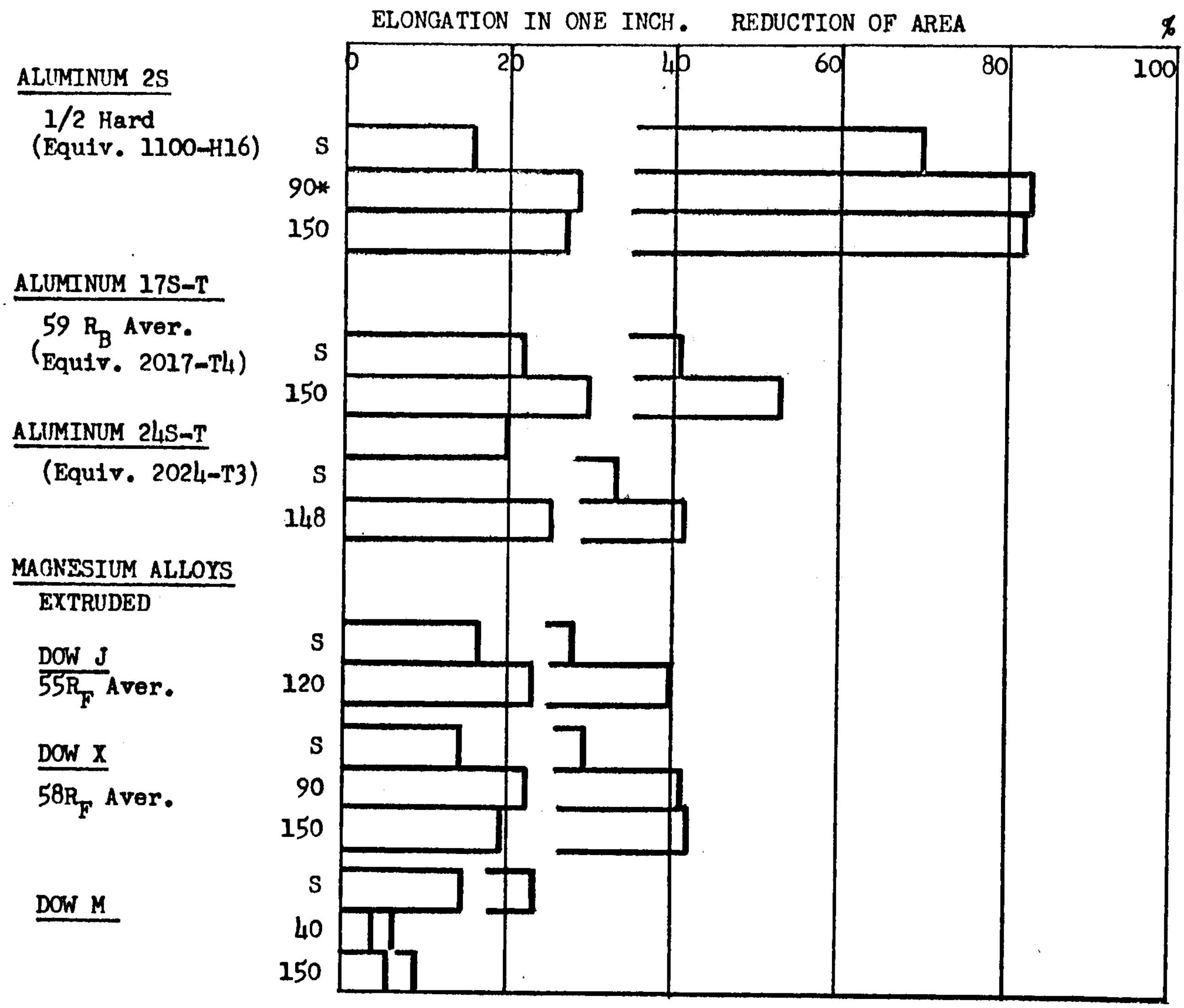

After D. S. Clark 1942 *Impact Velocity Feet/Second

STATIC AND DYNAMIC DEFORMATION IN TENSILE TESTING

CARBON STEELS, VARYING CONDITIONS

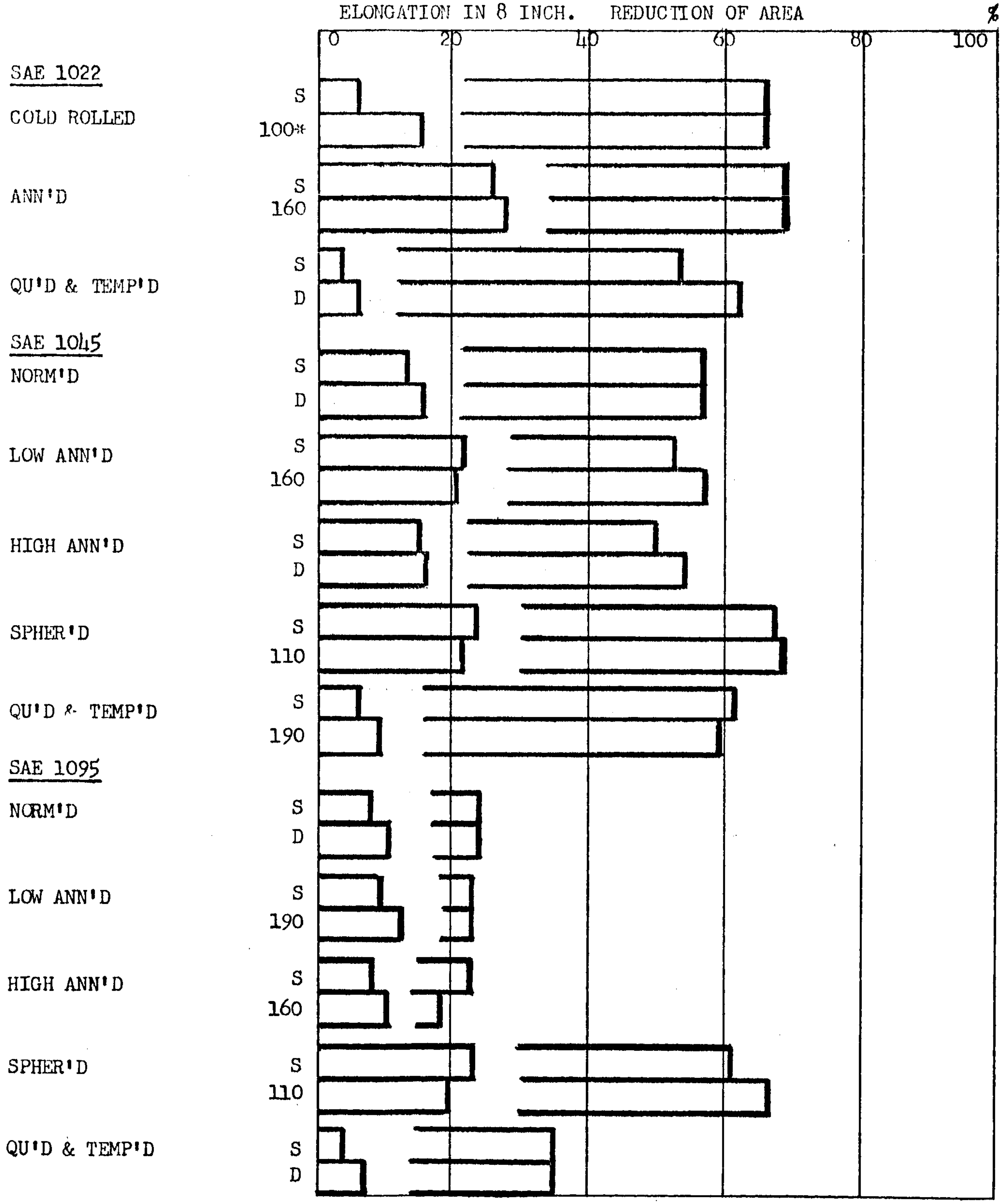

After Clark & Wood 1950 *Impact Velocity Feet/Second

STATIC AND DYNAMIC DEFORMATION

IN TENSILE TESTING

CARBON STEELS, ANNEALED

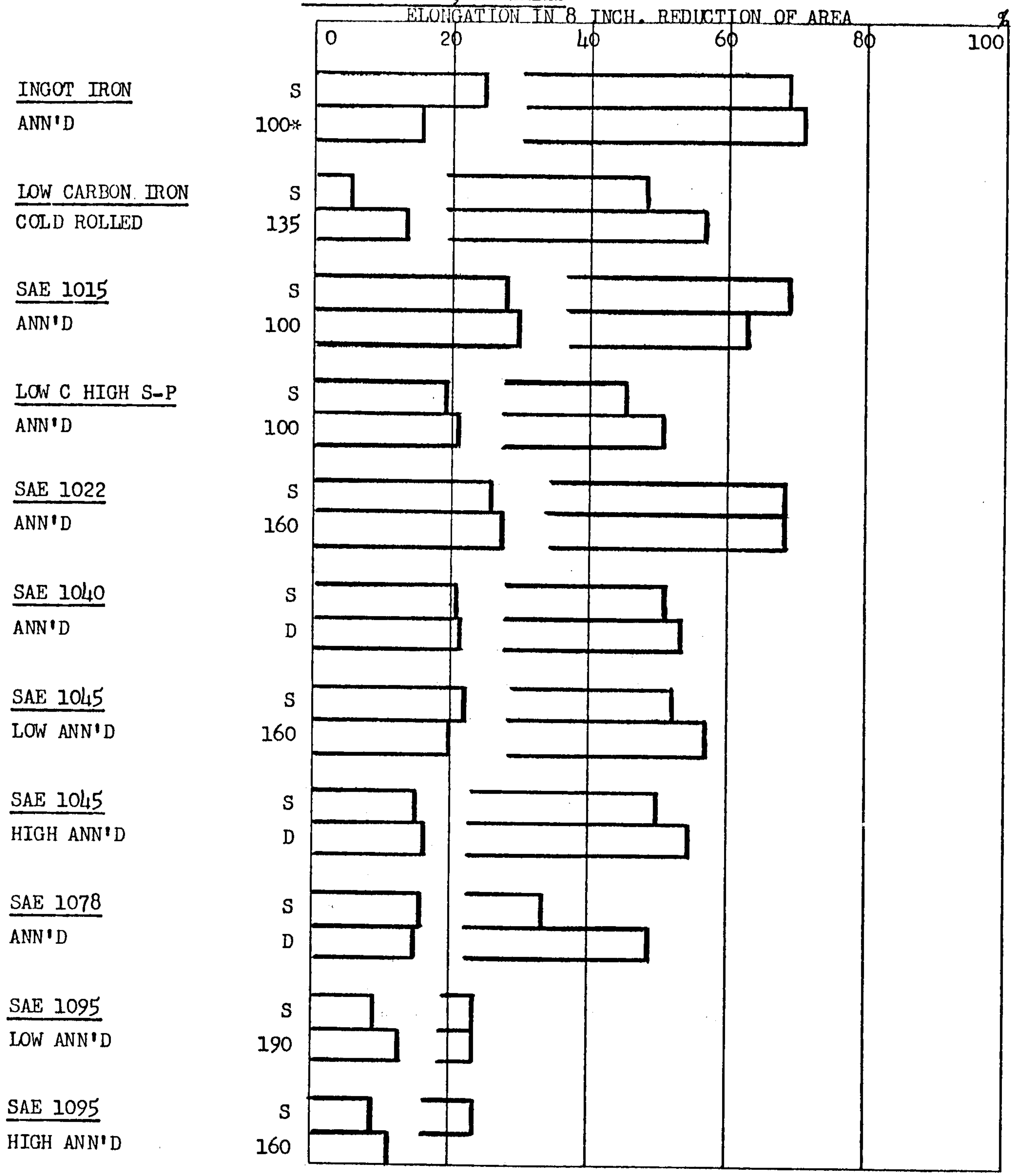

After Clark & Wood 1950 *Impact Velocity Feet/Second

STATIC AND DYNAMIC DEFORMATION IN TENSILE TESTING

LOW ALLOY STEELS, VARYING CONDITIONS -1

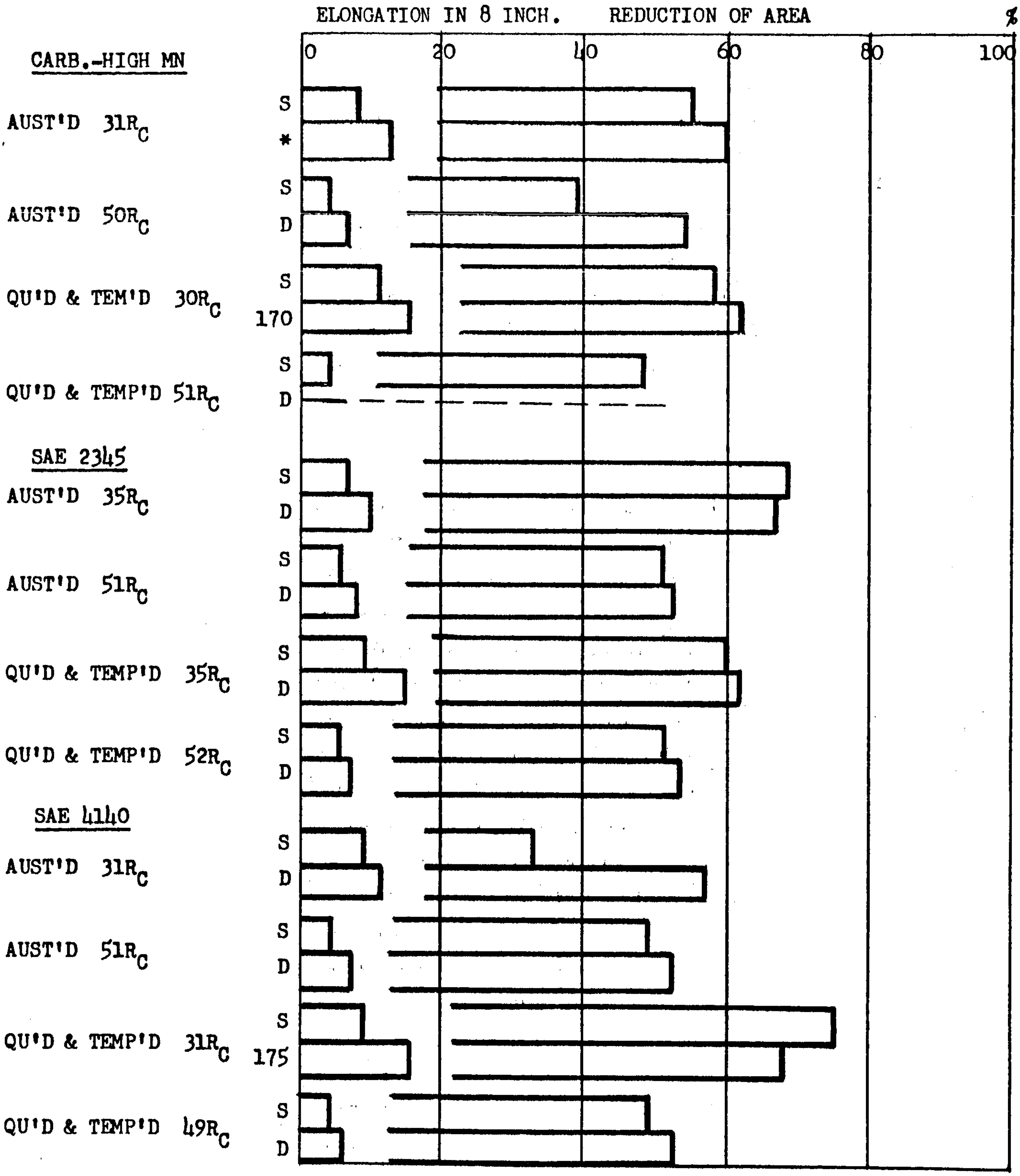

After Clark & Wood 1950 *Impact Velocity Feet/Second

STATIC AND DYNAMIC DEFORMATION IN TENSILE TESTING

LOW ALLOY STEELS, VARYING CONDITIONS -2

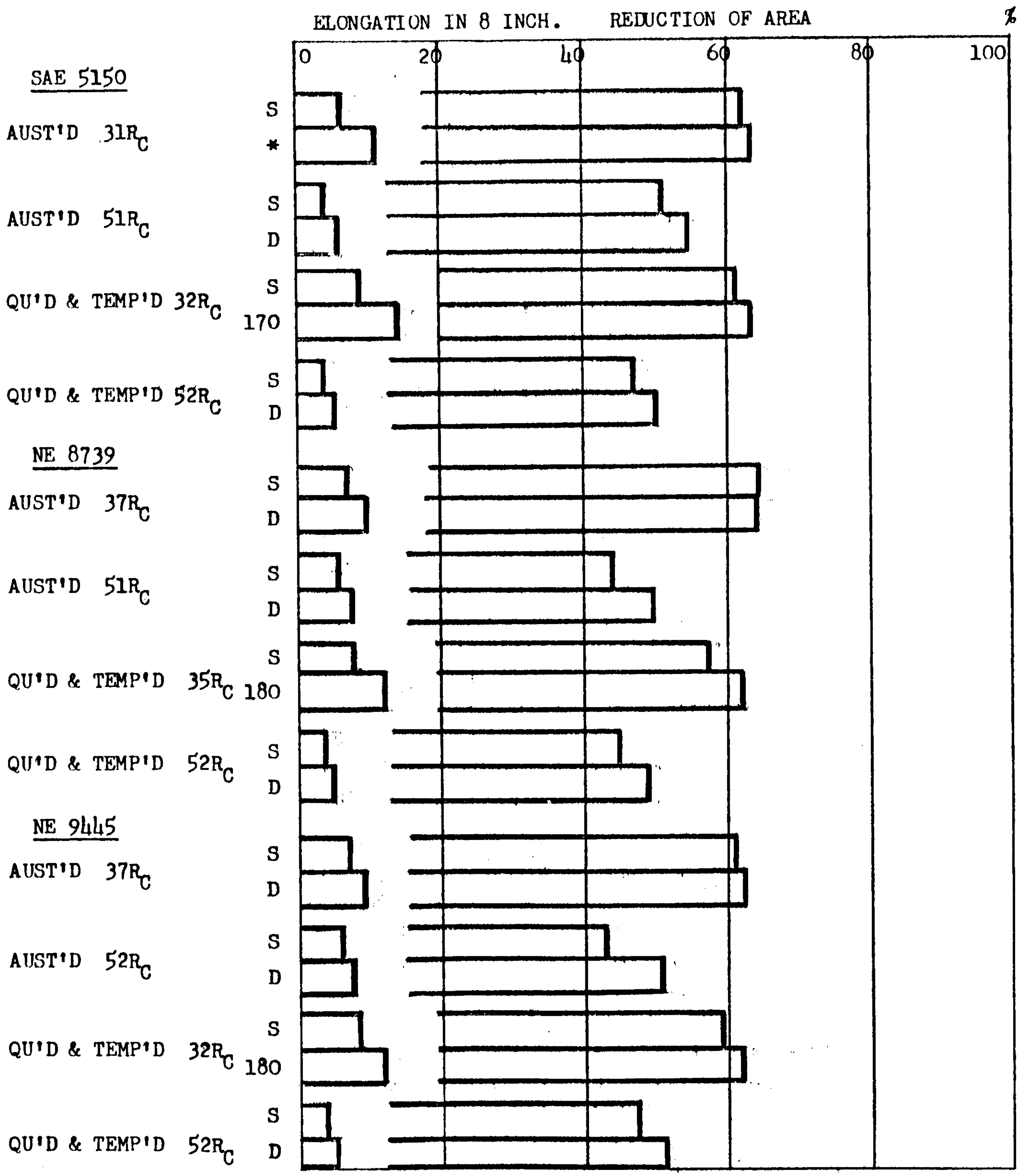

After Clark & Wood 1950 * Impact Velocity Feet/Second

STATIC AND DYNAMIC DEFORMATION IN TENSILE TESTING

VARIOUS ALLOY STEELS

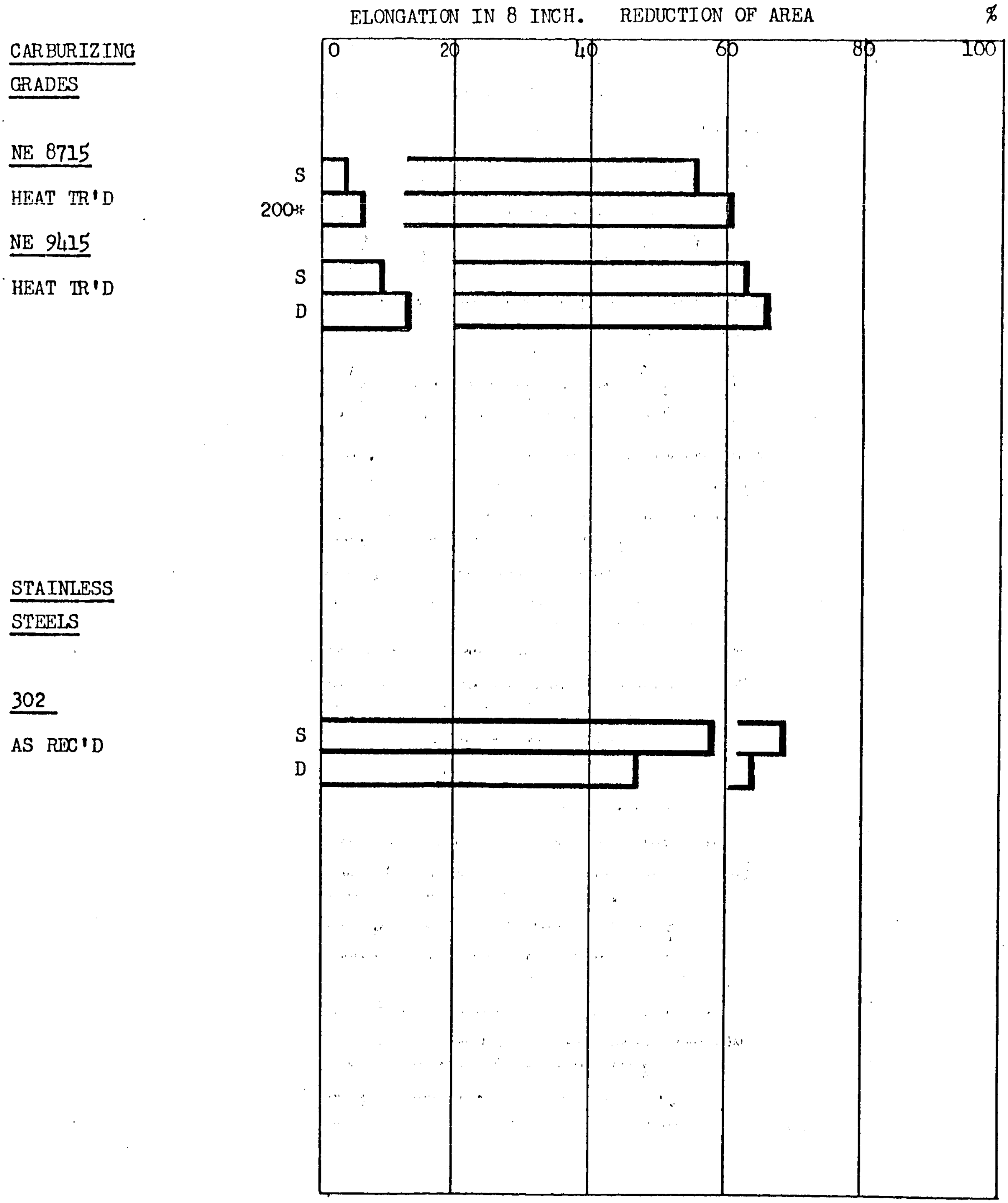

After Clark & Wood 1950 *Impact Velocity Feet/Second

STATIC AND DYNAMIC DEFORMATION IN TENSILE TESTING

COPPER AND ZINC MATERIALS

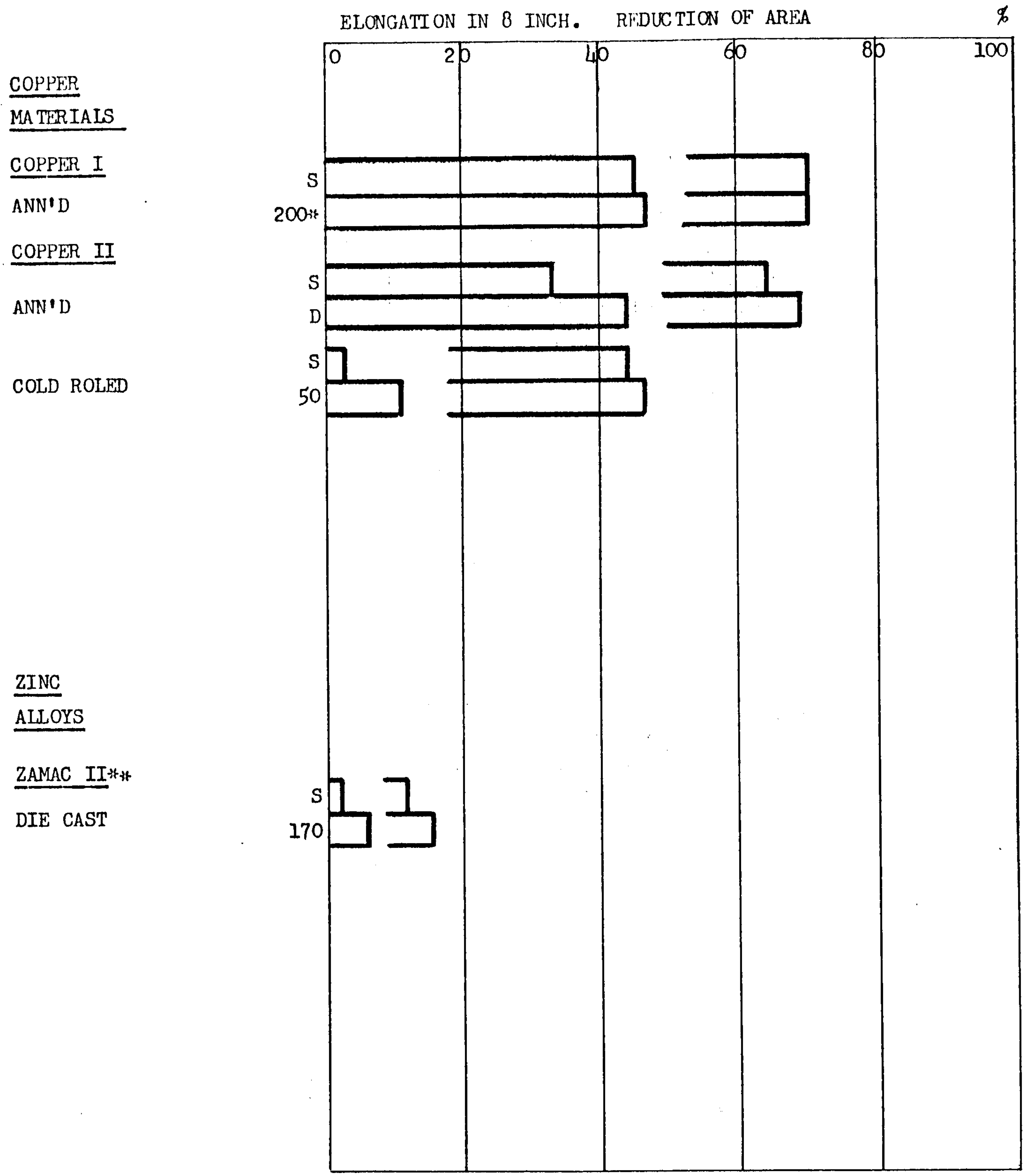

** 4" GAGE LENGTH

After Clark & Wood 1950 *Impact Velocity Feet/Second

STATIC AND DYNAMIC DEFORMATION IN TENSILE TESTING

ALUMINUM AND MAGNESIUM MATERIALS

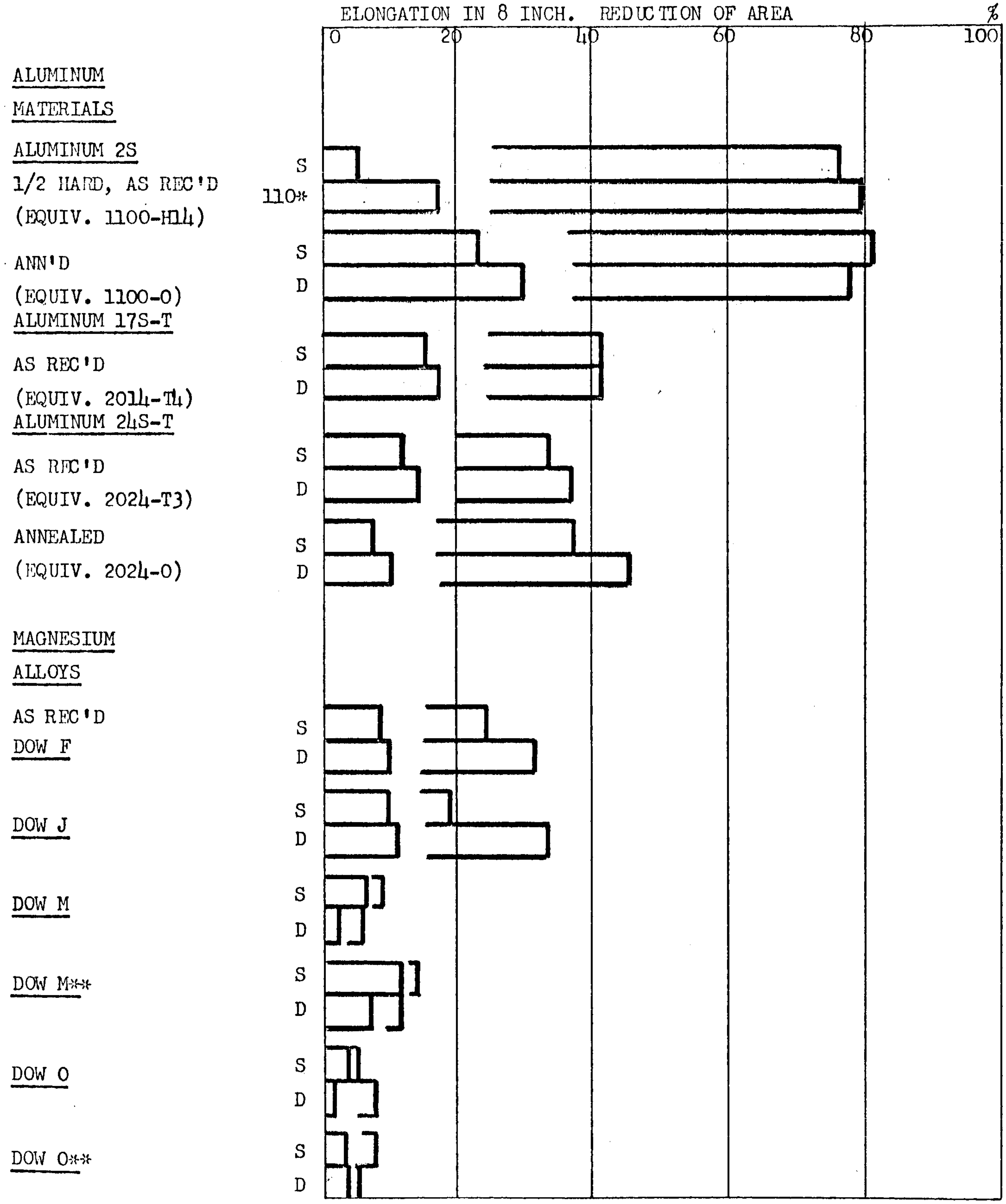

** 5 INCH FILLET RADIUS

After Clark & Wood 1950

*Impact Velocity Feet/Second

APPENDIX A2

BRITISH INVESTIGATIONS

1. Work by B. Hopkinson

The work by B. Hopkinson (Ref. 28) has been analyzed. Data are available for "Iron, annealed" (approximately equivalent to present-day low carbon mild steel), and for "Copper" (approximately equivalent to hard drawn copper wire). Impact was accomplished by loading wires with a falling weight. Comparable static and dynamic data could be extracted for the elastic limit.

The impact velocity could be calculated, being defined by the height of fall and the masses in the system. The strain ε at and after impact is given by

$$\varepsilon = 2 \frac{V}{a} e^{-\frac{\mu a t}{M}}$$

V = velocity just after impact,

$a = \sqrt{\frac{E}{\mu}}$ = propagation velocity of the elastic wave,

μ = mass of wire per foot,

M = mass of falling weight,

t = time elapsed since stress peak.

Hence the strain rate $\dot{\varepsilon}$ is

$$\dot{\varepsilon} = \frac{d\varepsilon}{dt} = -2\mu \frac{V}{M} e^{-\frac{\mu a t}{M}}$$

or

for iron $\dot{\varepsilon} = -1.496\ e^{-736.89t}$

for copper $\dot{\varepsilon} = -1.3188\ e^{-628t}$

By inserting the numerical values, the following results are obtained:

		Units	Iron	Copper
Elastic Limit	Static	psi	40,000	38,200
	Dynamic	psi	$\geqslant$ 75,000	$\geqslant$ 48,900
Increase, dynamic versus static		%	$\geqslant$ 87.5	$\geqslant$ 27.2
Impact velocity		ft/sec	17.2	12.4
Strain Rate	During Impact	in/in/sec	*)	*)
	Immediately after impact	in/in/sec	1.496	1.319

*) Not calculable from published data.

2. Work by Taylor, Whiffin and Carrington

The work by these investigators (Ref. 29) was concerned with the effect of rates of compressive strain, generated by firing cylindrical slugs against stationary armor plate. By measurement and analysis, it was found possible to determine not only the strain rate, but also the actual yield stress during the deformation process; in other words, to obtain elements of dynamic stress-strain curve.

High compressive strain rates, of 15,000 - 18,000 in/in/sec, were used. Steel materials ranged from 37,700 to 248,000 psi static yield strength. A considerable increase in yield strength, up to 250%, was found at these strain rates. The increase in yield strength was clearly a function of the static yield strength, regardless of heat treatment and chemical composition; the weakest materials showed the highest percent increase.

Whether the same or a similar relationship holds at lower strain rates was not determined conclusively. The results are summarized in two graphs on Figure A2-1.

3. Work by Brown and Vincent

Brown and Vincent (Ref. 30) investigated the effect of tensile loading at strain rates up to 900 inch per second. They used five different steels, representing a wide range of tensile strengths. The available materials analysis and properties are listed in Table A2-I.

The data for ultimate tensile strength and yield strength obtained under the various strain rate conditions are shown graphically in Figure A2-2, plotted over strain rate. It is clearly seen that yield strength is more strain rate sensitive than ultimate tensile strength, and that the strain rate sensitivity is generally greatest for the weaker steels and generally decreases as the strength of the material increases.

Three of the same materials were also tested in compression by Taylor et al (Ref. 29), using the very high strain rate of 18,000 inch per inch per second. The results are shown in comparison with the data by Brown and Vincent in Figure A2-3, plotted on a logarithmic scale for the strain rates in order to obtain a perspicuous presentation.

TABLE A2-I

Analysis and Properties of Steels Investigated by Brown and Vincent

Material	Ultimate Tensile Strength psi	Yield Strength psi	CHEMICAL ANALYSIS							
			C	Si	Mn	Ni	Cr	Mo	S	P
Best Yorkshire Iron	51,500	37,000	-	-	-	-	-	-	-	-
Medium-Carbon Steel	86,900	40,300	0.3	0.2	0.67	0.10	0.09	-	0.057	0.046
Low-Carbon Manganese Steel	118,700	100,800	-	-	-	-	-	-	-	-
Nickel-Chromium Steel	128,100	107,500	0.16	0.27	0.39	3.55	0.47	-	0.037	0.037
Vibrac Steel	161,300	145,600	0.33	0.22	0.73	2.64	0.56	0.64	0.037	0.035

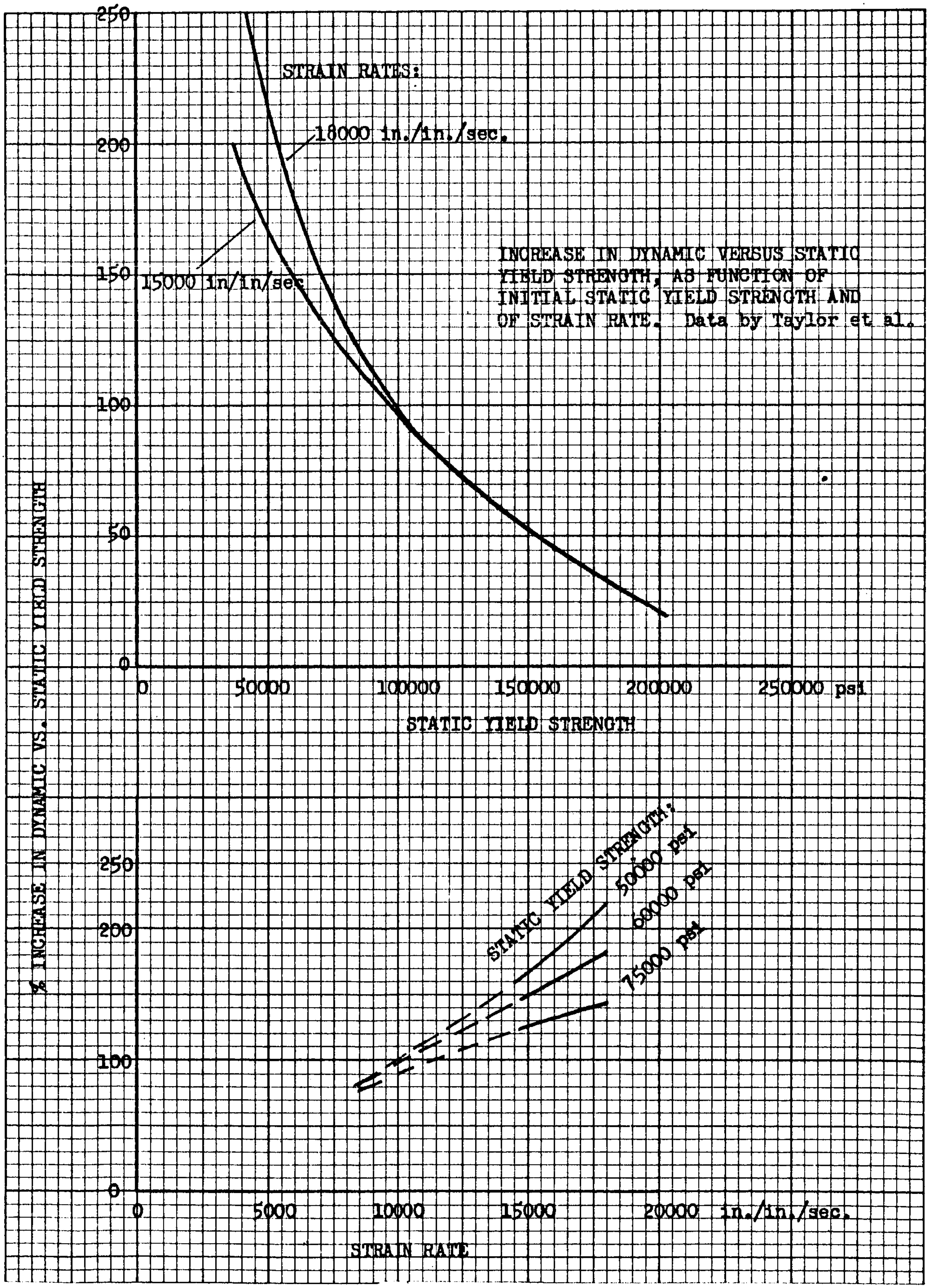

STRAIN RATES:
18000 in./in./sec.
15000 in/in/sec
INCREASE IN DYNAMIC VERSUS STATIC YIELD STRENGTH, AS FUNCTION OF INITIAL STATIC YIELD STRENGTH AND OF STRAIN RATE. Data by Taylor et al.
% INCREASE IN DYNAMIC VS. STATIC YIELD STRENGTH
250
200
150
100
50
0
0
50000
100000
150000
200000
250000 psi
STATIC YIELD STRENGTH
STATIC YIELD STRENGTH:
50000 psi
60000 psi
75000 psi
250
200
100
0
0
5000
10000
15000
20000 in./in./sec.
STRAIN RATE

Figure A2-1

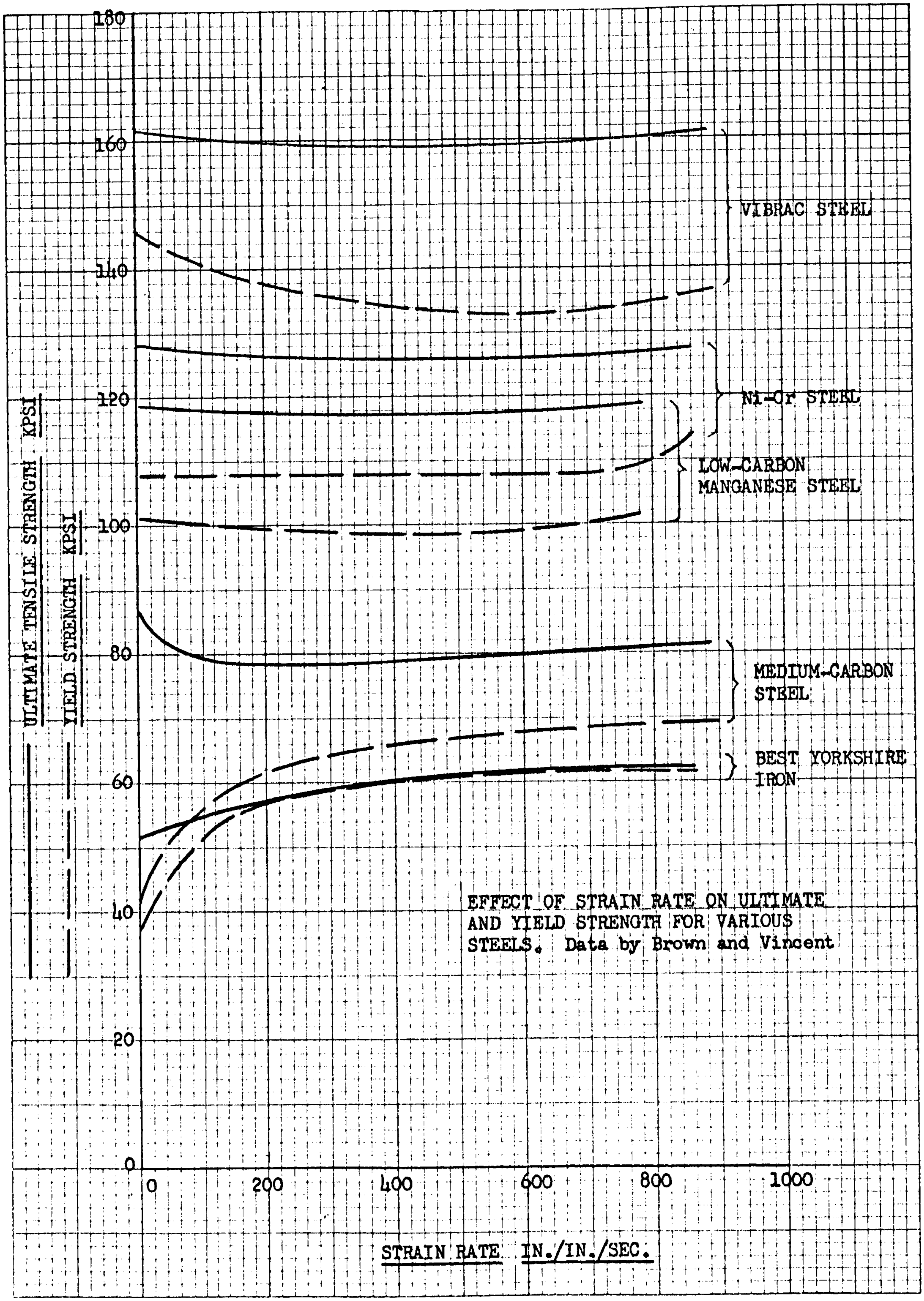
180
160
140
120
100
80
60
40
20
0
0
200
400
600
800
1000
ULTIMATE TENSILE STRENGTH KPSI
YIELD STRENGTH KPSI
VIBRAC STEEL
Ni-Cr STEEL
LOW-CARBON MANGANESE STEEL
MEDIUM-CARBON STEEL
BEST YORKSHIRE IRON
EFFECT OF STRAIN RATE ON ULTIMATE AND YIELD STRENGTH FOR VARIOUS STEELS. Data by Brown and Vincent
STRAIN RATE IN./IN./SEC.

Figure A2-2

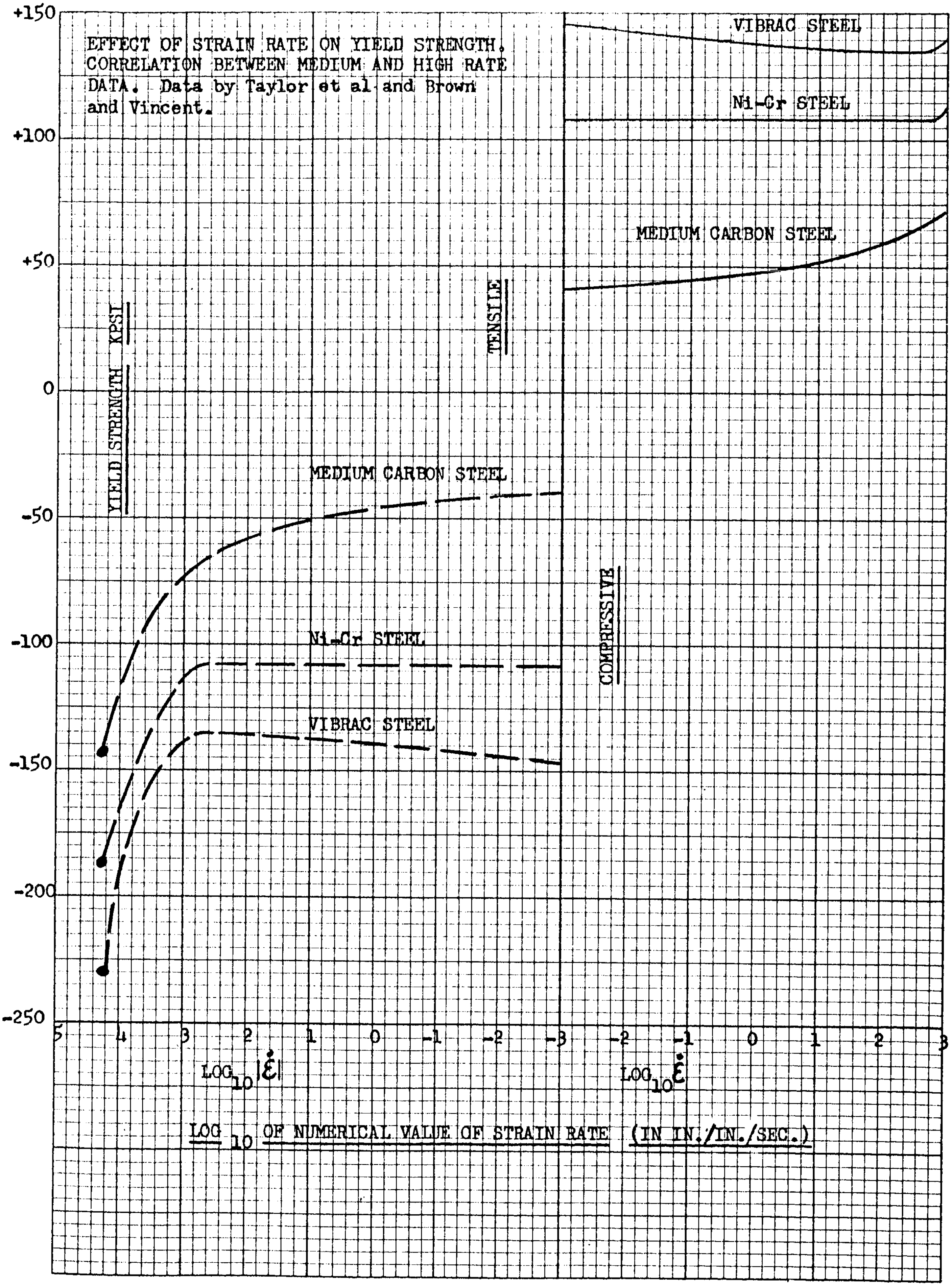
EFFECT OF STRAIN RATE ON YIELD STRENGTH. CORRELATION BETWEEN MEDIUM AND HIGH RATE DATA. Data by Taylor et al and Brown and Vincent.
YIELD STRENGTH KPSI
TENSILE
COMPRESSIVE
VIBRAC STEEL
Ni-Cr STEEL
MEDIUM CARBON STEEL
MEDIUM CARBON STEEL
Ni-Cr STEEL
VIBRAC STEEL
+150
+100
+50
0
-50
-100
-150
-200
-250
5
4
3
2
1
0
-1
-2
-3
-2
-1
0
1
2
3
$LOG_{10}|\dot{\varepsilon}|$
$LOG_{10}\dot{\varepsilon}$
LOG_{10} OF NUMERICAL VALUE OF STRAIN RATE (IN IN./IN./SEC.)

Figure A2-3

APPENDIX A3

DATA FROM WESTINGHOUSE

Comprehensive data on effects of strain rates up to 1000 inch per inch per second (and in a few cases even higher) have been published by Nadai and Manjoine (16,17) and by Manjoine (13). These data are considered particularly valuable, not only because they cover, to a large degree, the same range as is anticipated to be found in the explosive forming tests, but also because they are consistent and appear to be highly reliable. They are given with sufficient detail to permit an evaluation and to make them useful for comparison with the future findings of this project.

The loading is in tension and is applied by means of a special, controlled-speed testing machine, described by Manjoine, Wessel and Pryle (19). The major effort was concentrated on the strain rate effect on ultimate tensile strength, but one material, mild steel, was investigated for ultimate, yield, and elongation. In several cases, values were also given for true stress.

Five materials were investigated. They are listed in Table A3-I. The data have been consolidated and are presented graphically in Figures A3-1 through A3-5.

An important observation is the fact that material properties are, in several cases, affected strongly by moderate or even small strain rates, far below the rates to be encountered in explosive forming.

The data presented here are all for room temperature testing. Data for testing at elevated temperatures have been omitted because they fall outside of the scope of the project at the present time.

TABLE A3-I

MATERIALS INVESTIGATED BY NADAI AND MANJOINE

MATERIAL	GRADE	ANNEALING TREATMENT
Pure Iron	Wemco Research Iron 99.95% Fe	2 hr. at 700°C
Copper	Commercially Pure	5 hr. at 500°C
Aluminum	Commercially Pure Grade 2S	2 hr. at 400°C
Mild Steel	Commercial Low-Carbon, open-hearth	1 hr. at 920°C
Stainless Steel	Commercial 18Cr-8Ni	1 hr. at 1100°C

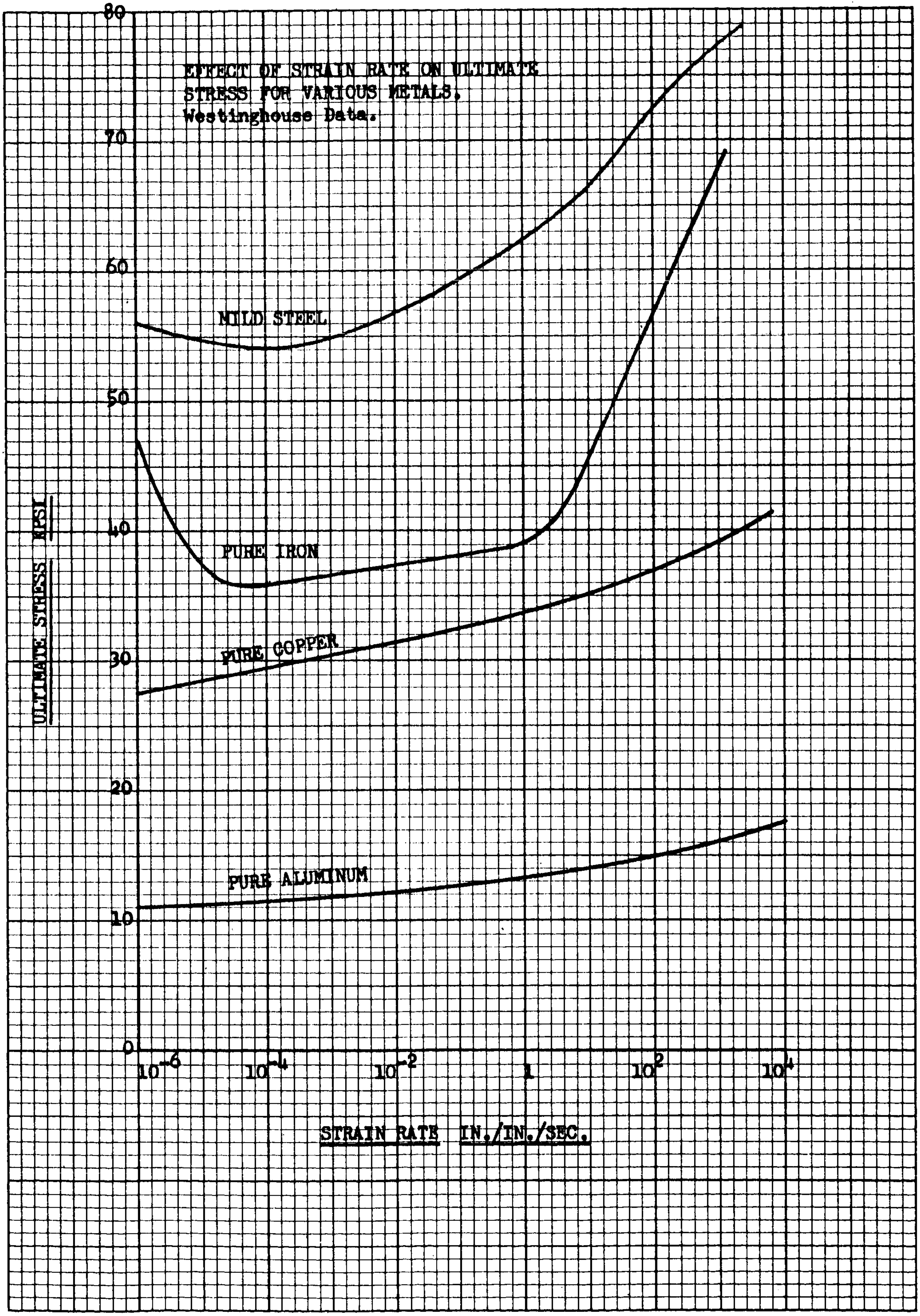
EFFECT OF STRAIN RATE ON ULTIMATE
STRESS FOR VARIOUS METALS.
Westinghouse Data.
80
70
60
50
40
30
20
10
0
MILD STEEL
PURE IRON
PURE COPPER
PURE ALUMINUM
ULTIMATE STRESS KPSI
10^{-6}
10^{-4}
10^{-2}
1
10^{2}
10^{4}
STRAIN RATE IN./IN./SEC.

Figure A3-1

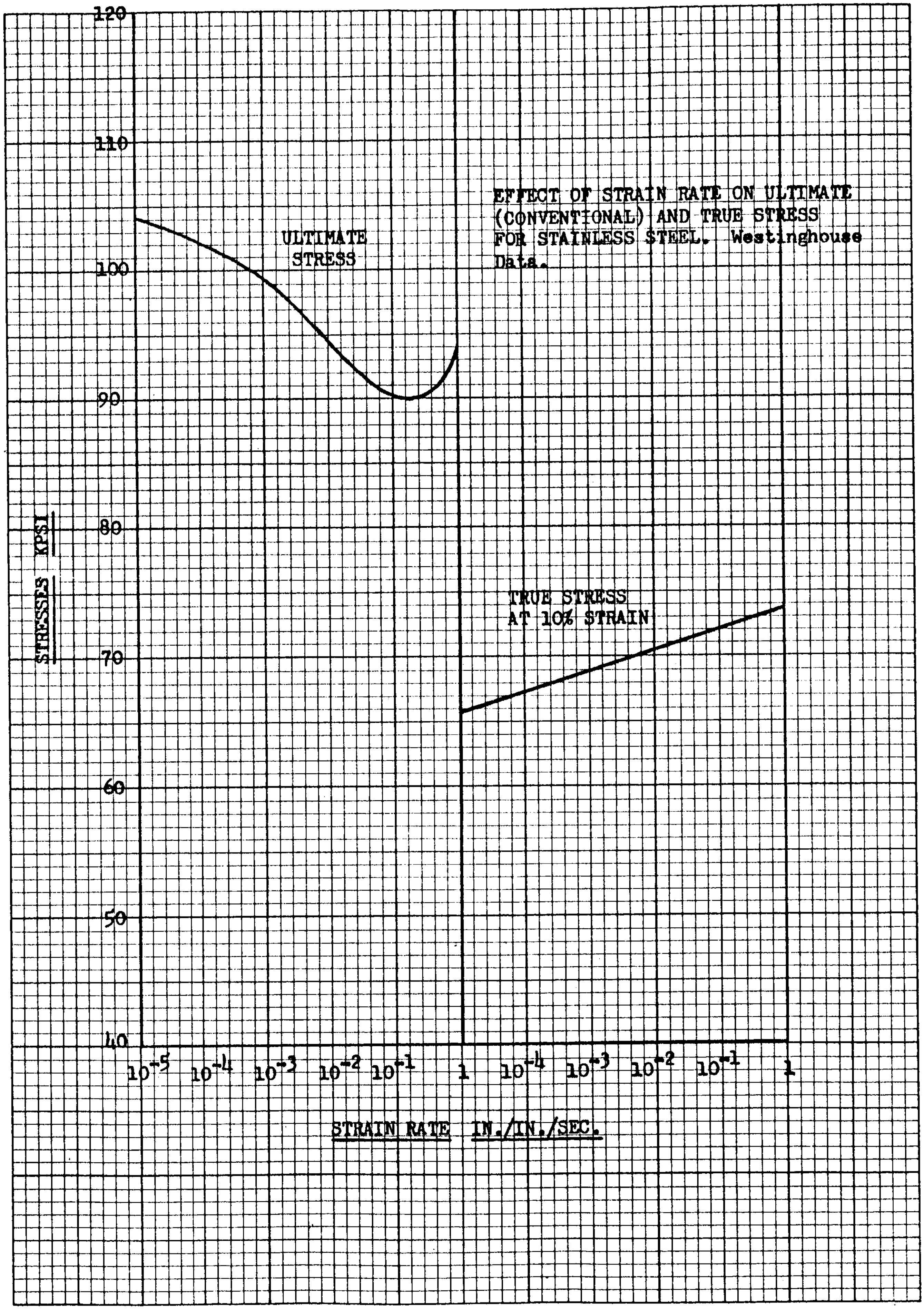
EFFECT OF STRAIN RATE ON ULTIMATE (CONVENTIONAL) AND TRUE STRESS FOR STAINLESS STEEL. Westinghouse Data.
ULTIMATE STRESS
TRUE STRESS AT 10% STRAIN
STRESSES KPSI
120
110
100
90
80
70
60
50
40
10^{-5} 10^{-4} 10^{-3} 10^{-2} 10^{-1} 1 10^{-4} 10^{-3} 10^{-2} 10^{-1} 1
STRAIN RATE IN./IN./SEC.

Figure A3-2

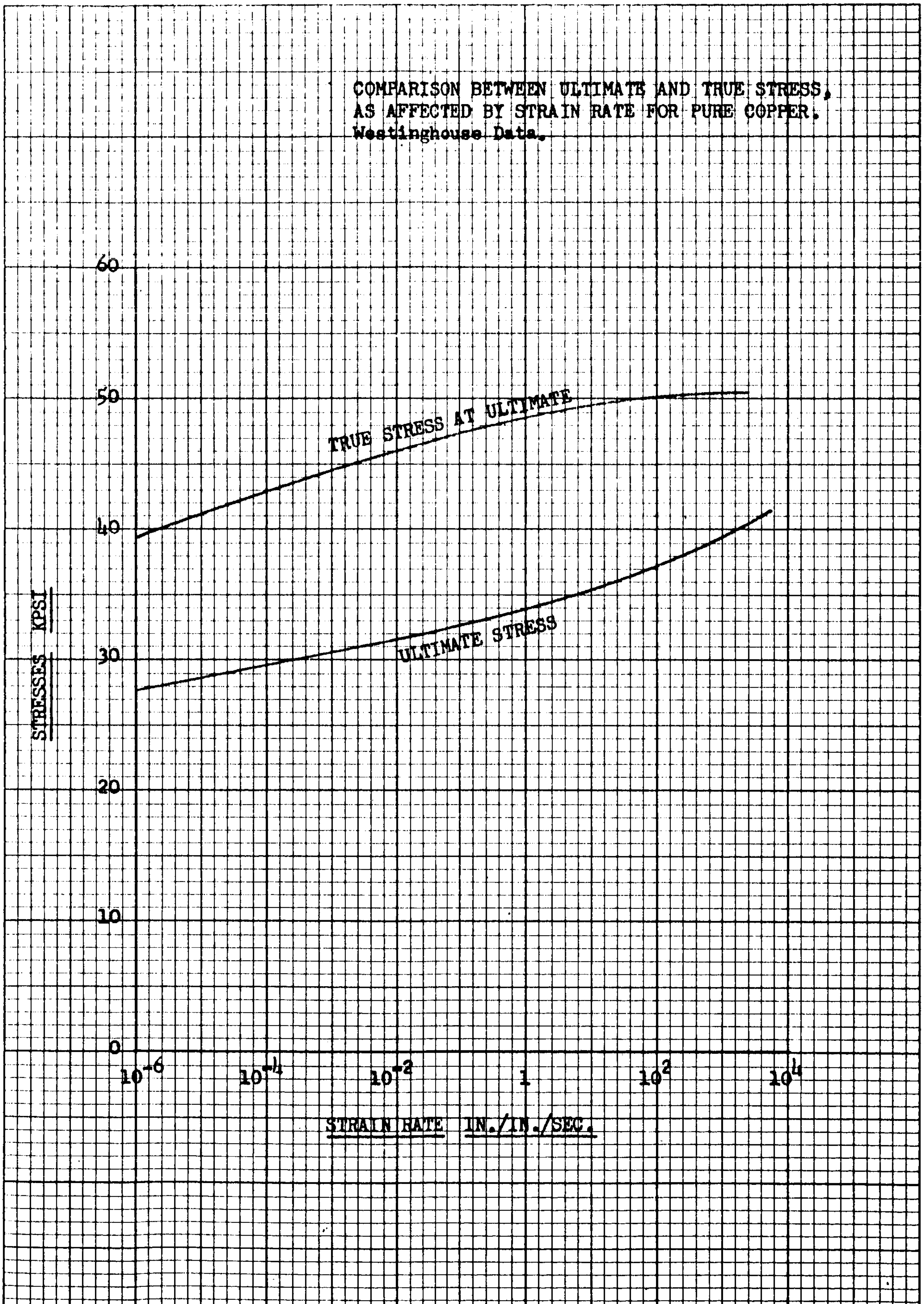
COMPARISON BETWEEN ULTIMATE AND TRUE STRESS,
AS AFFECTED BY STRAIN RATE FOR PURE COPPER.
Westinghouse Data.
TRUE STRESS AT ULTIMATE
ULTIMATE STRESS
STRESSES KPSI
60
50
40
30
20
10
0
10^{-6}
10^{-4}
10^{-2}
1
10^{2}
10^{4}
STRAIN RATE IN./IN./SEC.

Figure A3-3

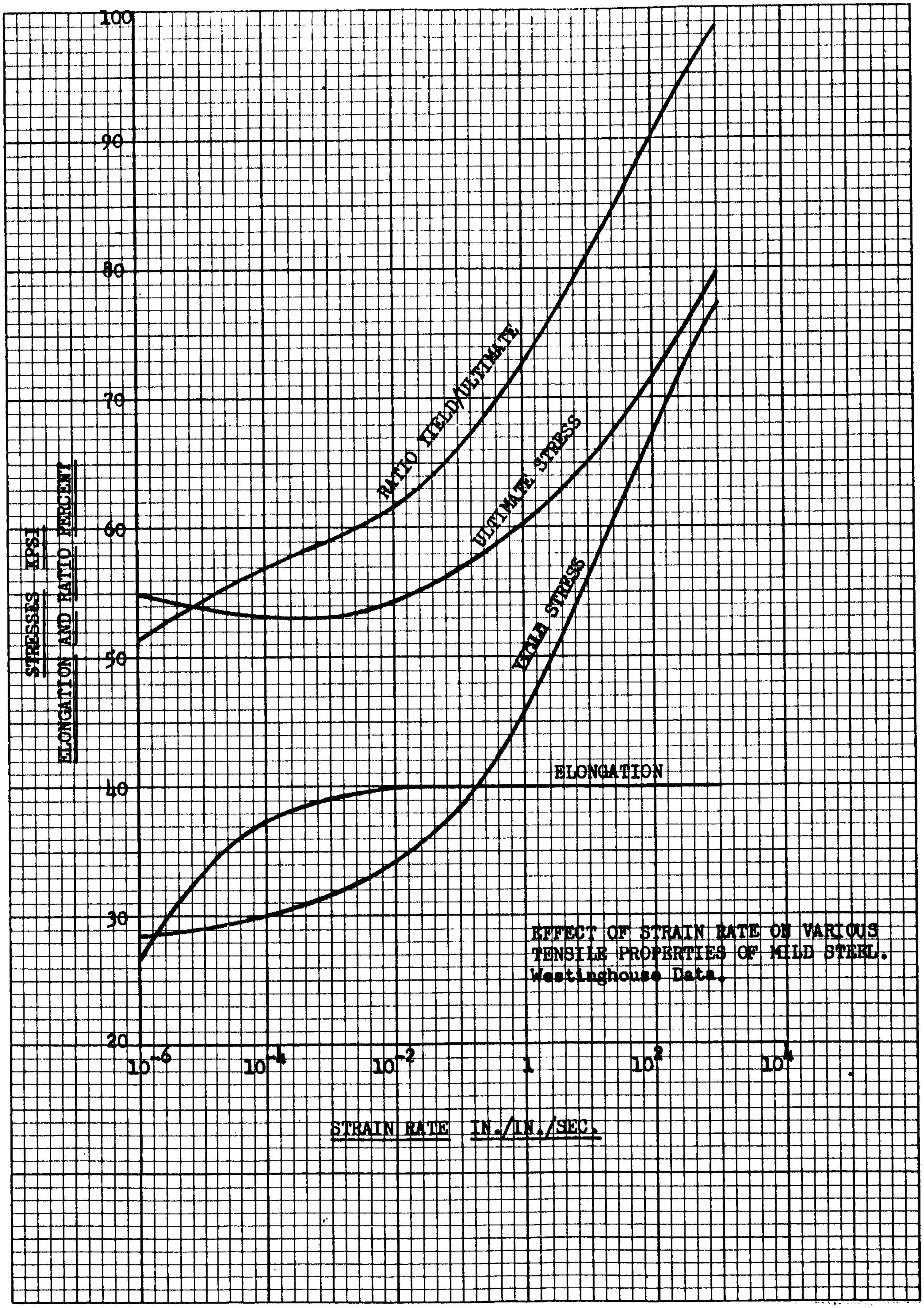

100
90
80
70
60
50
40
30
20
STRESSES KPSI
ELONGATION AND RATIO PERCENT
RATIO YIELD/ULTIMATE
ULTIMATE STRESS
YIELD STRESS
ELONGATION
EFFECT OF STRAIN RATE ON VARIOUS
TENSILE PROPERTIES OF MILD STEEL.
Westinghouse Data.
10^-6
10^-4
10^-2
1
10^2
10^4
STRAIN RATE IN./IN./SEC.

Figure A3-4

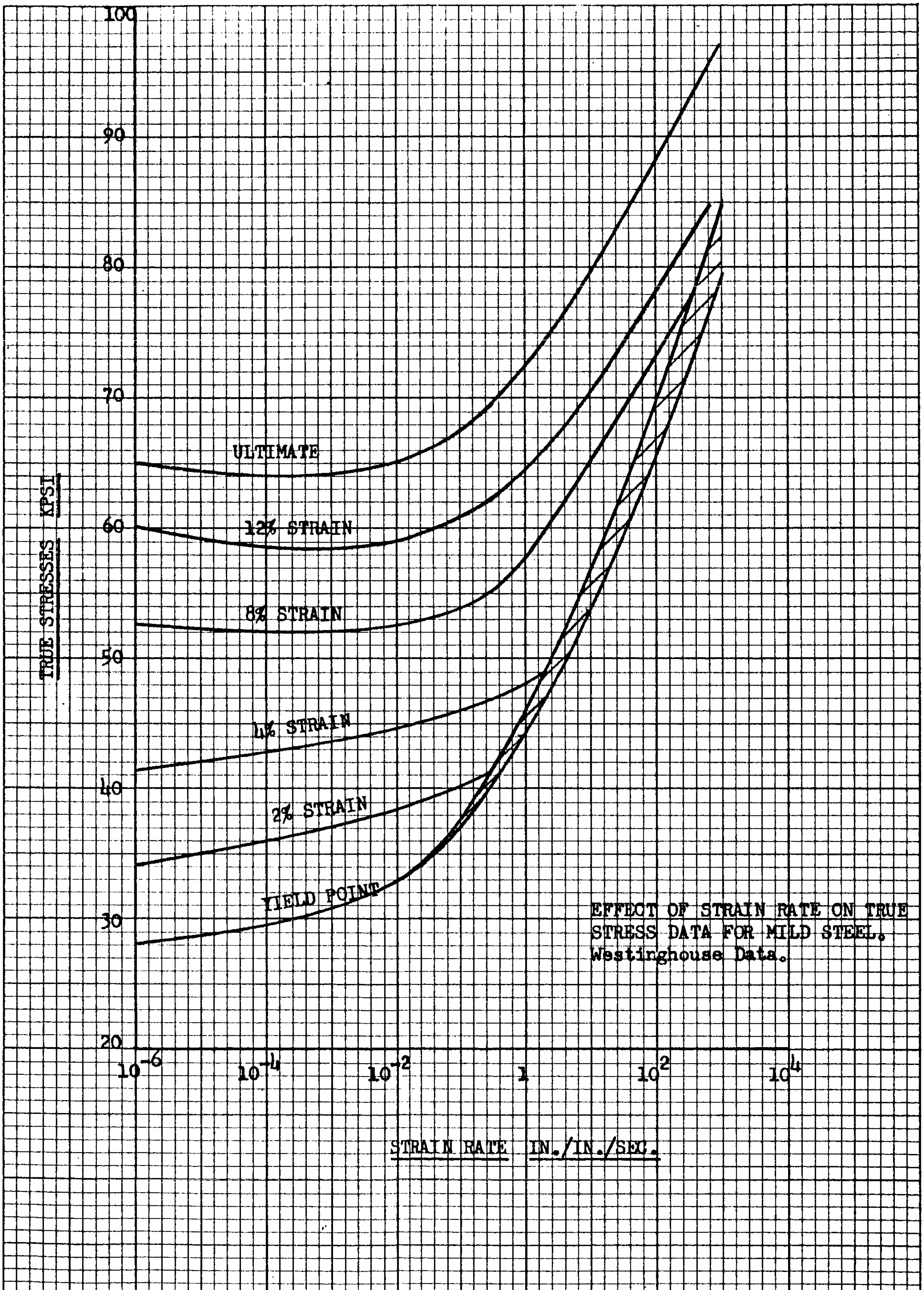

100
90
80
70
60
50
40
30
20
TRUE STRESSES KPSI
ULTIMATE
12% STRAIN
8% STRAIN
4% STRAIN
2% STRAIN
YIELD POINT
EFFECT OF STRAIN RATE ON TRUE STRESS DATA FOR MILD STEEL.
Westinghouse Data.
10^{-6}
10^{-4}
10^{-2}
1
10^{2}
10^{4}
STRAIN RATE IN./IN./SEC.

Figure A3-5

APPENDIX A4

EXTRACT FROM "BEHAVIOR OF METALS UNDER IMPULSIVE LOADS", BY JOHN S. RINEHART AND JOHN PEARSON

The following is an abbreviated extract from several sections of Rinehart and Pearson's book, with particular emphasis on definition of terms, explanation of elements of the microstructures of metals, and the general conclusions with regard to effect of high intensity impact loading on metals. It should be remembered that most of the findings are not applicable to explosive forming without serious modification because of the very large difference in loading conditions, particularly with respect to strain rate.

a. Definitions

(1) Strain Lines and Markings

Lines and markings, appearing on the surface of loaded bodies of polycrystalline metals, and caused by inhomogeneous (localized) plastic deformation.

They occur in materials exhibiting a yield point. They appear first as lines or narrow zones (Lueder's bands, Hartmann's lines), and spread gradually.

The planes defined by strain lines are approximately the planes of maximum shear stress. In tensile specimens of steel, the angle is 50 to 55 degrees with the axis. In objects of other shapes, the angle is roughly 45 degrees with the principal axes ("stretcher strains" in deep drawn parts).

Several intercepting line systems may appear, forming a crisscross pattern.

(2) Slip

Displacement of one part of the crystal relative to another along a definite crystallographic plane (slip plane) and in a crystallographic direction (slip direction).

The combination of a plane of slip and a direction of slip (in that plane) constitutes a slip system.

Slip (in a certain slip direction on a certain slip plane) starts when the stress component (a shear stress) in the slip direction reaches a value called the critical resolved shear stress.

A grain of a polycrystalline metal offers more resistance to slip than does a single crystal because of differences in orientation between adjacent grains. This restrictive effect causes less slip to occur near a grain boundary than at the center of the grain (Figure A4-1).

(3) Deformation Bands

Lamellar regions, formed on crystallographic planes, and within which different orientations are gradually developed as the deformation increases.

Deformation bands are formed in single crystals and in grains of polycrystalline metals. They occur in most face-centered and body-centered metals.

Banding may cause bending of lattice planes and considerable strain hardening.

"Kink bands" and "bands of secondary slip" are special types of deformation bands.

(4) Twinning, Deformation Twinning, Mechanical Twinning

Results from sliding of consecutive planes of atoms, the movement of each plane being proportional to its distance from "the twinning plane". A new lattice, of the same type as the original one, but with a different orientation, is formed.

Twinning is a result of a shearing action and occurs in definite crystallographic planes (twinning planes) and crystallographic directions (twinning directions). There is evidence of a critical shear stress for twinning.

Twinning is visible as lamella of readily visible width. They are quite common in close-packed hexagonal metals, do not appear to occur in face-centered cubic metals, and are relatively uncommon in body-centered cubic metals such as iron, under non-impulsive loads, but appear prominently after impact loading. The lamellae are known as Newmann bands or shock twins.

Two different forms of twins have been observed. Feathered twins are wide twins with irregular boundaries. Normal twins are thinner and have straight, parallel boundaries.

A family of twins (a twin family) is a group of parallel twins within a single grain. One grain may contain more than one twin family.

b. Strain Rate Effects in General

Increasing strain rate has the following effects:

(1) Increase of the yield strength.

(2) Increase of the entire stress level of the flow curve (i.e., the true-stress-strain curve).

(3) Increase of the ultimate strength of the material.

(4) In general, increase of the specific energy to fracture.

(5) Decrease of the fracture elongation (quote from p 107: "For example, at low temperature or under rapid rates of loading, very little plastic deformation precedes fracturing". Quote from p 109: "The tendency for a metal to deform by grain flow increases with high pressure and high temperature and decreases with low temperature and high strain rates).

The data given are, however, related to impact velocity rather than to actual strain rate, although strain rate will, in general, increase with impact velocity. A direct correlation with quantitatively defined actual strain ratio is not presented; nor, is there any comparison between specimens loaded impulsively and statically to the same amount of strain.

In general, the statements are valid only up to the critical impact velocity.

The effects of an increase in strain rate is usually equivalent to the effects of a decrease in temperature.

Primary strain rate effects on microstructures may be obscured by localized adiabatic heating due to plastic deformation work. Such local heating may be sufficient to cause a complete phase change, or to partly anneal or recrystallize the material.

c. Pressure Effects (pp 19-21)

Application of high strain rates may be associated with the simultaneous occurrence of high pressures, and high pressure effects may enter into the picture.

Such high pressure effects are:

(1) A transition from brittle to ductile failure.

(2) Extreme increase of fracture strain.

(3) Decrease of the compressibility (with the exception of the alkali metals).

(4) Increase of the strength for both tension and compression.

(5) Increase of the modulus of rigidity (G).

(6) Increase of Young's modulus (E).

(7) Some effect on Poisson's ratio, without generalized statements.

d. Effects of Impulsive Loading on Microstructural Elements

(1) Grain Distortions

Metals exposed to explosive or other type of impact loading will generally show grain distortion in areas adjacent to the load application and in areas of concentrated shear stress.

The distortion will take the shape of severe grain flow for ductile materials such as mild steel, and grain fragmentation for materials which fail in a brittle fashion.

(2) Slip

The distribution and characteristics of slip lines and bands are affected by strain rate and temperature.

Slip bands in aluminum and copper broken in tension at moderate impact velocities showed an increase in number and a decrease in distance as the strain rate increased. A similar effect was found for aluminum tested at constant strain rate and decreasing temperature.

Slip phenomena are usually not observed in materials which behave in a brittle fashion.

Ductile materials, exposed to high strain rates under explosive loads will usually exhibit extensive slip in multiple slip systems (Figure A4-2).

(3) Relation Between Slip and Neumann Bands (Twins)

Observations on specimens tested by mechanically produced impact loads indicate that grains which contain Neumann bands (shock twins) are almost, if not entirely, free from slip.

(4) Deformation Bands

Deformation bands, formed under impact, may sometimes be difficult to distinguish from other deformation phenomena, such as twins. However, one case is known where deformation bands were formed in duralumin, deformed in compression at impact velocities from 500 to 2160 ft/sec.

Each band was confined to a single grain. The bands were apparently formed at an early stage because they showed subsequent deformations in accordance with the general pattern of grain flow. In addition, there were slip lines in the same grains, and differential etching indicated that the slip lines were also formed subsequent to the formation of the bands.

(5) Twins

The general pattern of twin formation in explosively or otherwise impulsively loaded bodies shows the following variation in the direction outwardly from the point of load application:

(a) The extent of grain distortion decreases rapidly.

(b) The overall amount of shock twinning decreases.

(c) The number of grains containing twins decreases.

(d) Individual grains contain fewer twin families.

(e) Each twin family contains fewer twins.

(f) The number of grains containing several twin families decreases.

(g) The predominating form of twins changes gradually from feathered twins to normal (straight-sided) twins.

(h) The average width of twins decreases.

The amount of twins decreases with increased carbon content and with increased cold-work induced hardness.

The statements made above are illustrated by examples taken from several tests with explosively loaded specimens of annealed low-carbon steel. In one series of illustrations, comparison was made between structures taken at 1/64-inch, 5/64-inch, and 1-7/16-inch distance from the explosive charge. This variation corresponds undoubtedly to a qualitatively equivalent variation in strain rate (Figures A4-3, A4-4, and A4-5).

In another case, comparison was made between structures from a cylinder, loaded by an internal explosion, and a flat plate explosively loaded from one side. For this case, it is explained that the cylinder wall has been exposed to a load of longer duration than the flat plate.

An interference occurs between grain distortion (ductile flow) and twins. Close to the load application, the heavy grain flow obscures the twins. A short distance further out, both deformation modes are distinguishable. The twins appear distorted by the grain flow, indicating that twins were initiated prior to the onset of the flow.

Grain flow appears to stop rather abruptly at a certain distance from the load application, while shock twins continue to appear in considerable numbers beyond this limit, although the frequency gradually diminishes with increasing distance.

It is indicated that not only the number but also the form of the twin depend on the strain rate and that feathered twins are produced by more slowly applied stress (Figure A4-6).

The two different forms of twins may be found in the same grain; however, they will then tend to form two different twin families. If the twins from two such families cross, then the narrow twins are generally displaced (Figure A4-7).

Twins do not appear to contain any appreciable amount of stored energy. They are in themselves stable and require heating to the upper critical temperature for their removal by recrystallization. The situation is entirely different where the twinning is accompanied by grain distortion. The necessary temperature for recrystallization, including the complete removal of the twins, may, in such cases, be lowered by from 250 to 450°F.

SLIP LINES

Note that concentration of slip lines is greater at center of grain than at grain boundaries.

Note different directions of slip lines within a single grain.

Low Carbon Steel (Mag. 450X)

Figure A4-1

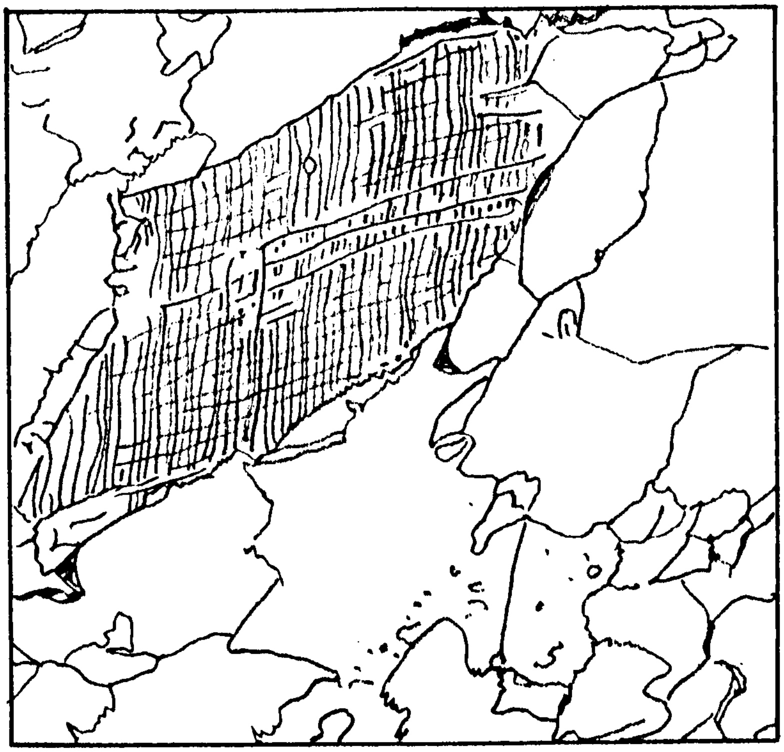

MULTIPLE (INTERSECTING) SLIP LINE SYSTEMS

Explosively Loaded Brass (Mag. 610X)

Figure A4-2

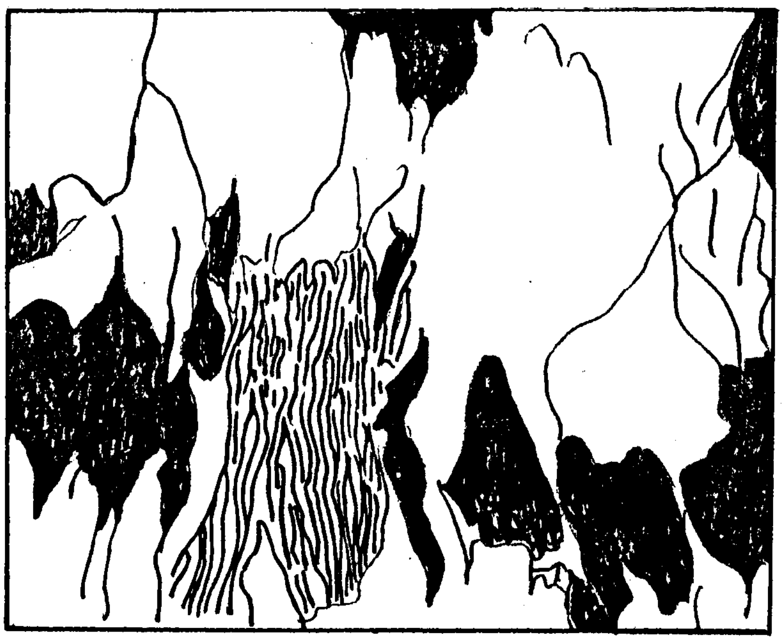

GRAIN DISTORTION

Heavy Ductile Flow Obscuring Twins.

Explosively Loaded Low Carbon Steel

1/64-inch from explosive charge. (Mag. 450X)

Figure A4-3

GRAIN DISTORTION AND TWINNING

Note that twins are distorted with grain.

Explosively Loaded Low Carbon Steel.

5/64-inch from explosive charge (Mag. 450X)

TWINNING, ABSENCE OF GRAIN DISTORTION

Explosively Loaded Low Carbon Steel

1-7/16 inch from Explosive Charge (Mag. 450X)

Figure A4-5

FEATHERED TWINS

Explosively Loaded Low Carbon Steel (Mag. 930X)

Figure A4-6

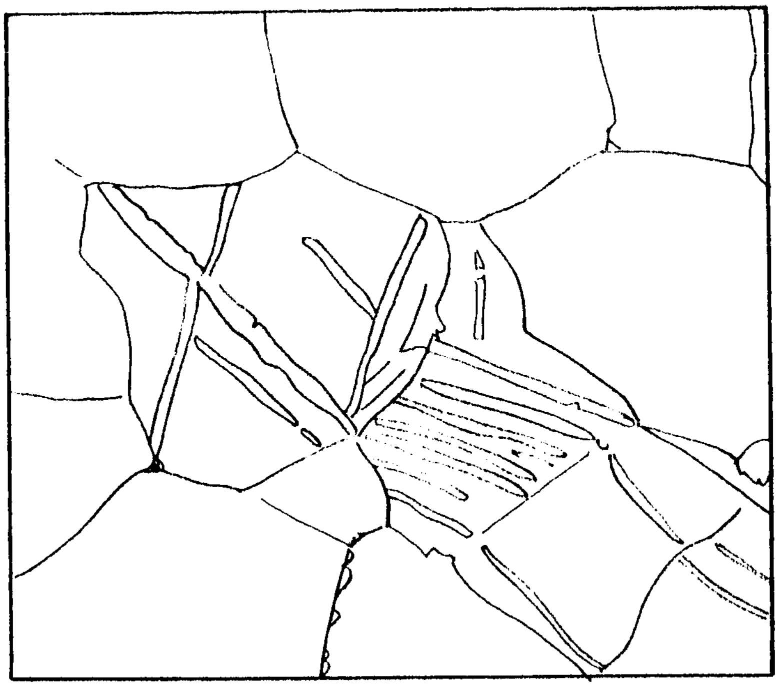

TWO INTERSECTING TWIN FAMILIES

Note that the normal (thin) twin is displaced at point of intersection with feathered twin.

Explosively Loaded Low Carbon Steel (Mag. 1060X)

Figure A4-7

APPENDIX - B

INVESTIGATION OF RESIDUAL STRESSES IN A CIRCULAR DOME

Definitions and Notations

In the problem of investigating the residual stresses in an explosively formed dome, the dome is considered to be a shell, that is, a structure in which one dimension, the thickness, can be considered small in comparison with the other dimension and with radius of curvature.

This leads to a number of simplifications, the justification for which is found in the generally recognized results of shell theory.

The surface that bisects the thickness dimension, is called the middle surface. While most measured dimensions are taken to the outer surface of the dome, they are converted to the middle surface by calculations, where appropriate.

The dome is considered to be axi-symmetrical, so that its middle surface is a surface of revolution.

Most notations used in this discussion are identical with the notations for shell analysis used in "Theory of Plates and Shells", by S. Timoshenko and S. Woinowsky-Krieger, Second Edition, 1959. References to this work are indicated by TWK. The notations, as used here, are listed in Table No. B-1. The most important deviation from TWK is that ρ with subscripts are used for radii of curvature, while r with subscripts are used for radii measured to the middle surface.

Some measurements were taken to the formed contour. Other measurements were taken to the circular photogrid applied to the blank prior to forming. A sample of the photogrid is shown in Figure B-1. When reference is made to the circles, the circles are numbered consequtively from the center, the center being No. 0.

Rings separated from the dome in the sectioning process are denoted by the number of the middle circle, that is, the circle which is located approximately at the middle of the ring surface. Thus the rings are numbered 8, 16, . . . , 80, and 90. The central member forms a small circular blank, not a ring, and is denoted as No. 2, from the circle located at the half-way point on the blank radius.

Subscripts 0 refer to dimensions and other quantities associated with the middle circles. Subscripts 1 and 2 refer to inner (upper) and outer (lower) edges of rings, including the center blank.

Most of the dimensional and force notations are shown in Figure B-2. Other notations are illustrated in Figures B-3 and B-7.

General Theory for a Dome

In the general theory of shells subjected to an external load, there are five unknowns, (see Figure B-2), the normal force N_ϕ, the sheering force Q_ϕ, and the bending mement M_ϕ, on a normal section along a parallel circle, and the normal force N_θ and the bending moment M_θ on a radial section. For reasons of symmetry, there is no shearing force on a radial section. In the general theory, there are also external loads which are known quantities.

The general theory provides three equilibrium equations, which include the five unknowns and the load terms (TWK, p. 534, eq. (312)). For residual stresses only, the load terms become zero and the equations read:

$$\left.\begin{aligned} \frac{d}{d\phi}(N_\phi r_o) - N_\theta \rho_1 \cos\phi - Q_\phi r_o &= 0 \\ N_\phi r_o + N_\theta \rho_1 \sin\phi + \frac{d}{d\phi}(Q_\phi r_o) &= 0 \\ \frac{d}{d\phi}(M_\phi r_o) - M_\theta \rho_1 \cos\phi - Q_\phi \rho_1 r_o &= 0 \end{aligned}\right\} \quad (1)$$

These equations are differential equations, developed for an infinitely small element, as shown in Figure B-3. For an element of finite width s, as the one shown in Figure B-2, the differential equations must be superseded by a set of difference equations, which shall now be developed.

While Figure B-2 shows only the directions and general notations for the unit forces and moments, the value of the actual resultant forces and moments are shown in Figure B-4, when ACB is the middle line of the element. The forces and moments are derived as follows:

With the element bounded by two radial sections with the included angle $d\theta$, the length of the side at the upper edge, measured in the middle surface, is $r_1\, d\theta$. The resultant of the forces $N_{\phi,1}$ is $N_{\phi,1}\, r_1 d\theta$. The resultants of Q_ϕ and M_ϕ are found analogously.

The length of the side in the radial sections, measured in the middle surface, is s, and the resultant of the forces N_θ acting on one side only is $N_\theta s$. The resultant of the forces N_θ acting on the two opposite sides is $N_\theta s d\theta$.

Likewise the resultant moment from M_θ on one side only is $M_\theta s$, and the resultant of the moments acting on the two opposite sides is $M_\theta\, s \cos \phi_o\, d\theta$ (see Figure B-5.)

Putting AB=s, assuming AB$\neq$tangent in C, projecting the forces on the axes Y and Z and taking moments around B results in the following three equilibrium equations:

$$\left.\begin{array}{ll}
N_{\phi,2}\, r_2\, d\theta \cos(\phi_2-\phi_o) - N_{\phi,1} r_1\, d\theta \cos(\phi_o-\phi_1) - N_\theta s d\theta \cos\phi_o & \\
- Q_{\phi,2} r_2\, d\theta \sin(\phi_2-\phi_o) - Q_{\phi,1} r_1\, d\theta \sin(\phi_o-\phi_1) & = 0 \\
N_{\phi,2} r_2 d\theta \cos\left[90-(\phi_2-\phi_o)\right] + N_{\phi,1} r_1 d\theta \cos\left[90-(\phi_o-\phi_1)\right] + N_\theta s d\theta \sin\phi_o & \\
+ Q_{\phi,2} r_2 d\theta \cos(\phi_2-\phi_o) \qquad - Q_{\phi,1} r_1 d\theta \cos(\phi_o-\phi_1) & = 0 \\
M_{\phi,2}\, r_2 d\theta \qquad - M_{\phi,1} r_1 d\theta \qquad - M_\theta s \cos\phi_o d\theta & \\
- Q_{\phi,1} r_1\, d\theta\, s \cos(\phi_o-\phi_1) + N_\theta s d\theta\, 1/2\, s \sin\phi_o & = 0
\end{array}\right\} (2)$$

which reduce to

$$\left.\begin{array}{llll}
N_{\phi,2} r_2 \cos(\phi_2-\phi_o) & -N_{\phi,1} r_1 \cos(\phi_o-\phi_1) & -N_\theta s \cos\phi_o & \\
- Q_{\phi,2} r_2 \sin(\phi_2-\phi_o) & -Q_{\phi,1} r_1 \sin(\phi_o-\phi_1) & & = 0 \\
N_{\phi,2} r_2 \sin(\phi_2-\phi_o) & +N_{\phi,1} r_1 \sin(\phi_o-\phi_1) & + N_\theta s \sin\phi_o & \\
+ Q_{\phi,2} r_2 \cos(\phi_2-\phi_o) & -Q_{\phi,1} r_1 \cos(\phi_o-\phi_1) & & = 0 \\
M_{\phi,2} r_2 & -M_{\phi,1} r_1 & -M_\theta s \cos\phi_o & \\
-Q_{\phi,1} r_1\, s \cos(\phi_o-\phi_1) & +1/2\, N_\theta s^2 \sin\phi_o & & = 0
\end{array}\right\} (3)$$

As a check on the correctness of (2) and (3) it can be shown, that they are transformed back to the original differential equations (1) by the following substitutions:

$$\left.\begin{array}{ll}
r_o \sim r_1 & r_o + dr_o \sim r_2 \\
\phi \sim \phi_1 & d + d\phi \sim \phi_2 \\
\cos\phi \sim \cos\phi_o & \sin\phi \sim \sin\phi_o \\
\cos(\phi_2 - \phi_o) = \cos(\phi_o - \phi_1) = 1 & \sin(\phi_2 - \phi_o) = \sin(\phi_o - \phi_1) = 1/2\, d\phi \\
ds \sim s & ds = \rho_1 d\phi \\
N_\phi \sim N_{\phi,1} & N_\phi + d N_\phi \sim N_{\phi,2} \text{ etc.}
\end{array}\right\} \quad (4)$$

It should be noted, that the first two of the equations (3) are free of moments and contain only three unknowns, N_ϕ, N_θ, and Q_ϕ. The forces can be eliminated and the normal and shearing stresses introduced by making use of the thickness h and substituting

$$\left.\begin{array}{l}
N = h\sigma \\
Q = h\tau
\end{array}\right\} \quad (5)$$

Formally, the equations (3) contain six unknowns, on account of the subscripts 1 and 2; it follows, however, from continuity reasons (see Figure B-6), that

$$N_{\phi,1}^{(n+1)} = N_{\phi,2}^{(n)} \quad \text{etc.} \qquad (5a)$$

Therefore, if the stresses with subscript 2 are known, the number of unknown are reduced to three. This is, a priori, the case for the last ring, because the outer edge is unloaded, i.e. all subscript 2 stresses equal zero. When the subscript 1 stresses for the last ring have been found, they automatically provide the subscript 2 stresses for the following ring, etc. The whole system of equations can thus be solved successively.

With this in mind, it will be convenient to separate unknown and known quantities by transposing the subscript 2 terms, while making the substitution (5), resulting in

$$\left.\begin{aligned}
&\sigma_{\phi,1} r_1 \cos(\phi_o - \phi_1) + \sigma_\theta s \cos\phi_o + \tau_{\phi,1} r_1 \sin(\phi_o - \phi_1) \\
&\qquad = \sigma_{\phi,2} r_2 \cos(\phi_2 - \phi_o) - \tau_{\phi,2} r_2 \sin(\phi_2 - \phi_o) = A \\
&\sigma_{\phi,1} r_1 \sin(\phi_o - \phi_1) + \sigma_\theta s \sin\phi_o - \tau_{\phi,1} r_1 \cos(\phi_o - \phi_1) \\
&\qquad = -\sigma_{\phi,2} r_2 \sin(\phi_2 - \phi_o) - \tau_{\phi,2} r_2 \cos(\phi_2 - \phi_o) = B
\end{aligned}\right\} \quad (6)$$

The still missing equation is obtained from deformation information.

With stresses $\sigma_{\phi,o}$ and σ_θ in an element located (see Figure B-7) on the middle circle of a ring, the peripheral strain ϵ_θ is given by

$$\left.\begin{aligned}
&\epsilon_\theta = \frac{1}{E}(\sigma_\theta - \nu\sigma_{\phi,o}) \\
&\sigma_\theta - \nu\sigma_{\phi,o} = E\epsilon_\theta
\end{aligned}\right\} \quad (7)$$

and is obtained from measurements before and after sectioning, as it shall now be explained.

Let the measured diameters on the middle circle in a ring be

D_1 before sectioning, under the action of the stresses $\sigma_{\phi,o}$ and σ_θ

$D_2 = D_1 + \Delta D_1$ after sectioning with $\sigma_{\phi,o} = \sigma_\theta = 0$

then

$$\epsilon_\theta = \frac{D_1 - D_2}{D_2} = -\frac{\Delta D_1}{D_2} \tag{8}$$

Finally by substituting

$$\sigma_{\phi,o} = 1/2 \ (\sigma_{\phi,1} + \sigma_{\phi,2}) \tag{9}$$

and rearranging the terms the deformation equation becomes

$$1/2\,\nu\,\sigma_{\phi,1} - \sigma_\theta = -1/2\,\nu\,\sigma_{\phi,2} - E\epsilon_\theta \tag{10}$$

Solution of the Equations

$\tau_{\phi,1}$ is first eliminated between the two equations (6) by multiplication by $\cos(\phi_o - \phi_1)$ and $\sin(\phi_o - \phi_1)$ respectively and adding, giving

$$\sigma_{\phi,1} r_1 \cos^2(\phi_o - \phi_1) + \sigma_\theta s \cos\phi_o \cos(\phi_o - \phi_1) + $$
$$+ \tau_{\phi,1} r_1 \sin(\phi_o - \phi_1)\cos(\phi_o - \phi_1)$$
$$= A\cos(\phi_o - \phi_1)$$

$$\sigma_{\phi,1} r_1 \sin^2(\phi_o - \phi_1) + \sigma_\theta s \sin\phi_o \sin(\phi_o - \phi_1)$$
$$- \tau_{\phi,1} r_1 \sin(\phi_o - \phi_1)\cos(\phi_o - \phi_1)$$
$$= B\sin(\phi_o - \phi_1)$$

$$\sigma_{\phi,1} r_1 + \sigma_\theta s \left[\cos\phi_o \cos(\phi_o - \phi_1) + \sin\phi_o \sin(\phi_o - \phi_1)\right]$$
$$= A\cos(\phi_o - \phi_1) + B\sin(\phi_o - \phi_1)$$

which reduces to

$$\sigma_{\phi,1} r_1 + \sigma_\theta s \cos\phi_1 = \sigma_{\phi,2} r_2 \cos(\phi_2-\phi_1) - \tau_{\phi,2} r_2 \sin(\phi_2-\phi_1) \qquad (11)$$

Next σ_θ is eliminated between (10)and (11) by multiplying (10) by $s \cos\phi_1$, giving

$$1/2\, \sigma_{\phi,1} \nu s \cos\phi_1 - \sigma_\theta s \cos\phi_1 = -1/2\, \sigma_{\phi,2} \nu s \cos\phi_1 - E\epsilon_\theta s \cos\phi_1$$

which, when added to (11) gives

$$\sigma_{\phi,1}(r_1 + 1/2\, \nu s \cos\phi_1) = \sigma_{\phi,2}(r_2 \cos(\phi_2-\phi_1) - 1/2\, \nu s \cos\phi_1) - \tau_{\phi,2} r_2 \sin(\phi_2-\phi_1) - E\epsilon_\theta s \cos\phi_1$$

or

$$\sigma_{\phi,1} = \frac{\sigma_{\phi,2}(r_2\cos(\phi_2-\phi_1) - 1/2\, \nu s \cos\phi_1) - \tau_{\phi,2} r_2 \sin(\phi_2-\phi_1) - E\epsilon_\theta s \cos\phi_1}{r_1 + 1/2\, \nu s \cos\phi_1}$$

$$= \frac{\sigma_{\phi,2}\, a - \tau_{\phi,2} r_2 \sin(\phi_2-\phi_1) - E\epsilon_\theta s \cos\phi_1}{r_1 + 1/2\, \nu s \cos\phi_1} = \frac{C}{F} \qquad (12)$$

where a, C, and F are introducted for convenience in the numerical computations.

No practical advantage is gained in writing the explicite term for σ_θ; it is more convenient for the numerical computations to take σ_θ from (7), giving

$$\sigma_\theta = \nu\sigma_{\phi,o} + E\epsilon_\theta \qquad (13)$$

Finally $\tau_{\phi,1}$ is taken from the first of the equations (6):

$$\tau_{\phi,1} r_1 \sin(\phi_o-\phi_1) = A - \sigma_{\phi,1} r_1 \cos(\phi_o-\phi_1) - \sigma_\theta s \cos\phi_o$$

$$\tau_{\phi,1} = \frac{A - \sigma_{\phi,1} r_1 \cos(\phi_o-\phi_1) - \sigma_\theta s \cos\phi_o}{r_1 \sin(\phi_o-\phi_1)} = \frac{G}{H} \qquad (14)$$

Modification of the Theory for Application to a Flange

For a dome with a flat flange it is necessary to develop formulas for flat rings. As an intermediate step consider the case that the ring becomes conical (Figure B-8), so that,

$$\phi_1 = \phi_2 = \phi_o$$

Equations (3) reduce to

$$\left.\begin{aligned} N_{\phi,2} r_2 - N_{\phi,1} r_1 - N_\theta s \cos \phi_o &= 0 \\ Q_{\phi,2} r_2 - Q_{\phi,1} r_1 + N_\theta s \sin \phi_o &= 0 \\ M_{\phi,2} r_2 - M_{\phi,1} r_1 - M_\theta s \cos \phi_o - Q_{\phi,1} r_1 s + 1/2\, N_\theta s^2 \sin \phi_o &= 0 \end{aligned}\right\} \quad (15)$$

Equations (7) - (10) remain unchanged.

When the ring is cut open, the ends moves a distance δ relative to each other, δ taken positive for separation; the radius to the middle surface changes from r_o to $r_o{}^*$ and the radius of curvature changes from ρ_2 to $\rho_2{}^*$. By this operation, the length of the periphery of the circle through C in the middle surface changes from

$$p = 2\pi r_o$$

to

$$p^* = 2\pi r_o{}^* = p + \delta = 2\pi r_o + \delta$$

hence

$$r_o{}^* = r_o + \frac{\delta}{2\pi}$$

Ignoring the very small change in ϕ_o the radii of curvature before and after the cut become

$$\rho_2 = \frac{r_o}{\sin \phi_o}$$

$$\rho_2{}^* = \frac{r_o{}^*}{\sin\phi_o} = \frac{r_o + \frac{\delta}{2\pi}}{\sin\phi_o} = \rho_2 + \frac{\delta}{2\pi \sin\phi_o} \quad (16)$$

and

$$\rho_2{}^* - \rho_2 = \frac{\delta}{2\pi \sin\phi_o}$$

The change in curvature, reckoned from the cut (stress-free) position to the uncut (stressed) position is

$$\left.\begin{aligned} \frac{1}{\rho_2^*} - \frac{1}{\rho_2} &= \frac{\rho_2 - \rho_2^*}{\rho_2^* \, \rho_2} \simeq \frac{\rho_2 - \rho_2^*}{\rho_2^2} = -\frac{\delta}{2\pi \sin\phi_o} \frac{\sin^2\phi_o}{r_o^2} \\ &= -\frac{\delta}{2\pi r_o^2} \sin\phi_o . \end{aligned}\right\} \quad (17)$$

The assignment of the sign to the relative displacement δ was actually arbitrary, while the sign convention used for forces and moments follows TWK. It is, therefore, now necessary to examine the sign relationship before associating the changes in curvature with a bending moment. It is seen from Figure B-9, that a positive δ corresponds to an existing negative moment M_θ and a negative change in curvature.

Hence, from the generaly theory of bending

$$\frac{1}{\rho_{2*}} - \frac{1}{\rho_2} = \frac{M}{EI} = \frac{M_\theta s}{EI} = \frac{M_\theta s}{E \; 1/12 \; sh^3} = \frac{12 M_\theta}{Eh^3} \quad (18)$$

and with (17)

$$\frac{12 \; M_\theta}{Eh^3} = -\frac{\delta}{2\pi \; r_o^2} \sin\phi_o$$

$$M_\theta = -\frac{Eh^3}{24\pi} \frac{\sin\phi_o}{r_o^2} \delta \quad (19)$$

For $\phi_o = 90^o$ the cone becomes a cylinder, and

$$M_\theta = -\frac{Eh^3}{24\pi} \frac{\delta}{r_o^2} \quad (20)$$

For $\phi_o = 0^o$ and $\sin\phi_o = 0$, the cone becomes a flat ring, and

$$M_\theta = 0 \quad (21)$$

unless the ring warps out of its plane when cut.

Now returning to the equations (15) in the case of a flat ring, they further reduce to

$$\left.\begin{aligned} N_{\phi,2}r_2 - N_{\phi,1}r_1 - N_\theta s &= 0 \\ Q_{\phi,2}r_2 - Q_{\phi,1}r_1 &= 0 \\ M_{\phi,2}r_2 - M_{\phi,1}r_1 - M_\theta s - Q_{\phi,1}r_1 s &= 0 \end{aligned}\right\} \quad (22)$$

Since $Q_{\phi,2} = 0$ for the outer ring, all Q's are zero for all the following flat rings. Since from (21) $M_\theta = 0$, the last of the equations reduces to

$$M_{\phi,2}r_2 - M_{\phi,1}r_1 = 0 \qquad (23)$$

and since $M_{\phi,2} = 0$ for the outer ring, all M_ϕ's are zero for all the following flat rings.

With (5) the first of the equations (22) is converted to

$$\sigma_{\phi,2}r_2 - \sigma_{\phi,1}r_1 - \sigma_\theta s = 0 \qquad (24)$$

which together with (7) - (10) can be solved for $\sigma_{\phi,1}$ and σ_θ, because $\sigma_{\phi,2}$ is a known quantity for each individual ring in the same manner as explained in connection with equation (5a).

Rearranged, the equations become

$$\left.\begin{aligned} \sigma_{\phi,1}r_1 + \sigma_\theta s &= \sigma_{\phi,2}r_2 \\ 1/2\,\sigma_{\phi,1}\mu - \sigma_\theta &= -1/2\,\sigma_{\phi,2}\nu - E\epsilon_\theta \end{aligned}\right\} \quad (25)$$

with the solution

$$\left.\begin{aligned} \sigma_{\phi,1} &= \frac{(r_2 - 1/2\,\nu s)\sigma_{\phi,2} + E\epsilon_\theta s}{r_1 + 1/2\,\nu s} \\ \sigma_\theta &= \frac{1/2\,\nu(r_1 + r_2)\sigma_{\phi,2} + E\epsilon_\theta s}{r_1 + 1/2\,\nu s} \end{aligned}\right\} \quad (26)$$

While the flat rings, when they stay flat after the second stage of sectioning, do not contain moments M_ϕ and M_θ perpendicular to their own plane, they still contain a moment M_a in their own plane. This is a case of a cylindrical ring, for which equation (20) was developed. In the present case, the axial "width" of the ring is h and the radial "thickness" is s, hence

$$M_a = -\frac{Es^3}{24\pi} \frac{\delta}{r_o^2} \tag{27}$$

The stresses from M_a are obtained by division by $1/6\ s^2$, and are with the adopted sign convention (see Figure B-9)

$$\left.\begin{matrix}\sigma_{B,\theta,1} \\ \\ \sigma_{B,\theta,2}\end{matrix}\right\} = \pm \frac{M_a}{\frac{1}{6}s^2} = \mp \frac{E}{4\pi} \frac{s}{r_o^2}\delta \tag{28}$$

which, when combined with the value for σ_θ from (26) give the stresses at the edges of the ring.

Experimental Work and Results

An application of the method described has been made on a dome. The material was low-carbon steel of 0.100 inch nominal thickness; the blank diameter was 11-3/4 inch, and the dome was formed in a 6-inch diameter free-forming die to a depth (deflection) of 1.8 inch. The dome contour is shown in Figures B-13 and B-14.

The grid shown in Figure B-1 was applied to the blank.

The circles 8, 16, 24 etc. as indicated in the figures were selected as measuring circles. Sectioning was performed along circles 4, 12, etc. The rings after first and second sectioning stage are shown in Figures No. B-10 and B-11. The coordinate cathetometer with the dome in measuring position is shown in Figure B-12.

The diameter change Δ D and the relative motion δ of the free ends were measured. The results are shown graphically in the curves in Figure B-13. The distribution of the resulting normal and shearing stresses is shown graphically in Figure B-14.

The stress at circle No. 2 cannot be calculated from the general theory because the circle is located in the center cap, not on a ring. The resultant of all normal forces on a diametral section of the dome must be zero. The total of all normal forces on the rings 8 through 90 is not exactly zero. The stress at circle No. 2 is, then, calculated in such a way that it compensates for this small difference and makes the resultant over the complete section equal to zero. The point is plotted in Figure B-14. It is seen, that it fits well with the curve and thus provides a final check on the computation.

TABLE B-I

NOTATIONS

r, θ	Polar coordinates in planes perpendicular to dome axis.
r_1, r_2, r_o	Radii to the middle surface, located at the inner (upper) or outer (lower) edge of a ring or at the middle circle.
ϕ	Slope of tangent to meridional contour of dome, equal to the angle between the normal to the contour and the axis of the dome.
1, 2, o	Subscripts 1, 2, o applied to ϕ have the same meaning as explained for radii r.
ρ_1, ρ_2	Principal radii of curvature
D	Diameter measured on a ring
ΔD	Change in diameter caused by first stage of sectioning
δ	Relative motion of adjacent points in a ring caused by second-stage of sectioning.
ϵ (with subscripts)	Components of elastic strain
N_ϕ	Normal force per unit length of a normal section along a parallel circle, acting in the direction of the tangent to the meridional contour.
N_θ	Normal force per unit length of a radial section, acting in the direction of the tangent to the parallel circle.
Q_ϕ	Shearing force per unit length of a normal section along a parallel circle, acting in the direction of the normal to the meridional contour.
M_ϕ	Bending moment per unit length of a radial section.
σ_ϕ	Normal stress component on a normal section along a parallel circle, acting in the direction of the tangent to the meridional contour.
σ_θ	Normal stress component on a radial section, acting in the direction of the tangent to the parallel circle.

TABLE B-I (Cont.)

τ_ϕ	Shearing stress component on a normal section along a parallel circle, acting in the direction of the normal to the meridional contour.
1, 2, o	Subscripts 1, 2, o applied to N_ϕ, σ_ϕ, Q_ϕ, τ_ϕ, and M_ϕ have the same meaning as explained for radii r.
E	Modules of elesticity, taken as 30×10^6 psi.
ν	Poisson's ratio, taken as 0.29.

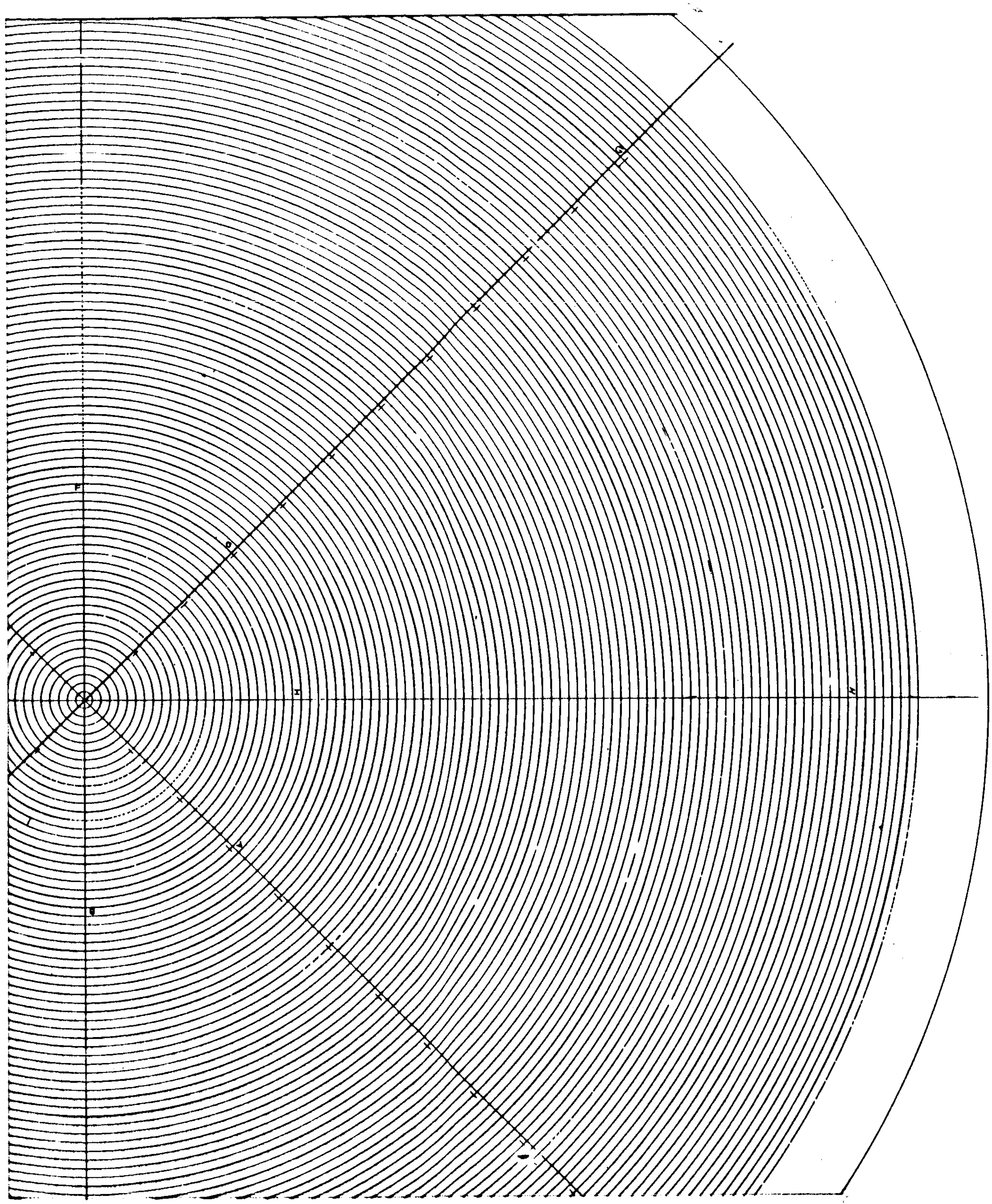

FIGURE B-1. Sample of Photogrid

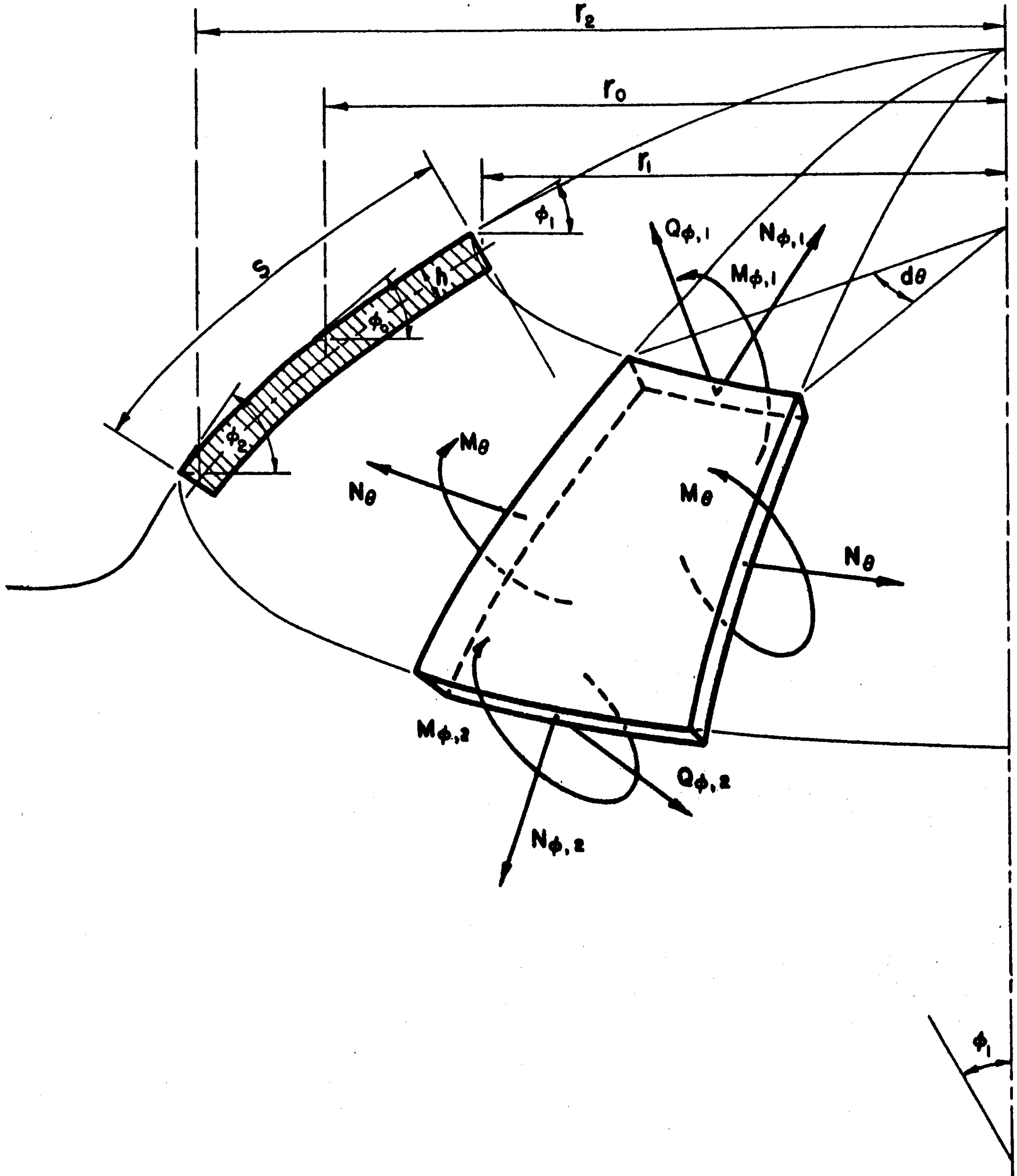

FIGURE B-2. Dome with Element of Finite Length

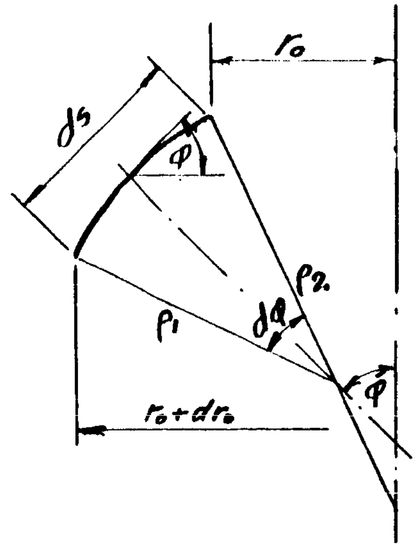

FIGURE B-3. Infinitely Small Element

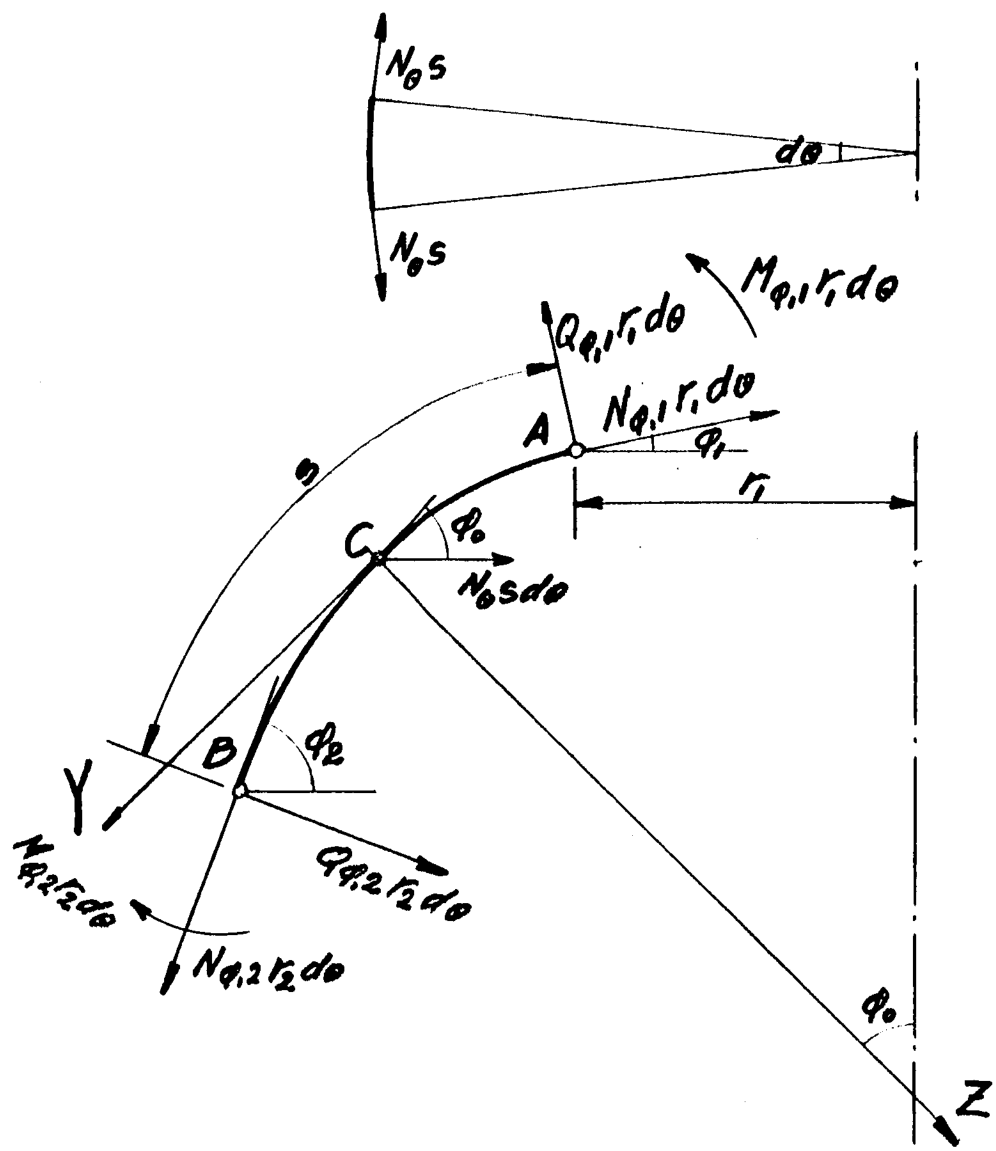

FIGURE B-4. Force Components

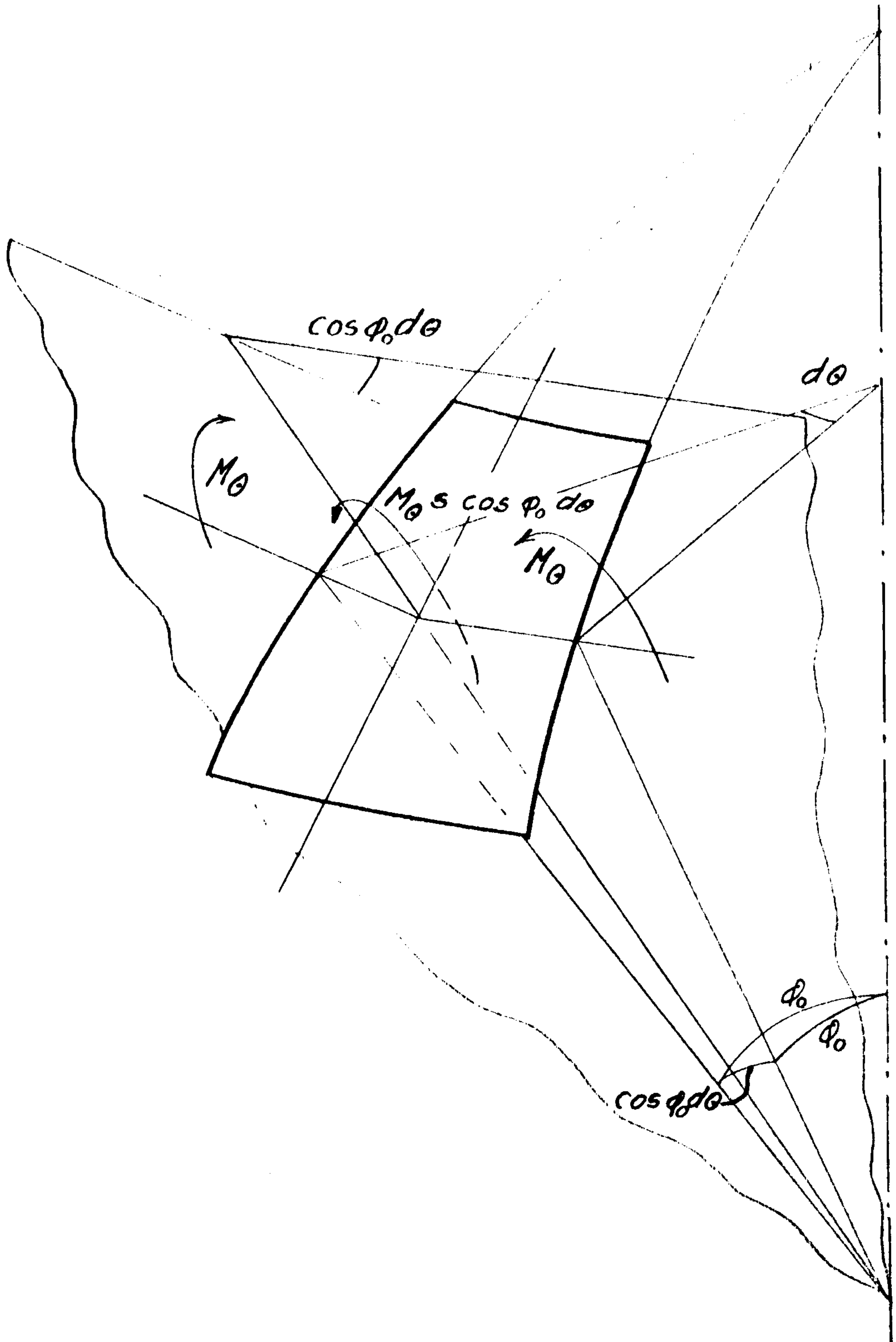

FIGURE B-5. Moment Components, M_{θ}, with Resultant Moment

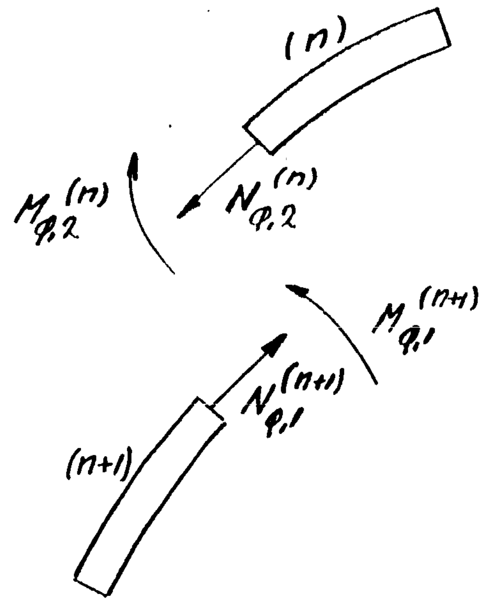

FIGURE B-6. Continuity of Forces and Moments

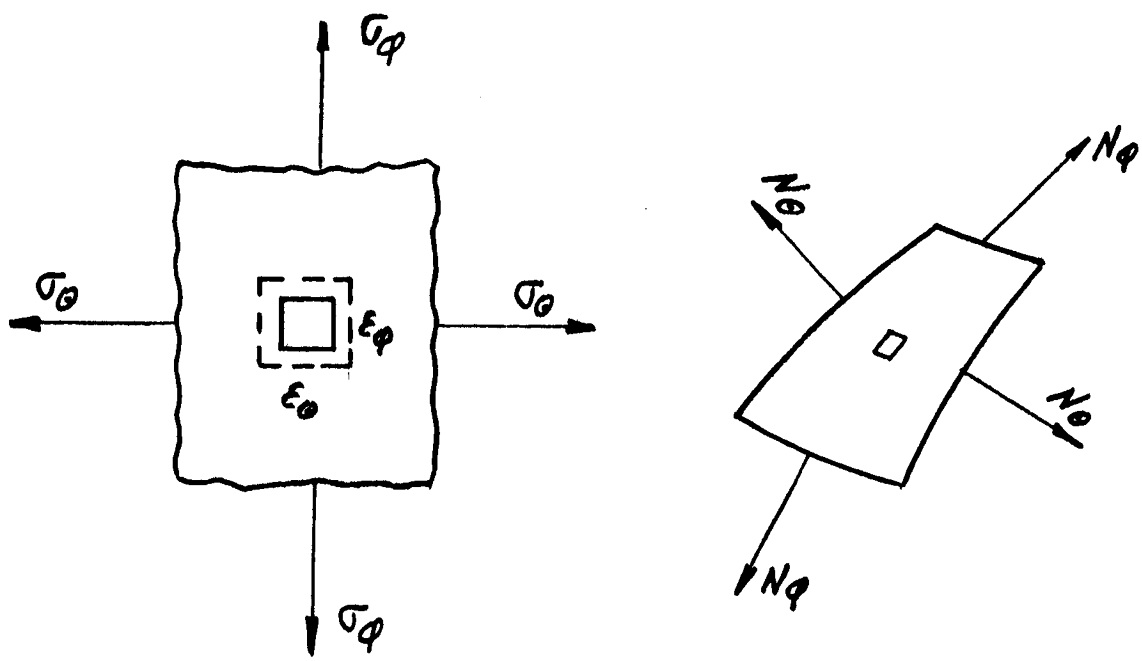

FIGURE B-7. Location of Stressed Element

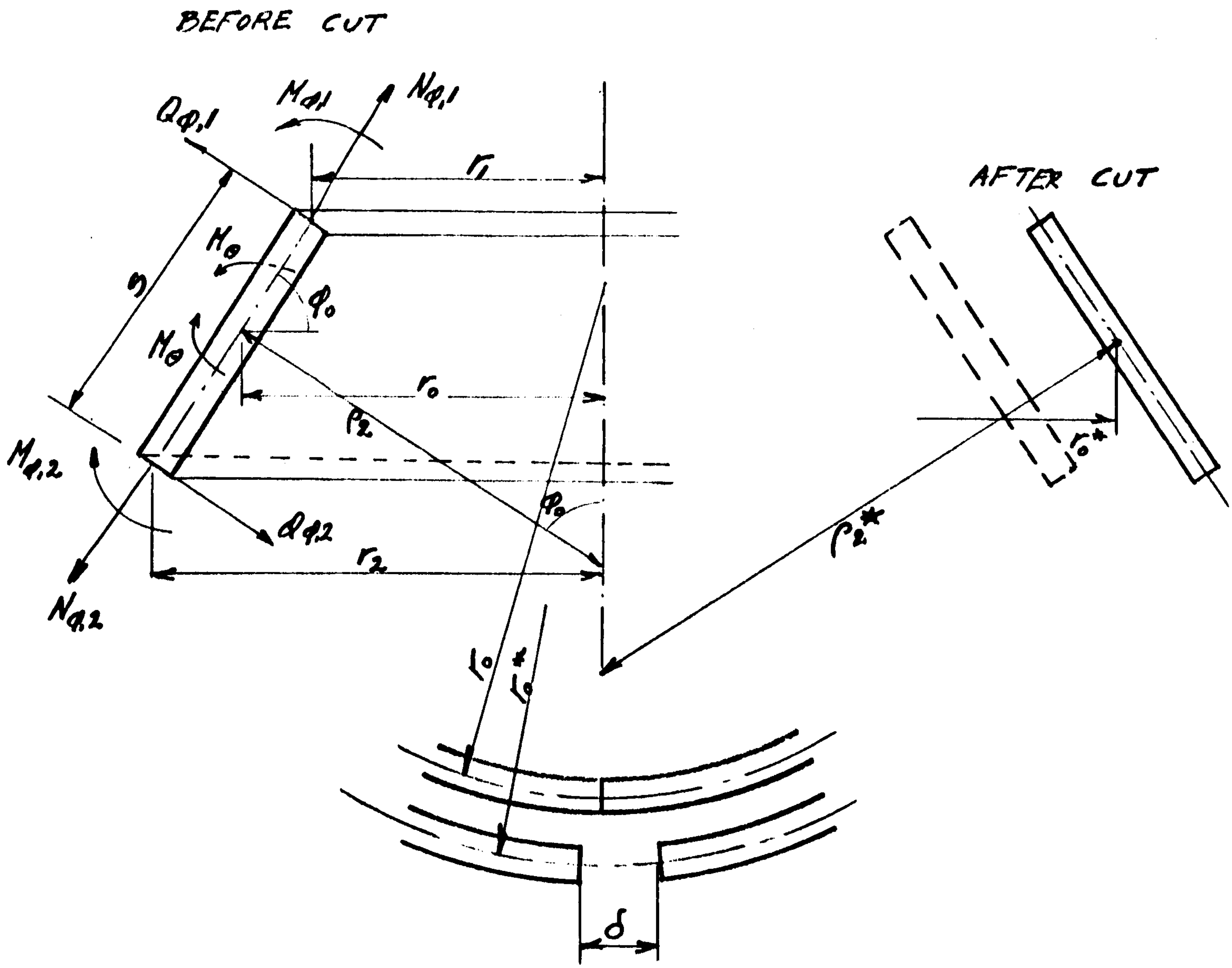

FIGURE B-8. Analysis of Conical Ring

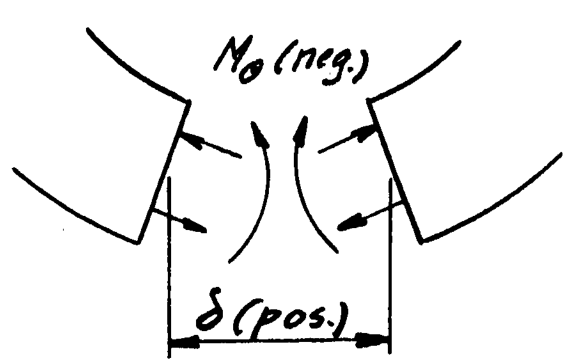

FIGURE B-9. Size Convention for Moments, M_θ

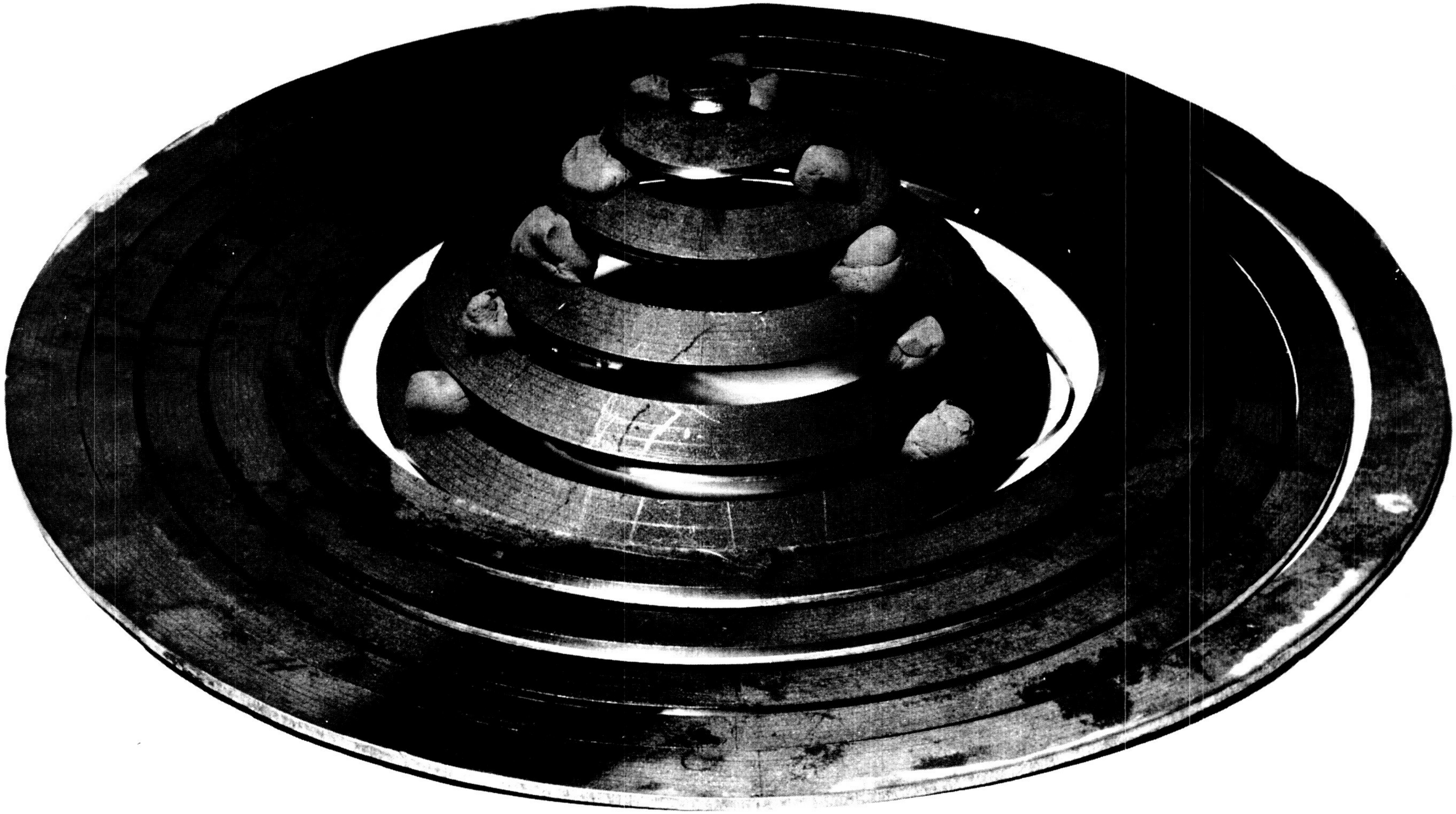

FIGURE B-10. Rings after First Sectioning

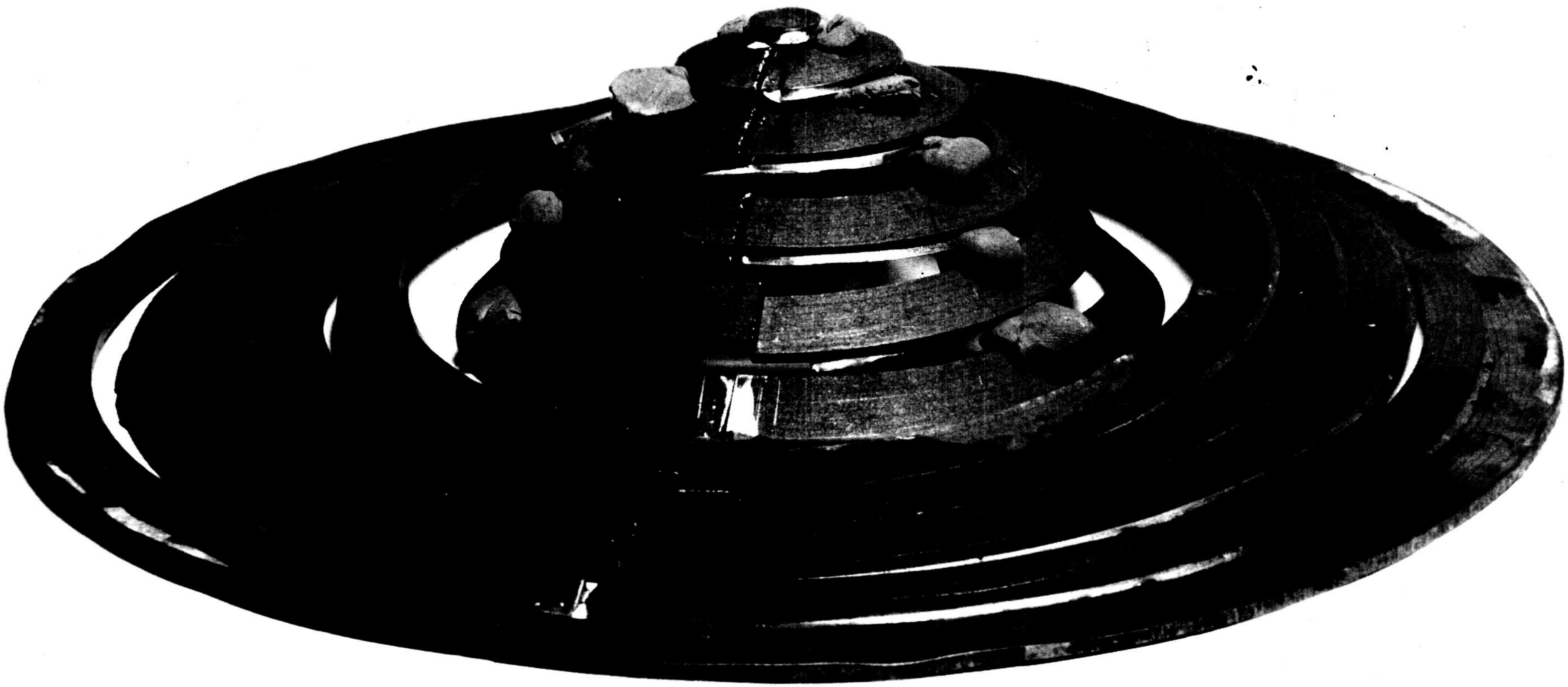

FIGURE B-11. Rings after Second Sectioning

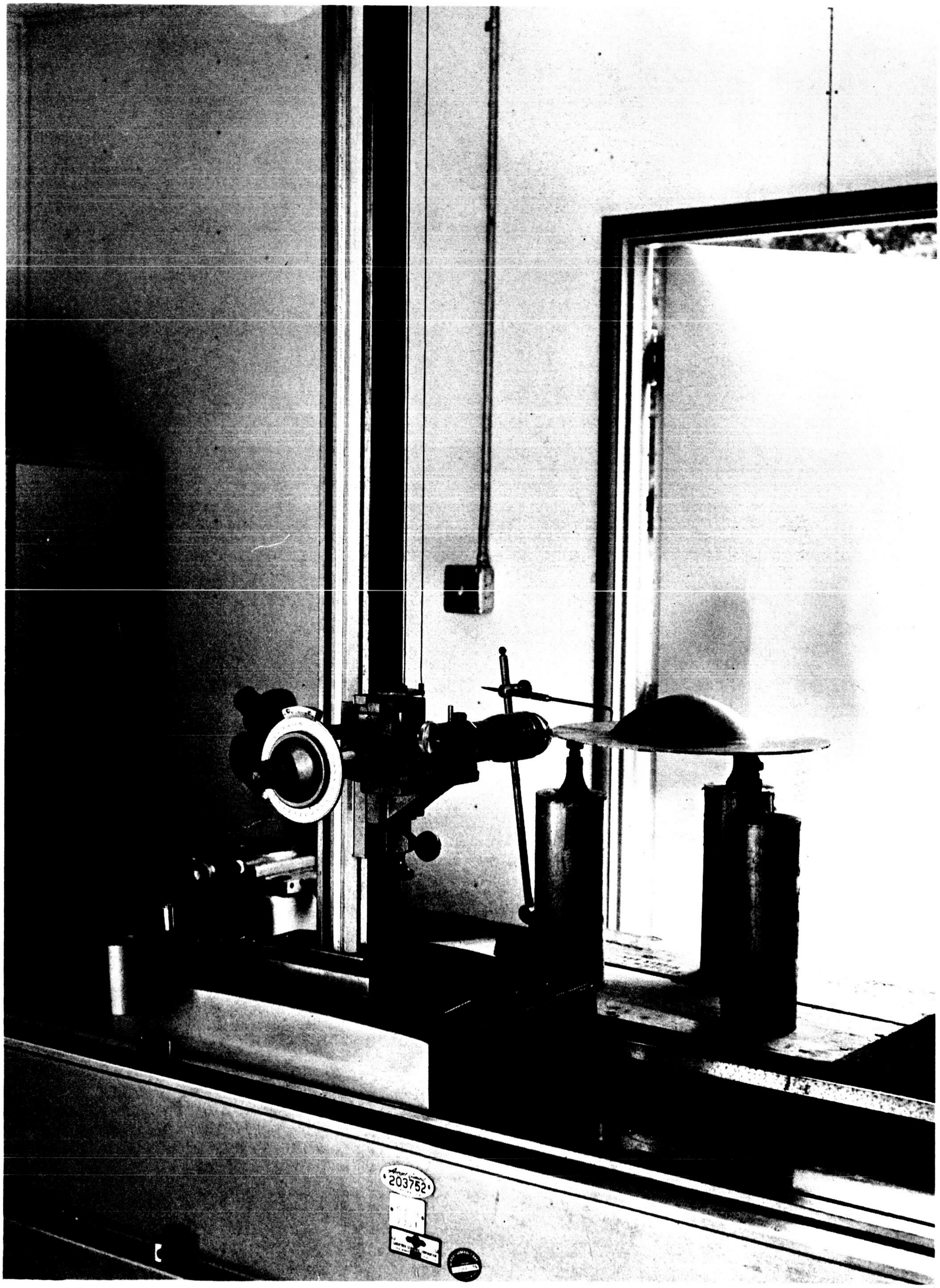

FIGURE B-12. Coordinate Cathetometer

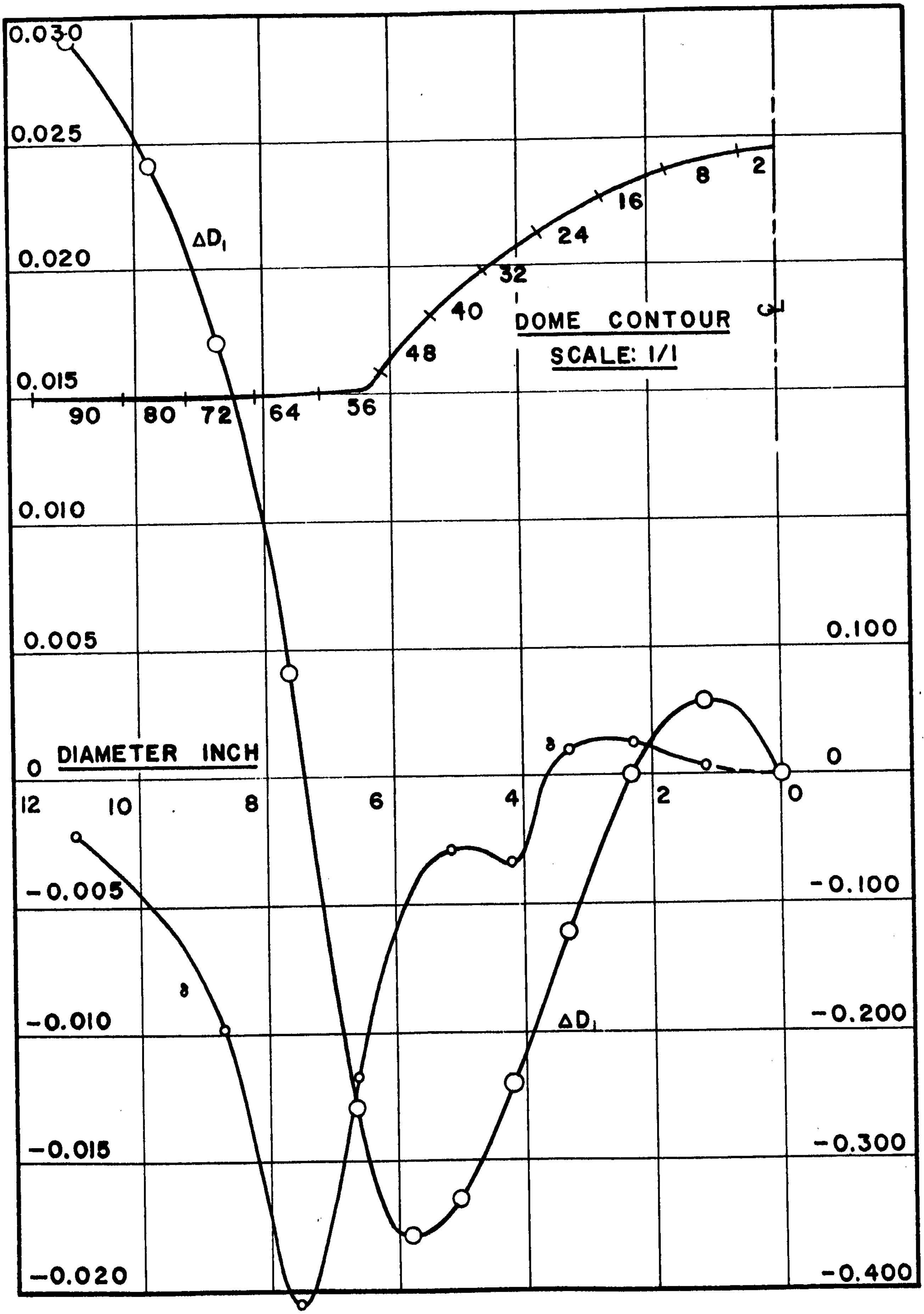

FIGURE B-13. Measured Deformations

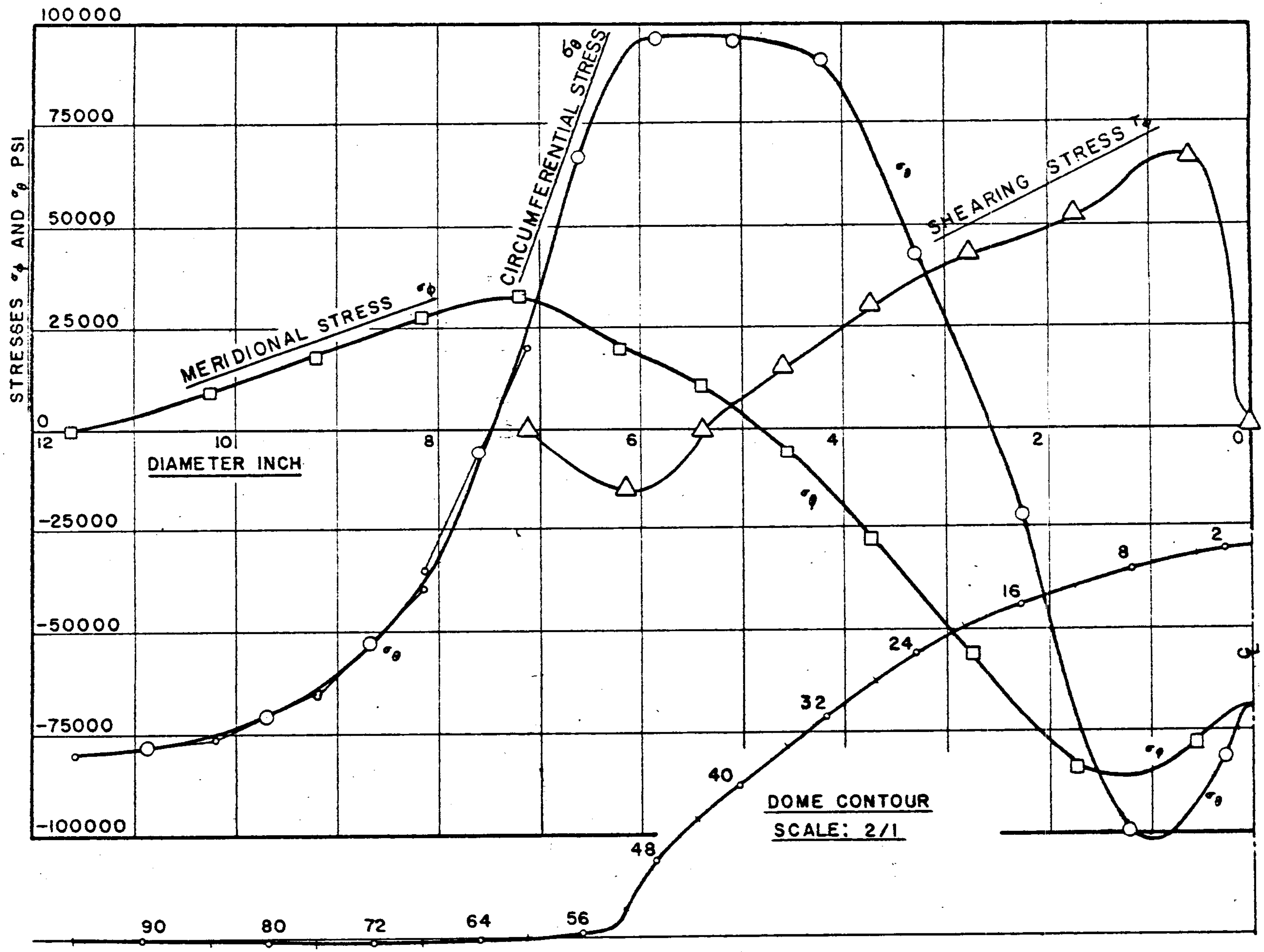

FIGURE B-14. Calculated Normal and Shearing Stresses